Impact Assessment of Climate Change on Hydro-meteorological Processes and Water Resources of Mahanadi River Basin

No. 16/22/2016-R&D/4015-4032

PROJECT COMPLETION REPORT
Submitted to

Indian National Committee on Climate Change (INCCC)
Ministry of Jal Shakti, Department of Water Resources
Government of India

Investigators:

Dr. V. V. Srinivas & Dr. D. Nagesh Kumar
Indian Institute of Science, Bangalore – 560012
(Lead Institute)

&

Dr. Arindham Sarkar
Indian Institute of Technology, Bhubaneshwar – 751013
(Partner Institute)

January 2023

Impact Assessment of Climate Change on Hydro-meteorological Processes and Water Resources of Mahanadi River Basin

No. 16/22/2016-R&D/4015-4032

1) **Title of the project**: Impact Assessment of Climate Change on Hydro-meteorological Processes and Water Resources of Mahanadi River Basin

2) **Name of the Lead Institution**: Indian Institute of Science, Bangalore

3) **Name of the Partner Institution**: Indian Institute of Technology, Bhubaneswar

4) **Investigators:** Dr. V. V. Srinivas & Dr. D. Nagesh Kumar
Department of Civil Engineering
Indian Institute of Science, Bangalore – 560012
(Lead Institute)

Dr. Arindham Sarkar
School of Infrastructure
Indian Institute of Technology, Bhubaneshwar – 751013
(Partner Institute)

5) **Acknowledgements:** Investigators duly acknowledge financial support provided by the Ministry of Jal Shakti, Department of Water Resources, Government of India, for the execution of the project.

6) **Date of Sanction & No.**: 16/22/2016-R&D/4015-4032 dated November 7, 2016

7) **Date of Order & No.**: 28/1/2016-R&D/228-245 dated February 8, 2018

8) **Duration of Project:** 4 years and 10 months
- Probable date of completion (PDC)
  - **Original:** 6th March 2021 (i.e., three years from the date of receipt of the first installment of the grant at IISc & IIT Bhubaneshwar)
  - **Revised**: 30th June 2022
    - Extension till 31.12.2021 (Ref. Ministry of Jal Shakti order No.28/1/2020-R&D/ dated 11th October 2021), due to delays related to the pandemic and non-release of 2nd and 3rd Installments of the grant towards salaries for the project team at IISc.
    - Extension till 30th June 2022 (Ref. Ministry of Jal Shakti order No.28/1/2020-R&D/ dated May 30, 2022), due to the reason mentioned above.

9) **Total Project Cost:** Rs.1,25,64,839 (IISc: Rs.99,40,141; IIT-BBS: Rs.26,24,698)

10) Sanctioned Amount: Rs. 74,61,781 (IISc: Rs.58,98,661; IIT-BBS: Rs.15,63,120)

1st year: Rs.68,60,221 (IISc: Rs.58,98,661; IIT-BBS: Rs.9,61,560) (Ref. Ministry of Water Resources, RD & GR, order No.28/1/2016-R&D/ 228-245 dated 8th February 2018)

2nd year: Rs.6,01,560 (IISc: NIL; IIT-BBS: Rs.6,01,560) (Ref. Ministry of Jal Shakti order No.28/1/2016-R&D/ 208-224 dated 23rd March 2020)

11) Total Expenditure: IISc: Rs. 60,55,995/-
IITBBS: Rs. 18,40,737/-

12) Significant Achievements/Deliverables (in terms of human resource development; patent; innovation; skill upgradation; publications etc):

(i) **Human resource development**: The following project staff and research students have been trained as part of this project.

Project Staff Trained at IISc

Name of Research Staff & Designation	Period of Employment
Ms. Nruthya, K (Senior Research Fellow, SRF)	3.5 months (28-05-2018 to 16-09-2018)
Dr. Shwetha, H. R (Research Associate, RA-1)	4.0 months (28-05-2018 to 25-09-2018)
Dr. Gouri R Laxmeshwar (Research Associate, RA-1)	7.5 months (29-08-2018 to 14-04-2019)
Mr. Kranthi Kumar Reddy (Project Associate)	12 months (24-09-2018 to 23-09-2019)
Ms. Shefali Gupta (Junior Research Fellow, JRF)	25 months (18-02-2019 to 31-03-2021)
Ms. Soumya S Nyamathi (Junior Research Fellow, JRF)	8 months (21-09-2020 to 10-05-2021)

Man-months sanctioned for IISc for the period from the date of sanction of the project (February 8, 2018 to February 7, 2021)

=36 months × 2 staff/month = 72 man-months

Cumulative Man-months utilized by IISc: 60 man-months.

Project Staff Trained at IIT Bhubaneswar

Name of Research Staff & Designation	Period of Employment
Mr. Rohan Kar (Senior Research Fellow, SRF)	34 months (10-05-2018 to 03-03-2021)

Man-months sanctioned for IITBBS for the period from the date of sanction of the project

= 36 man-months

Cumulative Man-months utilized by IITBBS: 34 man-months.

Research Students (Degree Awarded at IISc)

1) Kiran, K. G. (Ph.D)
2) Swapan Kumar Masanta (Ph.D)
3) Sreeparvathy Vijay (Ph.D)
4) Sarath Muralidharan [M.Tech (Research)]

Research Students (Degree Awarded at IITBBS)

1) Mr. Rohan Kar (Ph.D.)

(ii) Publications

Journal papers

1) Kiran K. G. and Srinivas V. V. (2021b) Fuzzy Ensemble Clustering Approach to Address Regionalization Uncertainties in Flood Frequency Analysis, Water Resources Research, American Geophysical Union & Wiley, Vol. 57, Issue 3, March 2021, e2020WR028412, https://doi:10.1029/2020WR028412

2) Kiran K. G. and Srinivas V. V. (2021a) A Mahalanobis distance based automatic threshold selection method for Peaks Over Threshold (POT) model, Water Resources Research, American Geophysical Union & Wiley, Vol. 57, Issue 1, January 2021, e2020WR027534, https://doi:10.1029/2020WR027534

3) Kiran, K. G., & Srinivas, V. V. (2022). Multivariate regional frequency analysis using conditional extreme values approach. Water Resources Research, 58, e2021WR031095. https://doi.org/10.1029/2021WR031095

4) Swapan Kumar Masanta and Srinivas, V. V. (2020a), Regionalization of evapotranspiration using fuzzy dynamic clustering approach. Part 1: Formation of regions in India. International Journal of Climatology, Wiley & Royal Meteorological Society, Vol. 40, Issue 7, pp.3514-3530, June 2020, https://doi.org/10.1002/joc.6411

5) Swapan Kumar Masanta and Srinivas, V. V. (2020b) Regionalization of evapotranspiration in India using fuzzy dynamic clustering approach. Part 2: Applications of regions, International Journal of Climatology, Wiley & Royal Meteorological Society, pp.1-25, https://doi.org/10.1002/joc.6773

6) Sreeparvathy, V., Srinivas, V. V., (2020), A fuzzy entropy approach for design of hydrometric monitoring networks. Journal of Hydrology, Elsevier, Netherlands, Vol. 586, pp.1-18, July 2020, 124797. https://doi.org/10.1016/j.jhydrol.2020.124797

7) Kar, R., & Sarkar, A. (2021), Anthropogenic influences on the variation of runoff and sediment load of the Mahanadi River basin. Hydrological Sciences Journal, 66(12), 1820–1844. https://doi.org/10.1080/02626667.2021.1967957

8) Kar, R., & Sarkar, A. (2022), Potential predictability of suspended sediment concentration in the data constrained regions of the Mahanadi River basin, Eastern India. International Journal of River Basin Management, 1–45. https://doi.org/10.1080/15715124.2021.2016782

9) Kar, R., & Sarkar, A. (2023). Assessment of the fraction of bed load concentration towards the sediment transport of a large river basin of Eastern India. (In Press)

10) Swapan Kumar Masanta and Srinivas, V. V. (2023) Future regional projections of potential evapotranspiration and fresh water availability in India using CMIP6 GCMs (manuscript in preparation)

Book Chapters

Kiran, K. G., and Srinivas V. V. (2022), Effect of identification of extremes on regional flood frequency analysis. In: Dikshit, A. K., Narasimhan, B., Kumar, B, Patel, A. K (Eds.), Innovative trends in hydrological and environmental systems: Select Proceedings of ITHES 2021, Lecture Notes in Civil Engineering, Vol. 234, Springer Nature Singapore, ISBN: 978-981-19-0303-8, June 2022, 329-340, https://doi.org/10.1007/978-981-19-0304-5_24.

Kar, R., & Sarkar, A (2022). Impact of Anthropocene on the Fluvial Sediment Supply: The Mahanadi River Basin Perspective. In: Pandey, M., Azamathulla, H., Jaan, H.P. (eds) River Dynamics and Flood Hazards: Studies on Risk and Mitigation. Disaster Resilience and Green Growth. Springer, Singapore. https://doi.org/ 10.1007/978-981-19-7100-6_14.

Patel, P., Kar, R., & Sarkar, A. (2022). Estimation of velocity index for flow calculation in open channels using geometric and hydraulic characteristics. Lecture Notes in Civil Engineering. Springer (Accepted)

Conferences

1) Kiran, K.G., Srinivas, V. V., Effect of identification of extremes on regional flood frequency analysis. International Conference on Innovative Trends in Hydrological and Environmental Systems (ITHES 2021), NIT Warangal, April 28-30, 2021.

2) Swapan Kumar Masanta and Srinivas V. V. (2020) Development of Nonstationary Standardized Precipitation-Evapotranspiration Drought Index (nSPEI) using climate indices as covariates. AGU Fall meeting (Online), 1-17, December 2020, H136-0003, https://agu.confex.com/agu/fm20/prelim.cgi/Paper/717311

3) Kiran K. G. and Srinivas V.V. (2020) A transformation-based method for automatic threshold selection in Peaks Over Threshold (POT) approach. AGU Fall meeting (Online), 1-17, December 2020, H172-0002, https://agu.confex.com/agu/fm20/prelim.cgi/Paper/727827

4) Jaya Bhatt and Srinivas V. V. (2020) Non-stationary Hershfield method for probable maximum precipitation estimation. AGU Fall meeting (Online), 1-17, December 2020, H172-0017, https://agu.confex.com/agu/fm20/prelim.cgi/Paper/737719

5) Sarath, M. and Srinivas, V. V. (2019) Short to medium range probabilistic streamflow forecasting for Tel river using the Hydrologic Ensemble Forecast Service. In proceedings of 'National conference on flood early warning for disaster risk reduction', Organised by NRSC, & CWC under National Hydrology Project, 30-31 May 2019, Hyderabad, pages 80-87.

6) Kar, R., & Sarkar, A. (2022). Geomorphic response of the mid-Mahanadi River towards inflowing runoff and sediment load variation. HYDRO 2022 International on December 22- 24, 2022, Chandigarh, India.

Table of contents

Table of contents (Continued…)

Table of contents (Continued…)

Executive Summary

Information on hydro-meteorological variables, hydrological processes and water resources in a river basin under the current conditions and possible impact on the same under future climate change scenarios is essential to address a wide spectrum of environmental, ecological, and water-related issues. Investigations were carried out to discern evidence of nonstationarity in hydrometeorological variables at daily, monthly and annual scales, and in annual maxima of precipitation and streamflows at daily scale. In general, various tests indicated nonstationarity in records of hydrometeorological variables for the majority of grids in the Mahanadi basin at the daily scale. The results obtained at both monthly and annual scales were almost consistent in indicating non-stationarity in wind speed, but stationarity in PET and minimum temperature for the majority of the grids. However, the results were contrasting for relative humidity, maximum temperature, and solar radiation for individual grids. Non-stationarity in annual precipitation, stationarity in annual maximum daily precipitation and peak flows was also evident at majority of locations. At regional scale, significant decreasing trend in wind speed and increasing trend in net solar radiation was evident at both annual and seasonal scales, and among the seasons decrease in wind speed was found to be the highest mostly during monsoon. The decrease in wind speed could be attributed to an increase in surface roughness owing to anthropogenic factors, which is widely referred to as global stilling effect. A significant increasing trend in mean daily Tmax was evident for (i) two seasons (post monsoon and pre-monsoon) in south, central and west part of the basin, and (ii) all the seasons in the deltaic region adjoining Bay of Bengal.

Hydrological processes in the Mahanadi river basin and its sub-basins are modeled using SWAT (Soil and Water Assessment Tool). Sensitive parameters influencing the hydrological processes in different sub-basins are identified for calibrating the SWAT model and the quantified water balance components (e.g., actual evapotranspiration, percolation, surface runoff, lateral flow, streamflow) are compared in terms of percentage of precipitation. The results indicate that variability of water balance components is high across different sub-basins. Estimates for ranges corresponding to Actual Evapotranspiration (AET), percolation, surface runoff, lateral flow and streamflow (in percentage of mean annual precipitation) were found to be 30%-71%, 3%-54%, 2%-49%, 0.2%-20%, and 24-52% respectively. At the river basin scale, the mean annual

precipitation is around 140 cm, whereas estimates corresponding to AET, percolation, surface runoff, return flow and lateral flow are about 48%, 20%, 49%, 13.4%, and 9.2% respectively. The validated model was forced with ensemble means of future projections of climate variables derived at 0.25° resolution from three GCMs (CanESM5 (2.7906°×2.8125°), INM-CM4-8 (1.5°×2°), and INM-CM5-0 (1.5°×2°)) to arrive at future projected streamflows in the basin corresponding to four CMIP6 climate change scenarios (SSP-1-2.6, SSP2-4.5, SSP3-7.0, and SSP5-8.5). The scenarios are also mentioned as SSPs 126, 245, 370 and 585 in the report, as noted in the literature. Scrutiny of plethora of CMIP6 GCMs indicated that only those three GCMs provide the necessary projections of various desirable climate variables. In general, streamflows are projected to increase in future for the scenarios. The increase is highest for SSP1-2.6 scenario in the initial two decades (2020-2040), thereafter it is highest for SSP5-8.5 scenario up to 2100. The impact of climate change on water availability at various gauging sites within the basin is investigated in terms of changes in flow duration curves. At majority of the stations, the future flows corresponding to different exceedance probabilities are projected to increase for all the climate change scenarios but there is no noticeable difference between the historical and future projected low flows. The increase is generally highest for SSP 5-8.5 scenario for major portion of the probability scale. Furthermore, the differences in FDCs corresponding to other SSP scenarios are marginal. In most of the sub-basins, the high flows (with exceedance probability lower than 1%) are projected to be highest in SSP3-7.0 scenario.

Water quantities needed for irrigation in an area are conventionally determined by taking into account evapotranspiration requirements. Hence, investigations are carried out on the Mahanadi basin to (i) discern prevailing regional patterns (homogeneous regions) of potential evapotranspiration (ET_0) and actual evapotranspiration (ET_a), (ii) determine regional trends and change point(s) of ET_0 and its predictor climate variables for the prevailing and future climate change scenarios, and (iii) identify key climate variables which govern ET_0 and annual surface runoff changes in various parts of the basin. For use in these investigations, new regionalization methodology is proposed in fuzzy framework, and an expression is derived for the third-order approximation of Taylor series expansion of ET_0. In addition, new relevance vector regression (RVR) relationships are developed to arrive at FAO-PM estimate of ET_0 in data-sparse areas of the basin. Investigations are also focused to examine validity of Bouchet's complementary relationship (i.e., feedback mechanism

between ET_0 and ET_a) for the basin, and to arrive at future projections for surface runoff changes over the basin using Budyko framework (which is an approximation of a complex rainfall-runoff process). Past regional change points of ET_0 and its predictor climate variables in a major part of the basin were noted in 1964 and over the period 1992-1997. Furthermore, the Bouchet's complementary relationship is found to be valid for the northeast part of the basin. At the annual scale, ET_0 and surface runoff are most sensitive to relative humidity (RH) followed by net solar radiation (Rad) and maximum temperature (Tmax). Wind speed mostly influences ET_0 changes in the basin. Among ET_0 and precipitation, variation of the latter is found to have more effect on surface runoff generated from the basin. In future period, Bouchet's complementary relationship was found to be valid for the basin for SSP-126 scenario. Future projections based on ensemble mean of the GCMs indicate an increase in freshwater availability (FWA) despite increase in ET_0, due to a significant increase in precipitation. Runoff estimate corresponding to CanESM5 was highest among the all three GCMs. The future FWA per capita is projected to increase significantly in the Mahanadi basin for SSP 126, 245 and 585 scenarios (due to high precipitation), and in contrast decrease significantly for the SSP-370 scenario (due to high population). The future projections of population obtained for different SSPs indicate an increase for all the SSPs up to the year 2050. Thereafter, it continues to increase up to 2100 for SSP-370 but decreases for other SSP-FS.

Mahanadi basin is frequently prone to floods triggered by extreme rainfall often associated with cyclones. Major floods were witnessed in 1855, 1933, 1937, 1955, 1980, 1982, 2001, 2003, 2006, 2008, 2011, 2013 causing substantial loss to life, property, and agricultural crops. Stationarity was evident in annual maximum daily precipitation and peak flows for the basin. Conventionally, the frequency analysis of hydrological extremes is performed based on the annual maximum series (AMS) of peak flows extracted from the available streamflow records. Peaks-over-threshold or Partial duration series (PDS) framework is deemed more efficient than AMS in depicting information on extremes. Despite its advantages, the use of PDS is less prevalent than AMS. It is due to the lack of a universally established systematic approach to select an appropriate threshold for PDS extraction. Various issues affect the performance of different methods available for threshold selection. A novel Mahalanobis distance-based automatic threshold selection method (MDM) is proposed to address those issues while extracting datapoints corresponding to hydrological extremes from the available records. CDFs of peak flows

constructed for stream gauge sites in the Mahanadi basin based on analysis with AMS and PDS extracted using the proposed MDM are compared. For majority of sites, PDS based flood quantile estimates are marginally higher for lower return periods (T<10 years) and considerably lower for higher return periods when compared to the corresponding estimates determined in analysis with AMS. Thus, design of civil infrastructure and risk analysis in the basin based on analysis with PDS (in lieu of conventional AMS) has implications.

In a previous study by Central Water Commission (CWC), the Indian subcontinent was delineated into 7 zones containing 26 contiguous sub-zones. The sub-zones are widely used by practitioners in India and the DRIP (Dam Rehabilitation and Improvement Project) initiative of CWC for flood estimation by considering them to be homogeneous. Sub-zone 3(d) containing Mahanadi basin is shown to be highly heterogeneous. To facilitate flood risk assessment at data sparse or ungauged locations, practitioners opt for Regional Frequency Analysis (RFA) approaches. They involve regionalization (locating groups/regions comprising resembling watersheds) and pooling of flood-related information from resembling watersheds to estimate desired flood quantile(s) at the target sites. Regionalization approaches are many, and their choice is ambiguous as none is established to be universally superior. They differ in their underlying assumptions and strategies and thus yield regions that vary in composition. A new entropy-based fuzzy ensemble clustering approach is proposed to address the uncertainty in regionalization. It forms effective fuzzy meta-regions by ameliorating information from regions derived using different procedures. The approach is used to identify groups of watersheds resembling those in the Mahanadi basin. Another important fact is that RFA of floods in a multivariate framework is deemed more appropriate, as floods can be better characterized by several correlated variables such as flood peak, volume, duration, and time to peak. However, RFA has received little attention in the multivariate framework. The available literature recommends using a multivariate extension of the index-flood-based approach, IFA (considering AMS), even though it has theoretical shortcomings. Against this backdrop, a novel multivariate RFA approach based on the conditional multivariate extreme values approach (CEA) is proposed. It facilitates flood risk assessment at sparsely gauged and ungauged locations by predicting the joint distribution of multiple flood-related variables using information pooled from resembling watersheds. Bivariate cumulative distribution functions (CDFs) are constructed for various sites in Mahanadi basin using at-site

frequency analysis and regional frequency analysis with CEA and IFA. The bivariate quantile estimates obtained using CEA for ungauged sites were found to be less biases than those obtained using IFA. The CDFs find use in multivariate risk analysis of civil infrastructure nearby those sites in the Mahanadi basin.

The Mahanadi basin receives uneven rainfall and drought prone areas are found in central part of the basin covering about 14 (5 of Chhattisgarh and 9 of Odisha) of 45 districts encompassing the basin. Future projections of ensemble means of PET and precipitation derived at 0.25° resolution from three GCMs (CanESM5 (2.7906°×2.8125°), INM-CM4-8 (1.5°×2°), and INM-CM5-0 (1.5°×2°)) were used to arrive at future projections of SPEI for near-future (2015-2040) and distant future (2041-2100) periods corresponding to 1-, 3- and 6-months Accumulation Periods (APs). The relative frequency (RF), mean annual critical severity and annual duration of droughts are projected to increase for future climate change scenarios when compared to historical period. The RF of occurrence was highest for moderate droughts and least for extreme droughts in the case of both historical and future climate change scenarios. The projected increase in RF of droughts is highest for SSP5-8.5 scenario and least for SSP1-2.6 scenario. When compared to far future (2041-2100), near future (2015-2040) is projected to experience droughts with highest RF, highest mean annual duration and mean annual critical severity. For SSP3-7.0 and SSP5-8.5 scenarios, the RFs of moderate drought events are projected to increase with accumulation period (AP) and they are found to be highest for SSP5-8.5 scenario with 6-month AP. Contrarily, the mean annual critical severity of droughts is found to be decreasing with increase in AP. The critical severity is found to be higher for SSP5-8.5 scenario in the near future period. Whereas in the case of far future, it is found to be highest for SSP1-2.6 scenario. Across all the APs considered, the mean annual duration of droughts for historical period is approximately 1-month. Across all the SSP scenarios considered, droughts events computed considering 6-month AP for SSP5-8.5 showed the highest mean annual drought duration.

Optimal hedging policies are developed for the operation of Hirakud reservoir in the Mahanadi basin by coupling fuzzy rule curve based hedging method with Borg multi-objective evolutionary algorithm (MOEA). Conventionally, multipurpose reservoir operation is guided by storage rule curves, which divide the reservoir storage into different zones for different purposes. Although such operation may be acceptable during normal years, it might lead to significant deficits for one or more purposes during droughts. Hedging policies are aimed at storing the water in the reservoir during the periods of

impending drought by accepting smaller deficits (hedging) and using it to reduce the likely risk of large deficits during the drought. To fuzzify the rule curves, transition rule curves are introduced around the original storage rule curves, wherein the hedging factors are varied linearly (within the transition zones) which helps the reservoir manager to gradually vary the releases with respect to change in initial storage.

Additionally, investigations are focused on detecting and quantifying trends and change points in the observed runoff and sediment load of the Mahanadi River basin, and also to explore the deltaic response due to the change in basin sediment yield and the related anthropogenic stresses influencing the evolution of delta. A suspended and bed sediment concentration model is proposed for the ungauged parts of the river basin. Finally, the implication of future sediment load on the capacity of the Hirakud reservoir is assessed. Overall, the following points could be summarized based on the investigations:

(i) The sediment load from the entire Mahanadi River basin has shown a significant decreasing trend (-0.511 Mt/yr) over the past forty-four years compared to the non-significant trend in the yearly runoff (-0.111 km^3/yr).

(ii) The quantitative figures of morphological changes (land lost and land gained) demonstrate that the coastal landforms susceptible to erosion are highly vulnerable. The quantitative role of various human interferences in reducing the yearly basin sediment load is nearly 40%. The significant anthropogenic stresses are identified as operations of large dams, increasing water allocation priorities for multiple industries, and diverse catchment soil conservation programs.

(iii) The findings demonstrate the distinct roles of factors impacting suspended sediment (SS) hysteresis loops during monsoon months across years and confirm the instability of the SS hysteresis loops. Linear mixed-effects models outperformed the traditional SS rating approach by increasing the mean covariance between observed and predicted data to nearly twice and significantly reducing the percentage bias across gauging stations in the Mahanadi basin.

(iv) The developed SS rating model provides accurate estimates for the larger area sub-catchments within the basin, but performs poorly at a station with a limited catchment area, where there is non-linearity in sediment transport with catchment area and other sampling problems.

(v) Bagnold's (1980) bed load functions performed most consistently in five of nine basin stations. Bed sediment is nearly 19% of suspended sediment concentration at the last gauging station of the basin. The sediments entering the Hirakud reservoir from the Mahanadi River account for approximately 5% of the reservoir's gross storage capacity.

Furthermore, a fuzzy entropy-based methodology is proposed for optimal design and performance assessment of hydrometric monitoring networks and it is used to arrive at an optimised hydrometric network for streamflow monitoring in the Mahanadi basin. Besides this, a model is developed for probabilistic riverine flood forecasting of daily streamflow from Tel river catchment in the Mahanadi basin using the Hydrologic Ensemble Forecast Service (HEFS). Finally, recommendations are made for the Mahanadi basin based on the investigations carried out in this study.

List of Tables

List of Tables (Continued…)

List of Tables (Continued…)

List of Figures

List of Figures (continued…)

List of Figures (continued…)

List of Figures (continued…)

List of Figures (continued…)

List of Figures (continued…)

List of Figures (continued…)

List of Figures (continued…)

Abbreviations

ADM: Anderson-Darling GoF test-based method

AET: Actual Evapotranspiration

AMS: Annual Maximum Series

AR-bias: Absolute Relative bias

ASTER: Advanced Spaceborne Thermal Emission and Reflection Radiometer

BLT: Bed Load Transport

BM: Block Maxima

CA: Clustering Approach

CartoDEM: Cartosat-1 digital elevation models

CCA: Canonical Correlation Analysis

CDFs: Cumulative Distribution Functions

CEA: Conditional Extreme values Approach

CFSR: Climate Forecast System Reanalysis

CMEV: Conditional Multivariate Extreme Values

CR: Complementary relationship

CRPSS: Continuous Ranked Probability Skill Score

CUP: Calibration and Uncertainty Programs

CWC: Central Water Commission

DEM: Digital Elevation Model

DoD: Digital Elevation Models of difference

DoWR: Department of Water Resources

DSAS: Digital Shoreline Assessment System

ET_0: Potential evapotranspiration

ET_a : Actual evapotraspiration

FAO: Food and Agricultural Organisation

FDCs: Flow duration curves

FEC: Fuzzy Ensemble Clustering

FRCH: Fuzzified Rule-curve based hedging

FWA: Fresh Water Availability

GCD: Geomorphic Change Detection

GCMs: General Circulation Models

GEFS: Global Ensemble Forecast System

GEV: Generalized Extreme Value

GFCM: Global fuzzy c-means

GHF: Ground Heat Flux

GIS: Geographic Information System

GLCC: Global Land Cover Characterization

GLO: Generalized Logistic

GMM: Gaussian Mixture Model

GNO: Generalized normal

GoF: Goodness of fit

GPA: Generalized Pareto

H: Heterogeneity measure

HA: Hybrid Approach which combines CCA with GMM based clustering

HEFS: Hydrologic Ensemble Forecast Service

HEPS: Hydrologic Ensemble Prediction Systems

HRUs: Hydrologic Response Units

IFA: Index Flood Approach

IMD: India Meteorological Department

IOA: Index of agreement

ISRO: Indian Space Research Organisation

JKM: Jackson kernel method

JRA: Japanese Reanalysis

KLD: Kullback-Leibler Divergence

KPSS: Kwiatkowski-Phillips-Schmidt-Shin

L-CV : Coefficient of *L*-variation

LKM: Lewis kernel method

LMM: L-moment ratio diagram based threshold selection method

LOOCV: Leave-one-out cross-validation

LULC: Landuse/Landcover

MAE: Mean Absolute Error

MAR: Mean annual runoff

MCRPS: Mean Continuous Ranked Probability Score

MCS: Monte Carlo simulations

MD: Mahalanobis Distance

MDM-A: Mahalanobis Distance threshold selection Method based on analytical formulations

MDM-M: Mahalanobis Distance threshold selection Method based on Monte Carlo simulations

MEFP: Meteorological Ensemble Forecast Processor

MK: Mann-Kendall test

MLR: Multiple Linear Regression

MMD: Maximum Mean Discrepancy

MoEF: Ministry of Environment and Forests

MRB: Mahanadi River Basin

MRFA: Multivariate Regional Frequency Analysis

MSI: Modified Shortage Indices

MTFC: Multivariate time varying fuzzy clustering

NASA: National Aeronautics and Space Administration

NBSS and LUP: National Bureau of Soil Survey and Land Use Planning

NCEP: National Centers for Environmental Prediction

NCMRWF: National Centre for Medium Range Weather Forecasting

NDVI: Normalized Difference Vegetation Index

NFRS: Normalized Friedman-Rafsky Statistic

NRLD: National register of large dams

NRSC: National Remote Sensing Centre

NS: Non-stationary

NSE: Nash-Sutcliffe Efficiency

OSDMA: Odisha State Disaster Management Authority

P: Mean Precipitation

PDS: Partial Duration Series

PE3: Pearson type III

PET: Potential Evapo-transpiration

PI: Persistence Index

PM: Penman–Monteith

POT: Peaks Over Threshold

Q: Water discharge

Rad: Net solar radiation

RCH: Rule-curve based Hedging

RCMs: Regional Climate Models

Rd: Root depth

RFFA: Regional Flood Frequency Analysis

RH: Relative Humidity

RME: Relative Mean Error

RMSE: Root Mean Square Error

ROI: Region of Influence

R-RMSE: Relative Root Mean Square Error

RS: Remote Sensing

RVR: Relevance Vector Regression

R_e: Extra-terrestrial radiation

S: Stationary

SRC: Sediment Rating Curve

SRTM: Shuttle Radar Topography Mission

SSC: Suspended Sediment Concentration

SSP-FS: Shared Socioeconomic Pathways forcing scenarios

SUFI: Sequential Uncertainty Fitting

SWAT: Soil and Water Assessment Tool

Tmax: Maximum temperature

Tmin: Minimum Temperature

TS: Threshold Selection

UNESCO: United Nations Educational, Scientific and Cultural Organisation

USGS: United States Geological Survey

W: Wind speed

WRIS: Water Resources Information System

Section 1
Introduction

1.1. Overview

In recent decades there is increase in evidence of impact of climate change on hydro-meteorological processes and water resources in various parts of the world. In this backdrop, Ministry of Jal Shakti (Department of Water Resources Government of India) has formulated National Water Mission (NWM) to meet challenges associated with impacts of climate change on water resources of India. The first and the foremost objective of this mission is to conduct basin-wise studies particularly for downscaling plausible future climate scenarios to basin/sub-basin scale and generating the corresponding probable hydrological scenarios to assess stress on water resources in the study areas. Several national institutes have been identified for the intended studies on basins across the country. In this regard, IISc Bangalore (as the lead institute) and IIT Bhubaneswar (as the partner Institute) have been identified to conduct a study on the Mahanadi basin.

The proposed study is motivated to model/analyze hydrometeorological and hydrological processes (including sediment transport) and extreme events (floods, droughts) in the Mahanadi river basin and assess the impact of climate change on the same. Understanding the implications of projected climate change on vulnerable resources would be useful to devise better strategies for the management and conservation of water resources in the basin. Various objectives (see Section 1.2) are envisaged to achieve the following deliverables, among which 1 to 8 are desired by INCCC, and the additional deliverables are achieved as they are deemed important for the basin.

1. Baseline analysis of data, information, and past studies
2. Results of tests for trend detection for hydro-meteorological and hydrological variables.
3. Calibrated and validated hydrological model(s)
4. Impacts on water availability at various gauging sites within the basin (in terms of change in flow duration curves)
5. Impacts on irrigation water demands
6. Identification of hydrological extremes based on the base line data
7. Impacts on meteorological/hydrologic droughts (in terms of change in frequencies of occurrence), Analysis of uncertainties in the impacts. The impacts and the associated uncertainties are to be assessed for the near future (2015-2040) and for the distant future (2040-2100)

8. Recommendations for adaptation measures/options
9. Additional deliverables:
   (i) New regionalization approach is developed in the fuzzy framework to delineate homogeneous evapotranspiration (ET) regions. Homogeneous evapotranspiration regions are demarcated over the entire India
   (ii) Novel Mahalanobis distance-based automatic threshold selection method is contributed for analysis of floods in a river basin using peaks over threshold model.
   (iii) Fuzzy entropy-based methodology is developed for optimal design and performance assessment of hydrometric monitoring networks in the river basin.
   (iv) Operating policies are developed for the Hirakud reservoir using two hedging models.
   (v) Research is undertaken on various objectives related to sediment transport in the Mahanadi basin (by Partner Institute, IIT Bhubaneswar)
   (vi) Probabilistic riverine flood forecasting in the Tel river catchment of Mahanadi basin using the Hydrologic Ensemble Forecast Service (HEFS).

Details of the investigations carried out and the aforementioned deliverables 1 to 9 are presented in Sections 1 to 9, respectively.

1.2. List of objectives

In this project, IISc Bangalore (Lead Institute) and IIT Bhubaneswar (Partner Institute) proposed to study impact of climate change on hydrological processes (including extremes) and sediment yield in the Mahanadi river basin. The list of proposed objectives (i to xv) is given below. Among those objectives (i) to (ix) were addressed by Investigators at IISc, objectives (x) to (xiii) were addressed by Investigator at IIT Bhubaneswar. Objectives (xiv) and (xv) were done together by all the investigators.

(i) Trend analysis of the observed meteorological and hydrologic data and exploration of possible causes for trend (if evident).

(ii) Modelling hydrological processes in Mahanadi basin utilizing historical data for baseline period.

(iii) Establishing relationships between components of hydrological cycle (i.e., water balance components) in the basin for the current (historical) scenario using baseline data.

(iv) Identification of hydro-meteorological extremes based on the baseline data, and developing equations to estimate their magnitude corresponding to various frequencies at target locations in the river basin.

(v) Assessment of changes in streamflows in the river basin for future climate change scenarios using downscaled projections on meteorological variables.

(vi) Assessment of impact of climate change on water availability at different locations (hot spots) in the basin in terms of change in flow duration curves.

(vii) Assessment of changes in irrigation water demands corresponding to various climate change scenarios.

(viii) Development of operating policies for the Hirakud reservoir.

(ix) Assessment of impact of climate change on magnitude and frequency of meteorological/hydrological extremes in the basin.

(x) Trend analysis of the observed sediment data.

(xi) Establishing a relationship between the suspended and bed sediment transport and the discharge in the river utilizing the past data.

(xii) Assessment of trend in the annual sediment yield of the Mahanadi river for future climate change scenarios.

(xiii) Assessment of trend in the variation of the reservoir capacity of the Hirakud dam for the current and future scenarios.

(xiv) Assessment of uncertainties in the impacts associated with the use of various GCMs, climate change scenarios and hydrological models.

(xv) Framing recommendations for adaptation measures/options to mitigate adverse impacts of climate changes in Mahanadi basin.

1.3. Brief description of the study area

Mahanadi river has catchment area of about 1,41,134 km^2 that lies in Chhattisgarh (75136 km^2), Orissa (65628 km^2), Maharashtra (238 km^2) and Jharkhand (132 km^2) states (Figure 1.1). The river originates in Chhattisgarh and traverses a length of about 357 km before entering Orissa state, where it further traverses about 494 km before it confluences with Bay of Bengal. Its tributaries include Ib, Jeera, Ong, Tel, Brutang, Manjore, Karandijore, Hariharjore, and Surubalijore (Source: Department of Water Resources, Government of Orissa).

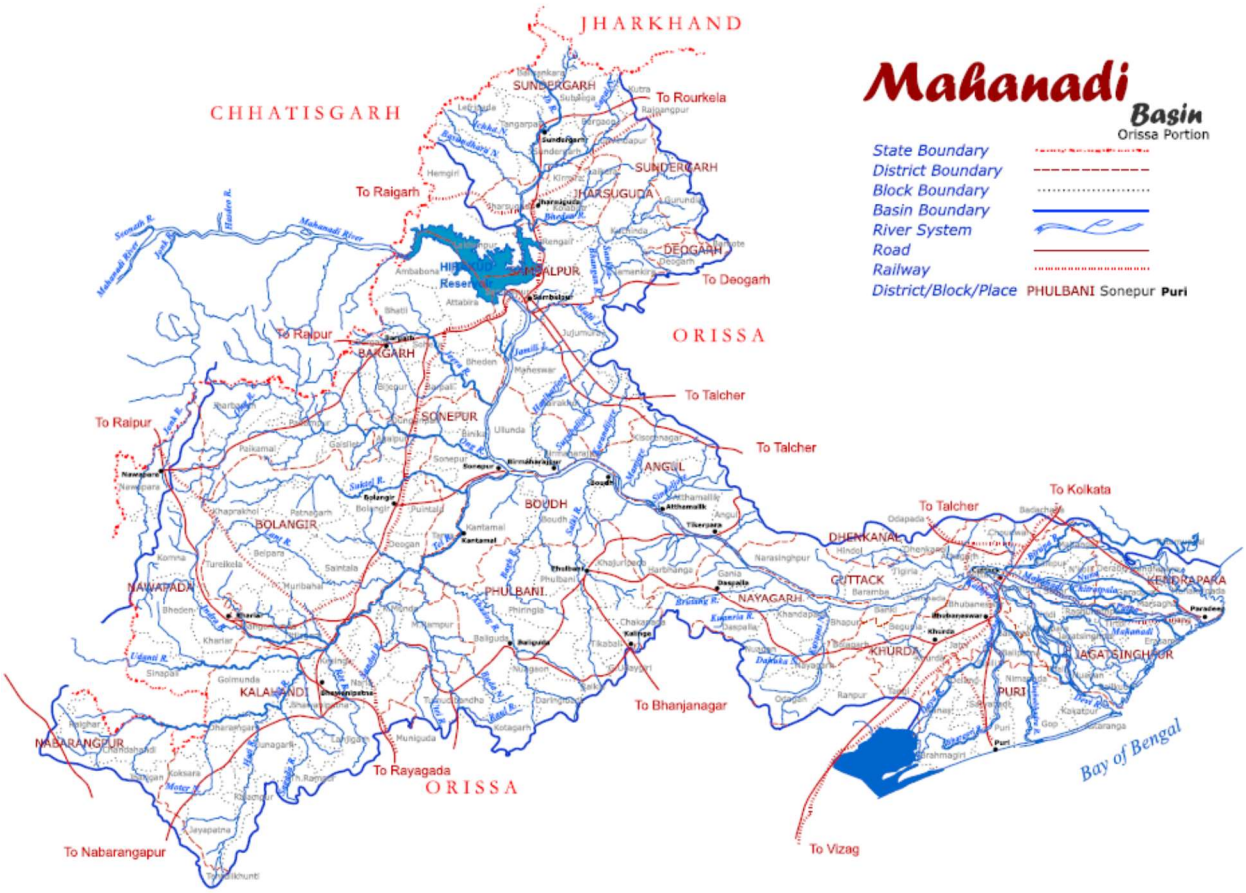

Figure 1.1: Mahanadi basin (Source: Department of Water Resources, Government of Orissa)

1.4. Review of literature & rationale for the study

Literature review on modeling hydrological/hydrometeorological processes and their extremes in river basins

The hydrological processes in a river basin, which depict the translation of rainfall to streamflow that finally leaves the basin, are many and complex. Modeling the processes is necessary to address a wide spectrum of environmental and water-related issues. The challenge in modeling the processes stems from the fact that they vary in both space and time. Rainfall-runoff models are widely used to model the hydrological processes, but there is ambiguity in their choice as several rainfall-runoff models are currently in use by hydrologists (Singh and Woolhiser, 2002; Singh et al., 2006; Jain et al., 2009). These models have found wide applications in water-supply forecasting, optimal design and/or operation of water storage and drainage networks, groundwater development and protection, planning and design of flood protection projects, and evaluation of floodplain management strategies and water

quality issues (Singh and Woolhiser, 2002; Wagener et al., 2008). An inventory of state-of-the-art models can be found at the website of Texas A&M University, United States <http://hydrologicmodels.tamu.edu/models.htm>. The rainfall-runoff models can be classified in terms of the processes represented, the time and space scales used, and the methods of solution to equations (Jain et al., 2009). The main distinguishing features for approaches to rainfall-runoff modeling are: (i) the nature of basic algorithms (empirical, conceptual, or process-based), (ii) assumptions concerning the nature of the process (e.g., deterministic, stochastic, chaotic), and (iii) spatial representation (lumped, distributed). An extensive review of the literature indicates that SWAT (Soil and Water Assessment Tool) is widely used by practitioners for modeling hydrological processes in a river basin and determining the impact of climate change on the processes. Hence it is adopted for investigations on the Mahanadi river basin in this study.

Detection and quantification of climate change's impact on hydrological processes (e.g., infiltration, soil water, evapotranspiration, and streamflow) in different climatic regions is a necessity for water resources planning and management in order to ensure water security for various purposes. A plethora of climate change impact studies have focused only on precipitation which triggers the hydrological processes (Maraun *et al.,* 2010, and references therein). In recent years, there has been growth in focus on other hydrometeorological variables such as temperature (e.g., Milly *et al.,* 2018), humidity (e.g., Gunawardhana *et al.,* 2017; Trenberth *et al.,* 2003), and wind speed (e.g., Liu *et al.,* 2014) which influence precipitation and evapotranspiration. Climate change-induced variation in meteorological variables will affect ET_0 or crop water requirements. Therefore, quantifying the specific influence of individual climatic variables on ET_0 and runoff in catchments will be helpful in identifying key variables and assessing the vulnerability of a water resource system to each key variable at various temporal scales (e.g., seasonal and annual). Furthermore, in the past few decades, several studies around the world (Hobbins *et al.,* 2004, and references therein) have reported declining evapotranspiration despite a significant increase evident in global air temperature, which is known as the evaporation paradox. Currently, there is a need to (i) investigate whether the evaporation paradox exists in India, (ii) determine the trend and change point(s) of ET_0, (iii) identify key climate variables influencing ET_0 in different parts of India, (iv) assess the vulnerability of runoff depicting freshwater resources to changes in each of the climate variables, and (v) verify Bouchet-Morton's hypothesis (Bouchet, 1963) on the complementary relationship between actual (ET_a) and potential evapotranspiration which could provide insight into the divergence of trends in ET_0 and ET_a. Another

issue worth noting is that FAO (Food and Agriculture Organization) recommends Penman-Monteith (PM) equation for ET_0 estimation, which requires information on several climate variables. The equation cannot be used in data-sparse areas where information/forecasts on one or more required climate variables are unavailable/unreliable. To address this, effective nonlinear relationships are desirable at the regional scale to arrive at the FAO-PM estimate of ET_0 even from a limited set of climate variables in data-sparse areas. There has been no prior attempt in this direction.

General Circulation Models (GCMs) are the most reliable resources available to investigate the possible climate change effects on hydrological processes. Earlier releases of GCMs (Coupled Model Intercomparison Project 5 (CMIP5) and its earlier versions) suffer from several drawbacks, including their coarse spatial resolution, which fails to capture the influence of local-scale features (such as topography, land-surface feedback, land-use changes, etc.) in reproducing present climatic conditions (Ghosh *et al.,* 2016; Jain *et al.,* 2019). The latest available CMIP6 models have improved parameterizations of cloud microphysics, and they are better at representing various Earth system processes, such as biogeochemical cycles and ice sheets. Furthermore, the average resolution of GCMs under CMIP6 is finer than that of CMIP5 GCMs. Hence, analysis based on CMIP6 information is expected to provide reliable estimates of future ET_0 and freshwater availability. In addition, incorporating the information on future projections of population and future freshwater availability in the analysis is useful for drawing meaningful inferences for practical applications. There is a need for studies in this direction.

Conventionally hydrologists use frequency analysis procedures to quantify the risk associated with extreme events (e.g., extreme rainfall, floods). The risk estimates find use in studies related to the design of water control (e.g., barrages, dams, levees) and conveyance structures (e.g., culverts, storm sewers, spillways), economic and risk evaluation of flood protection projects, land use planning, and management, flood insurance assessment, and other hydrological applications. Traditionally, frequency analysis is based on extreme value theory, which provides a general framework for modeling extremes. Approaches that are commonly used for statistical analysis of extremes could be broadly classified as those based on (i) Annual Maximum Series (AMS) or Block Maxima (BM), and (ii) Partial Duration Series (PDS) or Peaks Over Threshold (POT) series. The AMS approach involves the extraction of annual maxima (i.e., BM) values from the available records, whereas the PDS approach considers values exceeding a predetermined high threshold. Several studies (Cunnane, 1973, Wang, 1991, Madsen et al., 1997, Caires, 2009) have shown through Monte Carlo simulations and

real-world applications that the PDS approach is more effective in using information from the available records and variance of quantile estimates based on PDS approach is smaller than that based on AMS approach. Despite its advantages, the use of PDS is less prevalent than AMS due to the lack of a universally established systematic approach for extracting PDS. A major issue with the PDS approach concerns the selection of an appropriate threshold value. The threshold should ensure the extraction of maximum information from the time series without violating the PDS approach's statistical assumptions. When the threshold is too high, the sample size of PDS tends to be small. Consequently, estimates of distribution parameters have high variance and small bias (Coles, 2001). On the other hand, a low value for the threshold yields a large sample that could include values that may not necessarily be extremes. Therefore, the distribution of the PDS deviates from the Generalized Pareto distribution (GPD), which results in significant bias in the quantile estimates (Adamowski, 2000). Threshold selection is thus a trade-off between bias and variance. In recent decades, several methods have been proposed for the identification of optimal thresholds. The methods generally differ in their fundamental theoretical assumptions and in their performance, with data exhibiting different extreme behavior (e.g., fat or heavy-tailed, thin or light-tailed). There are various issues affecting the performance of different methods available for threshold selection. In this context, there is a need to develop a new approach that can address the issues in identifying the optimal threshold for PDS extraction for use in risk analysis of extreme hydrologic events.

Another issue is that conventional frequency analysis procedures quantify the risk associated with floods based on a single flood-related characteristic/variable (e.g., peak flow or flood volume) at the target location. However, the risk cannot be assessed holistically by frequency analysis in a univariate framework, as floods can be better characterized by several correlated variables such as flood peak, volume, duration, and time to peak. In this perspective, many studies (e.g., Ashkar et al., 1998; Buishand, 1984; Chebana & Ouarda, 2011; Yue, 1999; Zhang & Singh, 2006) have stressed the need to consider a multivariate approach to flood risk assessment. It enables modeling the joint distribution of these variables to completely characterize the extremes (Yue & Rasmussen, 2002), which is not possible with separate univariate analyses on each variable. Multivariate approaches are thus more appropriate. However, in a multivariate framework, RFA did not receive much attention till the advent of *L*-comoments (Serfling & Xiao, 2007) that can account for the dependence structure between variables. Chebana and Ouarda (2009) extended the univariate index-flood approach (Dalrymple, 1960) to a multivariate setting to predict multivariate quantiles at ungauged sites. The index-flood

approach has several shortcomings (e.g., Stedinger, 1983; Hosking & Wallis, 1997; Sveinsson et al., 2001, 2003; Basu & Srinivas, 2013), which are valid in both univariate and multivariate frameworks. Hence, there is a need to develop effective alternate procedures for multivariate RFA (MVRFA). For this purpose, one could explore the advantages of recent developments in multivariate extreme value theory.

Literature review on modeling sediment yield in river basins

Rivers constitute the crucial link between terrestrial and coastal ecosystems, which act as an active transporting medium for dissolved and particulate matter, suspended and bed sediments to the oceans, thus resulting in the formation of river deltas. According to Syvitski et al. (2003), greater than 90% of the natural erosion products (i.e., sediments) were conveyed by rivers to the ocean. In contrast, the remaining 10% gets deposited at different river stages. 26% of these sediments on a global scale were intercepted by anthropogenic retention (Yang et al., 2002; Syvitski et al., 2005). Broadly, land growth inside the river deltas is critically influenced by the conveyance of water and sediment load to the sea (Yu et al., 2011). As a result, river sediment flux plays a vital role in the sediment budget of the coast and sea, which is required for assessing the life of storage reservoirs, functioning and operation of hydraulic structures.

Moreover, in many worldwide catchments and mainly in developing countries like India, sediment gauging stations are inadequate in numbers and quality due to various operational constraints (Walling and Fang, 2003). The suspended form of the total load involves more complex attributes than its bedform (Zounemat-Kermani et al., 2016). The suspended load is a consolidation of the catchment characteristics upstream of the gauging station (Syvitski et al., 2000). Hence, the quantitative prediction of suspended sediment load in a basin becomes critical for the sustainable management of water resources.

Trend analysis is also essential to understand hydrological processes' recurrence and other attributes (Walling, 1995). Past investigations (Adarsh et al., 2016; Montanher et al., 2018) have used longer time series available near the mouth region of a river for trend analysis. However, Syvitski (2003) discussed that sediment studies based on data from the last gauging station of the basin do not give a complete comprehension of the inconsistent anthropogenic activities occurring in the catchment. Runoff reduction, reservoir trapping of sediments, soil and water conservation measures, and land-use change were some of the natural and human-induced attributes that caused a decline in sediment load

trend. These processes further result in the emergence of non-stationarity or change points in a hydrological time series (Zhongbao et al., 2015; Chen and Wang, 2019). Consequently, the detection of non-stationarity helps to understand further the runoff and sediment yield under the conditions of the shifting environment (Adarsh et al., 2016; Bastia and Equeenuddin, 2016; Adeyeri et al., 2020).

The delta is susceptible to the decrease in stream sediment load, which might be due to river damming to sustain various increasing demands (Lin et al., 2017; Song et al., 2020). However, further investigation of the sediment budget within the estuarine system needs to be carried out to monitor future coastal erosion. With the advancement of Remote Sensing (RS) and geographic information systems, numerous studies were also performed with remotely sensed data to detect the coastline change at higher spatial and temporal scales. It is an economical choice distinguished by alternative data origins (Ford, 2013; Xu, 2018). The method adopted worldwide to measure the volumetric change of sediment load applies Digital Elevation Models of difference (DoD) on RS data for a different series of timescales. It, therefore, provides a better understanding of erosional and accretional processes over various timescales (Wheaton et al., 2010). Mukhopadhyay et al. (2018), using the Digital Shoreline Assessment System (DSAS) tool of USGS, found that approximately 65% of the Mahanadi delta was under erosion, and it would deteriorate in the next few decades. However, there is a definite lack of information so far as the morphological response of the deltaic plain to the variation in sediment load from the catchment is concerned.

The suspended sediment load is controlled by the source and supply regions. However, it is relatively easy to measure but challenging to predict correctly. The Sediment Rating Curve (SRC) represents the relation between Suspended Sediment Concentration (SSC) and water discharge (Q) for a particular gauging station. Past researchers also investigated the physical interpretation of the rating parameters of SRC and related them to various catchment characteristics (Asselman 2000). The efficiency of SRC reduces due to the variation of catchment sediment supply, commonly defined as hysteresis, which the traditional SRC generally neglects. Therefore, the hysteresis effect results in a non-distinct relationship in SRC, depicting different sediment concentrations for identical discharge. So, in particular, the investigation of hysteresis loops of SRC assists us in interpreting the function of discharge for estimating SSC and gives us knowledge about the source of sediments in the catchment. Few recent studies on the hysteresis of SRC include findings on the types of loops, determination of hydrological influences during different events, temporal consistency of hysteresis curves, and various origins of

sediments in the catchment (Vercruysse et al. 2017; Sadeghi et al. 2019). However, no such studies incorporated the effect of hysteresis in estimating SSC for the Mahanadi River Basin (MRB).

Further, Saliha et al. (2011) discussed that estimating hydrological variables for data-constrained catchments is a significant challenge. In this context, regionalization is the most commonly used approach that relates the model parameters to catchment characteristics (Kokkonen et al. 2003; Saliha et al. 2011). Given the complex nature of the suspended load of a river basin, the development of an analytical relationship for its estimation is not practicable. Therefore, it is required to have more knowledge of the intensity of possible source terms influencing the transport of suspended sediments. This study primarily aims to measure the strength of the likely source and governing terms to obtain a functional relationship between the catchment characteristics and rating parameters and eventually SSC.

Further, a satisfactory evaluation of the components of a total load of a river is valuable in understanding the fluvial processes and geomorphic evolution (Rainato et al., 2016; Joshi and Xu, 2017). Because of the lack of bed load data for Indian alluvial rivers, precise assessment, validation, and segmentation of these rivers' total load transport rate remain an issue. The use of empirical bed load estimation methods is an alternative to the actual bedload measurements. For this purpose, several bed load formulae have already been established. At the same time, in most cases worldwide, the bed load component was either neglected or taken as a certain proportion of suspended load or calculated from the sediment rating curve (Maddock and Borland, 1950; Holeman, 1968; Milliman and Meade, 1983; Ellison et al., 2016). Many previous studies on bed load prediction found that stream power-based equations were efficient and comparable with observed bed load data for sandy rivers (Cantalice et al., 2013; Lemma et al., 2019; Armijos et al., 2021). Recent studies on bed load estimation were mainly based on various approaches (Cantalice et al., 2013; Asheghi and Hosseini, 2020; Ashley et al., 2020; Armijos et al., 2021). However, it was understood that such approaches require extensive in-situ bed load measurements, which are otherwise rarely available in India. Studies on bed load transport for Indian alluvial rivers were very limited in numbers. In this regard, few of them have evaluated the BLT (Bed Load Transport) rate of different rivers using approaches like effective shear stress, total load, and sediment rating curves (Yadav and Samtani, 2008; Waikhom and Yadav, 2017a, 2017b). To improve the model accuracy, Pektas and Dogan (2015) proposed the incorporation of the suspended load in predicting the bed load of a channel wherever possible.

The direct effects of climate change on suspended sediment transport are changes in the erosion intensity and sediment-transport-related processes caused by precipitation and river discharge. Several studies have been carried out on the influence of climate change on soil erosion between 1990 and 2050 using different GCMs as input models (Favis-Mortlock and Guerra, 1999; Pruski and Nearing, 2002). Further, other studies have attempted to evaluate the possible impacts of climate change on regional water resources (Reshmidevi et al., 2017, Mohammed et al., 2015, Demaria et al., 2016). Regional Climate Models (RCMs) or statistical downscaling models are often used to provide future projections of the climate variables (e.g., precipitation and temperature) relevant for hydrological assessments (Mehrotra and Sharma, 2004).

1.5. Baseline analysis of data on hydro-meteorological and hydrologic variables

Streamflow data were procured for 19 gauges in the Mahanadi basin (Figure 1.2) from the Water Resources Information System (WRIS) project (http://cwc.gov.in/water-resources-information-system-wris). The catchment of each gauge and stream network contained in it were delineated using DEM (Digital Elevation Model) data obtained from two different sources: (i) ASTER (Advanced Spaceborne Thermal Emission and Reflection Radiometer) DEM having 30 m resolution, available from the web site: http://reverb.echo.nasa.gov, and (ii) SRTM (Shuttle Radar Topography Mission) DEM having 90 m resolution, available from the web site: http://srtm.csi.cgiar.org/. The delineated stream network and catchments are shown in Figure 1.3.

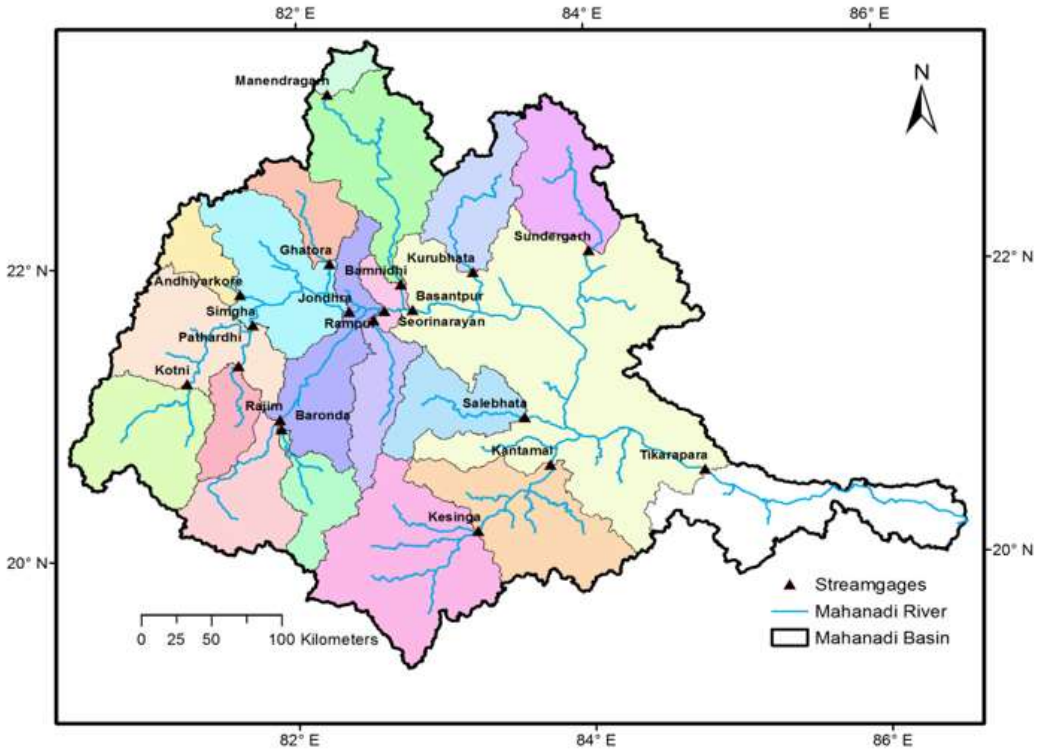

Figure 1.2. Topography of Mahanadi basin and location of 19 stream gauges considered.

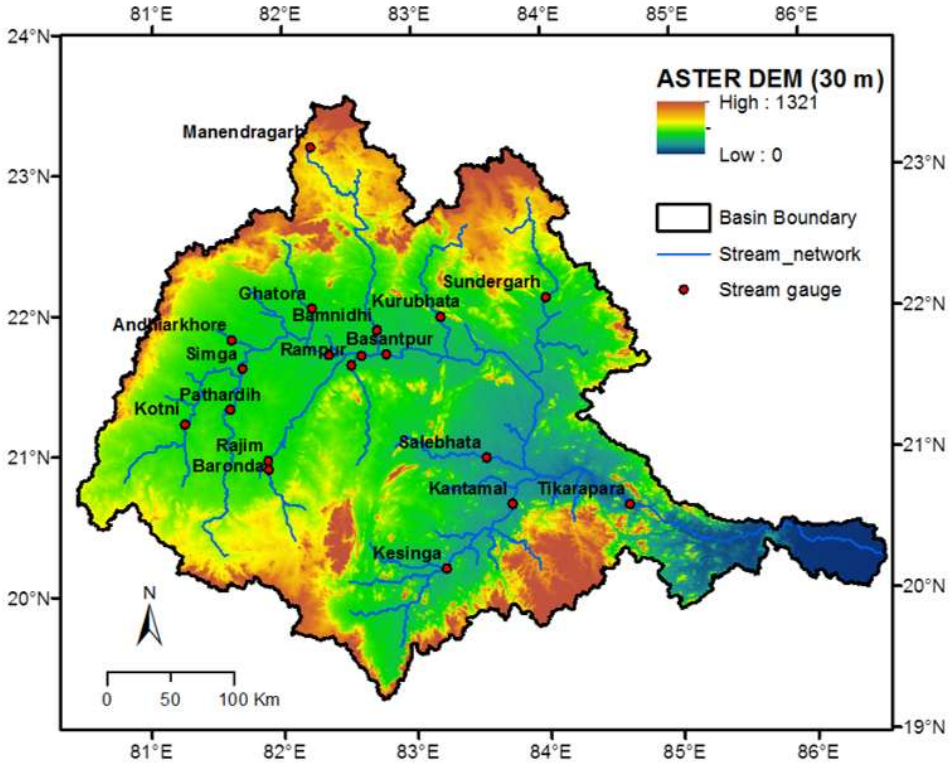

Figure 1.3. Catchments of CWC gauges delineated in the Mahanadi basin using ASTER DEM.

To assess the accuracy of the DEMs, error in the estimate of catchment area delineated based on each DEM (SRTM, ASTER) was quantified in terms of relative bias (R-bias) with respect to the estimate of catchment area (obtained based on topographical survey) which was available from CWC (2012). In general, the R-bias values (presented in Table 1.1) indicate that (i) DEM-based estimates are marginally deviated with respect to CWC estimates for most catchments (except Simga), (ii) the difference in estimates based on SRTM and ASTER DEMs is marginal for most catchments, and (iii) neither of the DEMs is consistent in yielding least bias over all the catchments. The latter point can be appreciated by noting that the error is significant in the case of both the DEMs for the Rampur and Simga catchments. Further, the error is large in the case of finer resolution ASTER DEM for the Jondhra catchment. Overall, the observations indicate that the source of DEM has an effect on the analysis for a catchment, and finer resolution DEM need not be the default choice for the application. Error is suspected in the CWC estimate of the catchment area in the case of the catchment delineated for the stream gauge located at Simga, as the CWC estimate is quite different from the estimates obtained using both the DEMs.

Table 1.1. Effect of DEM on catchment area delineated in the Mahanadi river basin.

S.No.	Catchment of gauge	Catchment area (km^2)			R-bias (%)	
		SRTM (90m)	ASTER (30m)	CWC estimate	SRTM (90m)	ASTER (30m)
1	Manendragarh	1017.17	1016.18	1100	-7.53	-7.62
2	Andhiarkhore	2133.38	2179.60	2210	-3.47	-1.38
3	Patherdih	2494.70	2481.91	2511	-0.65	-1.16
4	Ghatora	2935.10	3076.332	3035	-3.29	1.36
5	Baronda	3213.44	3205.76	3225	-0.36	-0.60
6	Rampur	3436.02	3433.51	2920	17.67	17.59
7	Salebhata	4632.10	4574.69	4650	-0.38	-1.62
8	Kurubhata	4763.69	4822.36	4625	3.00	4.27
9	Sundergarh	6061.67	5974.34	5870	3.27	1.78
10	Kotni	7063.33	7050.28	6990	1.05	0.86
11	Rajim	8494.70	8419.36	8760	-3.03	-3.89
12	Bamnidhi	9878.19	9869.70	9730	1.52	1.44
13	Kesinga	12004.34	11929.62	11960	0.37	-0.25
14	Kantamal	20237.98	20535.30	19600	3.25	4.77
15	Jondhra	29901.00	33086.59	29645	0.86	11.61
16	Seorinarayan	48265.56	47754.02	48050	0.45	-0.62
17	Basantpur	58647.15	58750.02	57780	1.50	1.68
18	Tikarapara	127415.20	127118.8	124450	2.38	2.14
19	Simga	16790	20668	30761	-45.42	-32.81

Flows in the Mahanadi basin noted during different months of the calendar year are shown in Table 1.2. It can be noted that flows are generally high around the south-west/summer monsoon season (June-October).

Table 1.2. Mean monthly and mean annual streamflows (in Mm^3) at different gauges in the Mahanadi basin.

Month	Andhiyarkore	Bamnidihi	Baronda	Basantpur	Ghatora	Jondhra
January	6.29	104.79	2.31	207.24	10.85	51.62
February	4.95	79.78	1.77	164.06	5.63	39.16
March	3.17	73.61	1.00	127.69	2.88	21.14
April	1.63	74.17	0.42	97.11	1.68	10.64
May	1.11	72.17	1.12	78.21	1.40	8.68
June	16.07	265.46	63.73	795.18	35.60	238.43
July	59.66	1027.36	280.31	4329.57	190.95	1622.82
August	90.18	1403.26	513.58	7667.34	295.40	2852.43
September	89.01	883.87	328.90	5209.28	256.62	2263.74
October	32.65	269.94	83.84	1792.97	71.38	776.24
November	13.03	150.19	16.38	603.82	20.41	218.80
December	8.51	134.36	4.93	293.96	11.49	75.84
Annual	326.27	4538.97	1298.31	21366.43	904.29	8179.52
Month	Kantamal	Salebhata	Seorinarayan	Simga	Kesinga	Kotni
January	103.88	5.21	81.86	28.77	67.88	4.05
February	70.64	6.12	63.47	22.76	58.61	4.03
March	59.17	5.00	31.83	12.23	59.44	0.54
April	53.34	3.07	19.85	8.40	57.66	0.12
May	81.79	2.12	15.83	7.62	85.57	0.22
June	476.66	78.44	568.05	148.54	416.53	83.90
July	2203.37	440.92	3497.09	941.48	1453.99	382.97
August	3596.50	785.97	5606.02	1757.70	2262.82	743.72
September	2495.13	493.09	4196.45	1298.04	1441.17	420.87
October	829.14	102.84	1482.26	470.01	520.30	147.72
November	363.18	23.90	421.70	117.81	220.02	31.57
December	180.65	5.40	132.44	42.12	127.54	6.68
Annual	10513.46	1952.06	16116.86	4855.46	6771.54	1826.40
Month	Kurubhata	Manendragarh	Pathardhi	Rajim	Rampur	Sundargarh	Tikarapara
January	33.42	4.51	3.12	5.72	2.49	36.11	865.27
February	18.50	3.43	3.84	4.49	1.70	18.17	759.29
March	10.41	3.26	1.73	2.85	1.18	9.95	822.03
April	3.80	1.59	1.57	1.96	0.96	4.69	801.64
May	4.00	0.09	2.23	2.97	0.38	5.76	785.49
June	114.77	24.28	29.45	119.40	60.21	214.86	1661.89
July	570.15	91.53	236.96	583.87	311.15	838.07	8770.42
August	745.11	96.68	381.23	1136.26	523.80	933.89	15566.34
September	581.95	80.07	250.76	719.88	335.21	802.69	11603.65
October	171.97	25.00	96.77	206.36	76.80	227.07	3762.75
November	68.42	7.61	16.66	44.42	19.43	88.86	1537.41
December	38.83	5.95	4.16	11.18	4.15	34.42	955.70
Annual	2361.32	344.01	1028.48	2839.34	1337.47	3214.54	47891.88

Gauged data on meteorological variables were procured from the India Meteorological Department (IMD) at a daily time scale. It included records of (i) rainfall, maximum, minimum, and dew point temperatures for 18 stations, (ii) relative humidity and wind speed at 17 stations, and (iii) sunshine hours at 2 stations. Baseline analysis performed on the gauged data indicated large gaps (missing values). Hence, gridded meteorological data available from various sources (Table 3) were considered for investigations.

Potential Evapotranspiration (PET) was estimated using the Food and Agricultural Organisation (FAO) Penman–Monteith (PM) method. Precipitation and climate variables required to estimate PET were obtained from National Centers for Environmental Prediction (NCEP), Japanese Reanalysis (JRA-55), and IMD data sources. Information on the temporal extent and resolution of the data sets is provided in Table 1.3.

Table 1.3: Datasets considered for PET estimation by FAO Penman–Monteith method.

Data	**Source**	**Quality**		
		Period	Time Scale	Grid Size (degrees)
Precipitation	IMD	1901 - 2011	Daily	0.25
Net Solar radiation (NS)	NCEP	1951 - 2018	Daily	1.88
Maximum Temperature (Tmax)	IMD	1958 - 2013	Daily	1
Minimum Temperature (Tmin)	IMD	1958 - 2013	Daily	1
Relative humidity (RH)	NCEP	1951 - 2018	Daily	1.88
	JRA	1958 - 2013	Daily	1.25
Wind Speed (WS)	NCEP	1951 - 2018	Daily	1.88
	JRA	1958 - 2013	Daily	1.25

Scrutiny of spatial variability of the variables in different seasons indicated different complex patterns (Figures 1.4 to 1.7). The Mahanadi basin receives most part of its precipitation in monsoon (June-September), with the highest rainfall occurring in the right half of the basin. In winter (considered as October to January) and summer (considered as February to May), the rainfall is considerably low. A major part of it is witnessed near the coastal area and it's adjoining interior part of the basin (Figure 1.4). On the other hand, the net solar radiation is high in summer, marginally low in monsoon, and much lower in winter. It decreases from south to north in summer and winter, but has a typical concave pattern during monsoon, with average values in the central part and increasing towards the periphery.

The maximum temperature (i) decreases with an increase in latitude during winter, (ii) is high in the central part of the basin and decreases towards the northern and southern parts of the basin in summer, (iii) is high along the periphery and low in the central part of the basin during monsoon. On the other hand, the minimum temperature is high during monsoons and low during winter. It has a steep gradient near the coastline. It first increases and then gradually decreases with distance from the coastline.

The relative humidity (RH) is high near the coastal area (southeast part of the basin), and it drops towards the west with an increase in distance from the coastline, as expected. Among the seasons, RH is high in the monsoon and low in the summer. Similarly, windspeed is high near the coastline and drops towards the central part of the basin with an increase in distance from the coastline, but it again increases towards the northwest. It is higher in monsoon, marginally lower in summer, and much lower in winter. The PET is highest in summer, exhibiting a pattern that is invariant in space over the right half of the basin and increases towards the northwest. It is low in winter and increases from the southeast to the northwest part of the basin. It has a typical concave pattern during monsoon with average values near the eastern coast and gradually increasing magnitude towards the inner periphery of the basin (Figures 1.4 to 1.7).

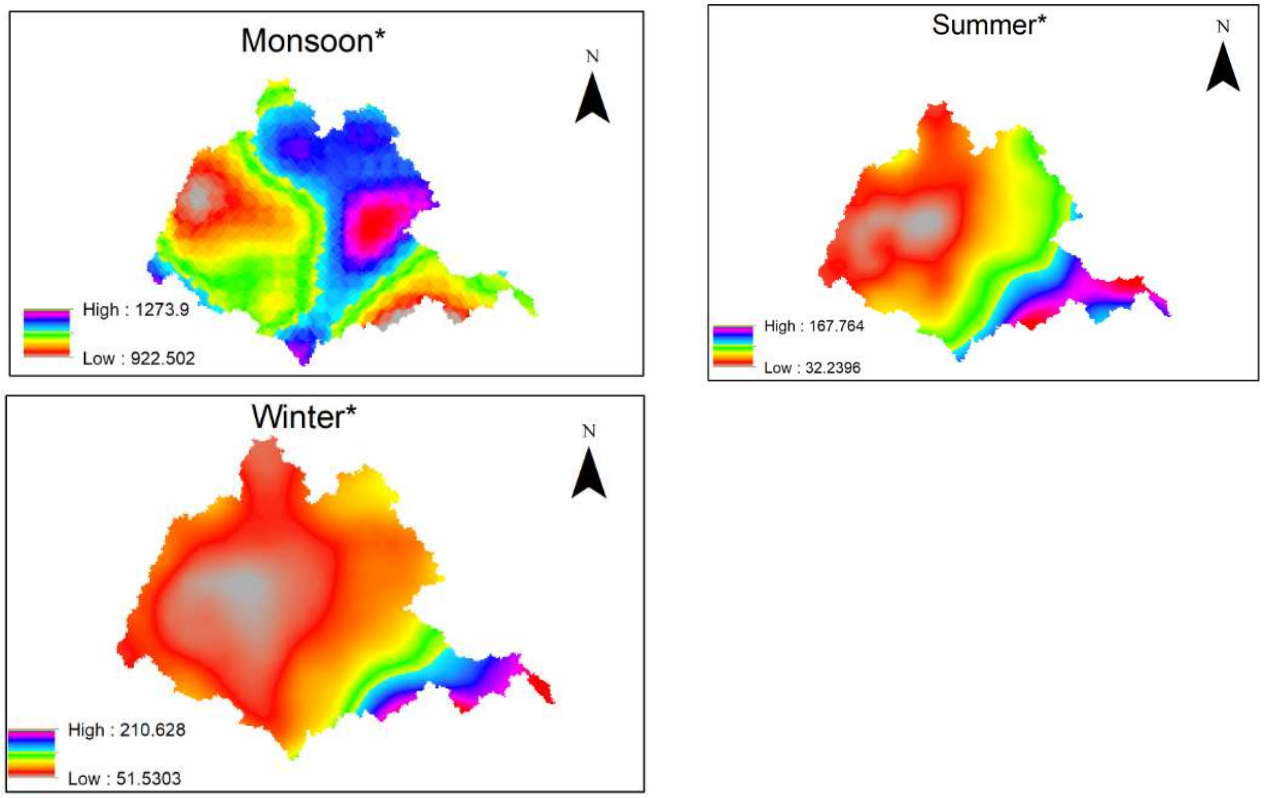

Figure 1.4: Seasonal variation of precipitation (mm) in the Mahanadi basin.

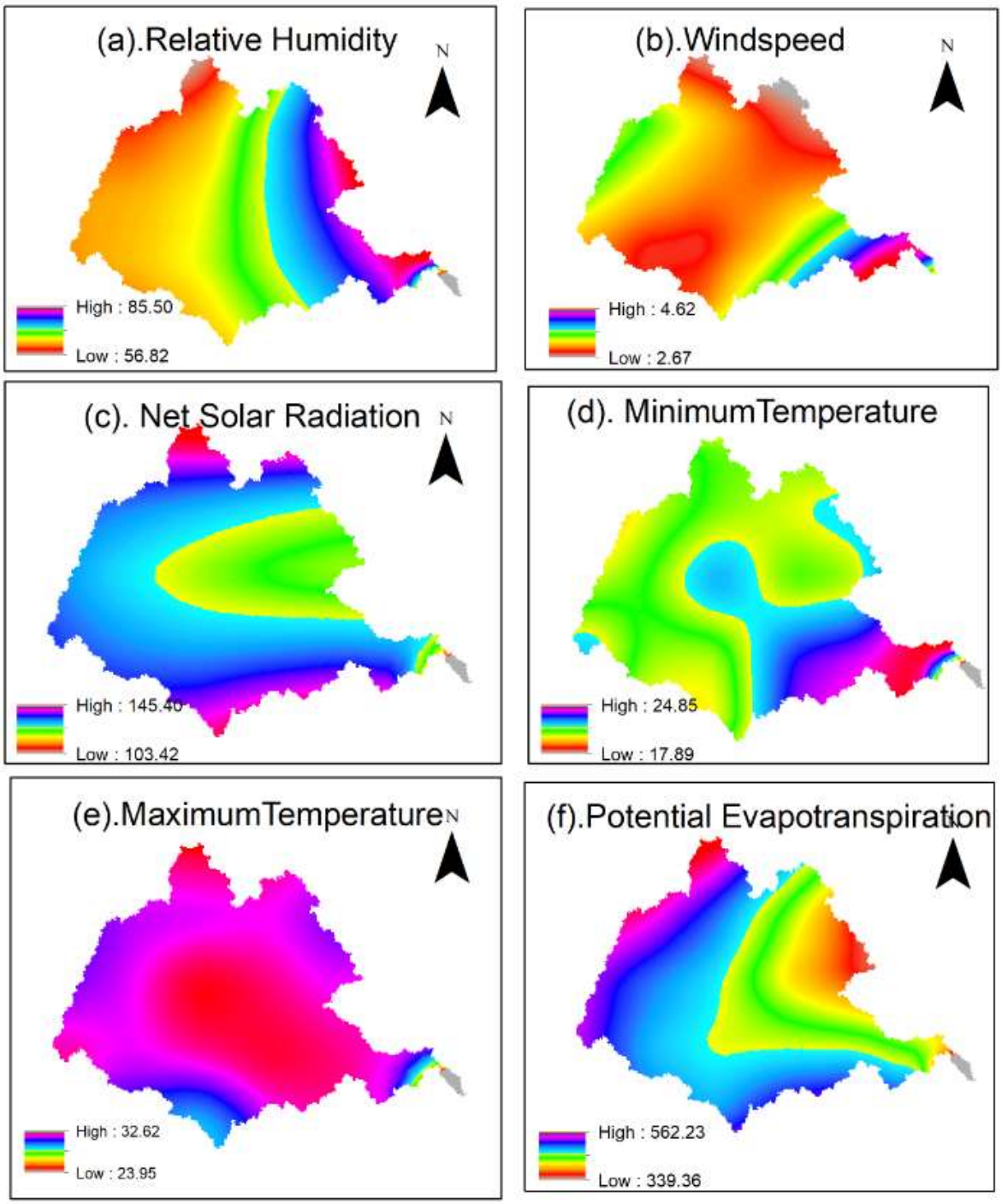

Figure 1.5: Spatial variability of climate variables across the Mahanadi basin in the monsoon season. The units of relative humidity, wind speed, net solar radiation, minimum and maximum temperatures, and potential evapotranspiration are %, m/s, W/m^2, °C and mm, respectively. (Monsoon: June-September), winter (October-January) and summer (February-May).

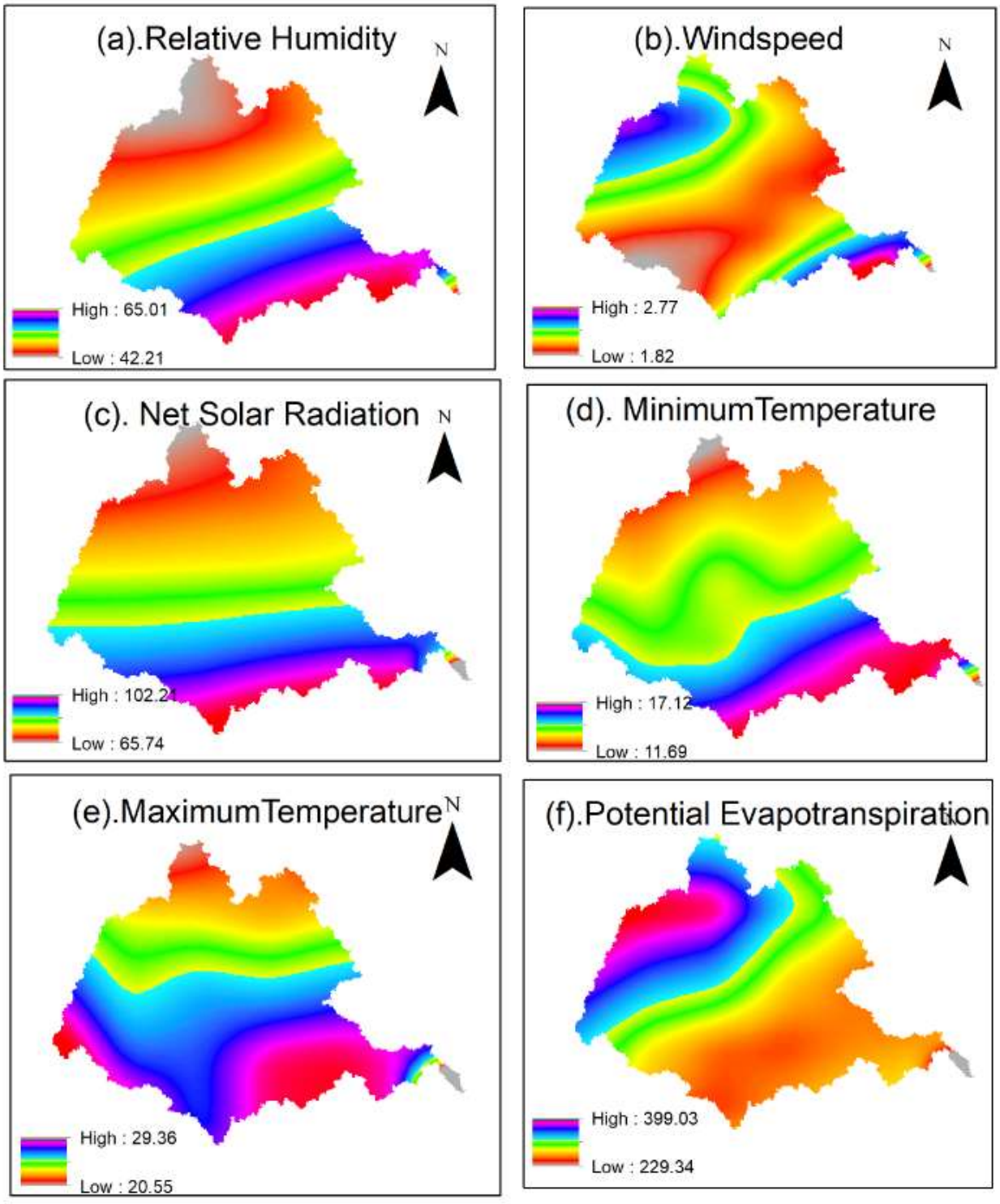

Figure 1.6: Spatial variability of climate variables across the Mahanadi basin in the winter season. The units of relative humidity, wind speed, net solar radiation, minimum and maximum temperatures, and potential evapotranspiration are %, m/s, W/m^2, °C and mm, respectively. (Monsoon: June-September), winter (October-January) and summer (February-May).

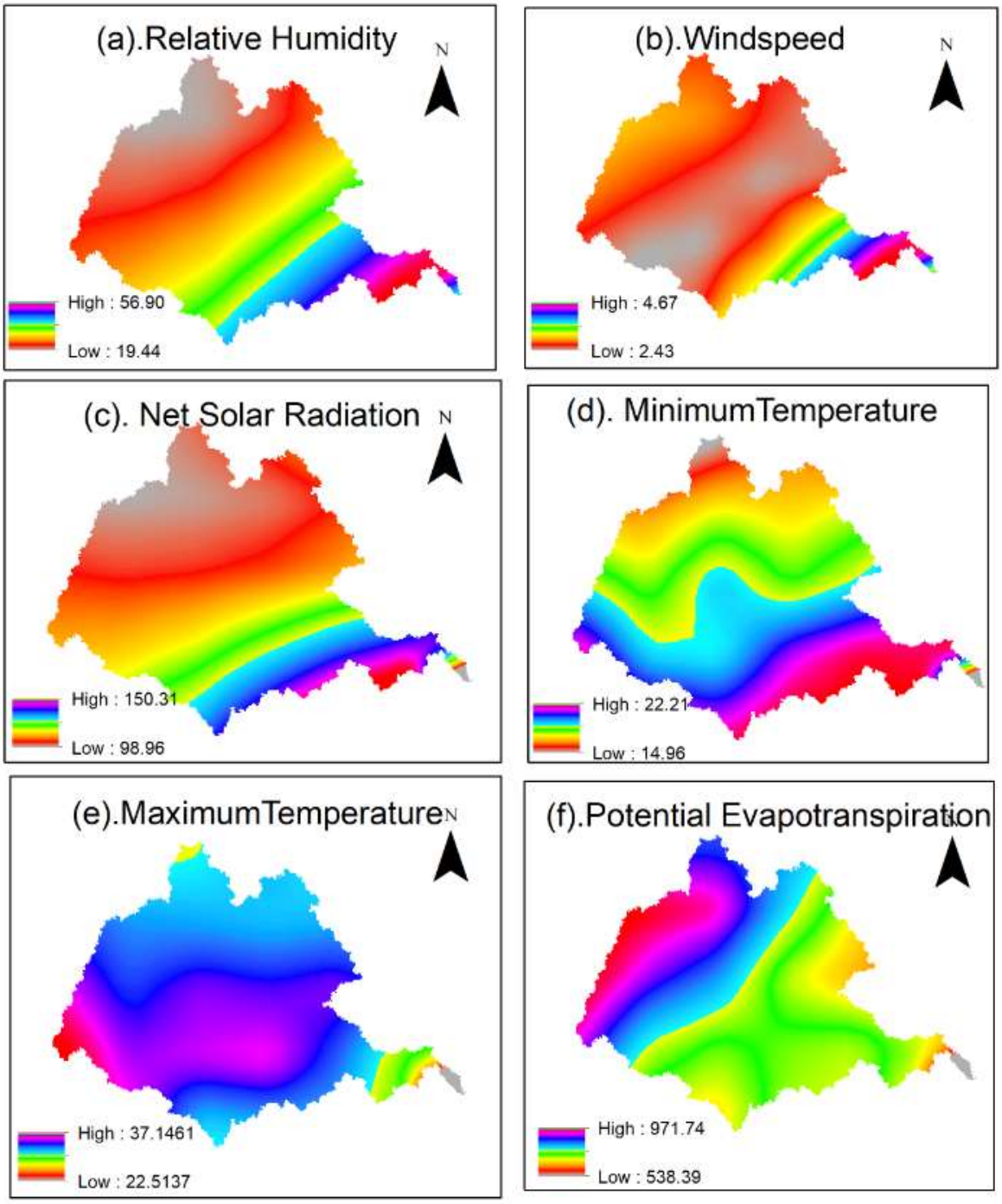

Figure 1.7: Spatial variability of climate variables across the Mahanadi basin in the summer season. The units of relative humidity, wind speed, net solar radiation, minimum and maximum temperatures, and potential evapotranspiration are %, m/s, W/m^2, °C and mm, respectively. (Monsoon: June-September), winter (October-January) and summer (February-May).

Section 2

Trend analysis of the observed hydro-meteorological and hydrologic variables

Investigations were carried out to verify the evidence of non-stationarity in the records of hydrometeorological variables by using (a) Seasonal and standard versions of the Mann-Kendall test (MK), (b) t-test, and (c) Kwiatkowski-Phillips-Schmidt-Shin (KPSS) test considering 5% significance level. A brief summary of the results obtained based on trend analysis is provided in Table 2.1. In general, the tests indicated nonstationarity in records of hydrometeorological variables for the majority of grids in the Mahanadi basin at the daily scale. The results obtained at both monthly and annual scales were almost consistent in indicating non-stationarity in wind speed and stationarity in PET and minimum temperature for the majority of the grids. However, the results were contrasting for the variables Relative Humidity (RH), maximum temperature (T-max), and solar radiation.

Table 2.1: Results from trend analysis of hydrometeorological variables.

Variable	Data source	Daily			Monthly			Annual		
		t-test	MK	KPSS	t-test	MK	KPSS	t-test	MK	KPSS
Wind speed	NCEP	NS (91.4)	NS (88.6)	NS (100)	NS (84.3)	NS (88.6)	NS (52.9)	NS (82.9)	NS (87.1)	NS (71.4)
	JRA	NS (90.0)	NS (90.0)	NS (100)	NS (78.6)	NS (88.6)	NS (92.9)	NS (78.6)	NS (80.0)	NS (98.6)
RH	NCEP	NS (67.1)	NS (74.3)	NS (100)	S (87.1)	NS (67.1)	S (100)	S (58.6)	S (62.9)	S (84.3)
	JRA	NS (100)	NS (100)	NS (100)	NS (95.7)	NS (100)	S (95.7)	NS (100)	NS (100)	S (72.9)
PET	NCEP	NS (64.1)	NS (73.4)	NS (100)	S (96.9)	S (54.7)	S (100)	S (76.6)	S (81.3)	S (87.5)
	JRA	NS (53.1)	S (51.6)	NS (100)	S (96.9)	NS (51.6)	S (100)	S (64.1)	S (68.8)	S (70.3)
Solar Radiation	NCEP	NS (98.6)	NS (98.6)	NS (95.7)	NS (74.3)	NS (98.6)	S (100)	NS (98.6)	NS (98.6)	S (91.4)
T-max	IMD	NS (75.0)	NS (84.4)	NS (100)	S (90.6)	NS (81.3)	S (100)	NS (60.9)	NS (60.9)	S (75.0)
T-min	IMD	NS (54.7)	NS (70.3)	NS (100)	S (100)	NS (65.6)	S (100)	S (70.3)	S (75.0)	S (57.8)

*( ) values indicate the percentage of grids in the Mahanadi basin
RH: relative humidity; PET: Potential evapotranspiration; Tmax: Maximum temperature; Tmin: Minimum Temperature; NS: Non-stationary; S: Stationary.

Results obtained from trend analysis on annual precipitation and annual daily maximum precipitation are provided in Figure 2.1. They indicate non-stationarity in annual precipitation and stationarity in annual maximum daily precipitation for most of the grids in the Mahanadi basin.

Annual maximum daily streamflow data of different gauges in the Mahanadi basin were prepared by extracting daily peak flows from the years in which data gaps (missing values) in monsoon season were less than 25% of the season span. Trend analysis of the data using t-test, Mann-Kendall, and KPSS tests indicated stationarity in the peak flows for almost all the stations, except Bamnidhi, Ghatora, and Manendragarh which are located on the upstream northside of the basin (Table 2.2). Non-stationarity in the peak flows at those three stations could be attributed to non-stationarity evident in the annual daily maximum precipitation data for most of the grids in the catchments of those stations.

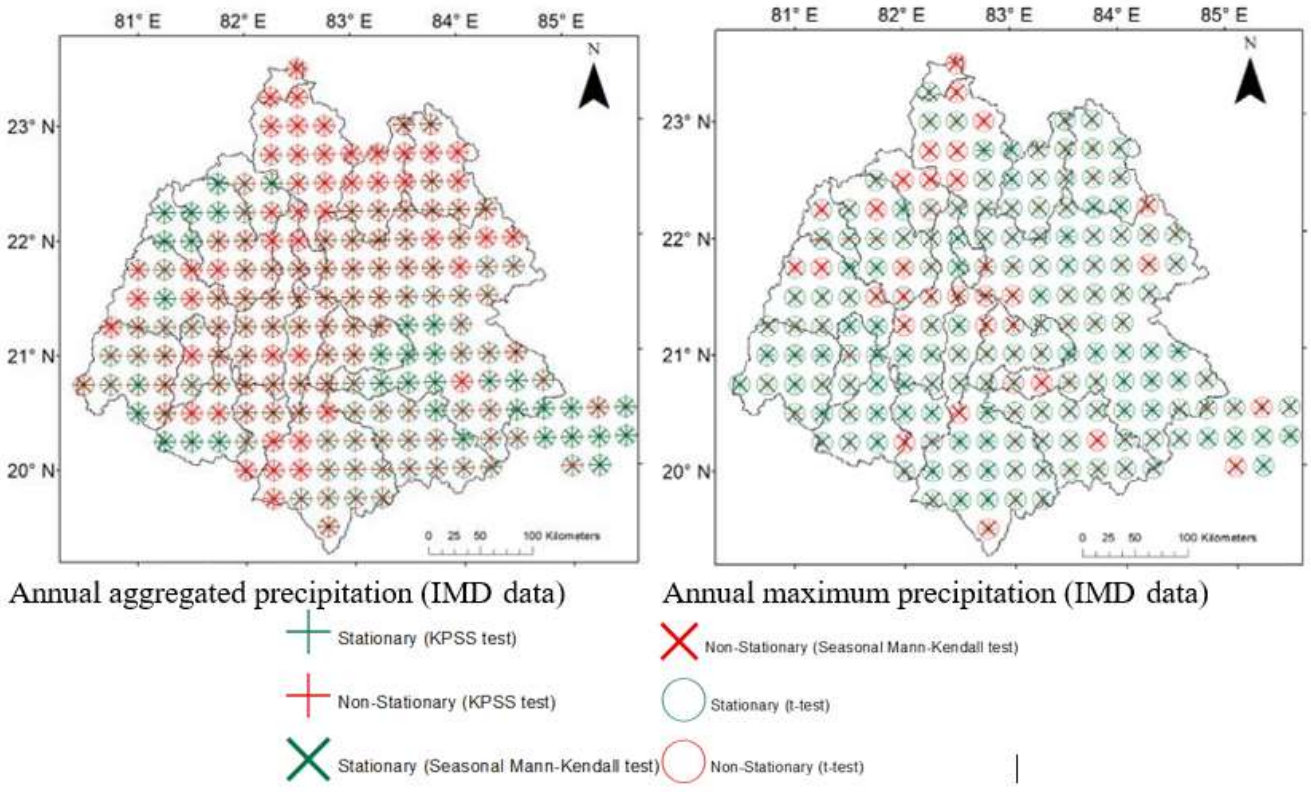

Figure. 2.1: Results of trend analysis on annual aggregated and annual daily maximum precipitation.

Table 2.2: Verification of stationarity in annual maximum daily flows.

Sl. No.	Stream Gauge location	Period of record	Mann-Kendall test		KPSS Test	
			Test statistic	Critical value at 5% significance	Test statistic	Critical value at 5% significance
1	Andhiyarkore	1977-2011	0.54	1.96	0.14	0.46
2	Bamnidihi	1971-2011	**3.78**	1.96	0.44	0.46
3	Baronda	1977-2011	1.11	1.96	0.38	0.46
4	Basantpur	1971-2011	1.48	1.96	0.23	0.46
5	Ghatora	1978-2011	**1.99**	1.96	0.19	0.46
6	Jondhra	1979-2011	1.64	1.96	0.41	0.46
7	Kantamal	1971-2012	0.71	1.96	0.21	0.46
8	Kesinga	1977-2012	0.73	1.96	0.29	0.46
9	Kotni	1977-2011	0.02	1.96	0.16	0.46
10	Kurubhata	1977-2012	1.05	1.96	0.22	0.46
11	Manendragarh	1987-2011	**2.54**	1.96	0.39	0.46
12	Pathardhi	1987-2011	0.73	1.96	0.29	0.46
13	Rajim	1971-2011	0.31	1.96	0.12	0.46
14	Rampur	1971-2011	0.06	1.96	0.22	0.46
15	Salebhata	1971-2012	0.00	1.96	0.13	0.46
16	Seorinarayan	1985-2011	0.91	1.96	0.32	0.46
17	Simga	1971-2011	0.66	1.96	0.18	0.46
18	Sundargarh	1977-2012	0.42	1.96	0.13	0.46
19	Tikarapara	1971-2012	0.86	1.96	0.26	0.46

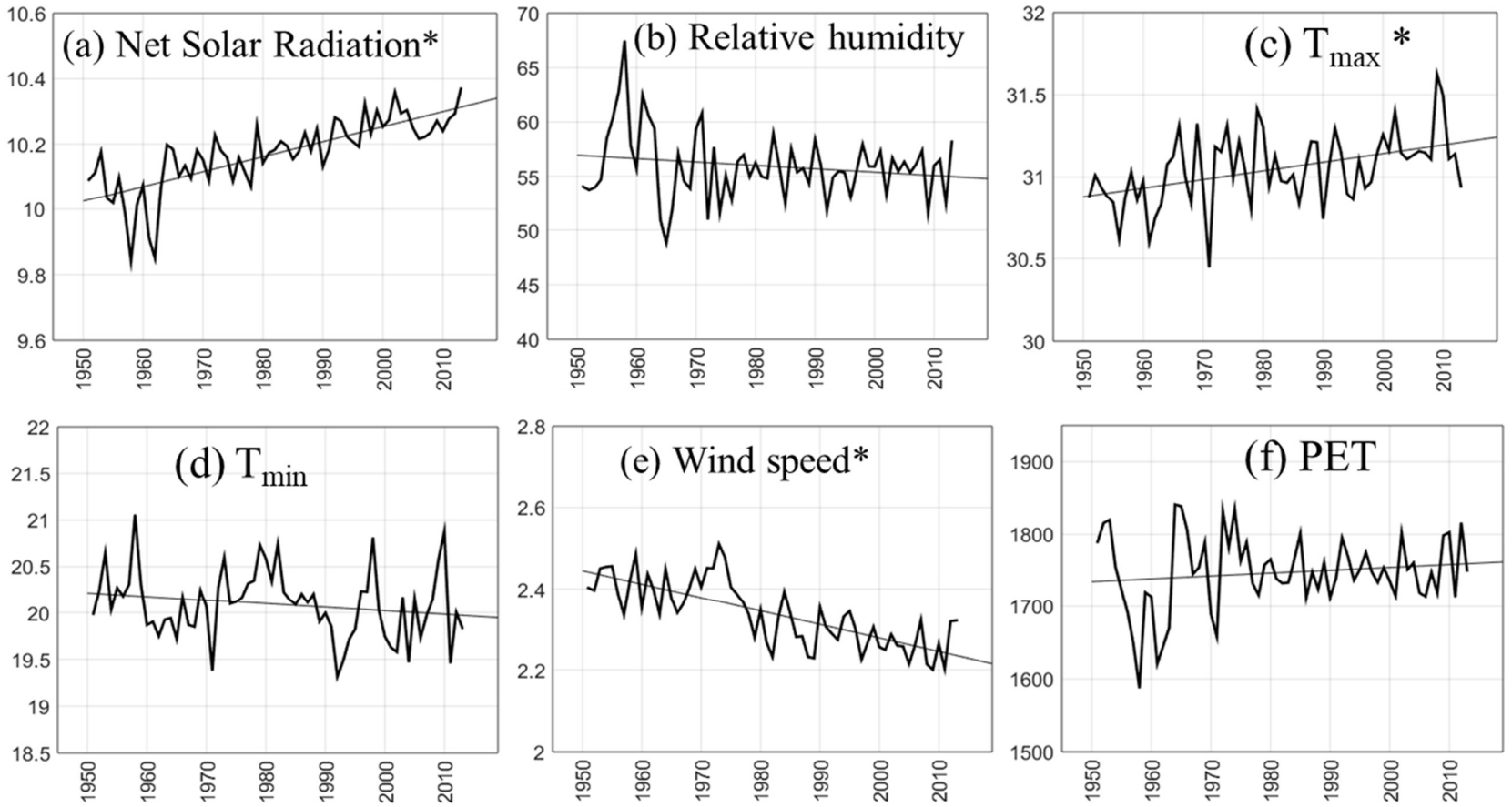

Figure 2.2: Trend lines fitted to annual time series of climate variables. Star symbol is shown as superscript for variables exhibiting nonstationarity.

Section 3
Calibrated and validated hydrological model(s)

Investigations were undertaken to model hydrological processes and establish relationships between components of the hydrological cycle (i.e., water balance components) in the Mahanadi river basin for the current (historical) scenario using baseline data. The Soil and Water Assessment Tool (SWAT) (Neitsch et al., 2011) was used to simulate hydrological processes in the basin.

Streamflows at the potential gauge locations in the Mahanadi basin were generated using ArcSWAT for the period 1989-2012, over which contemporaneous observed flows were available for 19 existing stations. SWAT is a physically-based, semi-distributed model which simulates hydrological processes (e.g., runoff/streamflow, evapotranspiration) in a river basin by dividing it into sub-basins, which are further discretized into various hydrological response units (HRUs) that are homogeneous in slope, soil, land-use/landcover, and management conditions. The model lumps the outflow of various HRUs in a sub-basin to obtain the total runoff (ensuring overall water balance), which is subsequently routed through the channel network in the river basin to obtain the total runoff at the basin outlet. Further details on SWAT can be found in Neitsch et al. (2011).

Input to a SWAT model includes data related to topography, climate, land-use/landcover (LULC), and soils. The topography of the basin was considered in the form of 90 m resolution SRTM (Shuttle Radar Topography Mission) Digital elevation model (DEM). Climate data included that on (i) daily rainfall (0.25° resolution) for the period 1979-2017, and daily temperature (1° resolution) for the period 1979-2012 procured from IMD (India Meteorological Department), (ii) wind speed, relative humidity and solar radiation (0.3125° resolution) for the period 1948-2015 from CFSR (Climate Forecast System Reanalysis) database. The LULC data was extracted from a 1 km resolution Global Land Cover Characterization (GLCC) database, which was prepared using AVHRR source imagery covering the period 1992-1993. Further, soil data was based on 1:5 million resolution world soil maps of FAO-UNESCO (Food and Agricultural Organisation of the United Nations-United Nations Educational, Scientific and Cultural Organisation).

To calibrate SWAT, the Mahanadi basin was delineated into sub-basins corresponding to the 19

gauging stations using ArcSWAT (Figure 3.1). The sub-basins encompass the entire basin area. The SWAT was calibrated using the SWAT-CUP to simulate flows in each of the 19 sub-basins for the period 1989-2012. The calibration involved identification of the sensitive parameters (out of the 20 parameters given in Table 3.1) for each basin separately by performing sensitivity analysis through Sequential Uncertainty Fitting (SUFI2) (Abbaspour et al., 2004) procedure using SWAT-CUP (Calibration and Uncertainty Programs). The model performance was found to be satisfactory when evaluated in terms of Nash-Sutcliffe efficiency (NSE) (Nash and Sutcliffe, 1970), coefficient of determination (R^2), Index of agreement (IOA) (Willmott, 1982), and persistence index (PI) (e.g., Kitanidis and Bras, 1980) (Figure 3.2).

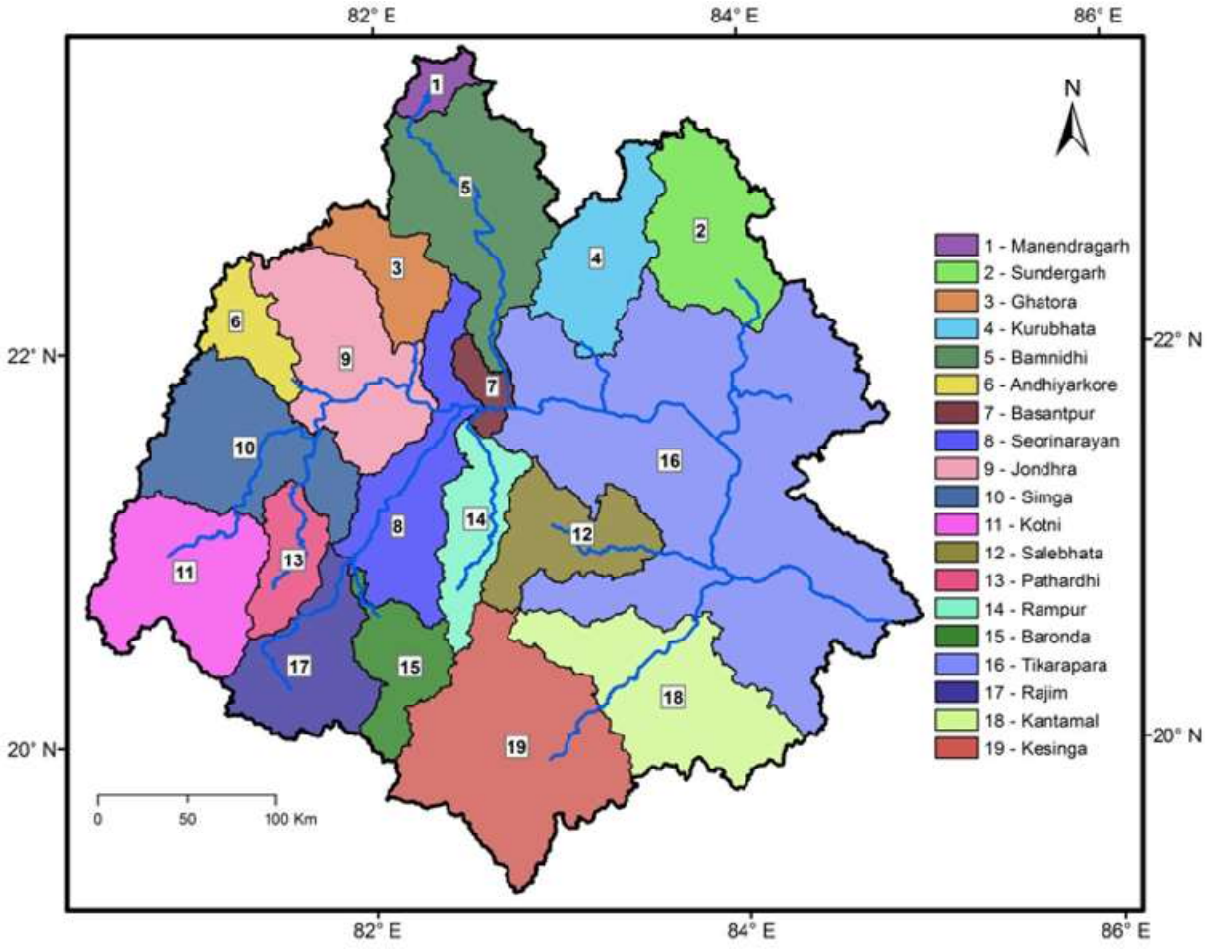

Figure 3.1: Sub-basins delineated corresponding to the gauging stations considered in the Mahanadi basin.

Table 3.1: Parameters considered to calibrate the SWAT model, and station numbers of catchments which are sensitive to each parameter. Station names corresponding to the station numbers are given in Figure 3.1.

Sl. No	Parameter	Unit	Range considered	Station numbers
1	CN2	-	[35, 98]	1, 3 to 12, 14 to 19
2	ALPHA_BF	days	[0, 1]	4, 6, 10, 14, 16, 17, 19
3	GW_DELAY	days	[0, 500]	3, 5, 7, 11, 12, 18
4	REVAPMN	mm H_2O	[0, 500]	6, 7, 10, 12, 14, 15, 18
5	GW_REVAP	-	[0.02, 0.2]	3, 7, 9, 15, 17, 19
6	RECHRG_DP	-	[0, 1]	1, 2, 7, 9 to 13, 15, 18, 19
7	GW_SPYLD	m^3/m^3	[0, 0.4]	1 to 3, 5, 7 to 13, 15 to 18
8	SOL_BD	Mg/m^3	[0.9, 2.5]	1 to 13, 15 to 19
9	SOL_K	mm/hr	[0, 2000]	1 to 19
10	SOL_AWC	mm H_2O/mm soil	[0, 1]	1 to 14, 16 to 19
11	SOL_ALB	-	[0, 0.25]	6, 15
12	HRU_SLP	m/m	[0, 1]	1 to 5, 8 to 14, 17, 18
13	SLSUBBSN	m	[10, 150	1, 2, 4 to 6, 8, 9, 11, 13, 14
14	ESCO	-	[0, 1]	4, 16, 17, 19
15	EPCO	-	[0, 1]	1,2, 4, 6 to 8, 13, 14, 17
16	CANMX	mm H2O	[0, 100]	4, 14, 19
17	EVPOT	-	[0, 2]	1, 2, 4 to 6, 8, 9, 11, 13, 14, 16, 17
18	OV_N	-	[0.01, 30]	1 to 3, 5, 8, 10 to 13, 15, 16, 18, 19
19	CH_N2	-	[-0.01, 0.3]	3, 7, 9, 10, 12, 14 to 16, 18
20	CH_K2	mm/hr	[-0.01, 500]	2 to 6, 8, 13, 14, 16, 19

Cn2: runoff curve number for moisture condition II; ALPHA_BF: Baseflow recession constant; GW_DELAY: delay time for aquifer recharge; REVAPMN: threshold water level in shallow aquifer for revap; GW_REVAP: Groundwater "revap" coefficient (evaporation from unsaturated zone; RECHRG_DP: deep aquifer percolation coefficient; GW_SPYLD: Specific yield of the shallow aquifer; SOL_BD: Moist bulk density; SOL_K: Saturated hydraulic conductivity; SOL_AWC: Available water capacity of the soil layer; SOL_ALB: Moist soil albedo; HRU_SLP: Average slope steepness; SLSUBBSN: Average slope length; ESCO: Soil evaporation compensation factor; EPCO: Plant uptake compensation factor; CANMX: Maximum canopy storage; EVPOT: Pothole evaporation coefficient; OV_N: Manning's "n" value for overland flow; CH_N2: Manning's "n" value for the main channel; CH_K2: Effective hydraulic conductivity in main channel alluvium.

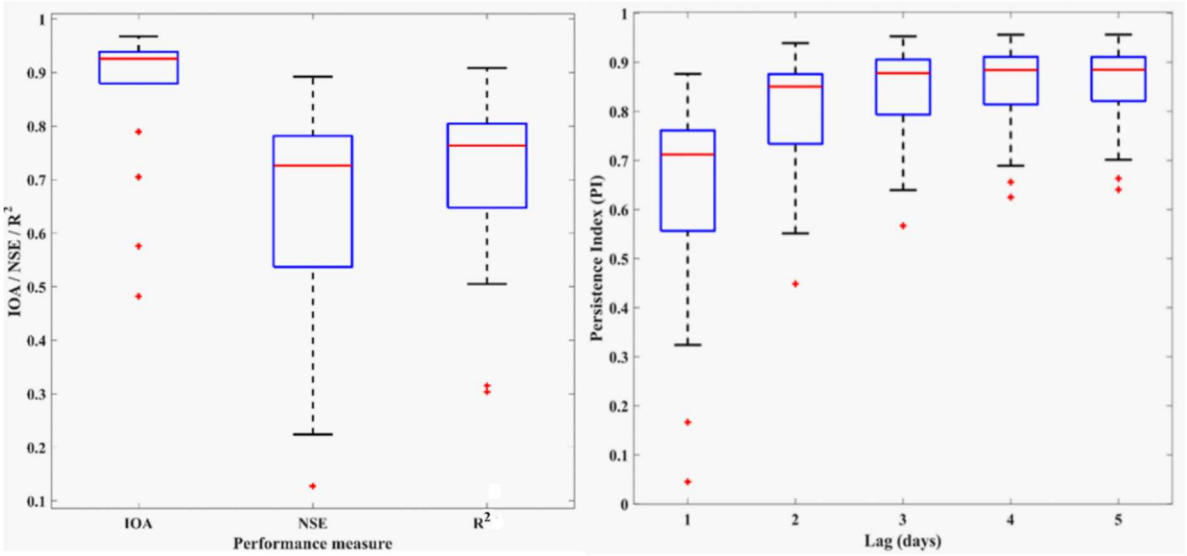

Figure 3.2: Performance evaluation of the calibrated SWAT model. IOA: Index of Agreement; NSE: Nash-Sutcliffe efficiency; R^2: coefficient of determination, PI: Persistence Index.

Water balance components were quantified for the Mahanadi basin based on the calibrated and validated SWAT model. The results indicate that the mean annual precipitation for the basin is 1406 mm, whereas estimates corresponding to Actual Evapotranspiration (AET), percolation, surface runoff, return flow and lateral flow are about 48%, 20%, 49%, 13.4%, and 9.2% respectively (Figure 3.3).

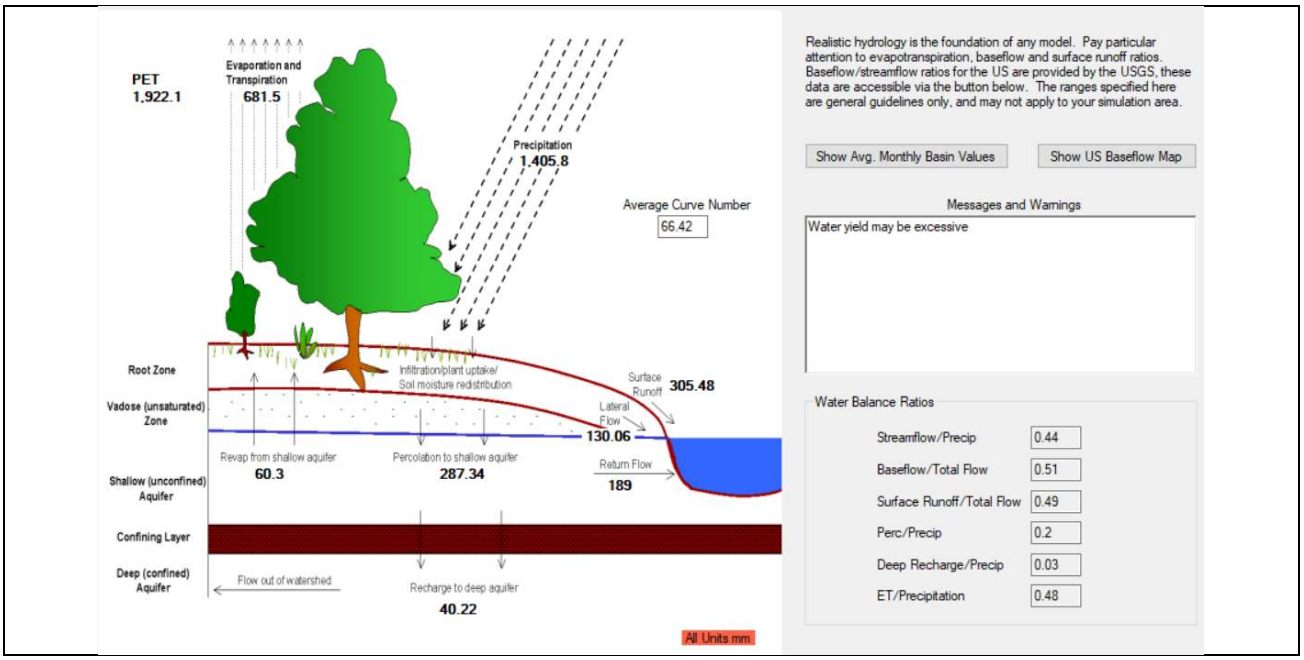

Figure 3.3: Water balance components for the Mahanadi basin determined using the SWAT model based on past observations of hydrometeorological variables.

The SWAT model was further calibrated considering daily data for the sub-basin corresponding to each of the stream gauges that are located upstream of Hirakud dam and also catchments of gauges on tributaries that contribute flow to the river downstream of the dam by fine-tuning estimates of the identified sensitive parameters. This is to enhance the performance of the model in simulating the water balance components of each of the sub-basins. The performance measures quantified corresponding to calibration and validation periods for all the catchments are provided in Table 3.2. It can be noted from the table that the coefficient of determination (R^2) and Nash Sutcliffe Efficiency (NSE) values are fairly high for most of the catchments (except Manendragarh and Andhiyarkore), indicating that the model simulated streamflows satisfactorily. For Manendragarh and Andhiyarkore catchments, simulated streamflow was found to be consistently inflated with respect to observed flows during wet as well as dry periods. This could be attributed to the fact that the catchments are located at the periphery (topographic water divide) of the Mahanadi river basin. Therefore, the groundwater divide is suspected to be located inside the topographic water divide of the two catchments, which causes the movement of infiltrated rainwater from these two catchments to other catchments located outside the Mahanadi river basin. This water movement cannot be accounted by the SWAT model.

Water balance components (Actual Evapotranspiration (AET), percolation, surface runoff, lateral flow, streamflow) were quantified for each of the 19 sub-basins based on the calibrated and validated SWAT models. The details are provided in Table 3.3. The results indicate that the variability of water balance components is high across the 19 sub-basins. Estimates for ranges corresponding to AET, percolation, surface runoff, lateral flow and streamflow (in the percentage of mean annual precipitation) are 30%-71%, 3%-54%, 2%-49%, 0.2%-20%, and 24-52%, respectively. Accounting for combined surface and groundwater analysis using models such as SWAT-MODFLOW could aid in further fine-tuning these estimates.

Table 3.2: Results from calibration and validation of SWAT for catchments in Mahanadi basin.

Sub-basin	Calibration Period		Validation Period	
	NSE	R^2	NSE	R^2
Manendragarh	0.44	0.67	0.19	0.58
Sundergarh	0.89	0.89	0.75	0.82
Ghatora	0.73	0.73	0.34	0.74
Kurubhata	0.70	0.71	0.71	0.74
Bamnidhi	0.50	0.53	0.58	0.59
Andhiyarkore	-1.70	0.44	-1.61	0.33
Basantpur	0.90	0.90	0.85	0.89
Seorinarayan	0.88	0.89	0.85	0.86
Jondhra	0.84	0.85	0.71	0.79
Simga	0.82	0.86	0.72	0.72
Kotni	0.79	0.81	0.69	0.70
Salebhata	0.74	0.77	0.71	0.71
Pathardhi	0.72	0.72	0.34	0.49
Rampur	0.67	0.67	0.59	0.61
Baronda	0.84	0.85	0.56	0.58
Tikarapara	0.84	0.88	0.44	0.94
Rajim	0.79	0.79	0.68	0.69
Kantamal	0.87	0.88	0.81	0.81
Kesinga	0.81	0.85	0.81	0.82

Table 3.3: Mean annual water balance components quantified using SWAT expressed in terms of percentage of precipitation.

Catchment of gauge	Area (km^2)	(% of precipitation)				
		AET	Perco-lation	Surface runoff	Lateral flow	Stream-flow
Manendragarh	1013.2	30.51	53.88	5.68	10.92	36.94
Sundergarh	5885.2	58.74	3.72	34.43	3.77	39.05
Ghatora	3045.3	38.72	50.02	2.99	8.34	25.46
Kurubhata	4777.8	36.85	40.99	20.75	1.39	39.99
Andhiyarkore	2270.6	50.34	13.01	35.77	0.25	39.09
Kotni	6968.4	43.62	35.59	17.87	3.02	25.32
Salebhata	4530.2	59.77	2.63	31.29	6.45	37.74
Pathardhi	2493.5	41.89	22.54	34.70	0.70	36.11
Rampur	3420.0	56.04	12.59	27.08	4.36	37.82
Baronda	3196.3	70.97	2.94	26.76	0.25	27.00
Rajim	5185.9	50.43	6.93	35.99	6.75	47.15
Kesinga	11750.0	44.61	3.71	48.45	3.58	52.04
Bamnidhi	8767.5	38.67	39.53	1.56	20.38	33.45
Basantpur	1055.9	48.77	22.03	22.97	6.33	33.89
Seorinarayan	6274.5	50.25	18.14	28.81	2.89	34.43

Jondhra	7495.6	50.14	25.64	21.26	2.88	27.45
Simga	7354.0	51.86	26.60	19.08	2.45	23.68
Tikarapara	32506.6	48.89	22.76	23.15	5.42	35.30
Kantamal	8462.5	42.58	15.45	32.28	9.82	43.32

In recent years, there has been an increase in research to assess the possible impacts of land-use/land-cover (LULC) change on hydrological processes in river basins, owing to an increase in awareness that changes in LULC could influence climate, ecosystem, and hydrological processes. The term land-use denotes the purposes (e.g., cultivation, settlement, recreation, rangeland) for which humans employ/utilize the land, whereas land-cover refers to the physical state of the land, which includes habitat or vegetation type present in an area, water and earth material (e.g., forest, lakes). Land-use change at any location may involve either a shift to a different land-use or an intensification of an existing land-use. LULC information available on the Mahanadi basin from the literature (Dadhwal et al., 2010) and multiple data sources including (i) 30 m resolution Landsat images for 1989-90; and (ii) pre-processed (classified) LULC images from NRSC (National Remote Sensing Centre) at the annual scale for the period 2004-2011 was analyzed. LULC changes were quantified in terms of percentage of the total area of the basin. The changes were found to be (i) decline in forest cover by 6.2% between 1985-2004 and negligible thereafter, and increase in (ii) agricultural land by 3.6% between 1985-2003 and negligible thereafter, (iii) surface water bodies by 0.73%, and (iv) built up land by 0.11%. Furthermore, information available on build-up area from the classified LULC images from NRSC appeared erroneous (0.31% in 2003; 0.43% in 2004-05, 0.36% in 2005-06, 0.28% in 2007-08; 0.33% during 2008-2011). Since the changes in LULC were minimal over the recent past, they are not expected to have any significant effect on components of the hydrological cycle in the river basin. In the future, investigations could be carried out to model LULC changes using information from raw (unprocessed) satellite imageries of the Mahanadi basin to verify the inferences drawn based on this study, if access to raw satellite products could be obtained from NRSC.

The validated SWAT model was forced with ensemble means of future projections of climate variables derived at 0.25° resolution from three GCMs (CanESM5 (2.7906°×2.8125°), INM-CM4-8 (1.5°×2°), and INM-CM5-0 (1.5°×2°)) corresponding to four CMIP6 climate change scenarios (SSP-1-2.6, SSP2-4.5, SSP3-7.0, and SSP5-8.5) to arrive at future projected streamflows in the basin. The streamflows were analyzed at the monthly scale to discern the projected future trend. The

scenarios are also mentioned as SSPs 126, 245, 370, and 585 in the later part of this report, as noted in the literature. Scrutiny of a plethora of CMIP6 GCMs indicated that only those three GCMs provide the necessary projections of various desirable climate variables. In general, streamflows are projected to increase in the future for the scenarios (Figure 3.4). The increase is highest for SSP1-2.6 scenario in the initial two decades (2020-2040). Thereafter it is highest for SSP5-8.5 scenario up to 2100.

Standardized seasonal streamflow values corresponding to each of the four future SSP forcing scenarios (2018-2100) were derived for each of the 19 sub-basins by deducting from them the mean of seasonal streamflows for the historical period (1989-2012) and then dividing the resulting values by the standard deviation of seasonal streamflows for the historical period. The seasons considered were winter (January-February), pre-monsoon (March-May), southwest monsoon (June-September), and post-monsoon (October-December). The results indicated that in the monsoon, post-monsoon, and winter seasons, streamflows are projected to increase in the future with respect to the mean seasonal flow observed in the past period (Figure 3.5). Furthermore, among the seasons, a substantial increase in flows is noted in post-monsoon and winter seasons.

Table 3.4: LULC information available for the Mahanadi basin from various sources.

LULC classes	1985	1989 -1990	2003	2004 -2005	2005 -2006	2006 -2007	2007 -2008	2008 -2009	2009 -2010	2010 -2011
Built up land (%)	0.22	0.31	0.31	0.43	0.36	0.36	0.28	0.33	0.33	0.33
Agriculture (%)	56.41	60.76	59.63	60.43	58.55	59.24	60.06	59.43	60.02	59.98
Forest (%)	37.56	36.80	33.48	31.03	31.38	31.39	31.46	31.36	31.34	31.36
Water Bodies (%)	1.19	1.51	1.62	2.22	2.77	2.11	2.19	2.51	2.06	1.92

1985: (AVHRR images -1 km resolution)-Dadhwal et al., 2010

1989-90: (Landsat images – 30m resolution)- Present study

2003: (AWiFs -56 m resolution) -Dadhwal et al., 2010

2004-2011: Information extracted in present study from NRSC processed data

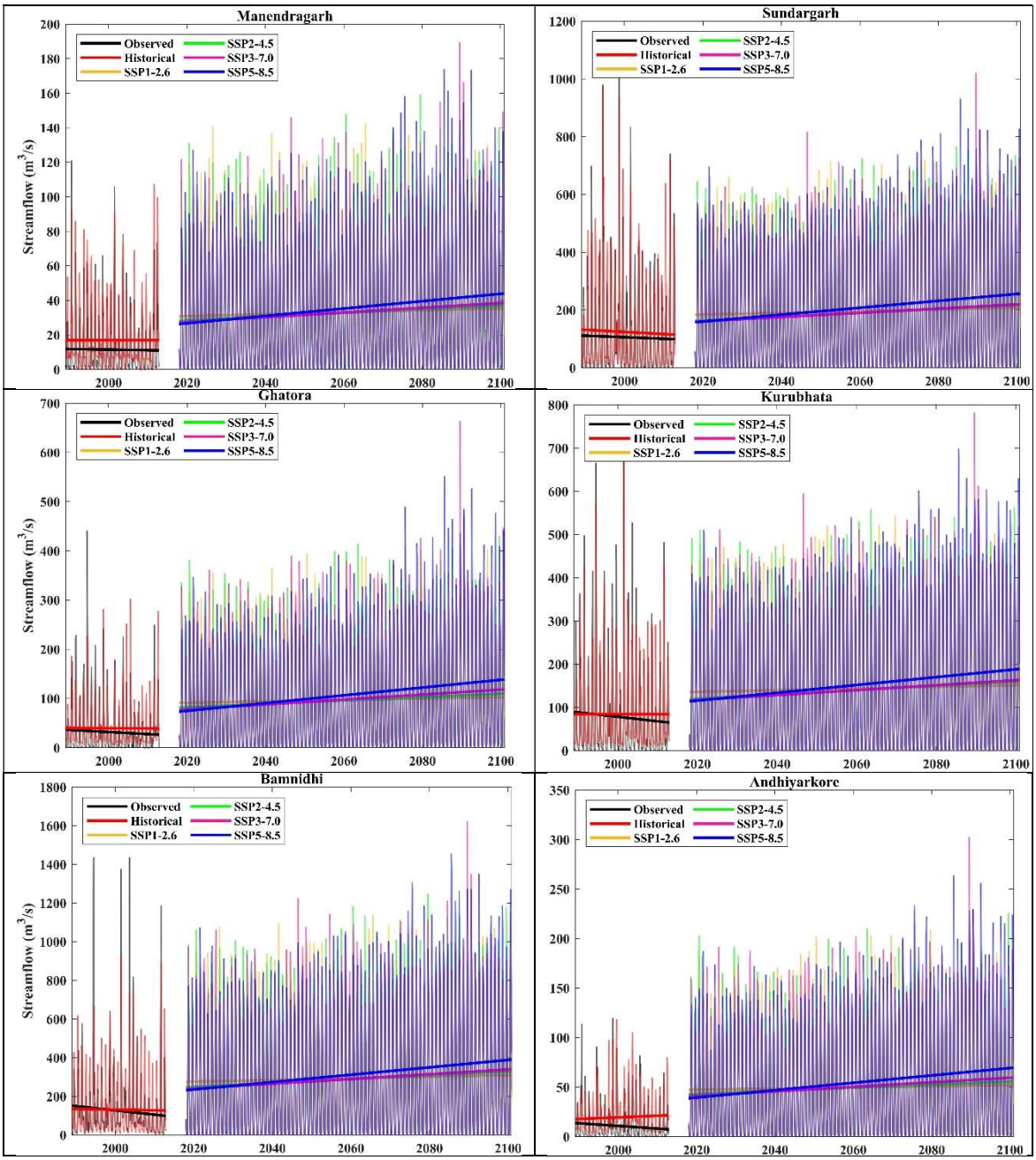

Figure 3.4: SWAT simulated monthly streamflows for the historical period and future projected period (corresponding to four CMIP6 SSP forcing scenarios) are compared with the observed streamflows.

Figure 3.4 (continued…)

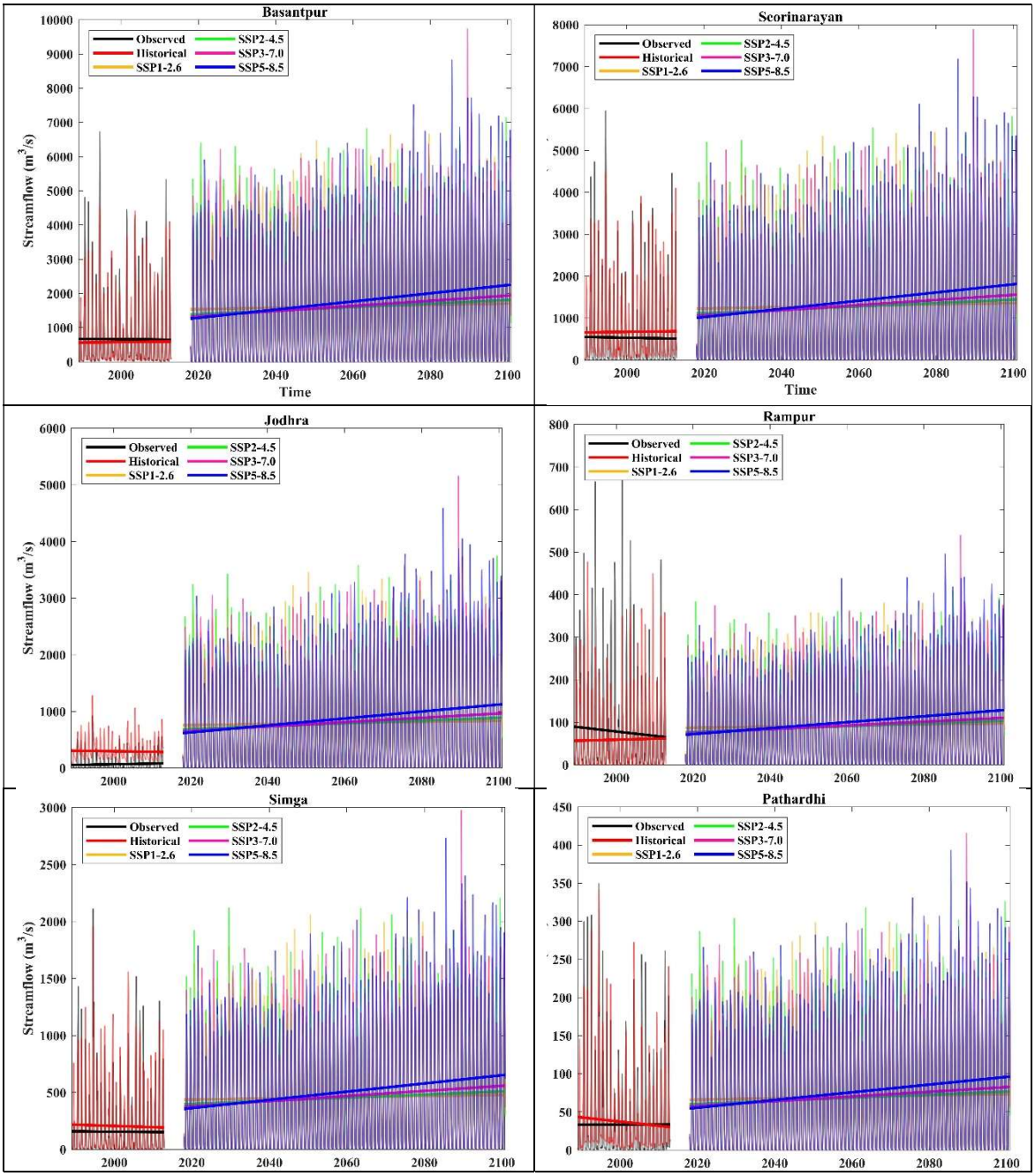

Figure 3.4 (continued…)

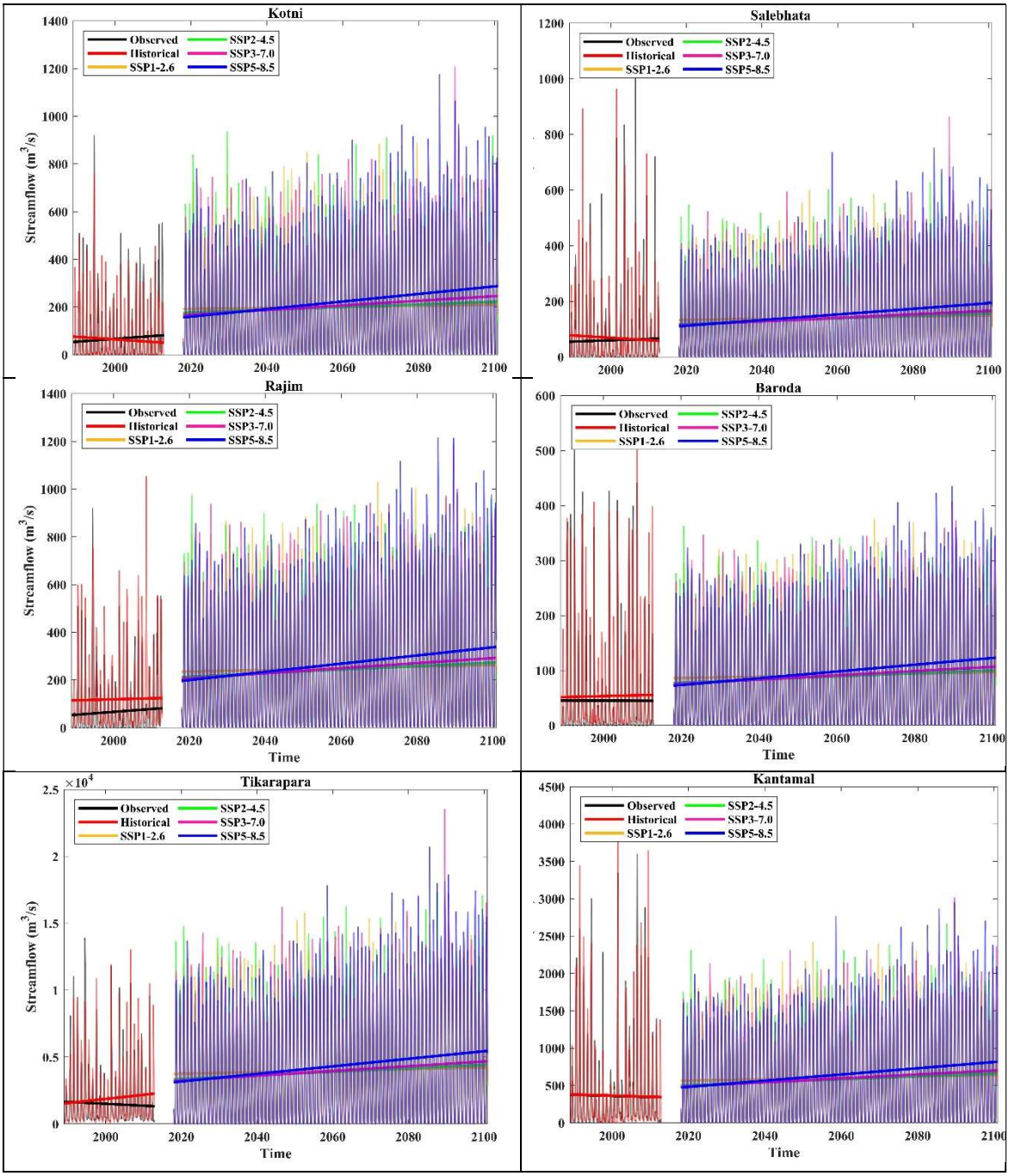

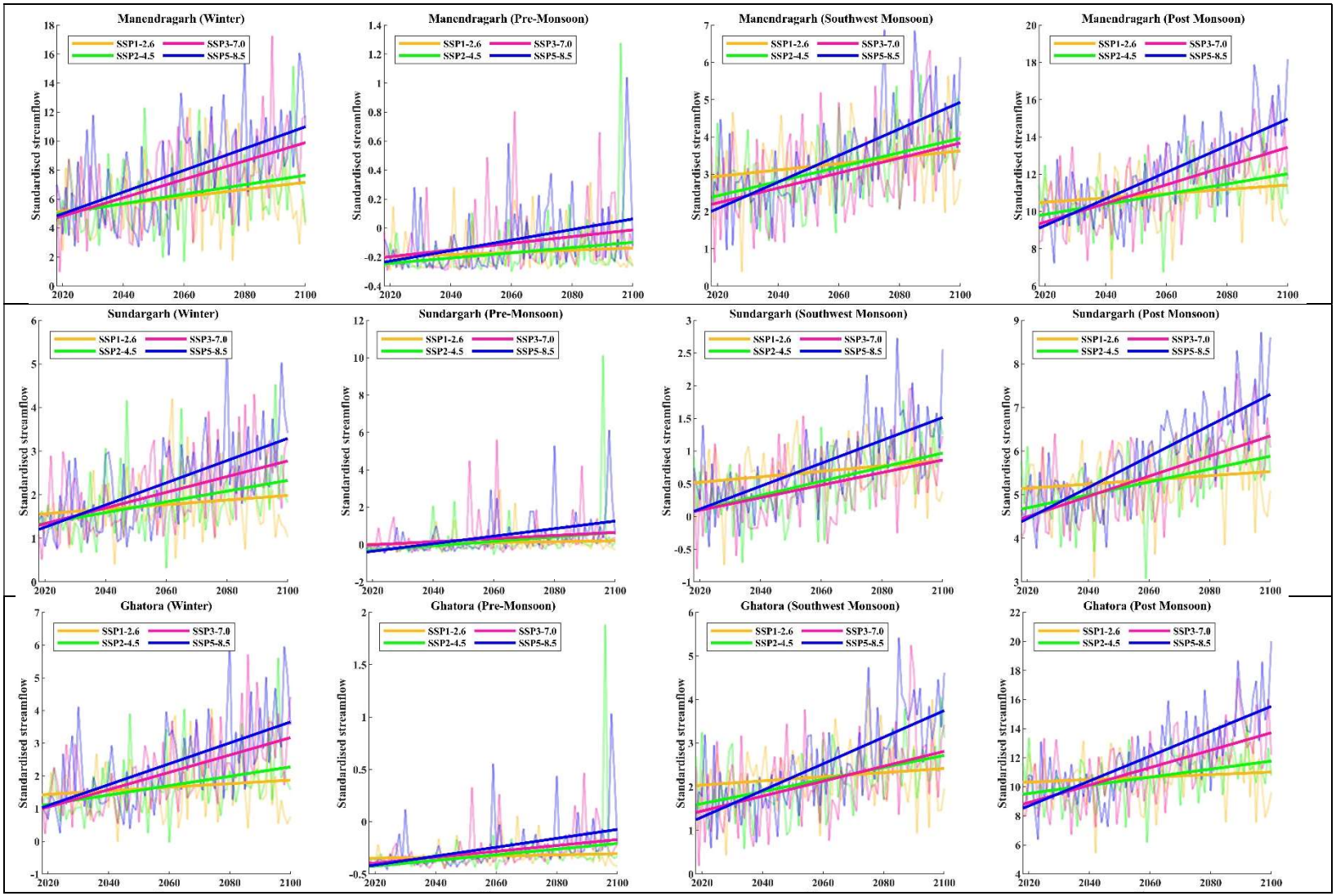

Figure 3.5: Standardised streamflow values of four future SSP forcing scenarios (2018-2100) with respect to the observed period (1989-2012) for four seasons corresponding to the 19 sub-basins. The four seasons considered are winter (January-February), pre-monsoon (March-May), southwest monsoon (June-September), and post-monsoon (October-December).

Figure 3.5 (continued…)

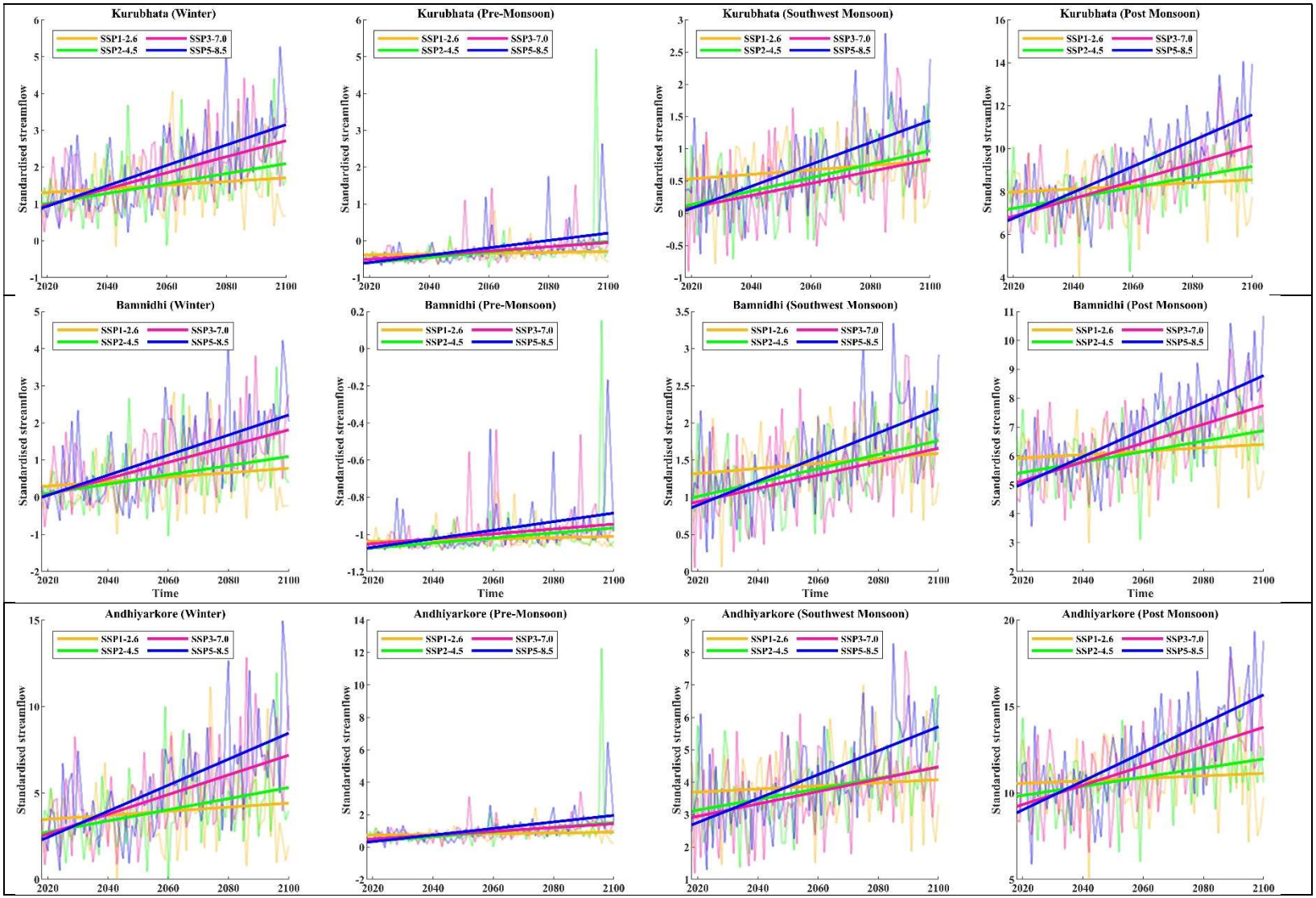

Figure 3.5 (continued…)

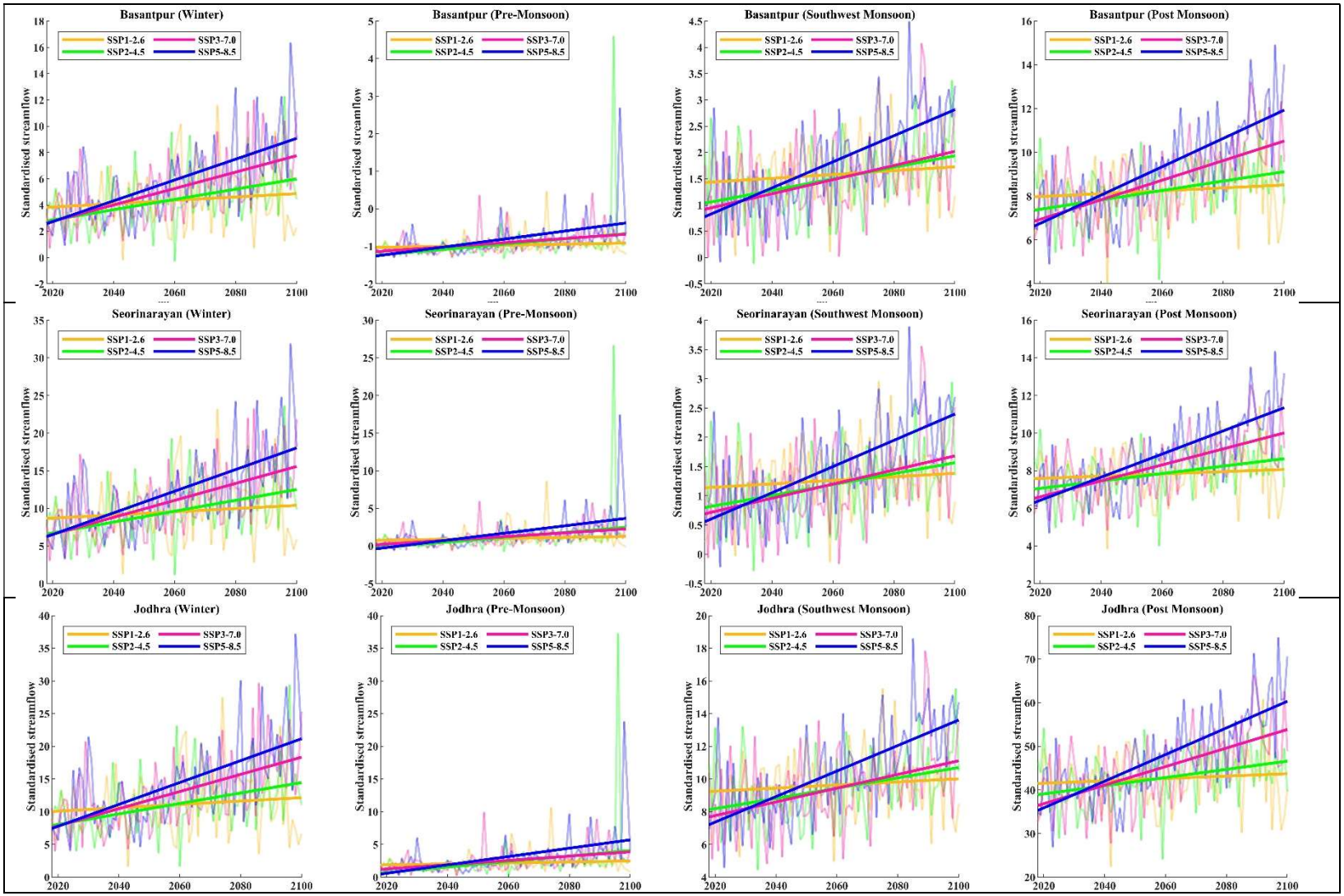

Figure 3.5 (continued…)

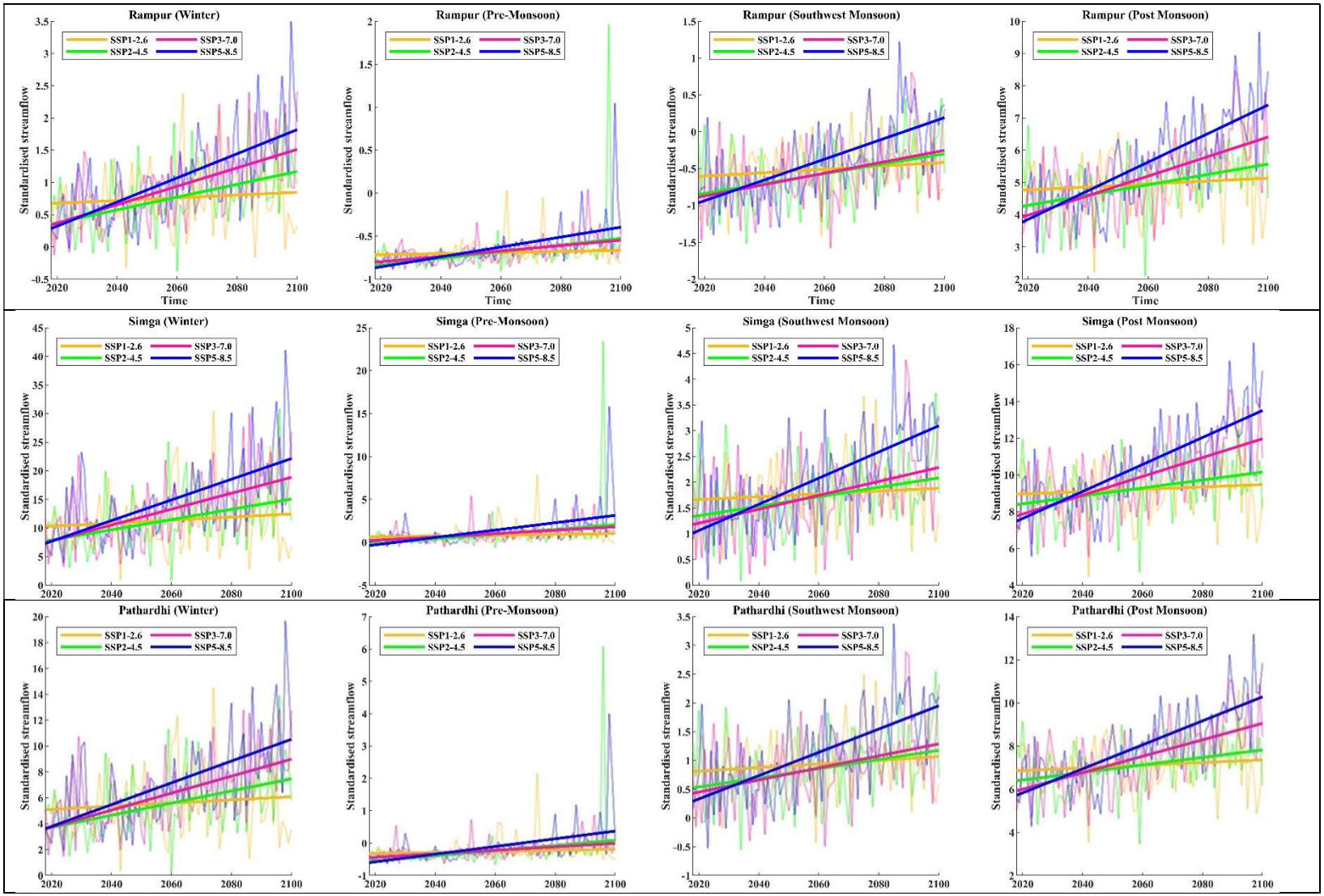

Figure 3.5 (continued…)

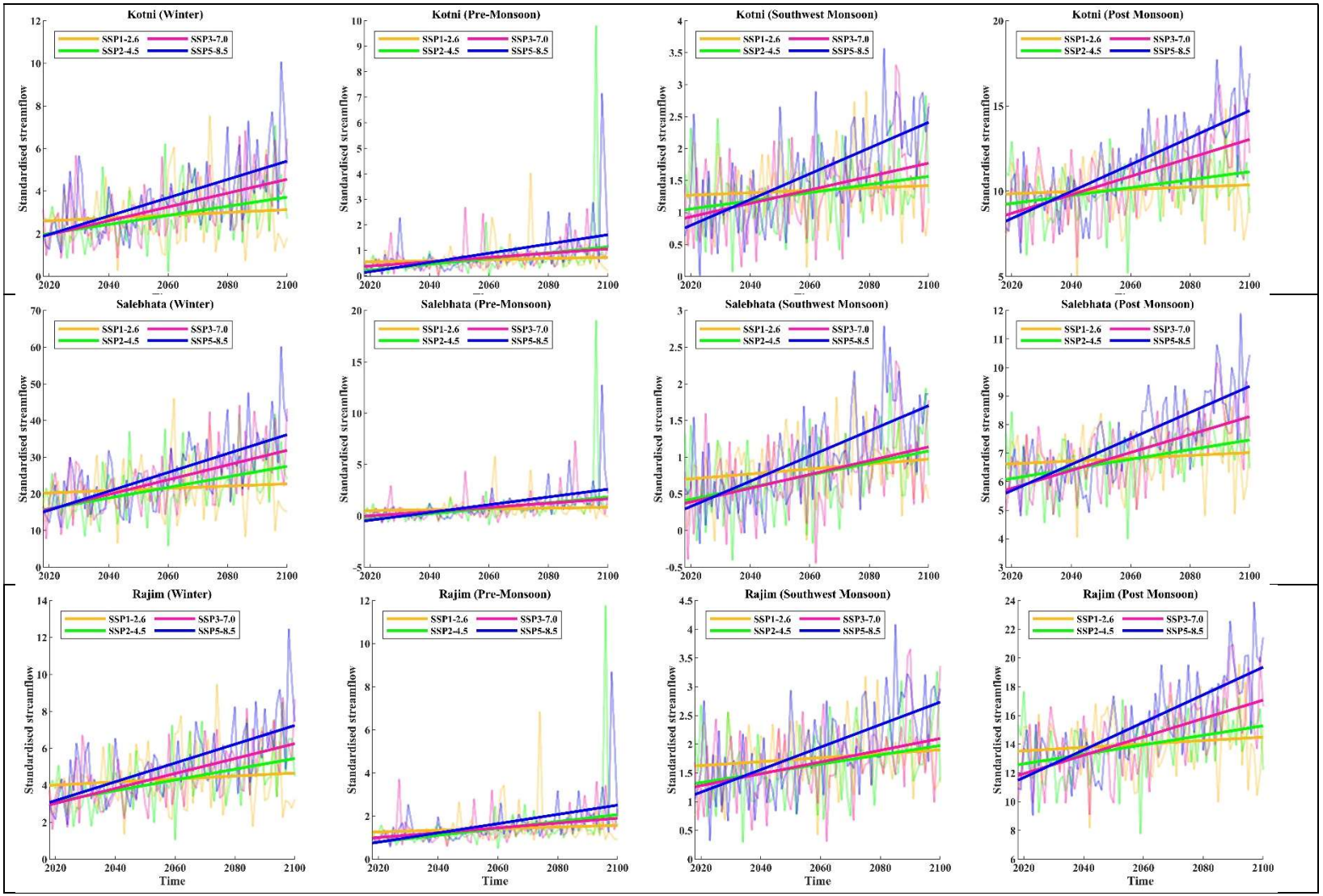

Figure 3.5 (continued…)

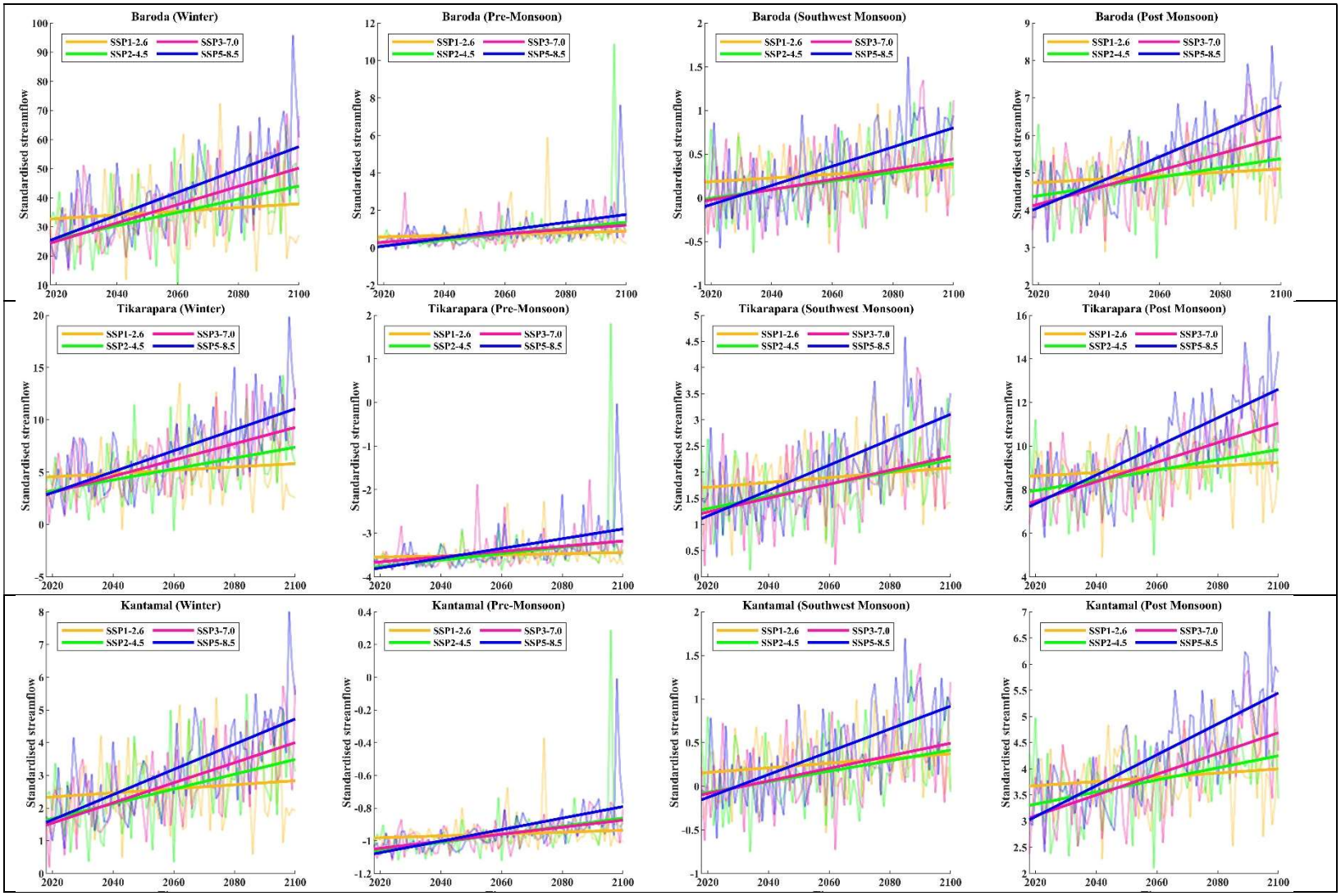

Figure 3.5 (continued…)

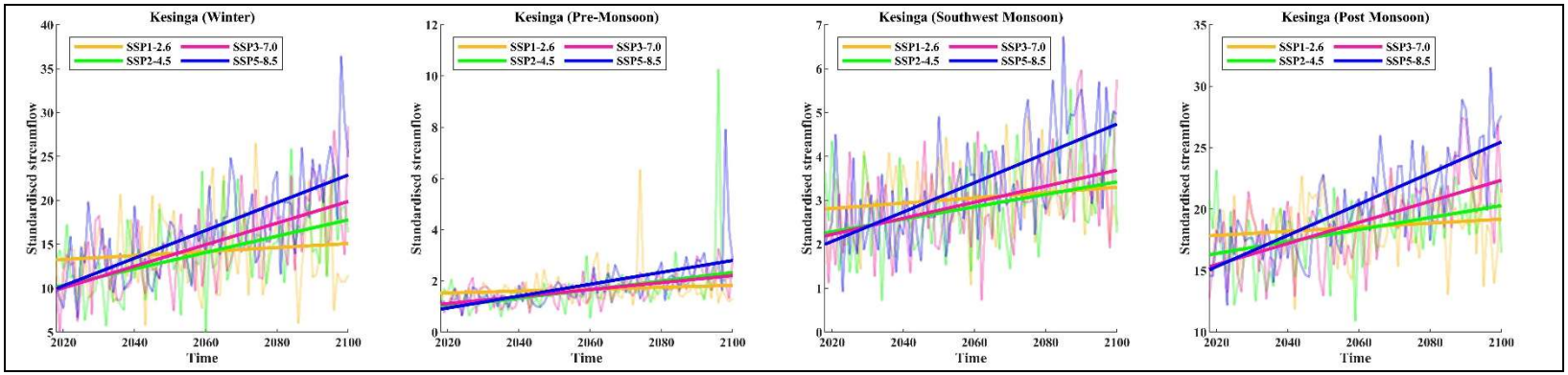

Section 4

Impacts on water availability at various gauging sites within the basin (in terms of change in flow duration curves)

Flow duration curves (FDCs) relate specific streamflow values with their corresponding exceedance probabilities. The FDC is constructed by (i) arranging the data points (flow values) in descending order of magnitude, (ii) assigning ranks to the data points such that the largest value has the rank 1, (iii) determining the exceedance probability corresponding to each data point using the Weibull plotting position formula (Equation 4.1 given below), and (iv) plotting the data points (streamflow values) versus exceedance probability and joining the points by a smooth curve.

$$P(X \geq x_m) = \frac{m}{n+1} \qquad (4.1)$$

where X is the random variable representing streamflow, x_m is the m-th ranked data point, and n is the total number of data points.

Using the future projected streamflows obtained from the SWAT model corresponding to various SSP-FS (Shared Socioeconomic Pathways forcing scenarios), namely SSP1–2.6, SSP2–4.5, SSP3–7.0 and SSP5–8.5, the FDCs for the future scenarios were prepared for the 19 sub-basins in the Mahanadi basin, and they were compared with FDCs corresponding to the past period (Figure 4.1). At the majority of the stations, the future flows corresponding to different exceedance probabilities are projected to increase for all the climate change scenarios, but there is no noticeable difference between the historical and future projected low flows. The increase is generally highest for SSP5-8.5 scenario for a major portion of the probability scale, as expected. Furthermore, the differences in FDCs corresponding to other SSP scenarios are marginal. The high flows (with exceedance probability lower than 1%) in the sub-basins Sundergarh, Rampur, Salebhata, Baronda, and Kantamal and low flows (with exceedance probability higher than 70%) in the sub-basins Bamnidhi and Tikarapara are projected to marginally decrease in the future climate change scenarios. In most of the sub-basins, the high flows are highest in SSP3-7.0 scenario, except Baronda (Rajim, and Kesinga) where the high flows are highest (comparable) for the scenario SSP5-8.5.

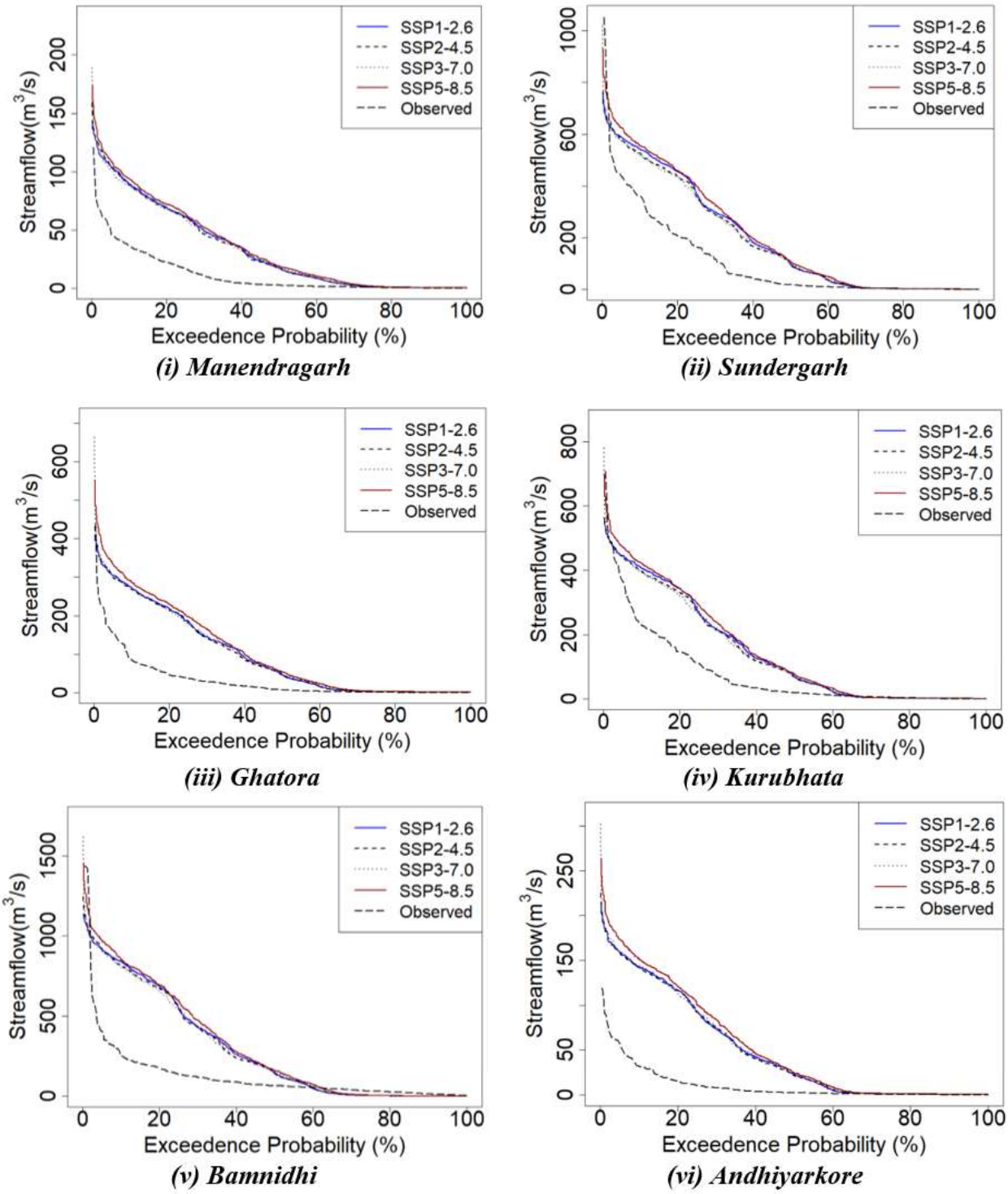

Figure 4.1: Comparison of past and future projected FDCs for the 19 sub-basins in the Mahanadi basin. The future projected streamflows are obtained from the SWAT model for CMIP6 SSP-FS (Shared Socioeconomic Pathways forcing scenarios) (SSP1–2.6, SSP2–4.5, SSP3–7.0, and SSP5–8.5).

Figure 4.1 (continued…)

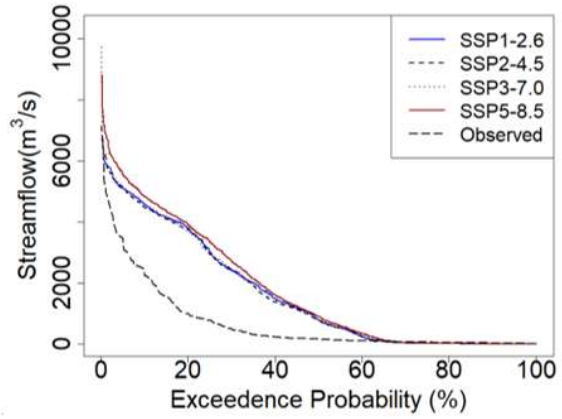

(vii) Basantpur

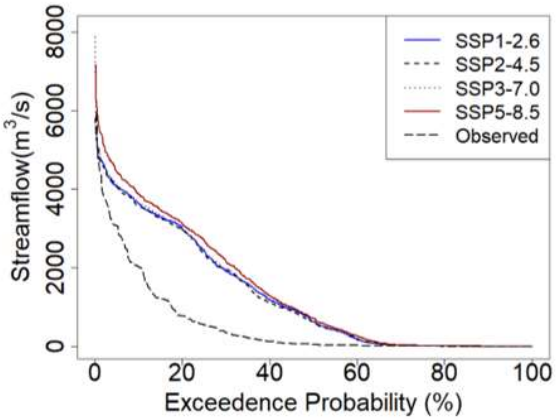

(viii) Seorinarayan

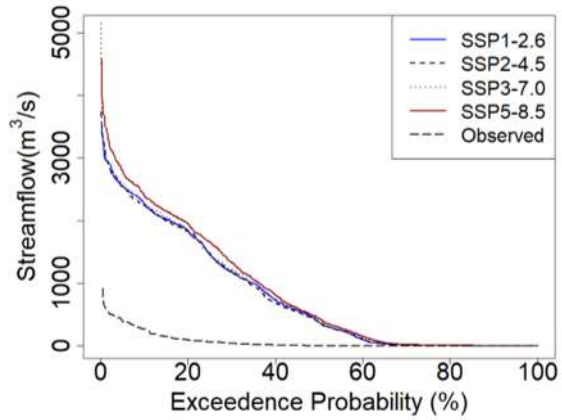

(ix) Jondhra

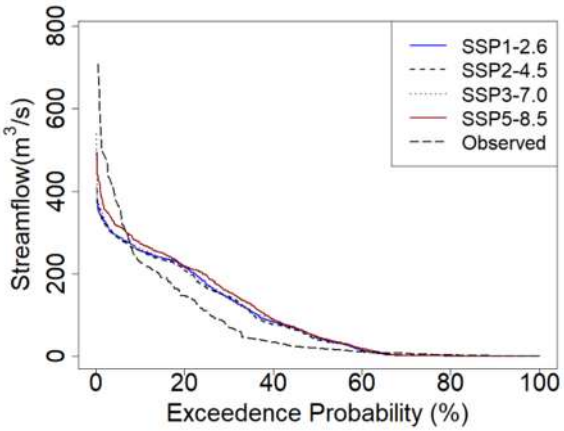

(x) Rampur

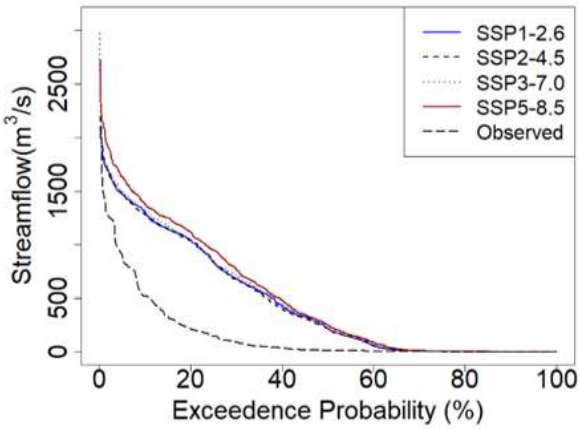

(xi) Simga

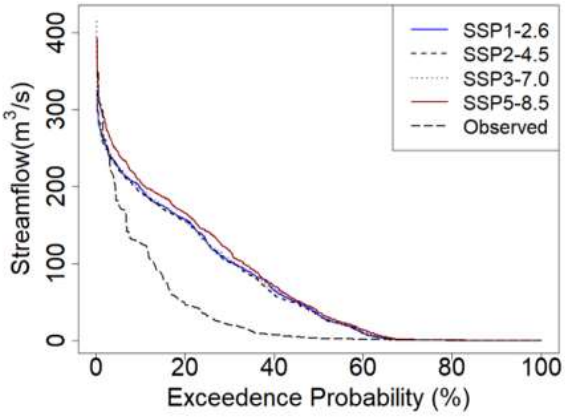

(xii) Pathardhi

Figure 4.1 (continued…)

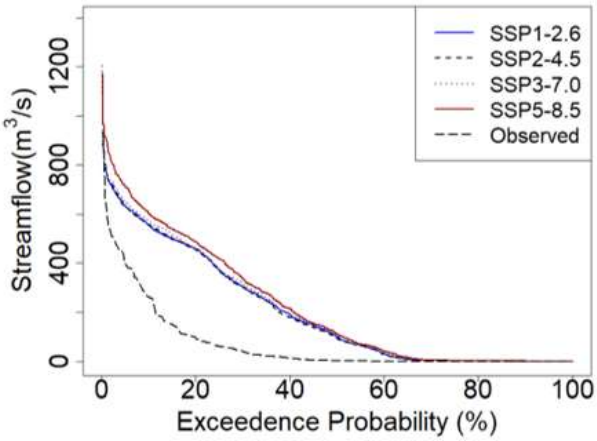

(xiii) Kotni

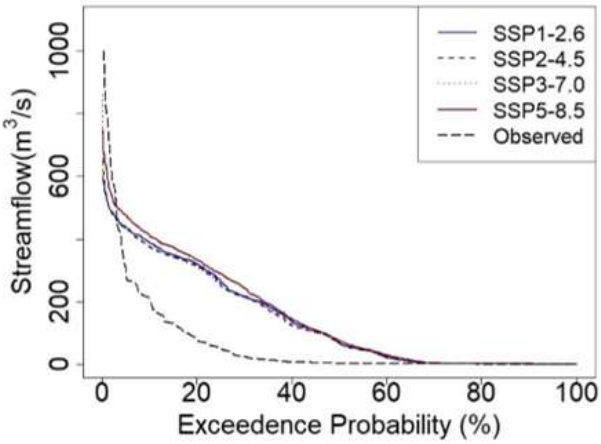

(xiv) Salebhata

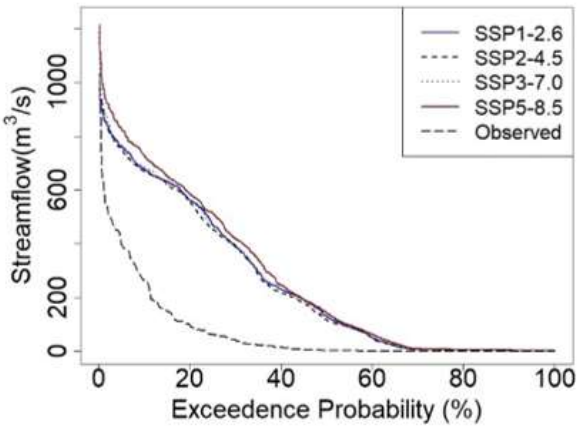

(xv) Rajim

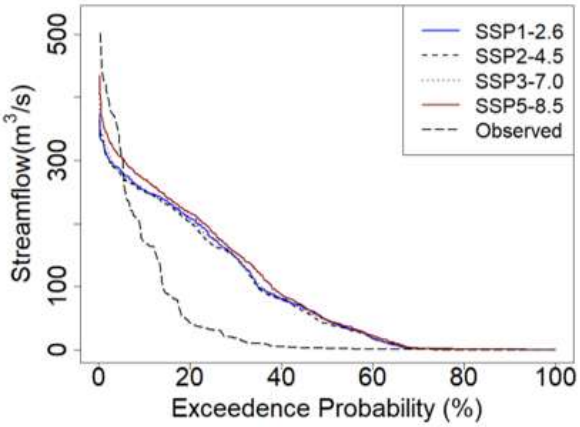

(xvi) Baronda

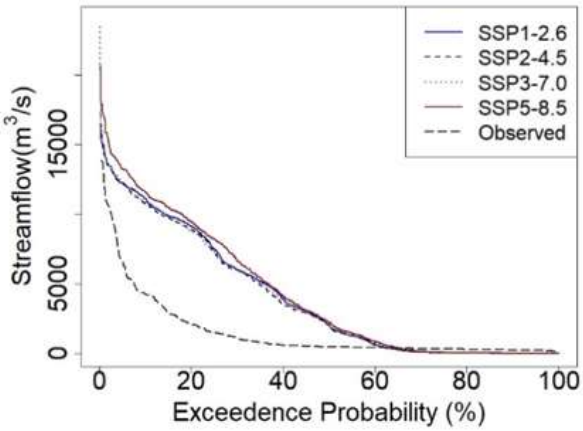

(xvii) Tikarapara

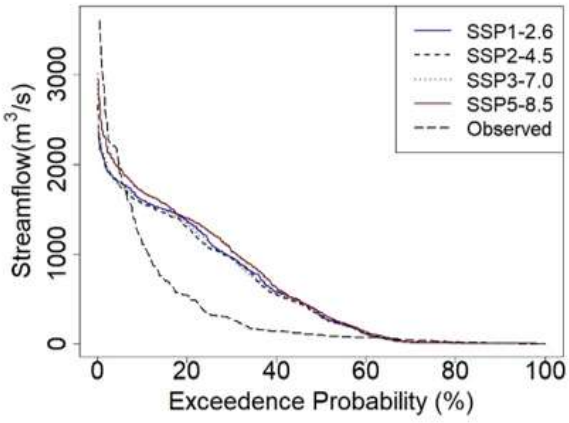

(xviii) Kantamal

Figure 4.1 (continued…)

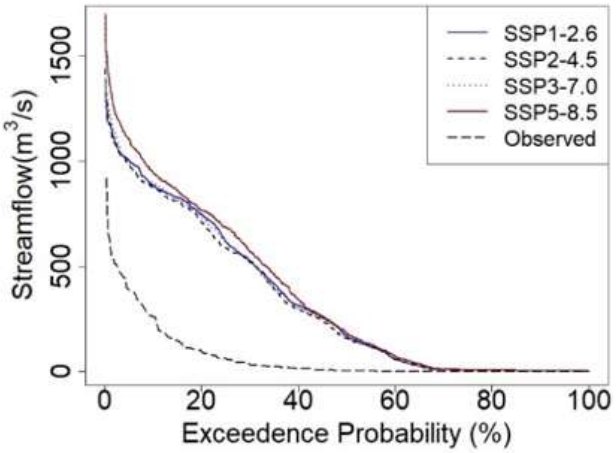

(xix) Kesinga

Section 5

Impacts on irrigation water demands

5.1. Introduction

Water quantities needed for irrigation in an area are conventionally determined by taking into account evapotranspiration requirements. Hence, investigations were carried out on the Mahanadi basin to (i) discern prevailing regional patterns (homogeneous regions) of potential evapotranspiration (ET_0) and actual evapotranspiration (ET_a), (ii) determine regional trends and change point(s) of ET_0 and its predictor climate variables for the prevailing and future climate change scenarios, and (iii) identify key climate variables which govern ET_0 and annual surface runoff changes in various parts of the basin. For use in these investigations, a new regionalization methodology is proposed, and expression is derived for the third-order approximation of the Taylor series expansion of ET_0. In addition, new relevance vector regression (RVR) relationships are developed to arrive at the FAO-PM estimate of ET_0 in data-sparse areas of the basin. Investigations were also focused on examining the validity of Bouchet's complementary relationship (i.e., feedback mechanism between ET_0 and ET_a) for the basin and on arriving at future projections for surface runoff changes over the basin using Budyko framework (which is an approximation of a complex rainfall-runoff process).

5.2. Regionalization of ET_0

The prevailing patterns of ET_0 were first determined through regionalization. Regionalization approaches are widely used for the delineation of homogeneous regions of different hydro-meteorological variables (including ET_0) for different applications such as (i) spatial aggregation or upscaling of information on climate variables to study their regional trend/behavior and change point(s), and (ii) to compensate lack of adequate at-site data on hydro-meteorological variable(s) by pooling regional information (i.e., trading space for time) to arrive at desired estimates. Conventional regionalization approaches consider lumped (time-invariant) statistics such as mean, median, or interquartile range of different hydro-climatic variables as attributes (covariates) to delineate homogeneous hydro-meteorological regions. Thus, information on the temporal dynamics of those attributes is lost, which should be averted because the use of that information could prove useful in delineating regions that are effective in regional homogeneity. To address this, a new methodology

called fuzzy dynamic clustering is developed for the regionalization of ET_0 in the fuzzy framework (see Appendix 5.1; Swapan and Srinivas, 2020a). Its effectiveness is demonstrated through a case study on India (containing the Mahanadi basin), which yielded eighteen regions (Figure 5.1a) that are shown to be statistically more homogeneous in ET_0 when compared to regions formed using global fuzzy c-means (GFCM) clustering method (Figure 5.1b) and existing agro-ecological regions (Figure 5.1c) in terms of (i) strength of inter-site correlations of ET_0, (ii) ANOVA based measure for the strength of regional average ET_0 time series, and (iii) spectral homogeneity measure (F-statistic). Finer details of this analysis can be found in Swapan and Srinivas (2020a).

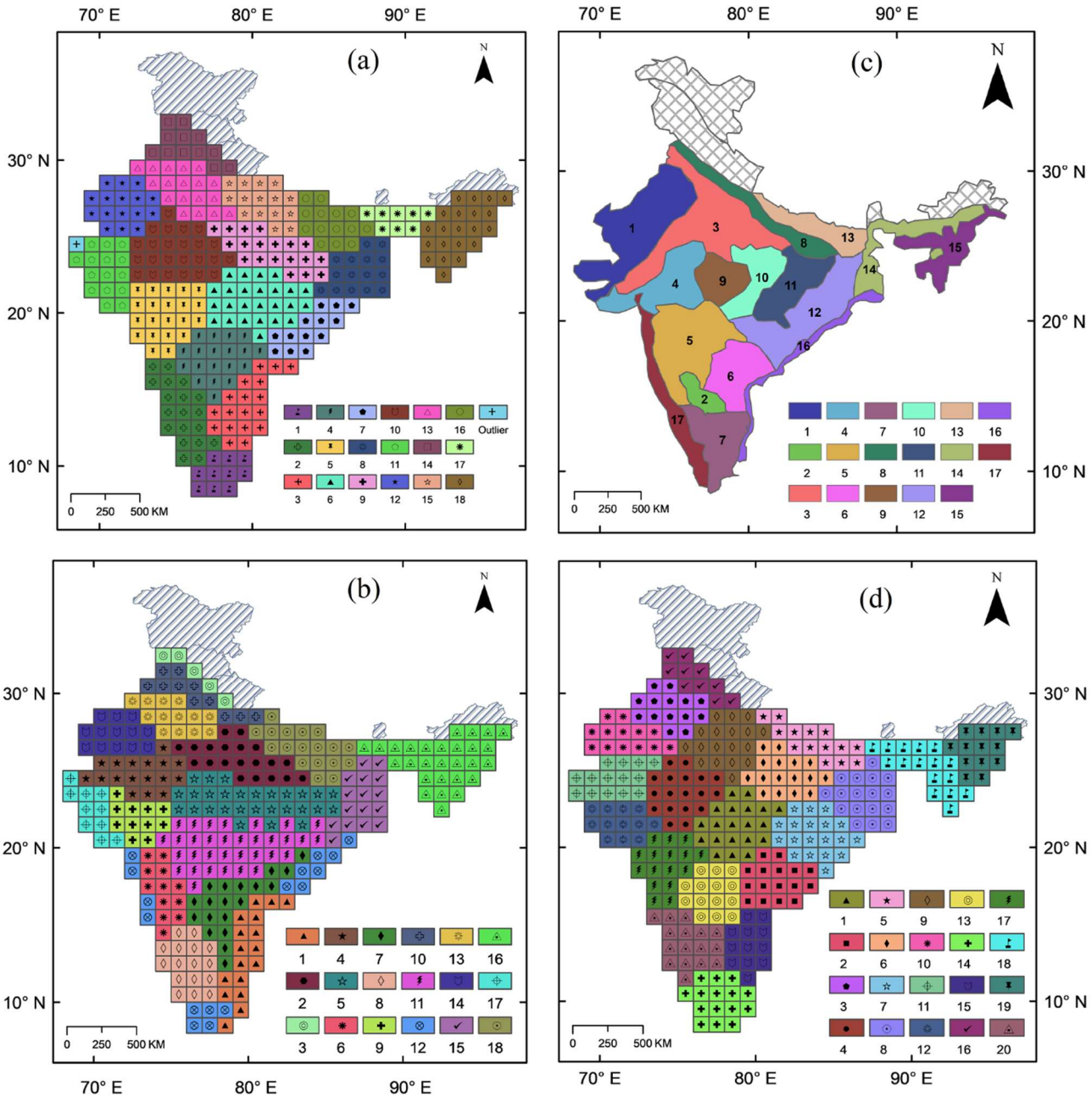

Figure 5.1: Homogeneous ET_0 regions formed using (a) fuzzy dynamic clustering and (b) GFCM method by considering predictors of ET_0 as attributes. (c) Agro-ecological regions of India (Sehgal et al. 1990) and (d) regions formed using fuzzy dynamic clustering method by considering the predictand ET_0 values as attributes.

Variation of ET_0 in each of the regions was examined by preparing box-plots corresponding to each month. The results presented in Figure 5.2 indicate that ET_0 and its variability are highest in May and low during December-January. The highest (low) variability could be primarily attributed to the high (low) magnitude and variability of temperature, net radiation, and wind speed (Figure 5.3).

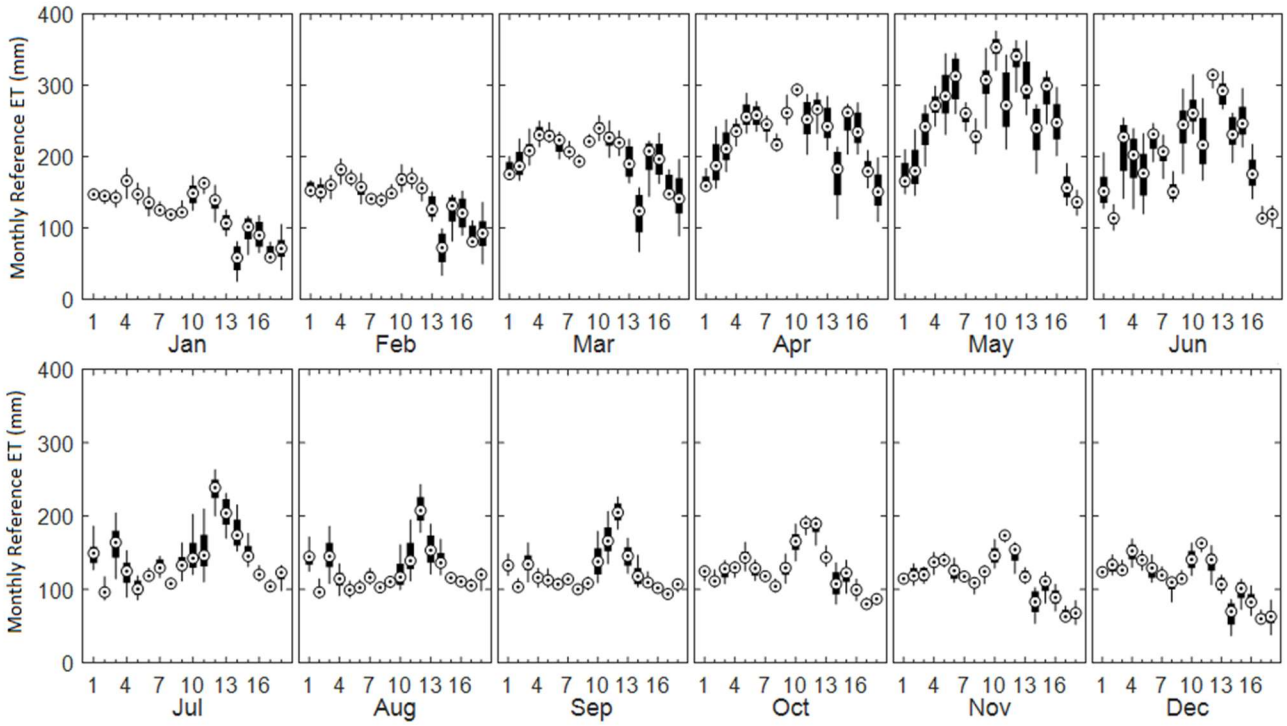

Figure 5.2: Variation of monthly ET_0 in the regions formed using fuzzy dynamic clustering methodology.

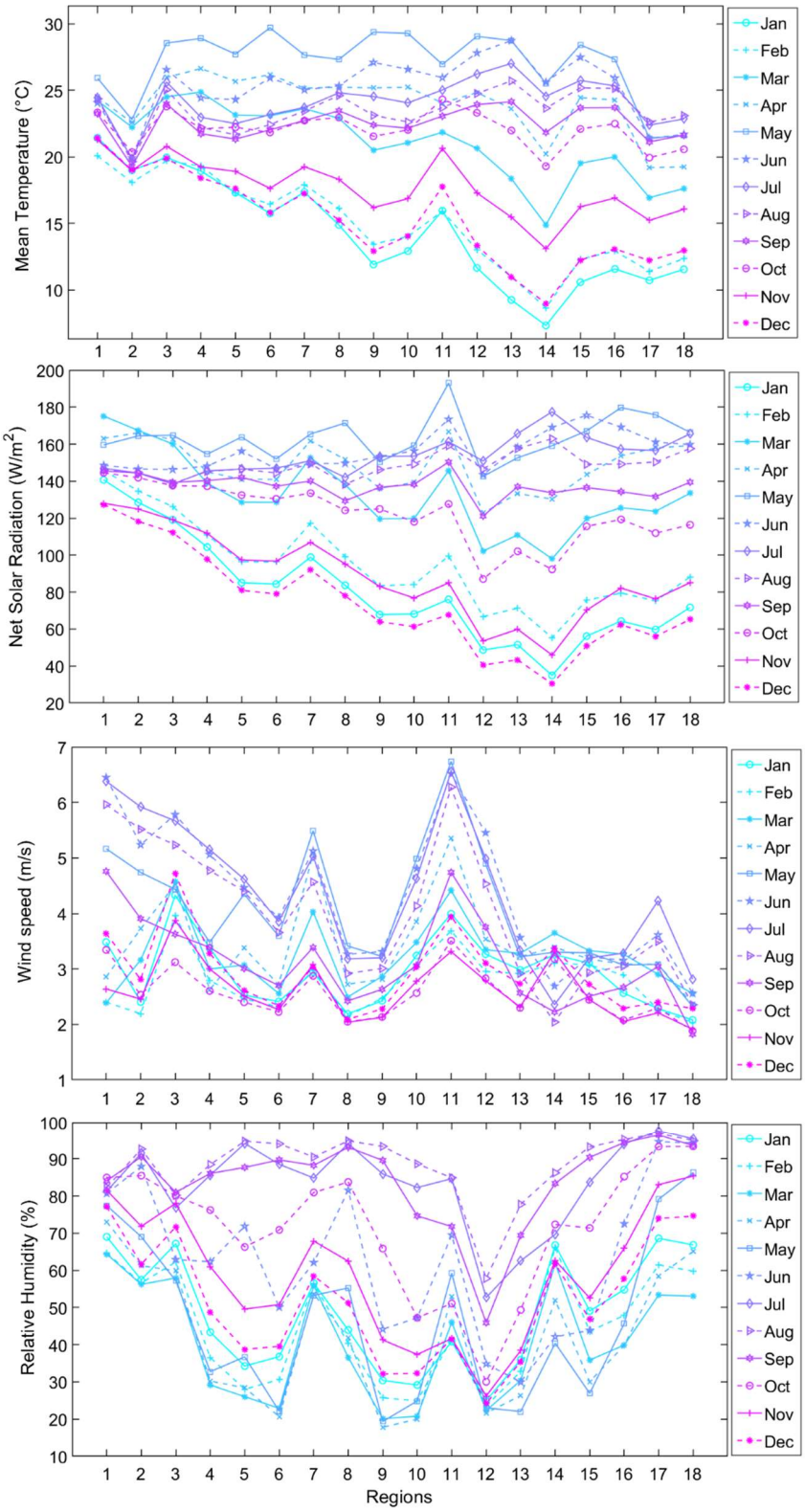

Figure 5.3: Monthly variation of climate variables in 18 homogeneous ET_0 regions formed using fuzzy.

5.3. Regionalization of ET_a

Satellite-derived monthly ET_a dataset was also considered for delineating homogeneous ET_a regions in the study area by using the proposed dynamic clustering method. Rescaled attribute vectors were prepared for each of the grids by considering attributes as monthly ET_a corresponding to 24-year period (1983-2006) and two location indicators (latitude and longitude). The possible number of clusters C was varied from 2 to 35 at the unit interval, and the value of the fuzzifier μ was varied from 1.1 to 1.5 with an increment of 0.1. The clusters resulting for different (C, μ) combinations were scrutinized to identify those for which at least 90% of intra-cluster inter-site correlations of monthly ET_a were positive and fairly large for each of the months. This resulted in the choice of regions corresponding to C=30 and μ=1.1 as the optimal partition (Figure 5.4).

The number of clusters/regions delineated for ET_a is higher than that delineated for ET_0. This was necessary as ET_a is influenced by multiple factors such as ET_0, type of vegetation and soil, and available water from natural (e.g., rainfall, groundwater) and irrigation source(s). Homogeneous ET_a regions have several important applications, which include information transfer across sites in sparsely gauged areas and filling of missing values in the time series of ET_a. The ET_a estimates are necessary at the regional scale for runoff estimation from catchments, predicting the suitability of a climate for dry-farmed crops, assessing the potential for increased growth achievable by irrigation, and for more precise studies of the effects of climate on natural vegetation (Arkley and Ulrich, 1962).

Examination of spatio-temporal variation of ET_a revealed that the windward side of western Ghats and north-east humid regions have the highest ET_a (where ET_0 is least) due to high precipitation throughout the year, whereas least ET_a is observed in regions surrounding the Thar desert in the western part of the country (where ET_0 is highest). Temporal variation of ET_a across months was minimum for the regions located along the east and west coasts and north-east regions where plenty of water is available throughout the year in the delta of rivers.

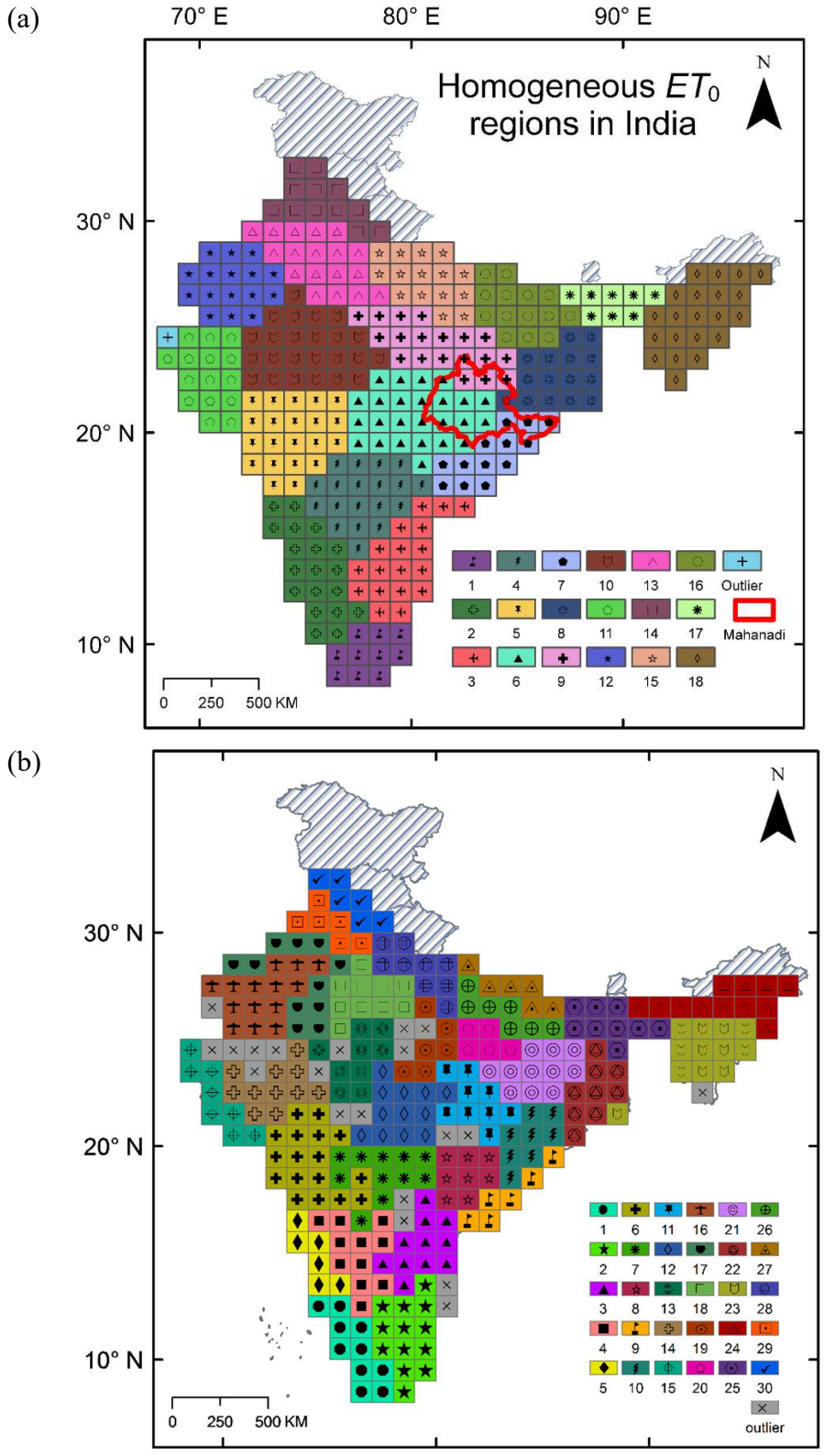

Figure 5.4: Homogeneous (a) ET_0 and (b) ET_a regions delineated in India using the dynamic fuzzy clustering method.

Spatial variability of ET_a was minimum across regions during the July-September months (Figure 5.5) due to the availability of ample quantity of water during these monsoon months when the country receives a major part of its annual rainfall. In the Western Ghats, southern region-1 has higher ET_a (112 cm/year) than its northern region-5 (90 cm/year) because of dense vegetation cover despite receiving less annual precipitation (220 cm) than region-5 (345 cm). Therefore, it can be said that other factors (including vegetation) besides precipitation influence ET_a values in a region. The spatial-temporal differences in ET_a and ET_0 regions reinforce the idea that characteristics of ET_0 could be determined with information on climate variables, whereas those of ET_a depend on several factors such as water availability (which is affected by precipitation, soil moisture storage, river and irrigation network, etc.), vegetation cover and ET_0. Mahanadi River basin lies within regions 6, 7, 8 and 9. The spatial-temporal differences in ET_a are large in regions 6, 7, and 8 compared to region 9, which is towards the northern part of the basin.

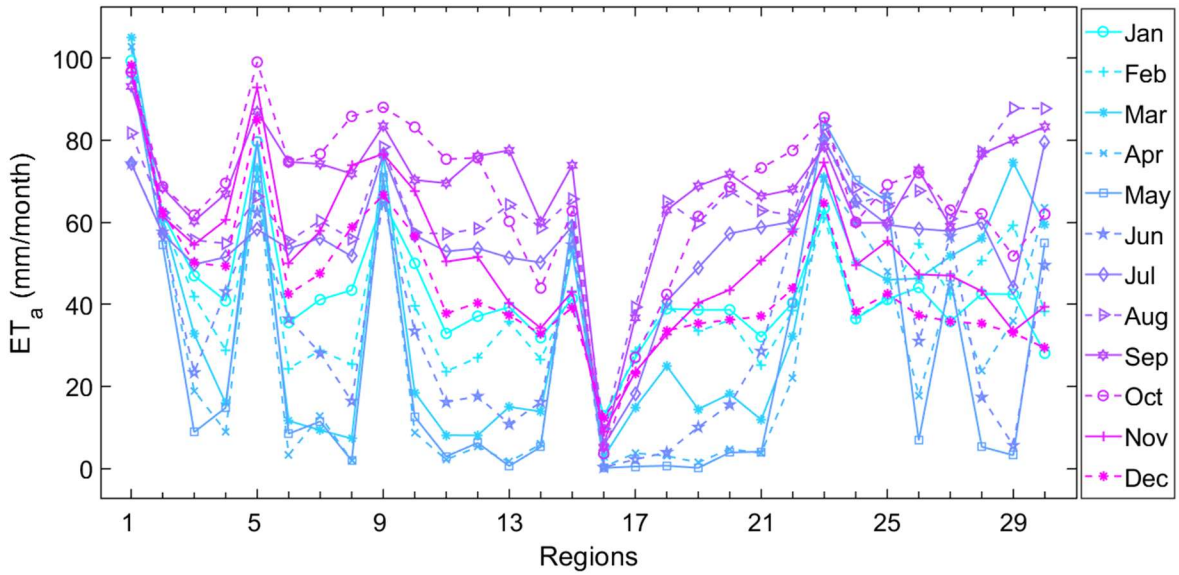

Figure 5.5: Monthly variation of actual evapotranspiration (ET_a) in 30 homogeneous ET_a regions of India formed using fuzzy dynamic clustering method.

5.4. Applications of the delineated ET_0 regions

As mentioned earlier, the Mahanadi River basin lies within regions 6, 7, 8 and 9 of the delineated eighteen homogeneous ET_0 regions (Figure 5.1a). This section presents details of various investigations carried out on those regions. Finer details of the same for entire India can be found in Swapan and Srinivas (2020b). For each of the regions, regional trend of ET_0 and its predictor climate

variables is determined (see Section 5.4.1). Further, the regional change point(s) of ET_0 and its predictor climate variables are identified, and time windows between the change points are analyzed to detect trends and key climate variable(s) which govern ET_0 changes (see Section 5.4.2). Furthermore, the effect of climate variables on ET_0 and long-term (annual) surface runoff changes in each of the delineated regions is quantified (see Section 5.4.3). The validity of Bouchet's complementary relationship (CR) is investigated (Section 5.4.4). In addition, for ET_0 estimation in data-sparse areas, new relevance vector regression (RVR) relationships are developed for the regions to arrive at FAO-PM estimate of ET_0 from subsets of its predictor climate variables, which could be typically expected in data-sparse areas (see Section 5.4.5). The developed relationships are found to be better in arriving at ET_0 estimates when compared to Multiple Linear Regression (MLR) relationships and three widely used empirical equations (Hargreaves, Mcguinnes-Bordne, Priestly-Taylor).

5.4.1. Regional trend of ET_0 and its predictor climate variables

The long-term regional trend of ET_0 was discerned at annual and seasonal time scales for each region over the entire time period/window of record and over time windows between the identified regional multivariate change points. For this purpose, the mean-daily time series of ET_0 and its predictor climate variables were determined at annual and seasonal (pre-monsoon, monsoon, post-monsoon, and winter) time scales over the period 1951–2013 for each of the grids in the study area. Subsequently, for each of the regions, the spatial average of the mean-daily time series (i.e., regional time series) was computed for ET_0 and each climate variable. Following this, the trend in the time series was examined using the nonparametric Mann-Kendall test (Kendall, 1955; Mann, 1945) by considering 5% and 10% significance levels. Table 5.1 provides the slope of the trend lines estimated using Sen's method (Sen, 1968).

Among the four regions (6, 7, 8, and 9) containing the Mahanadi basin, there is no consistency in trend across different time windows and for any chosen variable. At the annual scale (during the period 1951-2013), ET_0 was found to have a significantly decreasing annual trend for region 8, whereas the trend in the other three regions was not significant. An increasing trend in mean daily T_{max} over regions 6 and 7, decreasing trend in relative humidity for region 7, and an increasing trend in the same for region 8 were significant (Table 5.1). The trend in mean daily T_{min} was insignificant over all the

regions.

Table 5.1: Sen's slope of trend lines for ET_0 and climate variables at annual and seasonal scales for homogeneous ET_0 regions containing the Mahanadi basin.

Region	ET_0 (cm/ decade)	T_{max} (°C day^{-1}/ decade)	T_{min} (°C day^{-1}/ decade)	Relative humidity (%day^{-1}/ decade)	Wind speed (ms^{-1} day^{-1}/ decade)	*Rad* (watt day^{-1}/ decade)
6	**0.07**	**0.09***	**0.01**	**-0.14**	**-0.07***	**1.03***
	(-0.02)	(0.03)	(0.00)	(0.02)	(-0.04*)	(0.60*)
	[0.10]	[0.13*]	[-0.04]	[-0.25]	[-0.06*]	[2.22*]
	{-0.09}	{0.04}	{-0.01}	{0.09}	{-0.14*}	{0.87*}
	0.25	0.12*	0.07	-0.24	-0.01	0.89*
7	**0.61**	**0.12***	**-0.01**	**-0.43***	**-0.13***	**1.39***
	(0.07)	(0.12*)	(0.02)	(-0.51**)	(-0.09*)	(0.70*)
	[-0.17]	[0.12*]	[-0.05]	[-0.34]	[-0.18*]	[2.13*]
	{0.28}	{0.09*}	{-0.04}	{-0.08}	{-0.18*}	{1.63*}
	0.51*	0.14*	0.02	-0.66*	-0.01	0.54*
8	**-1.45***	**-0.01**	**0.02**	**0.44***	**-0.10***	**0.86***
	(-0.16)	(-0.08)	(-0.03)	(0.37)	(-0.05*)	(1.13*)
	[-1.31*]	[-0.08]	[-0.01]	[1.08*]	[-0.16*]	[2.18*]
	{-0.06}	{0.04}	{0.00}	{0.09}	{-0.13*}	{-0.05}
	0.03	0.03	0.05	0.23	-0.01	0.38*
9	**-0.82**	**0.04**	**0.01**	**0.20**	**-0.04***	**0.76***
	(-0.14)	(-0.07)	(-0.01)	(-0.03)	(-0.04*)	(0.69*)
	[0.01]	[0.06]	[0.00]	[0.34]	[-0.03*]	[1.96*]
	{-0.35}	{0.04}	{-0.05}	{0.31}	{-0.07*}	{0.30}
	0.07	0.06	0.09*	0.02	-0.01	0.38*

* trend is significant at 5 % significance level; ** trend is significant at 10 % significance level

Values shown in the bold front refer to the annual scale, and those shown without parenthesis refer to the post-monsoon season. Values shown in (),[],{} correspond to winter, pre-monsoon, and monsoon seasons, respectively. T_{max}: maximum temperature; T_{min}: minimum temperature; *Rad*: Net solar radiation.

In general, regions 6, 7 and 9 did not show any significant changes in ET_0 at both annual and seasonal scales, except for post-monsoon season in the case of region 7. Furthermore, all the four regions (6, 7, 8 and 9) were consistent in indicating a significant decreasing trend in wind speed and an increasing trend in net solar radiation at both annual and seasonal scales, and among the seasons decrease in wind speed was found to be the highest mostly during monsoon. The decrease in wind speed could be attributed to an increase in surface roughness owing to anthropogenic factors, which is widely referred to as the global stilling effect (e.g., Roderick et al., 2007). However, a recent study (Zeng et al., 2019) illustrated that decadal-scale variations of near-surface wind are probably determined by internal

decadal ocean–atmosphere oscillations, rather than by vegetation growth and/or urbanization as hypothesized earlier. A significantly increasing trend in mean daily T_{max} was evident for two seasons (post-monsoon and pre-monsoon) in region 6 and all the seasons in region 7. Discussion on similar results for the rest of the country (India) can be found in Swapan and Srinivas (2020 a,b).

5.4.2. Regional change point(s) of ET_0 and its predictor climate variables

Multivariate change points in regional time series of annual ET_0 and climate variables were identified using the nonparametric method advocated by Matteson and James (2014). The results presented in Figure 5.6 indicate that recent change points were noted over the period 1992-1997 for regions 6, 7 and 9, whereas previous change points were in 1964 for regions 6 and 7 (covering a major part of the basin), and 1979 for regions 8 and 9 (in the north-east part of the basin). There was a significant decrease in ET_0 during 1951-1964 in regions 6, 7, and 9. This is due to a significant increase in relative humidity during the period (Figure 5.6). Further, the predictor climate variables which have the most influence on ET_0 (i) in the time period between successive change points and (ii) for the overall period or entire duration of record are identified for each region.

5.4.3. Sensitivity of ET_0 and surface runoff to climate variables

The sensitivity of ET_0 to changes in climate variables indicated that at the annual scale, ET_0 is most sensitive to relative humidity (RH) followed by net solar radiation (*Rad*) and maximum temperature (T_{max}) for Mahanadi basin and the three homogeneous ET_0 regions encompassing the basin (Figure 5.7a, b). Annual surface runoff from different homogeneous ET_0 regions and the entire Mahanadi basin was estimated using the procedure described in Appendix A5.3. Further, the sensitivity of surface runoff to ET_0 (PET) and its predictor climate variables, annual precipitation, and Fu's Budyko parameter ω was determined using the Budyko framework (Appendix 5.3). The surface runoff is found to be most sensitive to ω, precipitation, and PET over the basin and the three regions. The parameter ω depicts land-use/land-cover and geomorphological characteristics of a region. Analysis of sensitivity coefficient estimates (SCEs) of runoff obtained with respect to climate variables affecting ET_0 (Figure 5.7c) indicated that the runoff is most sensitive to *RH* and relatively less sensitive to net solar radiation, T_{max}, wind speed, and T_{min} (in that order). For the Mahanadi basin, the estimates for dT_{max}/T_{max}, dT_{min}/T_{min}, dW/W, $d(\mathrm{RH})/\mathrm{RH}$, $d(\mathrm{Rad})/\mathrm{Rad}$ were found to be 2.09 %, -1.21%, -16.83%, -3.45%, and 7.18% respectively, during the period 1951-2013. Combining the information on regional trends

and sensitivity coefficients, it is found that during the study period, wind speed mostly influenced the ET_0 changes over regions 6 to 9, encompassing the Mahanadi basin (Table 5.2).

Estimates/records of ET_0, ET_a and precipitation were available over the periods 1901-2016, 1983-2006, and 1901-2013. The 24-year-long annual records of those variables corresponding to the contemporaneous period (1983-2006) were discretized into 4 non-overlapping segments, each 6-years long, and they were used to arrive at estimate of the parameter ω, as described in Appendix A5.3. Budyko curve constructed to estimate ω is shown in Figure 5.7b(iii). Subsequently, the estimated ω was utilized to determine annual surface runoff from the basin using Equation (A5.21) for the period 1901-2013 (Figure 5.7b(iv)). The estimated annual runoff series is found to have statistically significant decreasing trend at 99% confidence level.

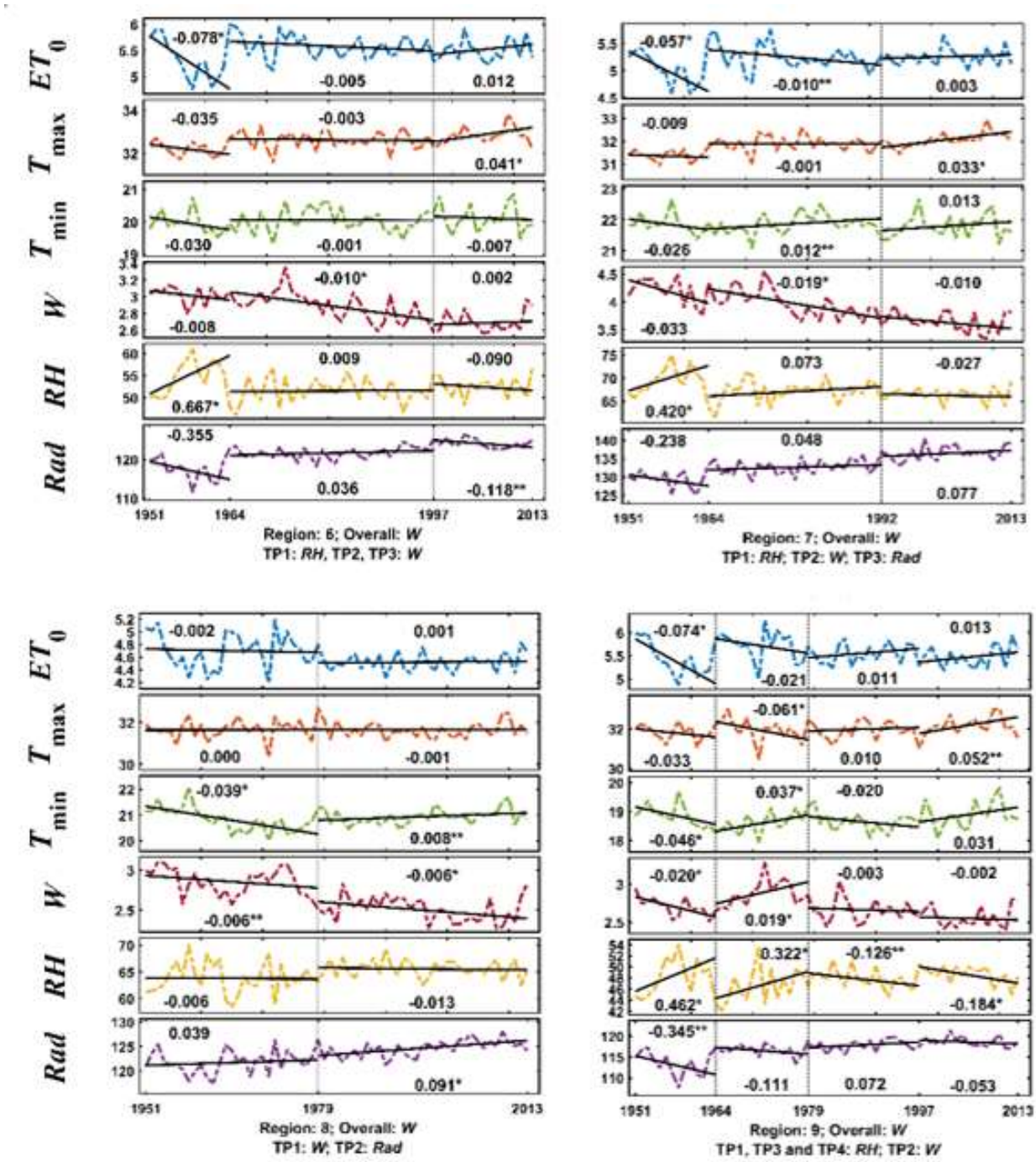

Figure 5.6: Multivariate change points of ET_0 and its predictor climate variables (T_{max}, T_{min}, wind speed (W), relative humidity (RH), and solar radiation (Rad)) are shown along with slopes of trend lines fitted between the change points for each of the regions containing Mahanadi basin. The predictor climate variable which has the most influence on ET_0 (i) in the time period (TP) between successive change points and (ii) for the overall period or entire duration of record are listed for each region. The time periods (TPs) are numbered in the order of their occurrence.

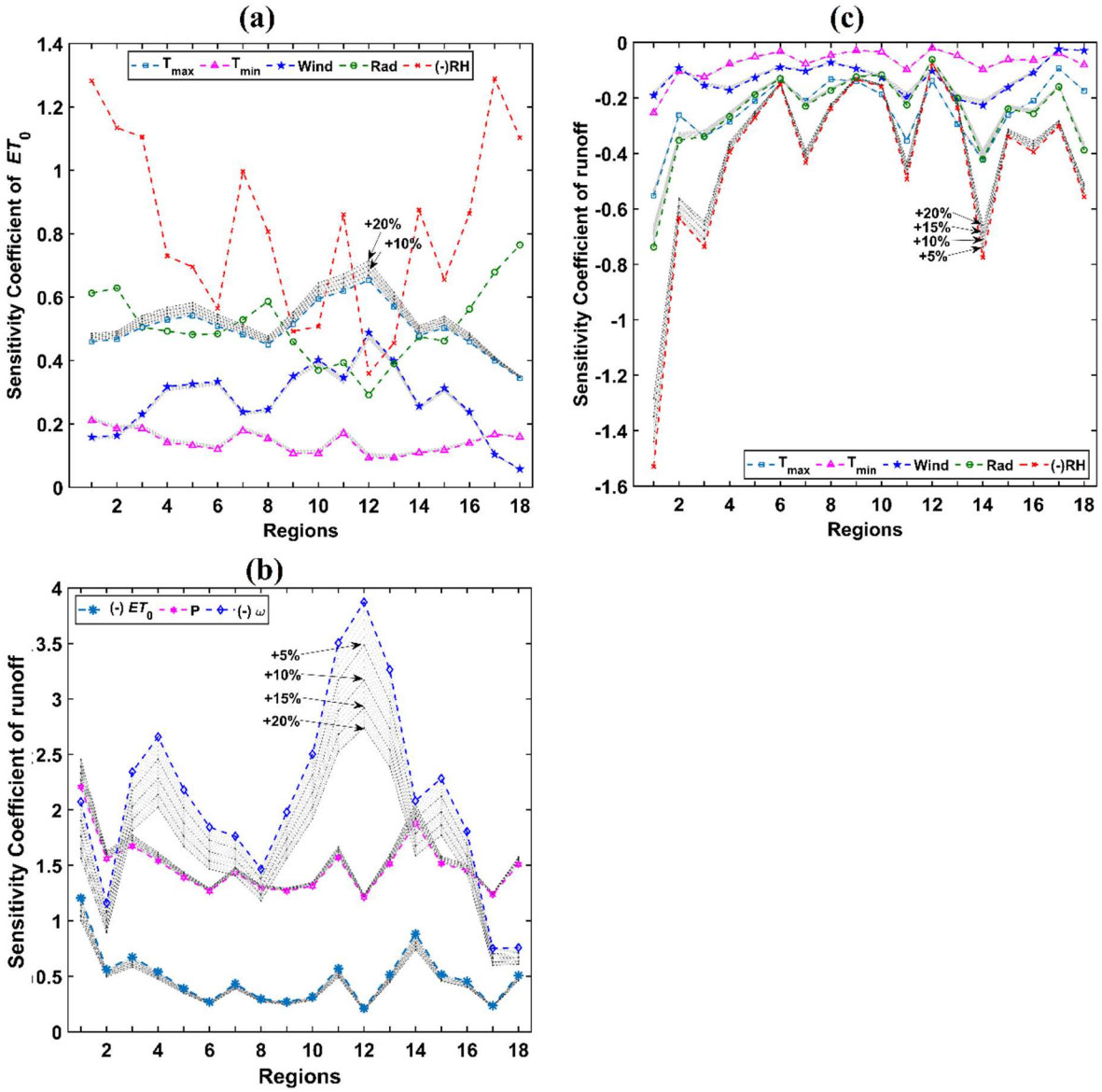

Figure 5.7a: Sensitivity coefficient of (a) annual ET_0 and (c) annual runoff with respect to climate variables (in FAO-PM ET_0 equation), and sensitivity coefficient of (b) annual runoff to changes in annual ET_0, annual precipitation and Fu's Budyko parameter ω for the homogeneous ET_0 regions. Lines with symbols show estimates of the sensitivity coefficient obtained by considering only the first-order approximation of the Taylor series expansion of ET_0, as done conventionally. Grey dotted lines denote estimates of the sensitivity coefficient obtained for 1 % to 20 % increase in the magnitude of climate variables when third-order approximation is considered. Dark grey denotes sensitivity coefficient estimates corresponding to 5%, 10%, 15%, and 20% increases in the climate variables. In the legend, (-) shown as a prefix for a variable indicates that the negative of the estimate obtained for the sensitivity coefficient is considered for plotting.

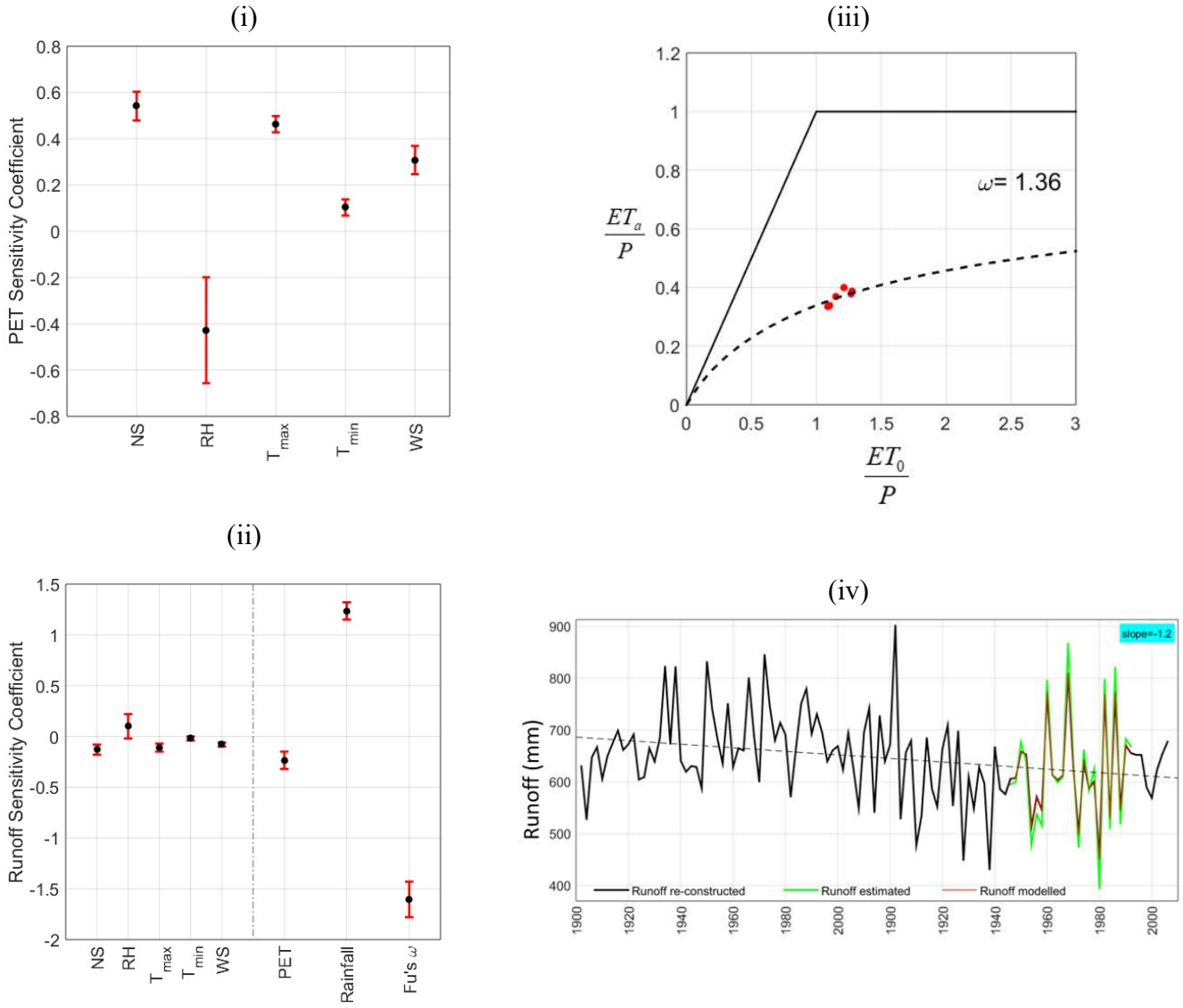

Figure 5.7b: Boxplots showing variation of annual sensitivity coefficients of (i) annual ET_0 (or PET) to its predictor climate variables in FAO-PM equation [Net solar radiation (NS), Relative Humidity (RH), T_{max}, T_{min}, wind speed (WS)], and (ii) annual surface runoff to its predictors (ET_0 and its predictor climate variables, annual precipitation, and Fu's Budyko parameter ω) for the Mahanadi basin over the period 1951-2013, (iii) Budyko curve constructed to estimate ω, and (iv) annual surface runoff in the basin re-constructed for the period 1901-2013 using the estimate of ω as $R = \left(P^{\omega} + ET_0^{\omega}\right)^{\frac{1}{\omega}} - ET_0$ is compared with runoff estimated as $R = P - ET_a$ for the period 1983-2006, and runoff modelled through Budyko model as $R = \left(P^{\omega} + ET_0^{\omega}\right)^{\frac{1}{\omega}} - ET_0$ for the period 1983-2006.

Table 5.2: Change in ET_0 over the period 1951-2013 for homogeneous ET_0 regions formed using multivariate time-varying fuzzy clustering (MTFC) method, and contribution to this change by its predictor climate variables (Maximum temperature (T_{max}), Minimum temperature (T_{min}), Wind speed, Relative humidity (RH), and Solar radiation). For each region, values of three predictor climate variables that have maximum influence on ET_0 are highlighted in bold font.

Region number	Mean annual ET_0 (mm)	Change in ET_0 (%)	Contribution to change in ET_0 by its predictor climate variables (%)					MAR from region (mm)	Change in MAR due to change in ET_0 (%)
			T_{max}	T_{min}	Wind speed	RH	Solar radiation		
6	2010	1.7	0.3* (0.2, 0.3)†	0.0* (0, 0)†	**-1.2*** (-1.1, -1.4)†	**0.4*** (0.4, 0.5)†	**0.8*** (0.7, 0.8)†	772	-0.5* (-0.5, -0.4)†
7	1898	2.9	0.5* (0.5, 0.6)†	0.0* (0, 0)†	**-1.8*** (-1.5, -2.2)†	**-1.8*** (-1.6, -2.1)†	**1.6*** (1.4, 1.7)†	708	-1.2* (-1.3, -1.1)†
8	1680	-5.4	0.0* (0, 0)†	0.0* (0, 0)†	**-1.3*** (-1.2, -1.7)†	**-0.9*** (-0.8, -1)†	**0.8*** (0.7, 0.8)†	982	1.6* (1.7, 1.4)†
9	2024	-1.3	0.1* (0.1, 0.2)†	0.0* (0, 0)†	**-0.9*** (-0.8, -1)†	**0.3*** (0.3, 0.4)†	**0.6*** (0.6, 0.7)†	678	0.3* (0.4, 0.3)†

*Median; †5 and 95 percentile confidence interval; MAR: Mean annual runoff

5.4.4. Bouchet's hypothesis

Bouchet's (Bouchet, 1963) complementary relationship (CR) hypothesizes that at a regional scale, there exists a feedback mechanism between ET_0 and ET_a for homogeneous surfaces having low advection of heat and moisture. It postulates that an increase in regional ET_a consumes energy, thereby resulting in a reduction of regional ET_0 through cooling and humidifying of the overpassing air. Similarly, when regional ET_a decreases (due to dry surface conditions), the available energy which is not used for ET_a increases regional ET_0 through the warming and drying of the atmosphere (Brutsaert and Parlange, 1998). Bouchet's hypothesis is useful for understanding regional-scale feedback between land and near-surface atmospheric boundary layer at various temporal scales. The CR between ET_0 and ET_a serves as the fundamental backbone of different relationships developed in the literature for estimating daily ET_a using the information of ET_0 only. The CRs were validated at the regional as well as river basin scale for the Mahanadi basin by considering several data products. It was found that the CR hypothesis is strictly valid (i.e., ET_0 decreases and ET_a increases along with an increase in precipitation) for regions 8 and 9 (Figure 5.8). In the study at the river basin scale, three out of four (except GLEAM v3b) ET_a data products considered confirmed the validity of the CR

relationship. All these findings are useful for assessing stress on freshwater availability for water resources planning and management policies for various applications.

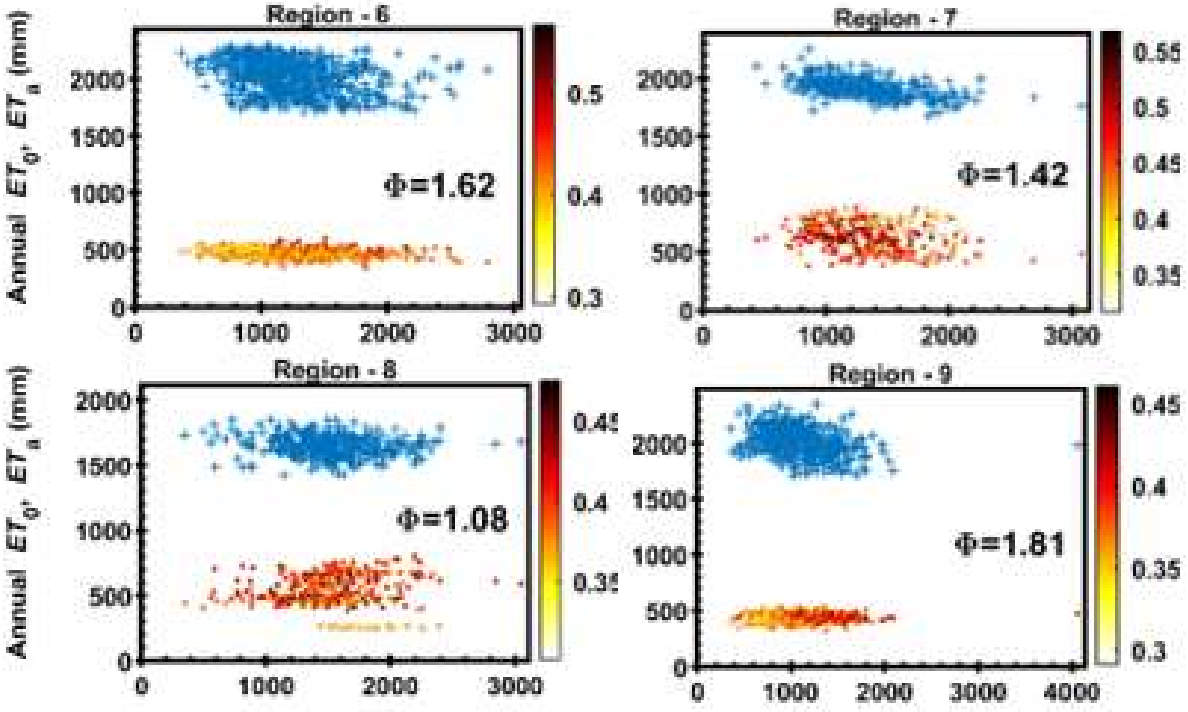

Figure 5.8: Bouchet's complementary relationship between ET_0, ET_a , and precipitation for homogeneous ET_0 regions in the Mahanadi basin. Points that depict the relationship between annual precipitation and annual ET_0 are shown as + symbols. Further, points that depict the relationship between annual precipitation and ET_a are shown as circles, whose colour corresponds to the Normalized Difference Vegetation Index (NDVI) magnitude (whose range is shown in the adjoining colour bar). $\Phi\left(=ET_0/P\right)$ denotes aridity or dryness index for a region.

5.5. ET_0 estimation from fewer meteorological variables

For each of the homogeneous ET_0 regions, the regional relationship was developed between daily FAO-PM ET_0 estimates and subsets of its predictor climate variables by using relevance vector regression (RVR) and multiple linear regression (MLR) methods. The subsets considered include (i) T_{max} and T_{min}; (ii) $T_{max,}$ $T_{min,}$ and extraterritorial radiation (R_e); and (iii) $T_{max,}$ $T_{min,}$ and net radiation (*Rad*). They comprise climate variables that are typically expected in data-sparse areas. The performance of the developed RVR relationships in yielding FAO-PM ET_0 estimate is assessed by comparing error in the estimates with that resulting from the use of MLR relationships and the three mostly used empirical methods, namely, Hargreaves (using $T_{max,}$ $T_{min,}$ and R_e; Hargreaves and Samani,

1985), McGuinness-Bordne (using $T_{max,}$ $T_{min,}$ and R_e; McGuinness and Bordne, 1972; Oudin *et al.* 2005) and Priestly-Taylor (using $T_{max,}$ $T_{min,}$ and *Rad*; Priestley and Taylor, 1972). Brief details of those empirical equations are provided in Appendix 5.2.

Error in ET_0 estimates is quantified in terms of six performance measures: MAE (Mean Absolute Error), R (Correlation coefficient), NSE (Nash–Sutcliffe Efficiency), RMSE (Root Mean Square Error), R-RMSE (Relative Root Mean Square Error), and AR-bias (Absolute Relative bias). The results obtained for regions encompassing the Mahanadi basin are presented in Table 5.4. In general, the results indicate that error in ET_0 estimates is least for RVR relationships and relatively higher for MLR relationships and the three empirical methods. The better performance of RVR relationships can be attributed to the theoretical advantages of RVR over MLR. The inferior performance of the empirical methods is expected, as they are not designed/developed to provide FAO-PM ET_0 estimates. Investigations were carried out to examine if the estimates obtained based on the empirical methods can be calibrated to provide FAO-PM ET_0 estimates (as shown below), following Allen *et al.* (1998).

$$ET_0^{FAO\text{-}PM} = f\left(ET_0^{method}\right) = a + b \times ET_0^{method} \tag{5.1}$$

where $ET_0^{FAO\text{-}PM}$ is FAO-PM ET_0 estimate, ET_0^{method} is ET_0 estimate obtained using an empirical method, a and b are parameters which can be estimated using regression analysis. Error in ET_0 estimates obtained using the calibrated models was generally less compared to the original/uncalibrated models, but they were still higher than those obtained with RVR and MLR models.

In the case of both RVR and MLR models, those considering $T_{max,}$ $T_{min,}$ and net solar radiation as predictors performed better (Table 5.4). The results for the rest of India can be found in Swapan and Srinivas (2020b). There is scope to improve the performance of RVR-based models over all the regions by including wind speed and *RH* as predictor variables (if available) in developing the relationships to estimate ET_0.

Table 5.3: Change in ET_0 over the period 1951-2013 for homogeneous ET_0 regions and contribution to this change by its predictor climate variables (Maximum temperature (T_{max}), Minimum temperature (T_{min}), Wind speed, Relative humidity (RH), and Solar radiation). For each region, values of three predictor climate variables that have maximum influence on ET_0 are highlighted in bold font.

Region	Mean annual ET_0 (mm)	Change in ET_0 (%)	Contribution to change in ET_0 by its predictor climate variables (%)					MAR from region (mm)	Change in MAR due to change in ET_0 (%)
			T_{max}	T_{min}	Wind speed	RH	Solar radiation		
1	1765	16.2	**2.3*** (2, 2.7)†	0.3* (0.3, 0.3)†	-1.5* (-1, -1.9)†	**7.5*** (6.6, 8.4)†	**7.2*** (6.5, 8.1)†	238	-16.8* (-19.0, -14.9)†
2	1642	12.6	1.0* (0.9, 1.2)†	0.0* (0, 0)†	**-1.5*** (-1, -1.8)†	**3*** (2.5, 3.4)†	**2.6*** (2.2, 3)	1288	-6.5* (-7.6, -5.7)†
3	2000	6.4	1.1* (0.8, 1)†	0.2* (0.2, 0.2)†	**-2.3*** (-1.9, -2.6)†	**3.2*** (2.9, 3.7)†	**2.7*** (2.5, 2.8))†	315	-4.1* (-4.3, -3.9)†
4	2053	1.9	0.9* (0.2, 0.3)†	0.0* (0, 0)†	**-2.8*** (-2.5, -3.1)†	**1.7*** (1.5, 2)†	**1.6*** (1.5, 1.7) †	269	-1.0* (-1.1, -1.0)†
5	2008	-0.8	**0.3*** (0.2, 0.3)†	0.0* (0, 0)†	**-1.6*** (-1.4, -1.8)†	0.1* (0.1, 0.1)†	**1*** (1, 1.1)†	831	0.3* (0.3, 0.3)†
6	2010	1.7	0.3* (0.2, 0.3)†	0.0* (0, 0)†	-1.2* (-1.1, -1.4)†	0.4* (0.4, 0.5)†	0.8* (0.7, 0.8)†	772	-0.5* (-0.5, -0.4)†
7	1898	2.9	0.5* (0.5, 0.6)†	0.0* (0, 0)†	**-1.8*** (-1.5, -2.2)†	**-1.8*** (-1.6, -2.1)†	**1.6*** (1.4, 1.7)†	708	-1.2* (-1.3, -1.1)†
8	1680	-5.4	0.0* (0, 0)†	0.0* (0, 0)†	**-1.3*** (-1.2, -1.7)†	**-0.9*** (-0.8, -1)†	**0.8*** (0.7, 0.8)†	982	1.6* (1.7, 1.4)†
9	2024	-1.3	0.1* (0.1, 0.2)†	0.0* (0, 0)†	**-0.9*** (-0.8, -1)†	**0.3*** (0.3, 0.4)†	**0.6*** (0.6, 0.7)†	678	0.3* (0.4, 0.3)†
10	2327	-4.5	0.3* (0.2, 0.3)†	0.1* (0.1, 0.1)†	**-1.4*** (-1.3, -1.6)†	**0.6*** (0.5, 0.7)†	**0.5*** (0.4, 0.5)†	440	1.4* (1.4, 1.3)†
11	2302	-1.1	**0.7*** (0.7, 0.8)†	0.3* (0.3, 0.3)†	**-1.3*** (-1.1, -1.4)†	0.4* (0.4, 0.4)†	**0.8*** (0.7, 0.8)†	121	0.6* (0.6, 0.6)†
12	2539	-5.8	**0.4*** (0.4, 0.4)†	0.0* (0, 0.1)†	**-1.5*** (-1.4, -1.6)†	0.1* (0.1, 0.1)†	**0.2*** (0.2, 0.2)†	137	1.2* (1.2, 1.1)†
13	2153	-7.5	0.2* (0.2, 0.2)†	**0.3*** (0.3, 0.3)†	**-2.9*** (-2.7, -3.1)†	**0.9*** (0.8, 1)†	**0.3*** (0.3, 0.4)†	90	3.7* (3.8, 3.5)†
14	1581	-5.1	0.0* (0, 0)†	0.3* (0.2, 0.3)†	**-1.9*** (-1.5, -2.2)†	**0.6*** (0.5, 0.7)†	**-2*** (-1.7, -2.3)†	305	4.3* (4.6, 3.9)†
15	1913	-6.5	**-0.1*** (-0.1, -0.1)†	0.0* (0, 0)†	**-1.5*** (-1.3, -1.7)†	**1.5*** (1.3, 1.7)†	0* (0, 0.1)†	354	3.2* (3.4, 3.0)†
16	1681	-12.5	0.0* (0, 0)†	-0.1 (-0.1, -0.1)†	**-1.3*** (-1.1, -1.6)†	**3.9*** (3.3, 4.3)†	**-0.6*** (-0.6, -0.7)†	675	5.3* (5.7, 4.8)†
17	1281	-20.8	0.1* (0.1, 0.2)†	0.0* (0, 0)†	**-0.4*** (-0.2, -0.7)†	**2.2*** (1.8, 2.6)†	**-2.3*** (-2.1, -2.7)†	2090	4.6* (5.2, 3.9)†
18	1274	-8.9	**0.4*** (0.4, 0.5)†	0.1 (0.1, 0.2)†	-0.3* (-0.1, -0.6)†	**3*** (2.3, 3.5)†	**-1.8*** (-1.4, -2.1)†	1329	4.3* (5.1, 3.5)†

*Median; †5 and 95 percentile confidence interval; MAR: Mean annual runoff

Table 5.4: Comparison of performances of different ET_0 estimation models

Region	Equation	MAE (mm/day)	R	NSE	RMSE (mm/day)	R-RMSE (%)	AR-bias (%)
6	Hargreaves (T_{max}, T_{min}, R_e)	1.20	0.87	0.58	1.63	24.97	20.77
	(Hargreaves calibrated)	(1.00)	(0.87)	(0.75)	(1.25)	(26.17)	(20.39)
	Priestly-Taylor (T_{max}, T_{min}, Rad)	2.06	0.50	-0.06	2.58	38.16	35.21
	(Priestly-Taylor calibrated)	(1.78)	(0.50)	(0.25)	(2.17)	(46.88)	(36.98)
	McGuinnes Bordne (T_{max}, T_{min}, R_e)	1.70	0.67	0.22	2.22	36.85	30.63
	(McGuinnes Bordne calibrated)	(1.59)	(0.67)	(0.45)	(1.86)	(44.32)	(34.91)
	MLR -1	0.91	0.88	0.78	1.18	23.75	18.17
	{MLR -2}	{0.89}	{0.89}	{0.79}	{1.16}	{22.68}	{17.33}
	[MLR -3]	(0.90)	(0.89)	(0.78)	(1.16)	(22.66)	(17.70)
	RVR -1	0.75	0.91	0.83	1.03	19.59	14.20
	{RVR -2}	{0.71}	{0.92}	{0.84}	{0.98}	{18.66}	{13.37}
	[RVR -3]	**(0.67)**	**(0.93)**	**(0.86)**	**(0.95)**	**(16.81)**	**(12.16)**
7	Hargreaves (T_{max}, T_{min}, R_e)	1.08	0.84	0.43	1.52	21.76	18.17
	(Hargreaves calibrated)	(0.85)	(0.84)	(0.71)	(1.08)	(22.70)	(17.57)
	Priestly-Taylor (T_{max}, T_{min}, Rad)	1.32	0.66	0.32	1.66	27.10	24.36
	(Priestly-Taylor calibrated)	(1.23)	(0.66)	(0.44)	(1.51)	(31.15)	(25.57)
	McGuinnes Bordne (T_{max}, T_{min}, R_e)	1.38	0.64	0.27	1.73	34.71	27.83
	(McGuinnes Bordne calibrated)	(1.33)	(0.64)	(0.41)	(1.55)	(35.76)	(28.95)
	MLR -1	0.87	0.84	0.70	1.10	23.02	17.92
	{MLR -2}	{0.85}	{0.85}	{0.71}	{1.08}	{22.33}	{17.42}
	[MLR -3]	(0.82)	(0.86)	(0.73)	(1.05)	(20.96)	(16.64)
	RVR -1	0.69	0.88	0.78	0.95	18.52	13.86
	{RVR -2}	{0.64}	{0.90}	{0.81}	{0.87}	{17.32}	{12.78}
	[RVR -3]	**(0.59)**	**(0.91)**	**(0.83)**	**(0.84)**	**(14.98)**	**(11.16)**
8	Hargreaves (T_{max}, T_{min}, R_e)	0.88	0.81	0.61	1.13	24.08	19.61
	(Hargreaves calibrated)	(0.86)	(0.81)	(0.65)	(1.07)	(25.33)	(20.15)
	Priestly-Taylor (T_{max}, T_{min}, Rad)	1.28	0.60	0.29	1.53	31.25	28.15
	(Priestly-Taylor calibrated)	(1.20)	(0.60)	(0.36)	(1.45)	(33.11)	(27.70)
	McGuinnes Bordne (T_{max}, T_{min}, R_e)	1.33	0.46	0.20	1.62	37.64	30.71
	(McGuinnes Bordne calibrated)	(1.35)	(0.46)	(0.22)	(1.60)	(38.71)	(31.59)
	MLR -1	0.77	0.84	0.70	0.99	23.31	17.85
	{MLR -2}	{0.73}	{0.86}	{0.72}	{0.95}	{22.04}	{16.76}
	[MLR -3]	(0.68)	(0.88)	(0.76)	(0.89)	(20.09)	(15.37)
	RVR -1	0.64	0.88	0.76	0.88	19.37	14.31
	{RVR -2}	{0.58}	{0.90}	{0.81}	{0.79}	{17.38}	{12.83}
	[RVR -3]	**(0.52)**	**(0.91)**	**(0.82)**	**(0.75)**	**(14.98)**	**(10.89)**

MLR: Multiple Linear Regression; RVR: Relevance Vector Regression; RMSE: Root Mean Square Error; MAE: Mean Absolute Error; R: Correlation coefficient; NSE: Nash–Sutcliffe model efficiency coefficient; AR-bias: Absolute Relative bias; R-RMSE: Relative Root Mean Square Error. RVR-1 and MLR-1 estimate ET_0 as a function of T_{max} and T_{min}, RVR-2 and MLR -2 estimate ET_0 as a function of T_{max}, T_{min}, R_e; RVR-3 and MLR -3 estimate ET_0 as a function of T_{max}, T_{min}, Rad. The least value for RMSE, MAE, AR-bias, and R-RMSE, and the maximum value for R and NSE indicates the best performance. The optimal values are highlighted in bold font.

Table 5.4 (continued…)

Region	Equation	MAE (mm/day)	R	NSE	RMSE (mm/day)	R-RMSE (%)	AR-bias (%)
9	Hargreaves (T_{max}, T_{min}, R_e)	1.25	0.83	0.54	1.75	25.05	20.94
	(Hargreaves calibrated)	(1.14)	(0.83)	(0.69)	(1.45)	(28.34)	(22.71)
	Priestly-Taylor (T_{max}, T_{min}, Rad)	2.21	0.50	-0.14	2.76	40.91	37.68
	(Priestly-Taylor calibrated)	(1.79)	(0.50)	(0.25)	(2.24)	(45.72)	(35.86)
	McGuinnes Bordne (T_{max}, T_{min}, R_e)	1.88	0.58	0.00	2.59	34.78	29.96
	(McGuinnes Bordne calibrated)	(1.73)	(0.58)	(0.33)	(2.12)	(46.40)	(35.87)
	MLR -1	1.09	0.84	0.70	1.42	27.37	21.25
	{MLR -2}	{1.00}	{0.86}	{0.73}	{1.35}	{24.91}	{19.24}
	[MLR -3]	(1.06)	(0.85)	(0.71)	(1.39)	(26.25)	(20.46)
	RVR -1	0.91	0.88	0.76	1.26	22.42	16.93
	{RVR -2}	{0.82}	**{0.90}**	**{0.80}**	**{1.15}**	{19.79}	{14.79}
	[RVR -3]	**(0.81)**	**(0.90)**	**(0.80)**	(1.16)	**(19.19)**	**(14.25)**

5.6. Future Regional Projections of Potential Evapotranspiration and Fresh Water Availability in Mahanadi basin using CMIP6 GCMs

5.6.1. Projected future regional trend of ET_0 and influencing climate variables

First future projections of ET_0 were determined for the Mahanadi basin and each of the homogeneous ET_0 regions 6, 7, 8 and 9 encompassing the basin. For this purpose, daily projections of climate variables (precipitation, maximum and minimum temperatures, relative humidity, near-surface wind speed, and net solar radiation) were obtained from the three GCMs (CanESM5 (2.7906°×2.8125°), INM-CM4-8 (1.5°×2°), and INM-CM5-0 (1.5°×2°)) for the period 2015–2100). A search on many available GCMs in the database (https://esgf-node.llnl.gov/search/cmip6/) indicated that information on all the desired climate variables corresponding to all four SSP-FS was available for only these three GCMs, for simulation variant r1i1p1. As the GCMs have different resolutions, they were regridded to a common spatial resolution (1°) using the Bessel interpolation technique. The regridded datasets were subsequently bias-corrected using the nonparametric Robust Quantile Mapping (RQM) technique (Appendix A5.4) available with R Package 'qmap' (Gudmundsson and Gudmundsson, 2012). For use in this analysis, CDFs for the historical period were constructed using (i) IMD observations on precipitation, maximum and minimum temperatures, and (ii) NCEP reanalysis data on relative humidity, near-surface wind speed, and net solar radiation. The bias-corrected climate variables were used in the FAO-PM equation to obtain future projections of ET_0 corresponding to different SSP-FS for each of the 1° grids formed in the study area. The bias-corrected precipitation and climate variables (T_{max}, T_{min}, wind speed, R_{net}, and RH) were considered for subsequent analysis.

Subsequently, regional mean- time series of ET_0 and its predictor climate variables were determined for Mahanadi basin and homogeneous ET_0 regions (6, 7, 8 and 9) at annual time scale for the period 2015–2100, corresponding to each SSP forcing scenario (SSP-FS) from simulations of the three GCMs. The presence of long-term monotonic trends in those time series was analyzed using nonparametric Mann-Kendall test (Kendall, 1955; Mann, 1945) considering 5% and 10% significance levels. Furthermore, the slope of the trend line was estimated using Sen's slope method (Sen, 1968). In addition, multivariate change point analysis was performed on the time series of each variable analyzed using the e-divisive hierarchical clustering nonparametric method (Matteson and James, 2014) to find the instance(s) of significant change (if any) in their trend. Furthermore, sensitivity coefficients (climate elasticity values) of ET_0 were estimated for each of the homogeneous ET_0 regions encompassing the Mahanadi basin by considering the expression derived for the third-order approximation of the Taylor series expansion of the ET_0 function (Equation A5.23 in Appendix A5.3). Estimates of the coefficients were analyzed along with trends of the predictor variables to identify the variables that have a considerable effect on ET_0.

Estimates of Sen's slope obtained are shown in Tables 5.5-5.10. Future projections of the estimated annual mean ET_0 for the period 2015-2100 revealed increasing regional trend (Table 5.5) in analysis based on simulations from individual GCMs and their ensemble mean. In general, the increasing trend was found to be statistically significant at 5% significance level for all the SSP-FS. For GCM INM-CM5-0, the increasing trend in annual ET_0 was not statistically significant for most of the SSP-FS. The trend in different predictor variables of ET_0 is also analyzed. A significantly increasing trend (at 5% significance level) is evident in the regional mean of annual T_{max}, T_{min} and net solar radiation over all the homogeneous ET_0 regions and for all the SSP-FS (Tables 5.6-5.8). The rate of increment of the aforementioned variables (ET_0, T_{max} , T_{min} and net solar radiation) was highest for CanESM5 among all three GCMs. It is to be noted that the rates of increment of ET_0, $T_{max,}$ and T_{min} in the future are increasing from scenario SSP 126 to SSP 585 for all the regions (Tables 5.5 to 5.7). The projected increase in future ET_0 can be attributed to a significant increase projected for net solar radiation and maximum and minimum temperatures (Figure 5.9). A significant increase in future regional mean annual RH was projected for the majority of regions in the case of SSPs 245, 370 and 585 in analysis with GCMs INM-CM4-8 and M-CM5-0, and the ensemble mean of GCMs (Table 5.9). Analysis of future wind speed projections at the annual scale revealed that the projected trend was not significant

for SSP-126, whereas it was significant and decreasing in regions 6 and 9 for SSP 245 and SSP 370 scenarios (Table 5.10).

Table 5.5: Sen's slope of trend lines fitted to future projections of annual mean ET_0 (mm/year) obtained from individual GCMs, and their ensemble mean.

Region No	CanESM5				INM-CM4-8				INM-CM5-0				Ensemble Mean			
	SSP 126	SSP 245	SSP 370	SSP 585	SSP 126	SSP 245	SSP 370	SSP 585	SSP 126	SSP 245	SSP 370	SSP 585	SSP 126	SSP 245	SSP 370	SSP 585
6	19.4*	24.8*	26.0*	45.1*	6.8	9.9*	11.5*	27.4*	9.4**	3.2	7.9	9.5	11.6*	13.3*	14.3*	26.5*
7	28.9*	27.8*	37.7*	61.1*	7.5*	8.6*	11.8*	25.3*	11.1*	4.3	8.9	16.8	15.5*	14.1*	18.1*	35.0*
8	30.9*	33.1*	39.9*	71.8*	10.2*	14.1*	12.9*	24.8*	12.3*	10.9	6.1	15.5	17.4*	19.5*	18.0*	36.9*
9	23.5*	29.0*	32.3*	49.7*	11.7*	11.3*	7.6	34.1*	12.2*	3.8	3.3	6.2	15.9*	15.9*	12.8*	31.2*

* Denotes trend is significant at 5% significance level.
** Denotes trend is significant at 10% significance level. Senslope is estimated per decade.

Table 5.6: Sen's slope of trend lines fitted to future projections of annual mean T_{max} (degree/day) obtained from individual GCMs, and their ensemble mean.

Region No	CanESM5				INM-CM4-8				INM-CM5-0				Ensemble Mean			
	SSP 126	SSP 245	SSP 370	SSP 585	SSP 126	SSP 245	SSP 370	SSP 585	SSP 126	SSP 245	SSP 370	SSP 585	SSP 126	SSP 245	SSP 370	SSP 585
6	0.12*	0.24*	0.42*	0.55*	0.05*	0.13*	0.26*	0.35*	0.07*	0.11*	0.23*	0.29*	0.07*	0.16*	0.31*	0.40*
7	0.10*	0.19*	0.38*	0.49*	0.05*	0.13*	0.25*	0.34*	0.07*	0.12*	0.22*	0.31*	0.07*	0.15*	0.28*	0.38*
8	0.14*	0.22*	0.43*	0.58*	0.07*	0.16*	0.25*	0.34*	0.10*	0.15*	0.21*	0.29*	0.09*	0.18*	0.29*	0.41*
9	0.11*	0.29*	0.48*	0.61*	0.08*	0.16*	0.30*	0.43*	0.09*	0.13*	0.25*	0.31*	0.09*	0.19*	0.35*	0.46*

* Denotes trend is significant at 5% significance level.
** Denotes trend is significant at 10% significance level. Senslope is estimated per decade.

Table 5.7: Sen's slope of trend lines fitted to future projections of annual mean T_{min} (degree/day) obtained from individual GCMs, and their ensemble mean.

Region No	CanESM5				INM-CM4-8				INM-CM5-0				Ensemble Mean			
	SSP 126	SSP 245	SSP 370	SSP 585	SSP 126	SSP 245	SSP 370	SSP 585	SSP 126	SSP 245	SSP 370	SSP 585	SSP 126	SSP 245	SSP 370	SSP 585
6	0.16*	0.33*	0.61*	0.77*	0.05*	0.18*	0.36*	0.46*	0.06*	0.21*	0.36*	0.48*	0.09*	0.24*	0.45*	0.57*
7	0.12*	0.22*	0.41*	0.52*	0.05*	0.20*	0.37*	0.49*	0.08*	0.20*	0.35*	0.46*	0.08*	0.20*	0.38*	0.49*
8	0.12*	0.25*	0.49*	0.63*	0.07*	0.19*	0.36*	0.49*	0.07*	0.19*	0.38*	0.50*	0.08*	0.21*	0.41*	0.54*
9	0.15*	0.39*	0.69*	0.85*	0.05*	0.18*	0.38*	0.47*	0.06*	0.21*	0.36*	0.49*	0.09*	0.26*	0.48*	0.61*

Table 5.8: Sen's slope of trend lines fitted to future projections of annual mean net solar radiation (watt/m^2/day) obtained from individual GCMs, and their ensemble mean.

Region No	CanESM5				INM-CM4-8				INM-CM5-0				Ensemble Mean			
	SSP 126	SSP 245	SSP 370	SSP 585	SSP 126	SSP 245	SSP 370	SSP 585	SSP 126	SSP 245	SSP 370	SSP 585	SSP 126	SSP 245	SSP 370	SSP 585
6	0.15*	0.23*	0.18*	0.28*	0.05*	0.08*	0.08*	0.16*	0.08*	0.08*	0.08*	0.13*	0.09*	0.13*	0.11*	0.19*
7	0.18*	0.23*	0.16*	0.30*	0.06*	0.08*	0.08*	0.16*	0.08*	0.07*	0.06*	0.13*	0.11*	0.13*	0.10*	0.20*
8	0.16*	0.25*	0.13*	0.26*	0.08*	0.10*	0.10*	0.19*	0.09*	0.10*	0.06*	0.15*	0.11*	0.15*	0.10*	0.20*
9	0.16*	0.26*	0.18*	0.31*	0.06*	0.10*	0.07*	0.17*	0.07*	0.09*	0.07*	0.15*	0.10*	0.15*	0.11*	0.21*

Table 5.9: Sen's slope of trend lines fitted to future projections of annual mean relative humidity obtained from individual GCMs, and their ensemble mean.

Region No	CanESM5				INM-CM4-8				INM-CM5-0				Ensemble Mean			
	SSP 126	SSP 245	SSP 370	SSP 585	SSP 126	SSP 245	SSP 370	SSP 585	SSP 126	SSP 245	SSP 370	SSP 585	SSP 126	SSP 245	SSP 370	SSP 585
6	0.08	0.48*	0.71*	0.63*	0.03	0.08	0.14	-0.02	-0.01	0.41*	0.36*	0.69*	0.14	0.93*	1.33*	1.26*
7	-0.10	0.25*	0.04	-0.01	0.01	0.10	0.21*	0.13**	-0.03	0.27*	0.31*	0.42*	-0.16	0.60*	0.70*	0.54*
8	-0.26	0.14	-0.22	-0.41*	-0.01	-0.06	0.25*	0.21*	-0.16	0.15	0.46*	0.48*	-0.35	0.34**	0.51*	0.29
9	0.15	0.37	0.89*	0.86*	-0.04	0.00	0.23	-0.12	-0.14	0.37*	0.42*	0.84*	0.05	0.71*	1.61*	1.56*

Table 5.10: Sen's slope of trend lines fitted to future projections of annual mean wind speed (m/s/year) obtained from individual GCMs, and their ensemble mean.

Region No	CanESM5				INM-CM4-8				INM-CM5-0				Ensemble Mean			
	SSP 126	SSP 245	SSP 370	SSP 585	SSP 126	SSP 245	SSP 370	SSP 585	SSP 126	SSP 245	SSP 370	SSP 585	SSP 126	SSP 245	SSP 370	SSP 585
6	-0.01	-0.01	0.01**	0.01*	0.00	-0.01	-0.03*	-0.02*	0.01	-0.01	-0.01*	0.00	0.00	-0.01*	-0.01*	0.00
7	0.02*	0.01**	0.04*	0.06*	0.00	-0.01	-0.01	-0.01*	0.00	-0.01	0.00	0.01	0.01	0.00	0.02*	0.02*
8	0.01	0.00	0.03*	0.06*	0.00	-0.01	-0.02*	-0.01	0.00	0.00	0.00	0.00	0.00	0.00	0.00	0.02*
9	0.00	-0.02*	0.02*	0.02*	0.00	-0.01*	-0.03*	-0.02*	0.00	-0.02*	-0.02*	-0.01**	0.00	-0.01*	-0.01*	0.00

Generally, the trend of different climate variables could change across different time windows chosen in the period considered for the analysis. Hence, for each of the homogeneous ET_0 regions, multivariate change points were identified by analyzing the regional average time series of annual ET_0 and climate variables over the period 2015-2100 using the e-divisive hierarchical nonparametric method (Matteson and James, 2014). Trend analysis was performed on data points in the time windows between different sets of consecutive change points. The change points corresponding to the SSP-585 scenario are presented in Figure 5.9 for brevity.

In SSP 126 scenario, the multivariate change point (MCP) was projected to occur only in Region 7 around 2037. In all other SSP-FS, MCPs are noted in all the regions. The near-future MCPs are speculated to occur during (i) 2049-2055 in SSP 245 scenario, (ii) 2029 in Regions 7 and 9, 2049-2053 in Regions 6, 7, and 9 in SSP 370 scenario, and (iii) 2039-2040, and 2058-2059 in SSP 585 scenario. The far-future MCP is speculated around 2077-2084.

Table 5.17: Future projected multivariate change points in each of the homogeneous ET_0 regions encompassing the Mahanadi basin for each of the four SSP scenarios.

Region No	SSP 126	SSP 245	SSP 370	SSP 585
6	-	2055	2049, 2088	2039, 2059, 2080
7	2037	2055, 2084	2029, 2053, 2063, 2080, 2090	2039, 2059, 2080
8	-	2049, 2079	2037, 2068	2048, 2058, 2077
9	-	2055	2029, 2049, 2081	2040, 2059, 2078

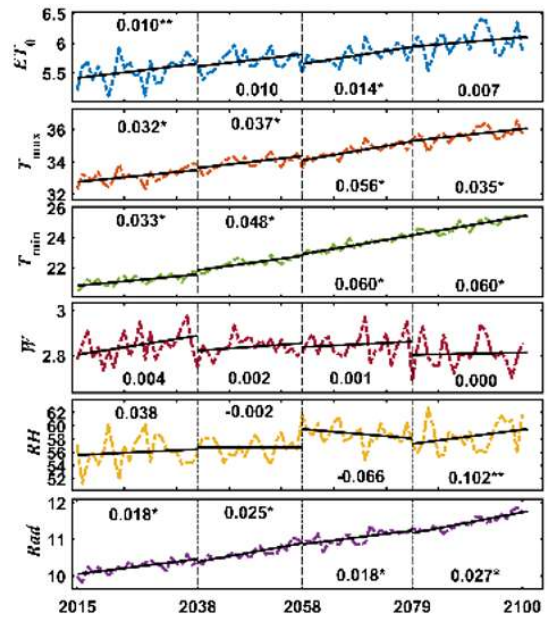

Region: 6: Overall: *Rad*
TP1 to TP4: *Rad*

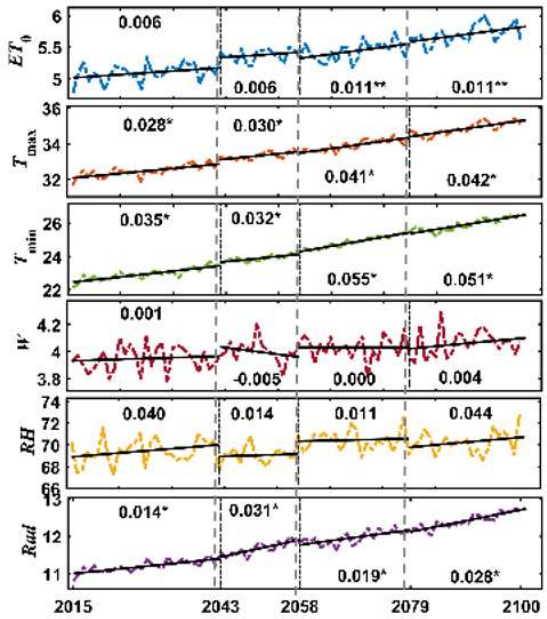

Region: 7: Overall: *Rad*
TP1 to TP4: *Rad*

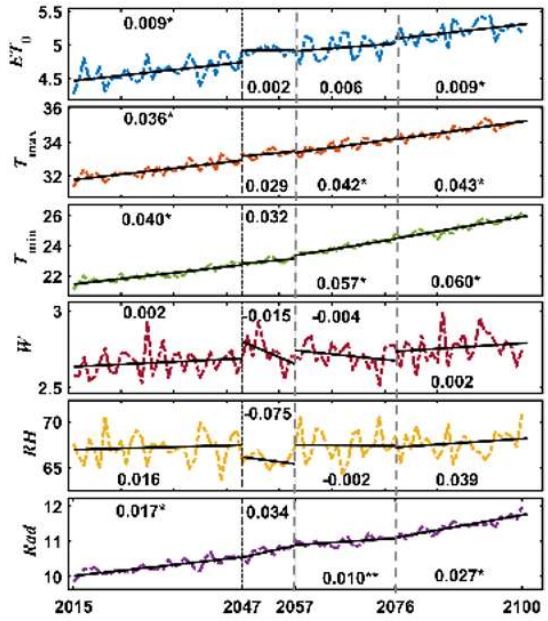

Region: 8: Overall: *Rad*
TP1, TP2, TP4: *Rad*, TP3: Tmax

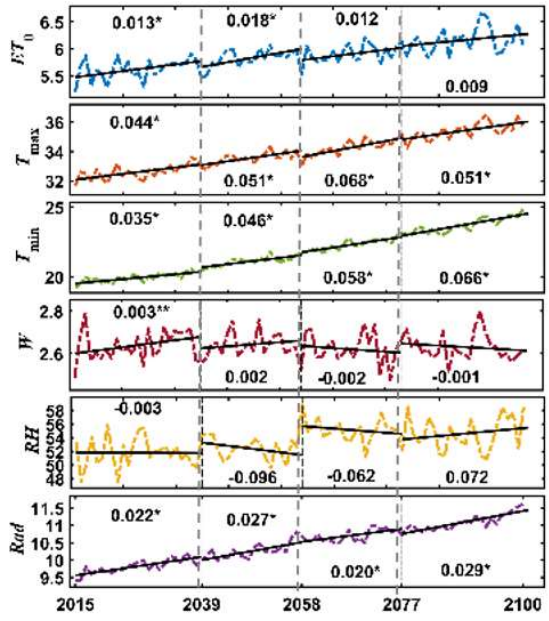

Region: 9: Overall: *Rad*
TP1, TP2, TP4: *Rad*, TP3: Tmax

Figure 5.9: Multivariate change points of ET_0 and its predictor climate variables (T_{max}, T_{min}, wind speed (W), relative humidity (RH), and solar radiation (Rad)) are shown along with slopes of trend lines fitted between the change points for each of the homogeneous ET_0 regions encompassing Mahanadi basin. The predictor climate variable which has the most influence on ET_0 (i) in the time period (TP) between successive change points and (ii) for the overall period or entire duration of record are listed for each region. The time periods (TPs) are numbered in the order of their occurrence.

5.6.2. Projected future freshwater availability in Mahanadi Basin

The future projections of freshwater availability (FWA) in the Mahanadi basin corresponding to CMIP6 SSP-FS were determined using Budyko framework (Appendix 5.3). As mentioned earlier, Budyko's framework is an approximation of a complex rainfall-runoff process. The framework considers only precipitation, actual- and potential- evapotranspiration as input to estimate runoff which is an approximation valid at the multiannual time scale. Regional mean- time series of ET_0 and precipitation obtained corresponding to the three CMIP-6 GCMs at annual scale for various SSP-FS were used to arrive at future projections for FWA from Mahanadi basin and each of the homogeneous ET_0 regions 6 to 9 encompassing the basin.

Despite an increase projected for ET_0, a significant increase in future freshwater availability is projected for (i) Regions 8 and 9 in the case of the SSP 126 scenario in analysis with climate projections from CanESM5 and ensemble mean of the GCMs, (ii) all the regions for SSP scenarios 245, 370, and 585 in analysis with CanESM5, INM-CM5-0 and ensemble mean of the GCMs (Table 5.11). This could be attributed to a significant increase in precipitation (Table 5.12). In most of the regions for all four SSPs, the runoff estimate (Table 5.11) corresponding to CanESM5 was the highest among all three GCMs. The future projections of the population obtained for different SSPs (Figure 5.10) indicate an increase for all the SSPs up to the year 2050. Thereafter, it continues to increase up to 2100 for SSP-370 but decreases for other SSP-FS. The information on future annual population for the period 2006-2100 is used to arrive at projections of future fresh water availability (FWA) per capita in each of the homogeneous ET_0 regions (6 to 9) and for the Mahanadi basin. The information on future population was obtained corresponding to different climate scenarios from ISIMIP2b (Inter-Sectoral Impact Model Intercomparison Project protocol 2b) at a spatial resolution of 0.125°. The FWA per capita is projected to increase significantly in the Mahanadi basin and all the associated homogeneous ET_0 regions (6 to 9) for SSPs-126, 245 and 585, except Regions 6 and 7 for SSP 245 scenario (Table 5.13; Figure 5.11). In contrast, it is projected to decrease significantly in the basin all the regions for the SSP-370 scenario due to the highest population among all scenarios.

For the Mahanadi basin, the projected changes in ET_0 and its predictor climate variables (with respect to historical period) are visualized at annual scale (Figure 5.11b) and for different seasons (Figures A5.2-A5.20). For preparing the figures, the seasons were considered as monsoon (June-September),

winter (October-January), and summer (February-May). Discussion on the same is provided in Appendix A5.4.

Table 5.11: Sen's slope of trend lines fitted to future projections of annual runoff (mm/year) determined in analysis with climate projections from individual GCMs and their ensemble mean.

Region No	CanESM5				INM-CM4-8				INM-CM5-0				Ensemble Mean			
	SSP 126	SSP 245	SSP 370	SSP 585	SSP 126	SSP 245	SSP 370	SSP 585	SSP 126	SSP 245	SSP 370	SSP 585	SSP 126	SSP 245	SSP 370	SSP 585
6	31.80	70.34*	112.67*	167.22*	10.99	0.86	16.74	-6.08	-4.87	14.03	31.49*	51.21*	9.11	29.28*	52.87*	76.85*
7	10.59	42.44*	51.16*	77.47*	2.38	24.61*	42.53*	15.82	-4.52	21.78*	23.84*	52.74*	1.78	29.15*	38.84*	48.81*
8	22.07*	62.74*	42.32*	63.01*	10.06	44.18*	70.13*	87.91*	5.61	54.74*	86.66*	100.55*	12.82**	56.64*	67.24*	83.48*
9	35.02*	57.94*	83.76*	139.76*	8.28	4.49	-8.39	-5.05	25.10*	52.22*	48.62*	61.63*	22.33*	38.85*	37.90*	62.37*

Table 5.12: Sen's slope of trend lines fitted to future projections of annual precipitation (mm/year) obtained from individual GCMs, and their ensemble mean.

Region No	CanESM5				INM-CM4-8				INM-CM5-0				Ensemble Mean			
	SSP 126	SSP 245	SSP 370	SSP 585	SSP 126	SSP 245	SSP 370	SSP 585	SSP 126	SSP 245	SSP 370	SSP 585	SSP 126	SSP 245	SSP 370	SSP 585
6	37.84	83.63*	131.74*	193.9*	13.3	1.48	19.75	89.69*	-5.68	15.81	36.41*	59.7*	11.93	35.09*	62.32*	89.69*
7	15.25	56.57*	66.73*	100.01*	4.44	31.41*	51.04*	62.65*	-3.99	27.12*	29.56*	65.28*	3.9	36.96*	50.06*	62.65*
8	29.33**	75.72*	50.47*	81.85*	13.99	50.65*	80.36*	97.92*	7.67	63.21*	97.71*	113.4*	17.56*	65.9*	78.04*	97.92*
9	44.08*	69.73*	101.73*	162.72*	11.01	6.8	-10.2	75.47*	30.47*	61.05*	55.4*	70.46*	27.94*	46.63*	44.35*	75.47*

Table 5.13: Sen's slope (m^3/yr) of future (2015-2100) fresh water availability per capita for different SSPs.

Region	SSP-126	SSP-245	SSP-370	SSP-585
6	1199.21*	214.47	-1099.35*	3219.94*
7	352.89*	151.75	-462.81*	1094.07*
8	154.83*	140.8*	-133.81*	578.14*
9	869.6*	280.15*	-634.24*	1527.64*

* trend is significant at 5 % significance level; ** trend is significant at 10 % significance level

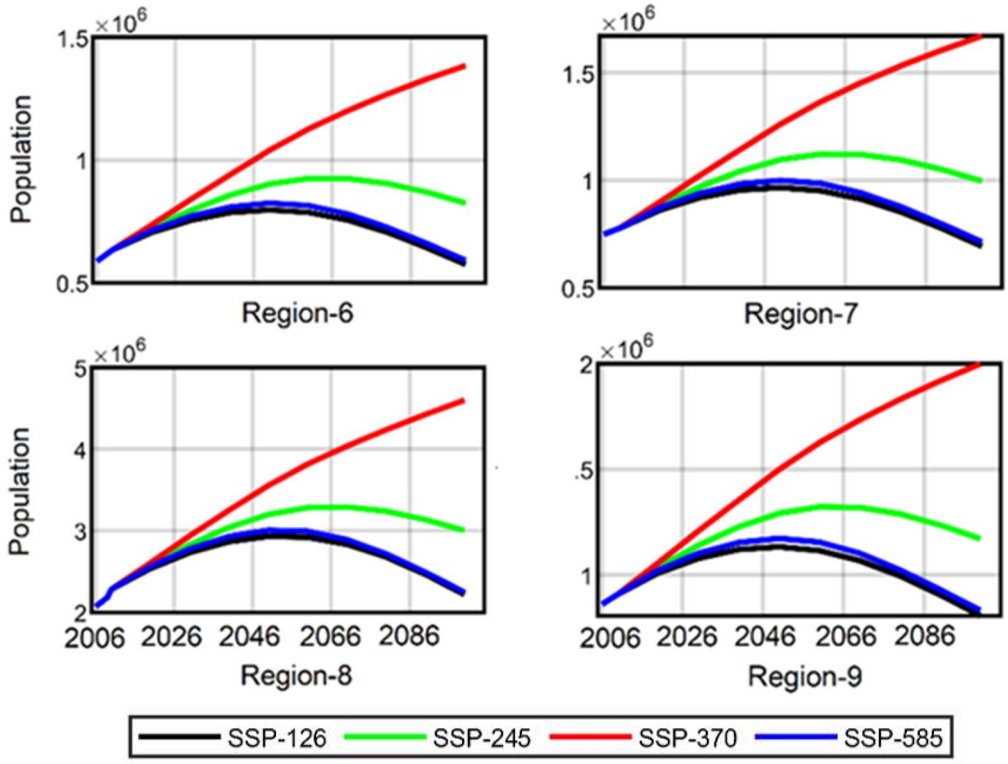

Figure 5.10: Future population per 10,000 Km^2 in different regions.

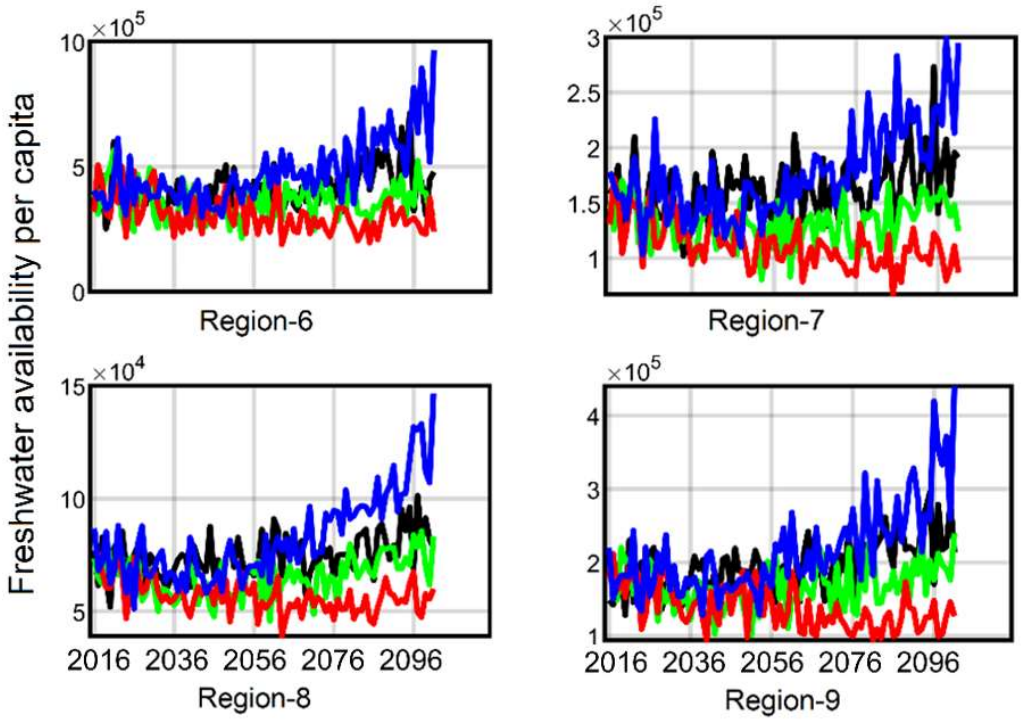

Figure 5.11(a): Future per capita freshwater availability (m^3) in different regions.

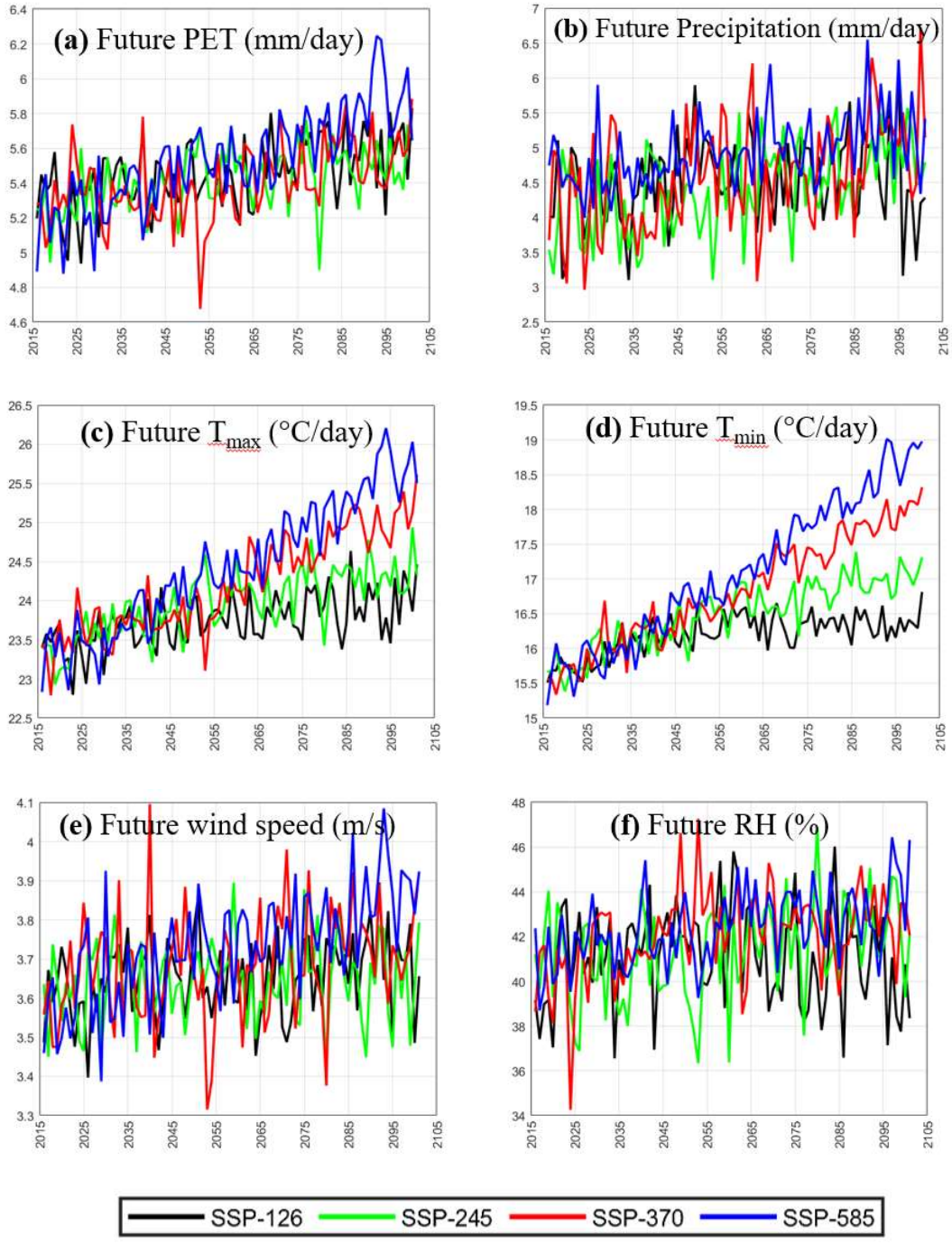

Figure 5.11(b): Future projections of climate variables, freshwater availability, population (per 10,000 km^2), and freshwater per capita in the Mahanadi basin.

Figure 5.11(b) (Continued…)

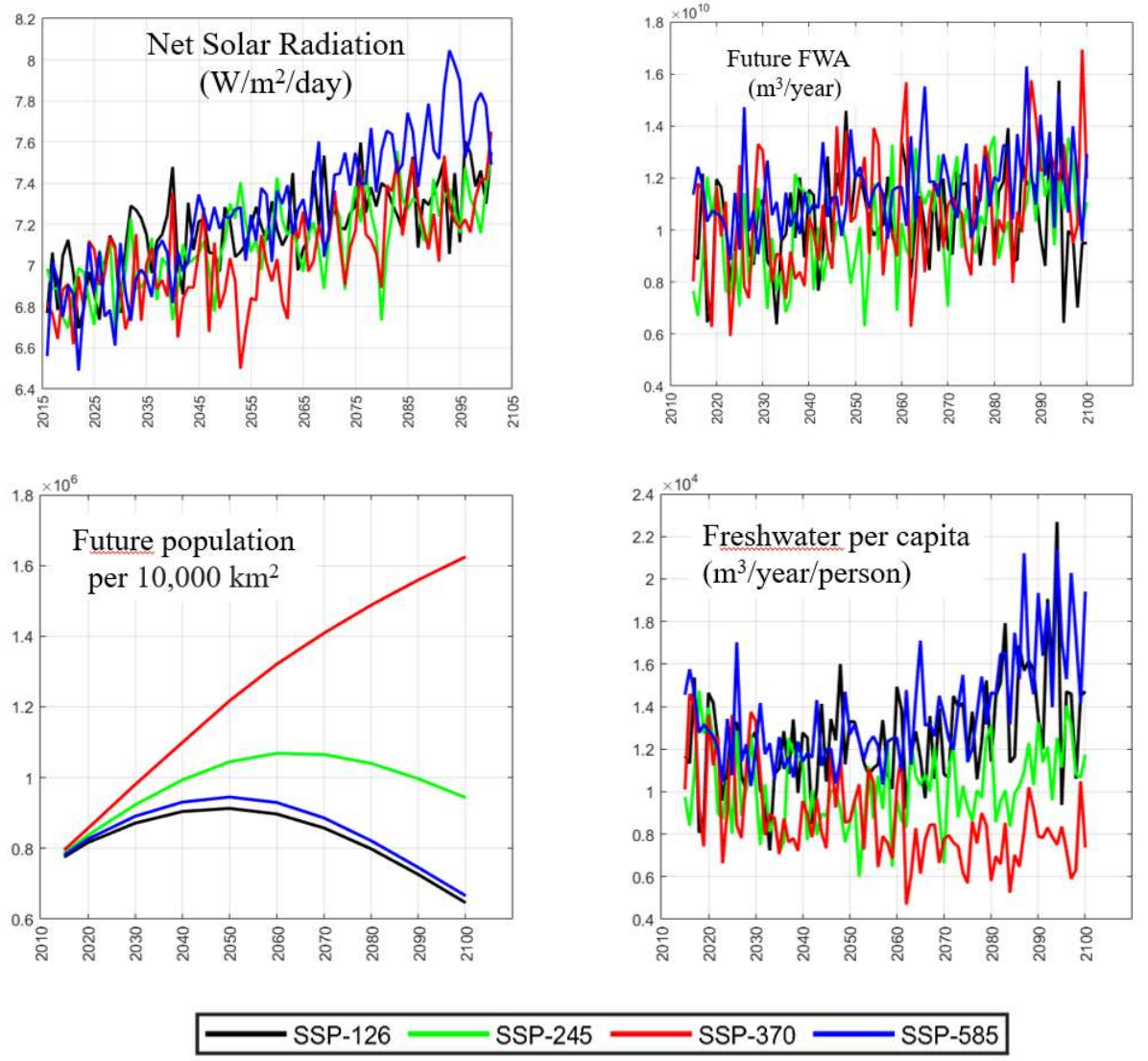

Appendices

A5.1: Methodology proposed for regionalization of evapotranspiration

Suppose there are N sites (or grids) in the study area that are to be delineated into homogeneous ET_0 regions. Let n denote the number of attributes that influence ET_0 in the area. They could be identified by analyzing different analytical expressions which are in use for ET_0 estimation. Typical examples of attributes include maximum, minimum and mean air temperatures, net solar radiation, relative humidity, and wind speed. Geographically nearby sites could have similarities in ET_0 due to similarity in climate conditions influencing ET_0. Therefore, location indicators (latitude, longitude and elevation) are deemed useful attributes.

Attribute vector depicting each site i could be prepared as $Y_i = \left\{ y_{i,j,t} : j = 1,...,n;\ t = 1,...,T \right\}$, where $y_{i,j,t}$ denotes the observed value of the j-th attribute at time t for the i-th site. Rescaling of the attribute vector is required to eliminate heterogeneity among the attributes due to differences in their distribution and unit of measurement. Mean $\overline{y}_{\bullet,j,\bullet}$ and unbiased standard deviation σ_j corresponding to each attribute j could be used to rescale the attribute as,

$$x_{i,j,t} = \left\{ \frac{y_{i,j,t} - \overline{y}_{\bullet,j,\bullet}}{\sigma_j} : i = 1,...,N; j = 1,...,n;\ t = 1,...,T \right\} \tag{A5.1}$$

where, $\overline{y}_{\bullet,j,\bullet} = \sum_{t=1}^{T}\sum_{i=1}^{N} y_{i,j,t} \Big/ \left(N \times T\right)$ and $\sigma_j = \sqrt{\sum_{t=1}^{T}\sum_{i=1}^{N}\left(y_{i,j,t} - \overline{y}_{\bullet,j,\bullet}\right)^2 \Big/ \left(N \times T - 1\right)}$ (A5.2)

The rescaled attribute vectors $\mathbf{X} = \left\{ x_{i,j,t} : i = 1,...,N; j = 1,...,n;\ t = 1,...,T \right\} \in \Re^{N \times n \times T}$ are partitioned into C clusters using the fuzzy dynamic clustering approach, which considers multivariate time-varying fuzzy clustering (MTFC; D'urso, 2004) algorithm. It can account for time-evolving properties of attributes in regionalization. It involves performing iterations to arrive at an optimum value of the following objective function.

$$\text{Minimize } J = \sum_{i=1}^{N}\sum_{c=1}^{C}\left(u_{i,c}^{\mu} \sum_{s=1}^{S}\sum_{t=1}^{T}\left(w_{s,t} d_{i,c,s,t} \right)^2 \right) \tag{A5.3}$$

Subject to the following constraints,

$$\sum_{c=1}^{C} u_{i,c} = 1,\ u_{i,c} \geq 0,\ \forall i \in \{1,...,N\} \tag{A5.4}$$

$$\sum_{t=1}^{T} w_{s,t} = 1,\ w_{s,t} \geq 0,\ \forall s \in \{1,2,3\} \tag{A5.5}$$

Where $u_{i,c}$ denotes the membership of *i*-th site's attribute vector X_i in the *c*-th fuzzy cluster; $\boldsymbol{U} = \{u_{i,c} : i = 1,...,N; c = 1,...,C\}$ denotes fuzzy membership matrix; $\mu \in (1,\infty)$ is fuzzifier or fuzziness weighting factor which depicts the degree of fuzziness of the clusters; $d_{i,c,s,t}$ denotes Euclidian distance between trajectories of the *i*-th site and *c*-th cluster centroid at time instance *t* which is measured in terms of *s*-th instantaneous feature (e.g., location (*s*=1), or evolutive dynamic features such as velocity (*s*=2) or acceleration (*s*=3)) as shown in equation (A5.6); and $w_{s,t}$ denotes weight assigned to $d_{i,c,s,t}$. In equation (A5.3), weighted Euclidian distance provides higher importance (i.e., lower weight, as the objective function is to be minimized) to similar instantaneous and evolutive characteristics (i.e., velocity and acceleration) and penalizes dissimilarity to get compact homogeneous clusters.

$$\left.\begin{aligned}
d_{i,c,1,t} &= \left\|\boldsymbol{x}_{i,t} - \boldsymbol{h}_{c,t}\right\| = \sqrt{\sum_{j=1}^{n}\left(x_{i,j,t} - h_{c,j,t}\right)^2} && i = 1,...,N;\ c = 1,...,C;\ t = 1,...,T \\
d_{i,c,2,t} &= \left\|\boldsymbol{v}_{i,t} - \boldsymbol{v}_{c,t}\right\| = \sqrt{\sum_{j=1}^{n}\left(v_{i,j,t} - v_{c,j,t}\right)^2} && i = 1,...,N;\ c = 1,...,C;\ t = 2,...,T \\
d_{i,c,3,t} &= \left\|\boldsymbol{a}_{i,t} - \boldsymbol{a}_{c,t}\right\| = \sqrt{\sum_{j=1}^{n}\left(a_{i,j,t} - a_{c,j,t}\right)^2} && i = 1,...,N;\ c = 1,...,C;\ t = 3,...,T
\end{aligned}\right\} \tag{A5.6}$$

where $\boldsymbol{x}_{i,t} = \{x_{i,j,t} : j = 1,...,n\}$ and $\boldsymbol{h}_{c,t} = \{h_{c,j,t} : j = 1,...,n\}$ denote respectively the locations of the *i*-th site (grid) and *c*-th cluster centroid in rescaled attribute space at time *t*; $\boldsymbol{v}_{i,t}$ and $\boldsymbol{a}_{i,t}$ denote the velocity and acceleration of the time trajectory of the i-th site in the time interval [t-1, t] respectively; $\boldsymbol{v}_{c,t}$ and $\boldsymbol{a}_{c,t}$ denote the corresponding values for the time trajectory of the *c*-th cluster centroid. Velocity measures the slope of the straight line between each successive pair of time points, whereas

acceleration measures the concavity or convexity of each pair of time segments of trajectories. $\boldsymbol{v}_{i,t}$ and $\boldsymbol{a}_{i,t}$ can be computed as,

$$\begin{aligned}\boldsymbol{v}_{i,t} &= \frac{\boldsymbol{x}_{i,t}-\boldsymbol{x}_{i,t-1}}{t-(t-1)} = \boldsymbol{x}_{i,t}-\boldsymbol{x}_{i,t-1} = \left\{x_{i,j,t}-x_{i,j,t-1} : j=1,...,n\right\} \\ &= \left\{v_{i,j,t} : j=1,...,n\right\} \qquad i=1,...,N;\ t=2,...,T\end{aligned} \tag{A5.7}$$

$$\begin{aligned}\boldsymbol{a}_{i,t} &= \frac{\dfrac{\boldsymbol{x}_{i,t}-\boldsymbol{x}_{i,t-1}}{t-(t-1)} - \dfrac{\boldsymbol{x}_{i,t-1}-\boldsymbol{x}_{i,t-2}}{(t-1)-(t-2)}}{t-(t-2)} = \frac{\boldsymbol{v}_{i,t}-\boldsymbol{v}_{i,t-1}}{2} = \left\{\frac{v_{i,j,t}-v_{i,j,t-1}}{2} : j=1,...,n\right\} \\ &= \left\{a_{i,j,t} : j=1,...,n\right\} \qquad i=1,...,N;\ t=3,...,T\end{aligned} \tag{A5.8}$$

The subsequent steps involved in the MTFC-based regionalization methodology (presented as a flowchart in Figure A5.1) are as follows:

(1) Define $C_{\min}$ and C_{max} as, respectively, the lower and the upper bound for the possible number of clusters that can be discerned from the data, and set the value for C (number of clusters) to $C_{\min}$. Let δC denote increment for the parameter, which could be chosen to be 1.

(2) Define $\mu_{\min}$ and $\mu_{\max}$ as the lower and the upper bounds for fuzzifier value, respectively, and set the value of μ to $\mu_{\min}$. Let $\delta\mu$ denote increment for the parameter, which could be chosen to be 0.1. Set iteration count to 1.

(3) Initialize cluster membership matrix $\boldsymbol{U}_{(N\times C)}$ by generating uniformly distributed random numbers and rescale elements of the matrix to satisfy the constraint on membership (i.e., equation (A5.4)).

(4) Using the updated membership matrix $\boldsymbol{U}_{(N\times C)}$ calculate the location $\boldsymbol{h}_{c,t}$, velocity $\boldsymbol{v}_{c,t}$, and acceleration $\boldsymbol{a}_{c,t}$ of the time trajectory of the *c*-th cluster centroid $(c=1,\ldots,C)$ and the weights $\left\{w_{s,t}, s=1,2,3; t=1,...,T\right\}$.

$$\boldsymbol{h}_{c,t} = \sum_{i=1}^{N} u_{i,c}^{\mu}\boldsymbol{x}_{i,t} \Big/ \sum_{i=1}^{N} u_{i,c}^{\mu} \tag{A5.9}$$

$$\boldsymbol{v}_{c,t} = \sum_{i=1}^{N} u_{i,c}^{\mu}\boldsymbol{v}_{i,t} \Big/ \sum_{i=1}^{N} u_{i,c}^{\mu} \tag{A5.10}$$

$$\boldsymbol{a}_{c,t} = \sum_{i=1}^{N} u_{i,c}^{\mu}\boldsymbol{a}_{i,t} \Big/ \sum_{i=1}^{N} u_{i,c}^{\mu} \tag{A5.11}$$

$$w_{s,t} = 1 \Big/ \sum_{t^*=1}^{T} \left(\frac{\sum_{i=1}^{N} \sum_{c=1}^{C} u_{i,c}^{\mu} d^2{}_{i,c,s,t}}{\sum_{i=1}^{N} \sum_{c=1}^{C} u_{i,c}^{\mu} d^2{}_{i,c,s,t^*}} \right) \tag{A5.12}$$

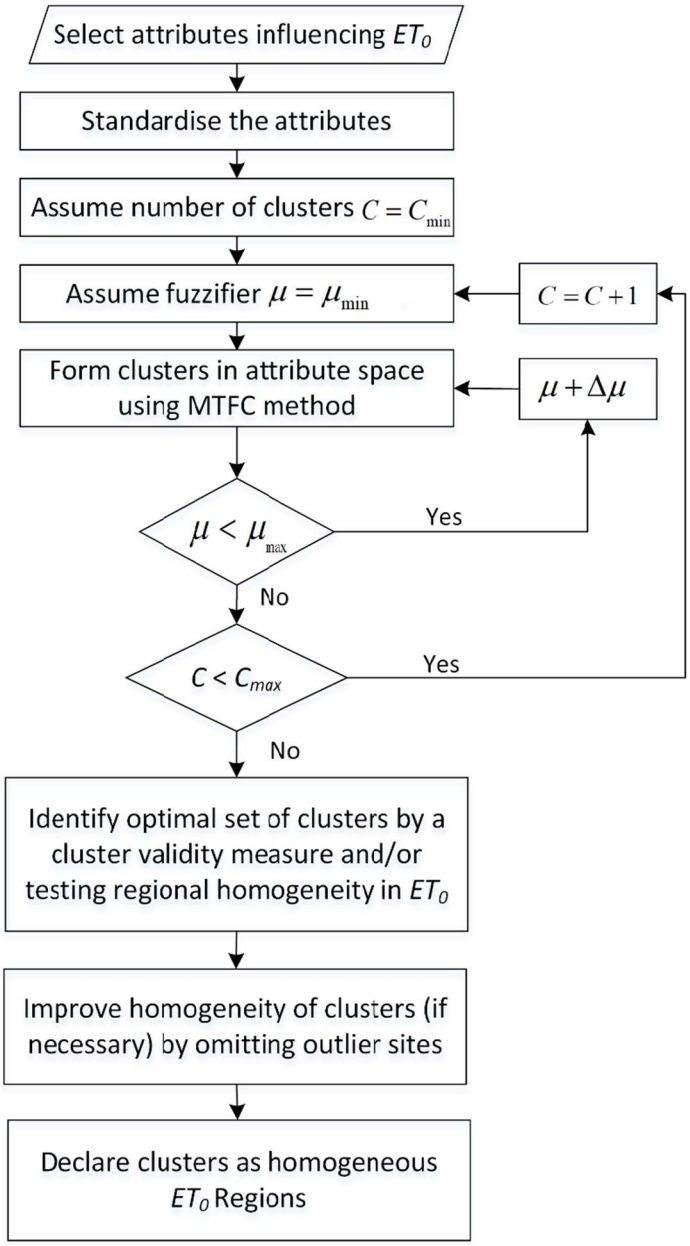

Figure A5.1. Flow chart of fuzzy dynamic clustering (MTFC) methodology proposed for regionalization of ET_0.

(5)Update the memberships as,

$$u_{i,c} = 1 \Big/ \sum_{c^*=1}^{C} \left(\frac{\sum_{s=1}^{S}\sum_{t=1}^{T}\left(w_{s,t}d_{i,c,s,t}\right)^2}{\sum_{s=1}^{S}\sum_{t=1}^{T}\left(w_{s,t}d_{i,c^*,s,t}\right)^2} \right)^{\frac{1}{\mu-1}} \tag{A5.13}$$

(6) Compute the value of the objective function J (equation (A5.3)) for the current iteration. If the iteration count is 1, increment the count by unity and proceed to step (4). For any higher iteration count, compute the difference in the value of J between the current and previous iterations. If the difference is sufficiently small (<0.001) or if the iteration count is equal to a pre-specified upper bound on the number of iterations (e.g., 500), store $\boldsymbol{U}_{(N\times C)}$ and J values, and proceed to step (7). Otherwise, increment the iteration count by unity and proceed to step (4).

(7) Update μ to $(\mu+\delta\mu)$. If the updated μ is greater than $\mu_{\max}$ proceed to (8), else proceed to step (3).

(8) Update C to $C+\delta C$. If the updated C is less than $C_{\max}$ proceed to (2), else store both $\boldsymbol{U}_{(N\times C)}$ and J values.

To address the uncertainty in initializing memberships in step (3), steps (1) to (8) could be repeated several times (e.g., 100) and all the resulting clusters could be analyzed to determine the best set of clusters and the corresponding optimal values for C and μ. D'urso (2004) suggested declaring optimal values for the number of clusters and fuzzifier μ as those for which the following Xie-Beni cluster validity index is minimum.

$$\min_{\substack{\mu\in\Omega_\mu \\ C\in\Omega_C}} V(C,\mu) = \frac{\sum_{i=1}^{N}\sum_{c=1}^{C}\left(u_{i,c}^{\mu}\sum_{s=1}^{S}\sum_{t=1}^{T}\left(w_{s,t}d_{i,c,s,t}\right)^2 \right) \Big/ N}{\min\limits_{\substack{\forall c,c' \\ c\neq c'}} \sum_{s=1}^{S}\sum_{t=1}^{T}\left(w_{s,t}d_{c',c,s,t}\right)^2} \tag{A5.14}$$

Regions are formed by assigning each site (grid) to a cluster in which it has maximum membership. Each region is subsequently evaluated for homogeneity by computing inter-site correlations of the predictand ET_0 at the monthly scale. A region is considered to be acceptably homogeneous if the median of inter-site correlations is fairly high and the minimum of the correlations is significant and

positive. The homogeneity of a region could be improved (if necessary) by moving discordant sites to other regions in which they have reasonably large fuzzy membership.

Different validity indices are used in cluster analysis, and none of those is proven to be universally superior (Basu & Srinivas, 2014). If the indices are found to be ineffective in yielding clusters that are either homogeneous or closer to being homogeneous, then optimal partition could be identified by checking the homogeneity of the clusters obtained for different combinations of C and μ.

A5.2: Empirical methods for estimation of daily ET_0 (mm)

FAO-PM: $$ET_0 = \frac{0.408\Delta\left(Rad - GHF\right) + \gamma \frac{900}{0.5\left(T_{\max} + T_{\min}\right) + 273} W\left(e_s - e_a\right)}{\Delta + \gamma\left(1 + 0.34W\right)} \quad \text{(A5.15)}$$

Hargreaves: $$ET_0 = 0.0023 \frac{R_e}{\lambda}\left[0.5\left(T_{\max} + T_{\min}\right) + 17.8\right] \times \sqrt{T_{\max} - T_{\min}} \quad \text{(A5.16)}$$

Mcguinnes-Bordne: $$ET_0 = \frac{R_e}{\lambda} \frac{\left(0.5\left(T_{\max} + T_{\min}\right) + 5\right)}{68} \quad \text{(A5.17)}$$

Priestly-Taylor: $$ET_0 = 1.26 \frac{\Delta}{\Delta + \gamma}\left(Rad - GHF\right) \quad \text{(A5.18)}$$

where Δ and γ are the slope of saturated vapour pressure curve and psychometric constant (kPa/°C) respectively; Rad, R_e and GHF are respectively net solar radiation, extra-terrestrial radiation, and ground heat flux (MJ/m^2-day); W is wind speed (m/s); e_s and e_a are saturated and actual vapour pressures (kPa) respectively; $T_{\max}$ and $T_{\min}$ denote the maximum and minimum temperature (°C) respectively; and λ is the latent heat of vaporization (MJ/kg).

A5.3: Climate elasticity of surface runoff through Budyko type model

Changes occurring in surface runoff from an area (e.g., grid) due to changes in climate can be quantified using the climate elasticity concept. An analytical relationship could be developed between runoff and climate variables based on the Budyko hypothesis, which relates ET_a to ET_0 and precipitation (e.g., Dooge *et al.,* 1992; Sankarasubramanian *et al.*, 2001; Yang and Yang, 2011; Yang *et al.*, 2014; Singh and Kumar, 2015; Berghuijs *et al.*, 2017). Budyko (Budyko, 1974) postulated that mean precipitation (P) in an area could be partitioned into runoff (R) and ET_a at the annual/decadal

scale. The partitioning is conditional on competition/balance between water availability (from precipitation) and available energy in the area depicted by ET_0. Originally proposed Budyko model assumes a space-time invariant relationship between P, ET_a, and ET_0. It has no parameters, and it cannot account for the effect of catchment and climate characteristics. To address this, several parametric Budyko-type models are proposed (e.g., Fu, 1981; Choudhury, 1999; Zhang *et al.*, 2001). In this study, the effect of change in climate variables (T_{max}, T_{min}, relative humidity, wind speed, and solar radiation) on runoff or Fresh Water Availability (FWA) from a homogeneous ET_0 region is determined using Fu's Budyko type model (Fu, 1981; Zhang *et al.* 2004), which relates aridity index (ET_0/P) and evaporation ratio (ET_a/P) at the local scale as,

$$\frac{ET_a}{P} = 1 + \frac{ET_0}{P} - \left(1 + \left(\frac{ET_0}{P}\right)^{\omega}\right)^{\frac{1}{\omega}} \tag{A5.19}$$

where ω denotes a parameter accounting for catchment properties such as catchment slope, soil type, soil depth, geologic substrate, and vegetation (e.g., Wang and Fu, 2018). An estimate of the parameter could be obtained for each grid using equation (A5.19) by considering annual average estimates of ET_0, ET_a, and P. The parameter ω could also be estimated by accounting for inter-annual variability in average annual values of ET_0, ET_a, and P. For this purpose, the N-year-long annual records of those variables could be discretized into N/n non-overlapping segments, each n-years long. Subsequently, annual average values of ET_0, ET_a and precipitation, and the corresponding ET_0/P and ET_a/P values could be estimated for each of the segments. Following this, each of the N/n segments could be plotted as a point in a graph between ET_a/P and ET_0/P. Then, the best-fit curve connecting the N/n points could be determined by optimizing the parameter ω in Equation (A5.19).

A relationship could be developed to quantify the change in runoff or freshwater originating from a region (in depth units) for any specified changes in climate variables (see Equation A5.23). Estimates of sensitivity coefficients of runoff ($\xi_{(\bullet)}$) to different climate variables and the parameter ω are required at the regional scale for use in the equation. They are considered to be the arithmetic average (mean) of their respective estimates for grids in the region.

A key assumption of the Budyko-type model is that storage change ΔS is negligible and ET_a is the only source of water loss at the local scale over long-term (decadal scale), under steady-state conditions. Thus, mean precipitation (P) over a region could be partitioned into ET_a and mean runoff (R), by neglecting ΔS .

$$P = R + ET_a \tag{A5.20}$$

Expression for the relative change in runoff as a function of relative changes in ET_0, precipitation, and ω considering third-order approximation can be derived following Yang *et al.* (2014) as,

$$R = P - ET_a$$

$$= P - \left[P + ET_0 - \left(P^{\omega} + ET_0^{\omega} \right)^{\frac{1}{\omega}} \right] \quad \text{(using expression for } ET_a \text{ from Equation A5.19)}$$

$$= \left(P^{\omega} + ET_0^{\omega} \right)^{\frac{1}{\omega}} - ET_0 = g\left(ET_0, P, \omega \right) \tag{A5.21}$$

$$\frac{dR}{R} = \left[\frac{\partial R}{\partial ET_0} + \frac{1}{2!} dET_0 \frac{\partial^2 R}{\partial ET_0^{\,2}} + \frac{1}{3!} \left(dET_0 \right)^2 \frac{\partial^3 R}{\partial ET_0^{\,3}} + \ldots \right] \frac{dET_0}{ET_0} \times \frac{ET_0}{R} +$$

$$\left[\frac{\partial R}{\partial P} + \frac{1}{2!} dP \frac{\partial^2 R}{\partial P^2} + \frac{1}{3!} \left(dP \right)^2 \frac{\partial^3 R}{\partial P^3} + \ldots \right] \frac{dP}{P} \times \frac{P}{R} + \left[\frac{\partial R}{\partial \omega} + \frac{1}{2!} d\omega \frac{\partial^2 R}{\partial \omega^2} + \frac{1}{3!} \left(d\omega \right)^2 \frac{\partial^3 R}{\partial \omega^3} + \ldots \right] \frac{d\omega}{\omega} \times \frac{\omega}{R}$$

$$= \left[\frac{\partial R}{\partial ET_0} \times \frac{ET_0}{R} + \left(\frac{1}{2!} dET_0 \frac{\partial^2 R}{\partial ET_0^{\,2}} \times \frac{ET_0}{R} + \frac{1}{3!} \left(dET_0 \right)^2 \frac{\partial^3 R}{\partial ET_0^{\,3}} \times \frac{ET_0}{R} + \ldots \right) \right] \frac{dET_0}{ET_0} +$$

$$\left[\frac{\partial R}{\partial P} \times \frac{P}{R} + \left(\frac{1}{2!} dP \frac{\partial^2 R}{\partial P^2} \times \frac{P}{R} + \frac{1}{3!} \left(dP \right)^2 \frac{\partial^3 R}{\partial P^3} \times \frac{P}{R} + \ldots \right) \right] \frac{dP}{P} +$$

$$\left[\frac{\partial R}{\partial \omega} \times \frac{\omega}{R} + \left(\frac{1}{2!} d\omega \frac{\partial^2 R}{\partial \omega^2} \times \frac{\omega}{R} + \frac{1}{3!} \left(d\omega \right)^2 \frac{\partial^3 R}{\partial \omega^3} \times \frac{\omega}{R} + \ldots \right) \right] \frac{d\omega}{\omega}$$

$$= \left(\frac{\partial R}{\partial ET_0} \times \frac{ET_0}{R} + \Xi\left(ET_0 \right) \right) \frac{dET_0}{ET_0} + \left(\frac{\partial R}{\partial P} \times \frac{P}{R} + \Xi\left(P \right) \right) \frac{dP}{P} + \left(\frac{\partial R}{\partial \omega} \times \frac{\omega}{R} + \Xi\left(\omega \right) \right) \frac{d\omega}{\omega} \tag{A5.22}$$

$$= \left(\xi_{ET_0} + \Xi\left(ET_0 \right) \right) \frac{dET_0}{ET_0} + \left(\xi_P + \Xi\left(P \right) \right) \frac{dP}{P} + \left(\xi_{\omega} + \Xi\left(\omega \right) \right) \frac{d\omega}{\omega}$$

where ξ_{ET_0}, ξ_P and ξ_{ω} are the first-order approximations of the sensitivity coefficients of runoff with respect to ET_0, precipitation, and ω, respectively. Further, $\Xi(\cdot)$ denotes the difference between the sensitivity coefficient estimates obtained corresponding to first- and third-order approximations. The dET_0/ET_0 can be expressed as,

$$\frac{dET_0}{ET_0}=\left[\begin{array}{l}\frac{dT_{\max}}{T_{\max}}\left(\frac{\partial ET_0}{\partial T_{\max}}\Big/\frac{ET_0}{T_{\max}}+\Xi\left(T_{\max}\right)\right)+\frac{dT_{\min}}{T_{\min}}\left(\frac{\partial ET_0}{\partial T_{\min}}\Big/\frac{ET_0}{T_{\min}}+\Xi\left(T_{\min}\right)\right)+\\ \frac{dW}{W}\left(\frac{\partial ET_0}{\partial W}\Big/\frac{ET_0}{W}+\Xi\left(W\right)\right)+\frac{dRH}{RH}\left(\xi_{RH}\right)+\frac{dRad}{Rad}\left(\xi_{Rad}\right)\end{array}\right] \quad \text{(A5.23)}$$

$$=\frac{dT_{\max}}{T_{\max}}\left(\xi_{T_{\max}}+\Xi\left(T_{\max}\right)\right)+\frac{dT_{\min}}{T_{\min}}\left(\xi_{T_{\min}}+\Xi\left(T_{\min}\right)\right)+\frac{dW}{W}\left(\xi_{W}+\Xi\left(W\right)\right)+\frac{dRH}{RH}\xi_{RH}+\frac{dRad}{Rad}\xi_{Rad}$$

Substituting for dET_0/ET_0 in Equation (A5.22), we obtain the third-order approximation for climate elasticity of runoff,

$$\begin{aligned}\frac{dR}{R}=&\left(\xi_{ET_0}+\Xi\left(ET_0\right)\right)\left[\frac{dT_{\max}}{T_{\max}}\left(\xi_{T_{\max}}+\Xi\left(T_{\max}\right)\right)+\frac{dT_{\min}}{T_{\min}}\left(\xi_{T_{\min}}+\Xi\left(T_{\min}\right)\right)+\right.\\ &\left.\frac{dW}{W}\left(\xi_{W}+\Xi\left(W\right)\right)+\frac{dRH}{RH}\xi_{RH}+\frac{dRad}{Rad}\xi_{Rad}\right]+\left(\xi_{P}+\Xi\left(P\right)\right)\frac{dP}{P}+\left(\xi_{\omega}+\Xi\left(\omega\right)\right)\frac{d\omega}{\omega}\end{aligned} \quad \text{(A5.24)}$$

By omitting the higher order terms, first-order approximation for climate elasticity of runoff (Yang and Yang, 2011) can be expressed as,

$$\frac{dR}{R}\approx\xi_{ET_0}\left[\xi_{T_{\max}}\frac{dT_{\max}}{T_{\max}}+\xi_{T_{\min}}\frac{dT_{\min}}{T_{\min}}+\xi_{W}\frac{dW}{W}+\xi_{RH}\frac{dRH}{RH}+\xi_{Rad}\frac{dRad}{Rad}\right]+\xi_{P}\frac{dP}{P}+\xi_{\omega}\frac{d\omega}{\omega} \quad \text{(A5.25)}$$

A5.4: Projected changes in ET_0 and its predictor climate variables visualized at the annual scale

Figures are presented showing projected future seasonal changes (with respect to historical values) for different climate variables across the Mahanadi basin. For preparing the figures, the seasons were considered as monsoon (June-September), winter (October-January), and summer (February-May). The units of relative humidity, wind speed, net solar radiation, minimum and maximum temperatures, and potential evapotranspiration are %, m/s, W/m^2, °C and mm, respectively. The changes are determined using the ensemble mean of climate variables obtained from GCMs.

The increase projected for future precipitation in the monsoon season is more in the area adjoining the coastline than in interior parts of the basin (Figure A5.2). Contrarily, the increase in precipitation is more in the interior parts of the basin than in the area adjoining the coastline in the winter season (Figure A5.3). On the other hand, for the summer season, an increase in precipitation for the interior parts of the basin and a decrease in the same for the area adjoining the coastline is projected (Figure

A5.4). Projected future changes (with respect to historical) for PET indicate (i) a considerable increase for the monsoon season, with the magnitude of increment increasing from the south-east to north-west part of the basin (Figure A5.5), (ii) a marginal drop in projected PET for the winter season, with the magnitude of the drop increasing from south-east to north-west part of the basin (Figure A5.6), and (iii) drop over the lower part of the basin and increase over the upper part in summer season (Figure A5.7). The change in the overall basin average for the projected change in PET for summer does not appear substantial. An increase in maximum temperature is projected over a major part of the basin in all seasons, except for a small area near the coastline (Figures A5.8 to A5.10).

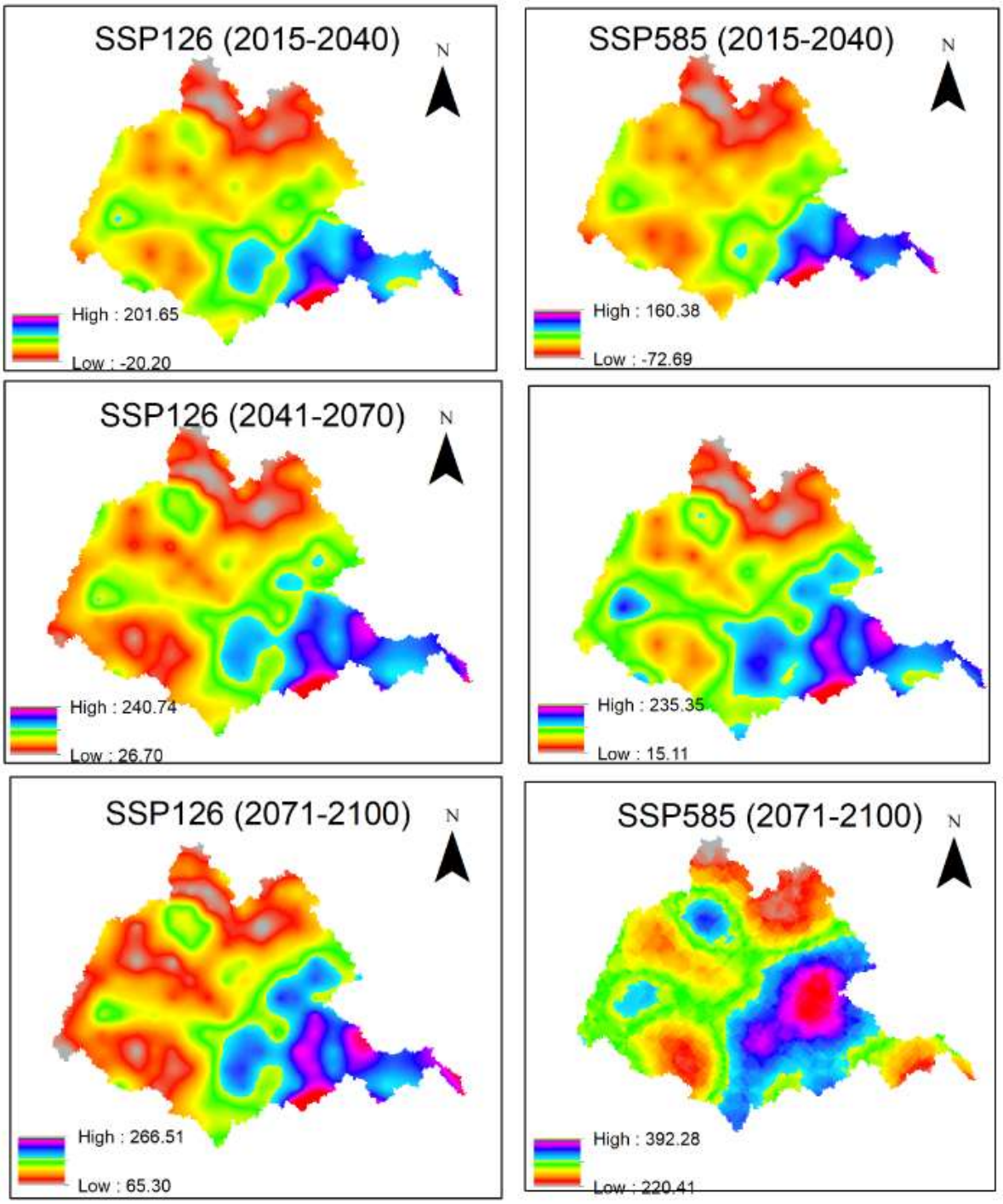

Figure A5.2: Projected future changes (with respect to historical) for precipitation (mm) across the Mahanadi basin in the monsoon season (June-September). An increase in precipitation is more in the area adjoining the coastline than in interior parts of the basin.

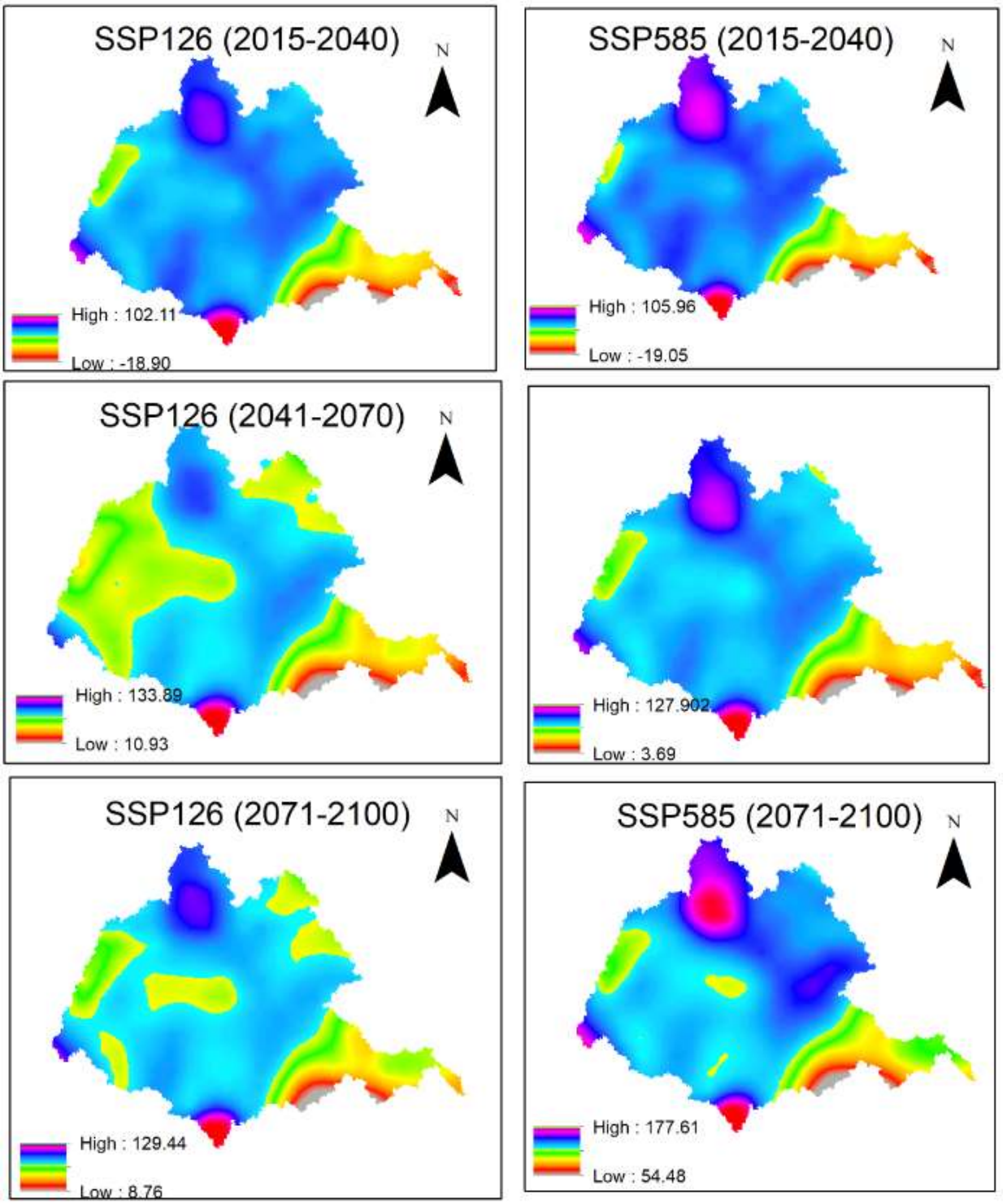

Figure A5.3: Projected future changes (with respect to historical) for precipitation (mm) across the Mahanadi basin in the winter season (considered as October to January). An increase in precipitation is more in the interior parts of the basin than the area adjoining the coastline (where it is projected to drop marginally in the near-future window 2015-2040).

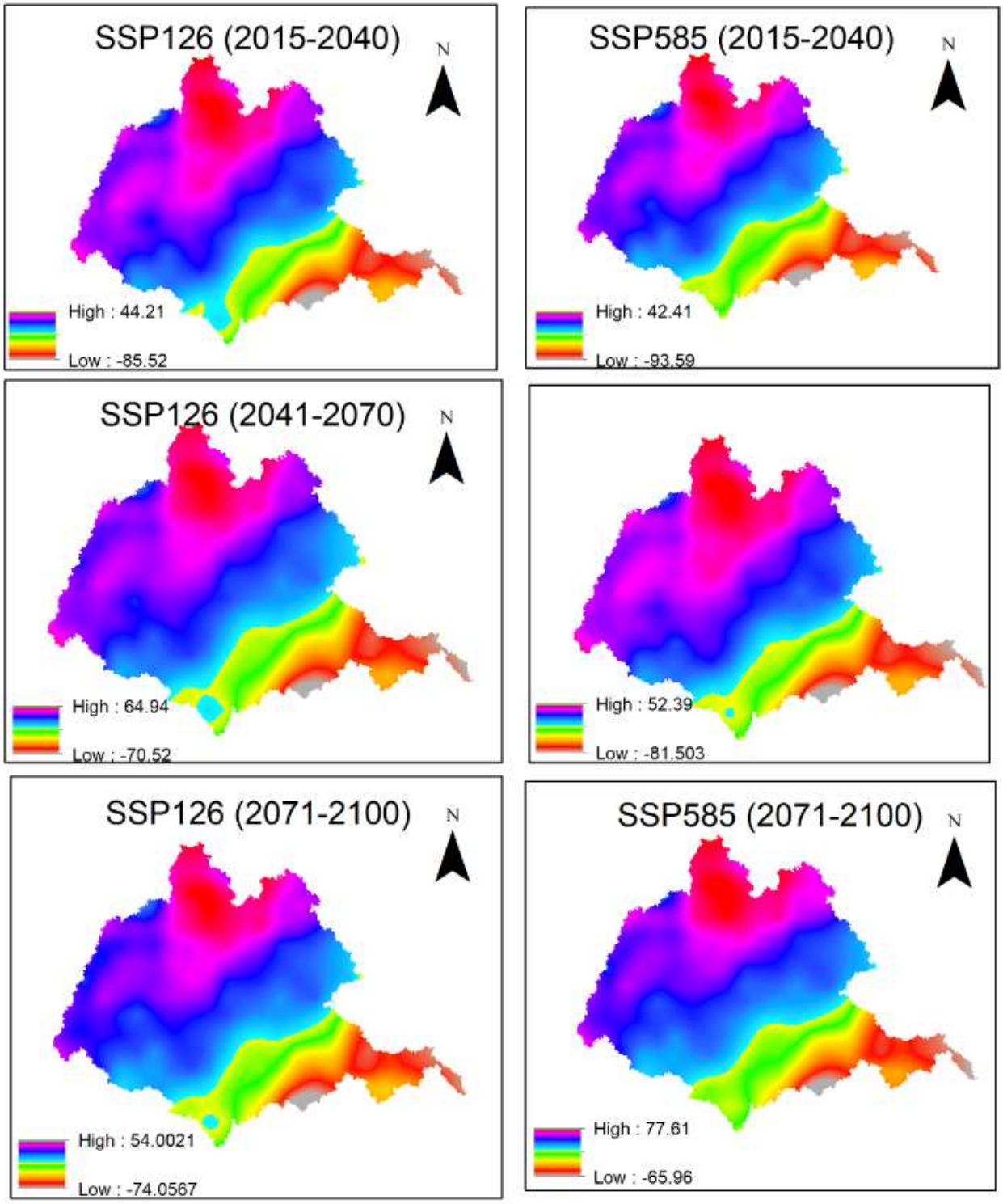

Figure A5.4: Projected future changes (with respect to historical) for precipitation (mm) across the Mahanadi basin in the summer season (considered as February to May). An increase in precipitation for the interior parts of the basin and a decrease in the same for the area adjoining the coastline is projected.

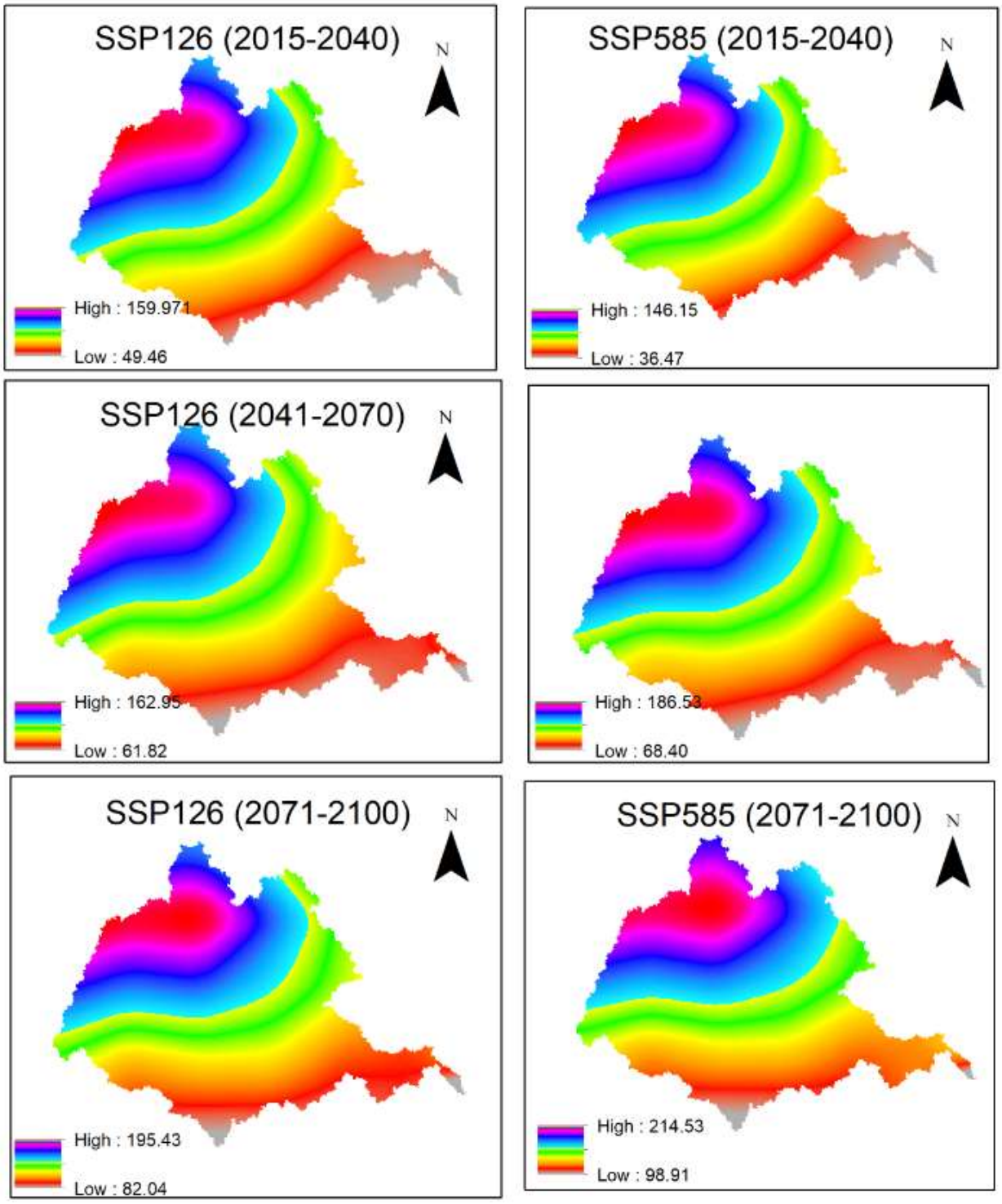

Figure A5.5: Projected future changes (with respect to historical) for PET (mm) over the Mahanadi basin in the monsoon season (June-September). There is an increase in projected PET, with the magnitude of the increment (i) increasing from the southeast to the northwest part of the basin and (ii) being higher for the SSP585 scenario.

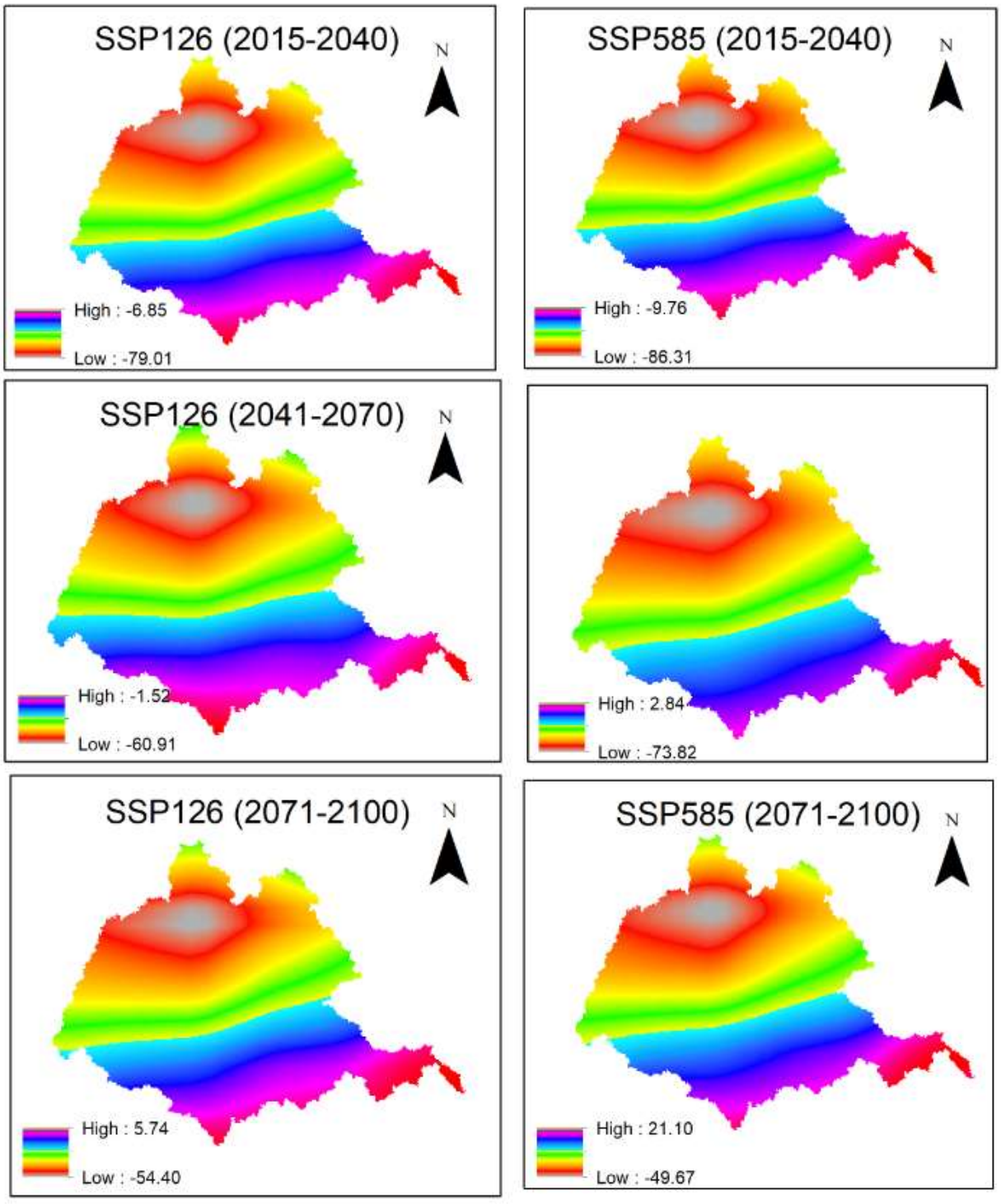

Figure A5.6: Projected future changes for PET (mm) over the Mahanadi basin in the winter season (considered as October to January). There is a drop in the projected PET, with the magnitude of the drop increasing from the southeast to the northwest part of the basin.

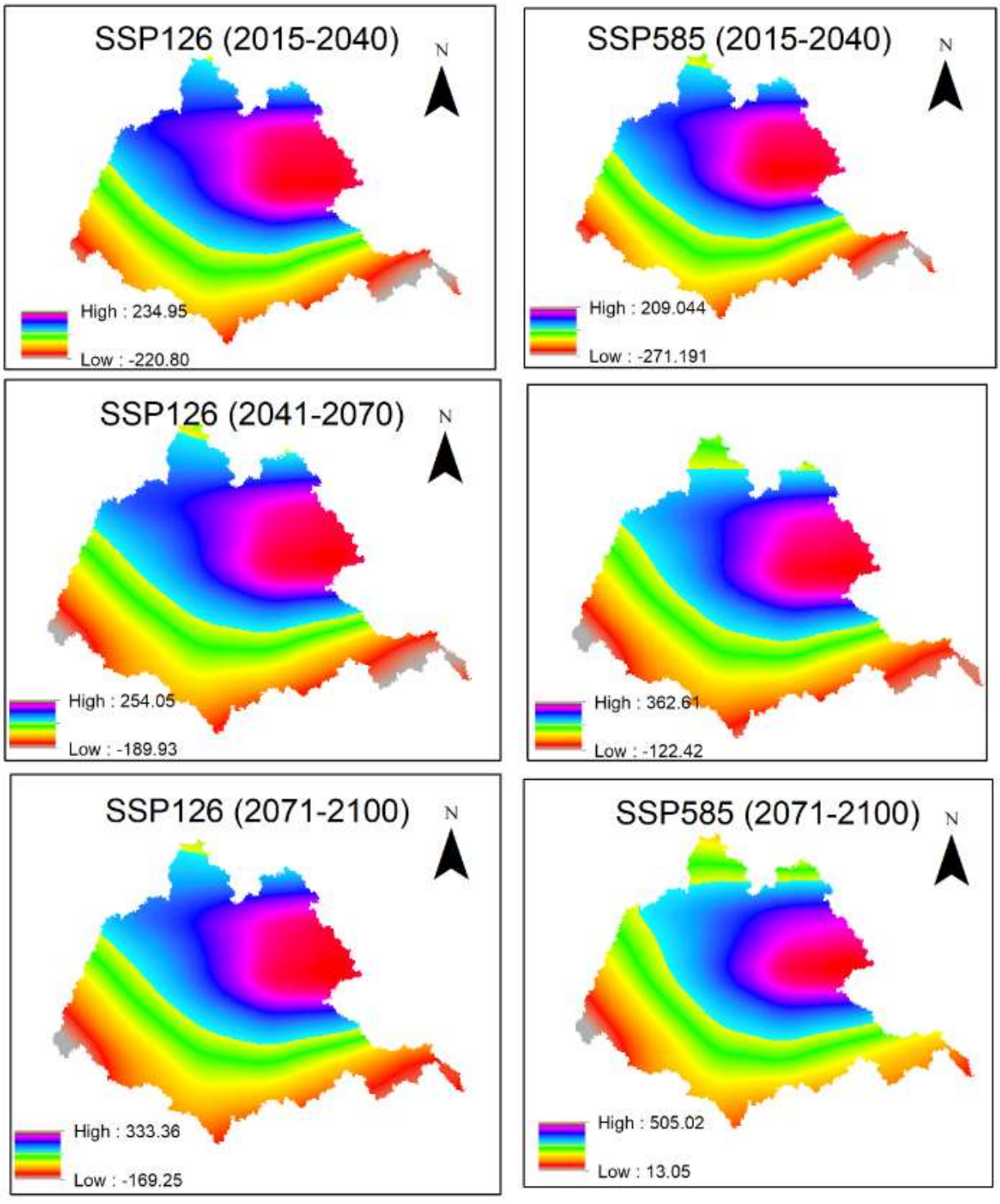

Figure A5.7: Projected future changes for PET (mm) over the Mahanadi basin in the summer season (considered as February to May). A drop in PET over the lower part of the basin and an increase in the PET over the upper part of the basin are witnessed. Overall, the basin average for the projected change in PET does not appear substantial (with respect to the historical period).

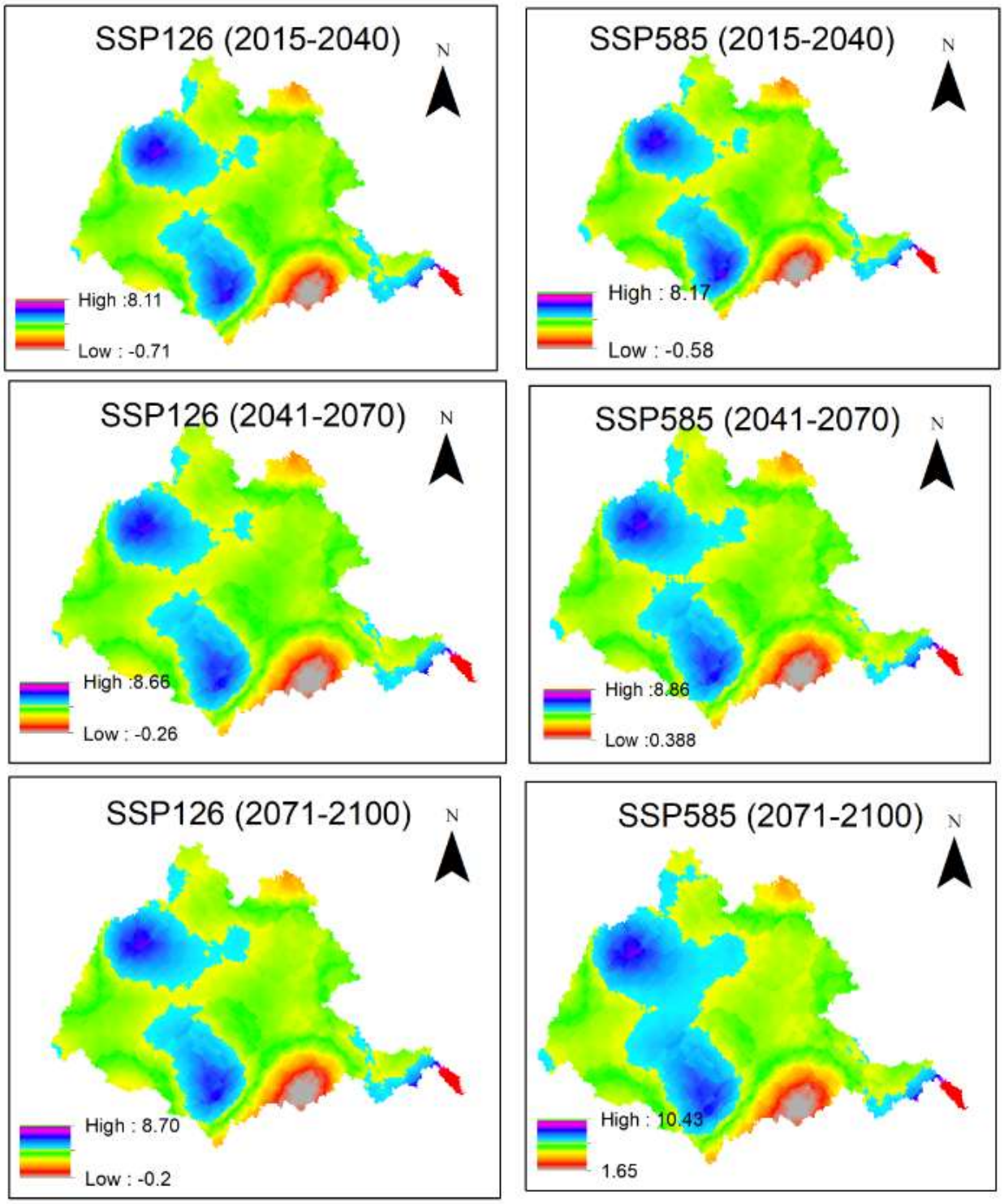

Figure A5.8: Projected future changes for maximum temperature over the Mahanadi basin in the monsoon season (June-September). An increase in maximum temperature can be noted over a major part of the basin. The increase is higher for the SSP585 scenario than the SSP126 scenario.

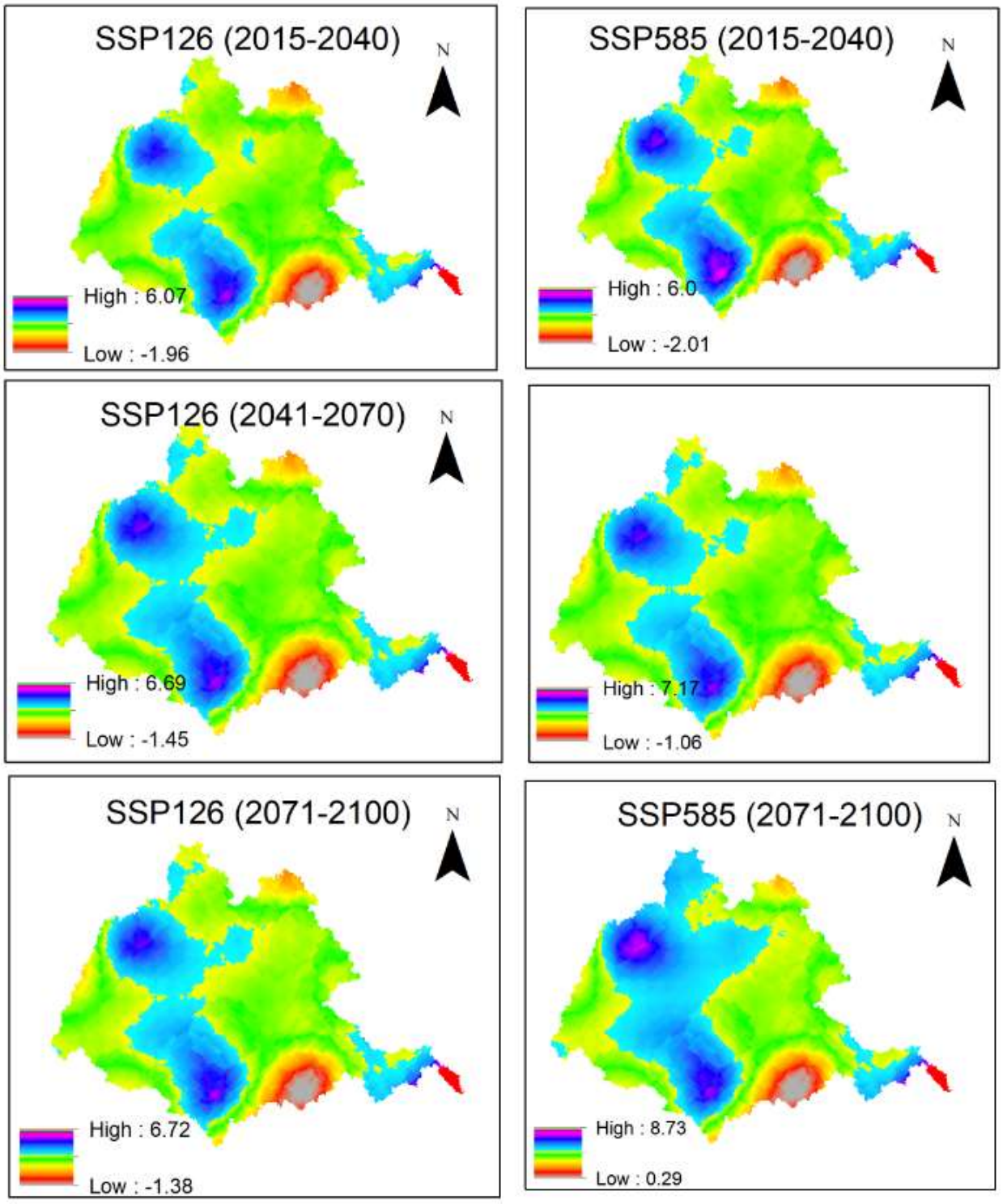

Figure A5.9: Projected future changes for maximum temperature over the Mahanadi basin in the winter season (considered as October to January). An increase in maximum temperature is evident over a major part of the basin. The increase is higher for the SSP585 scenario than the SSP126 scenario (except for the near future window, where the difference is marginal).

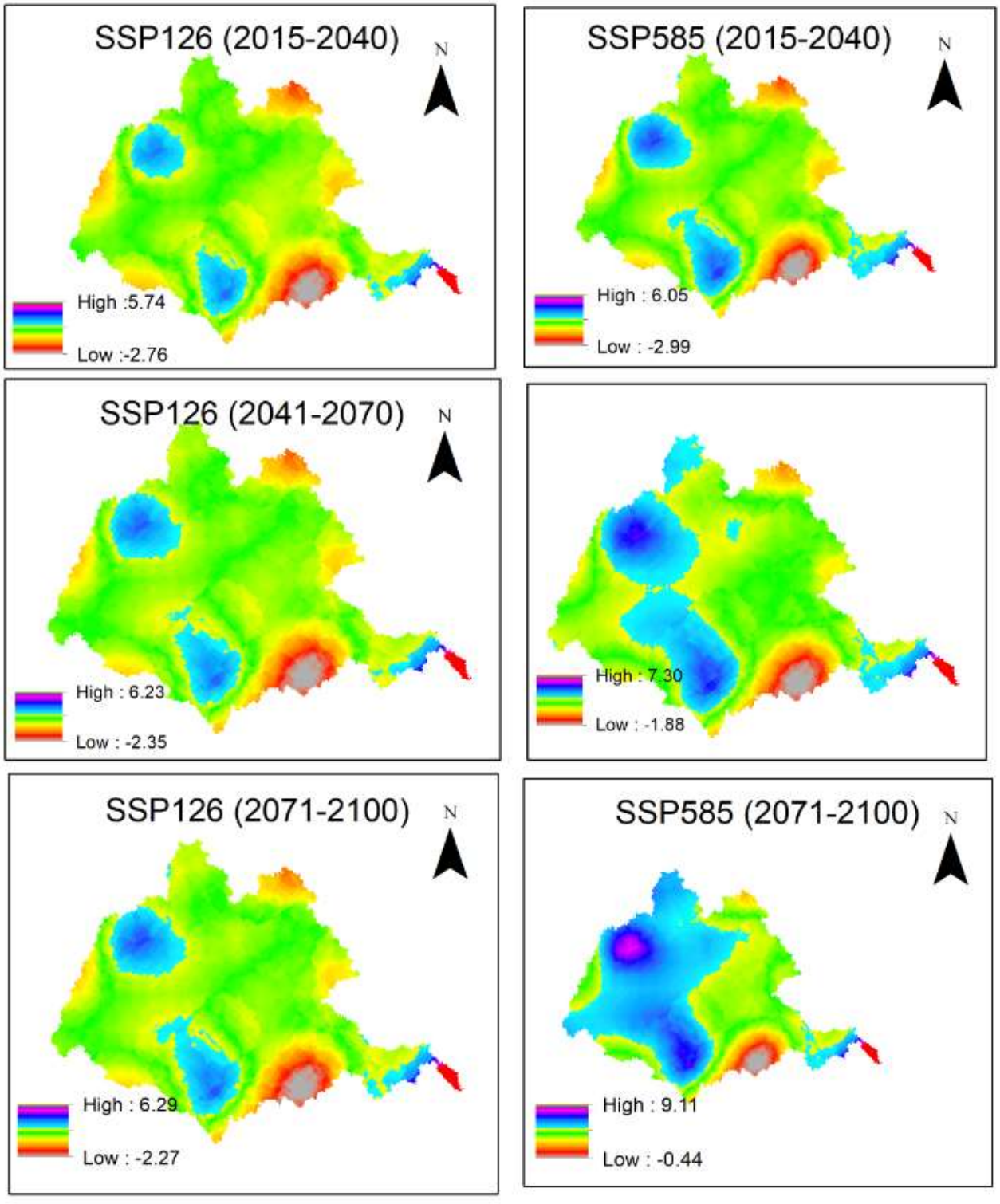

Figure A5.10: Projected future changes for maximum temperature over the Mahanadi basin in the summer season (February to May). An increase in maximum temperature can be noted over a major part of the basin. In general, the increase is higher for the SSP585 scenario than the SSP126 scenario.

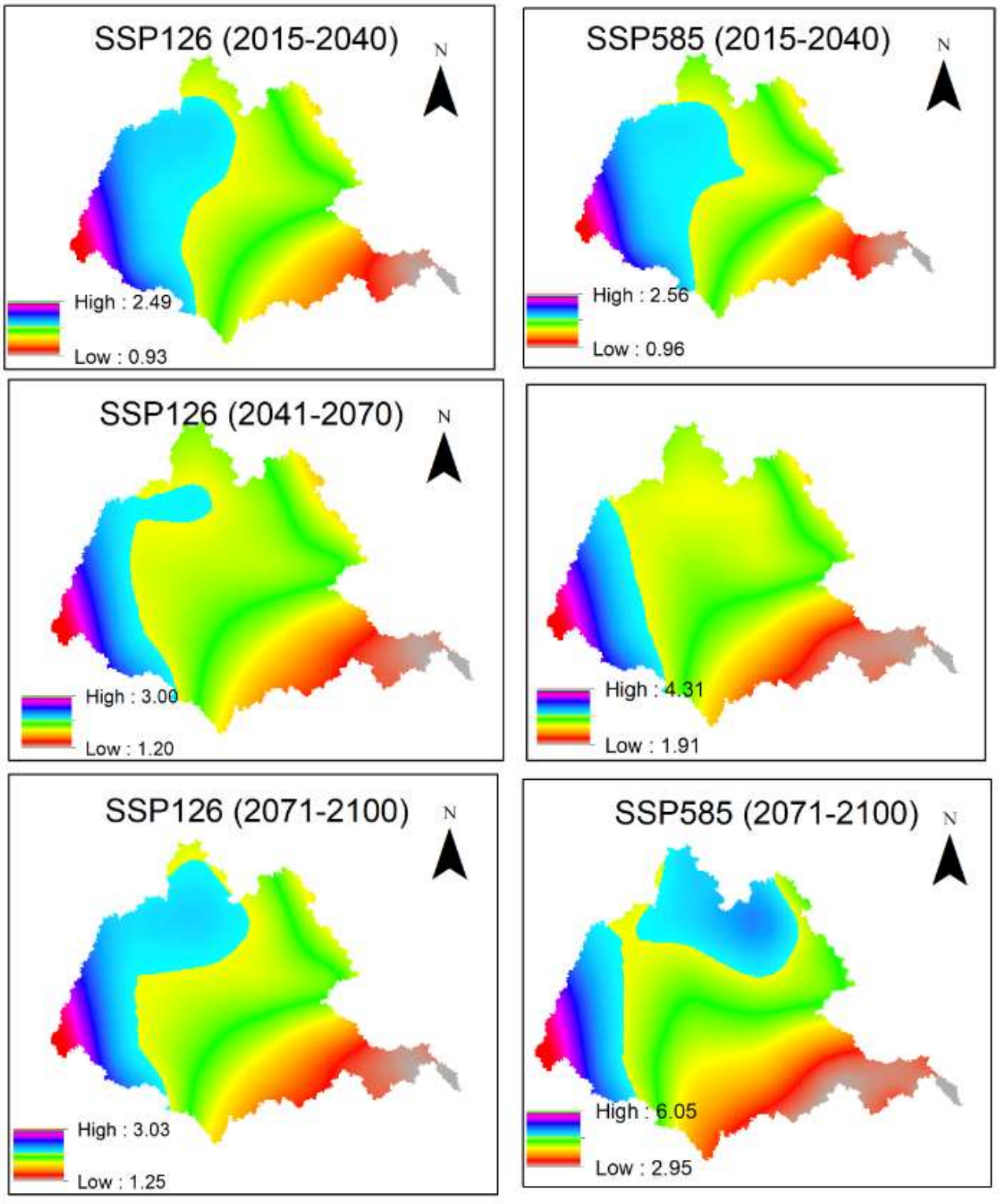

Figure A5.11: Increase projected for future monsoon (June-September) minimum temperature (°C) over the Mahanadi basin. The increase is higher for the SSP585 scenario than the SSP126 scenario.

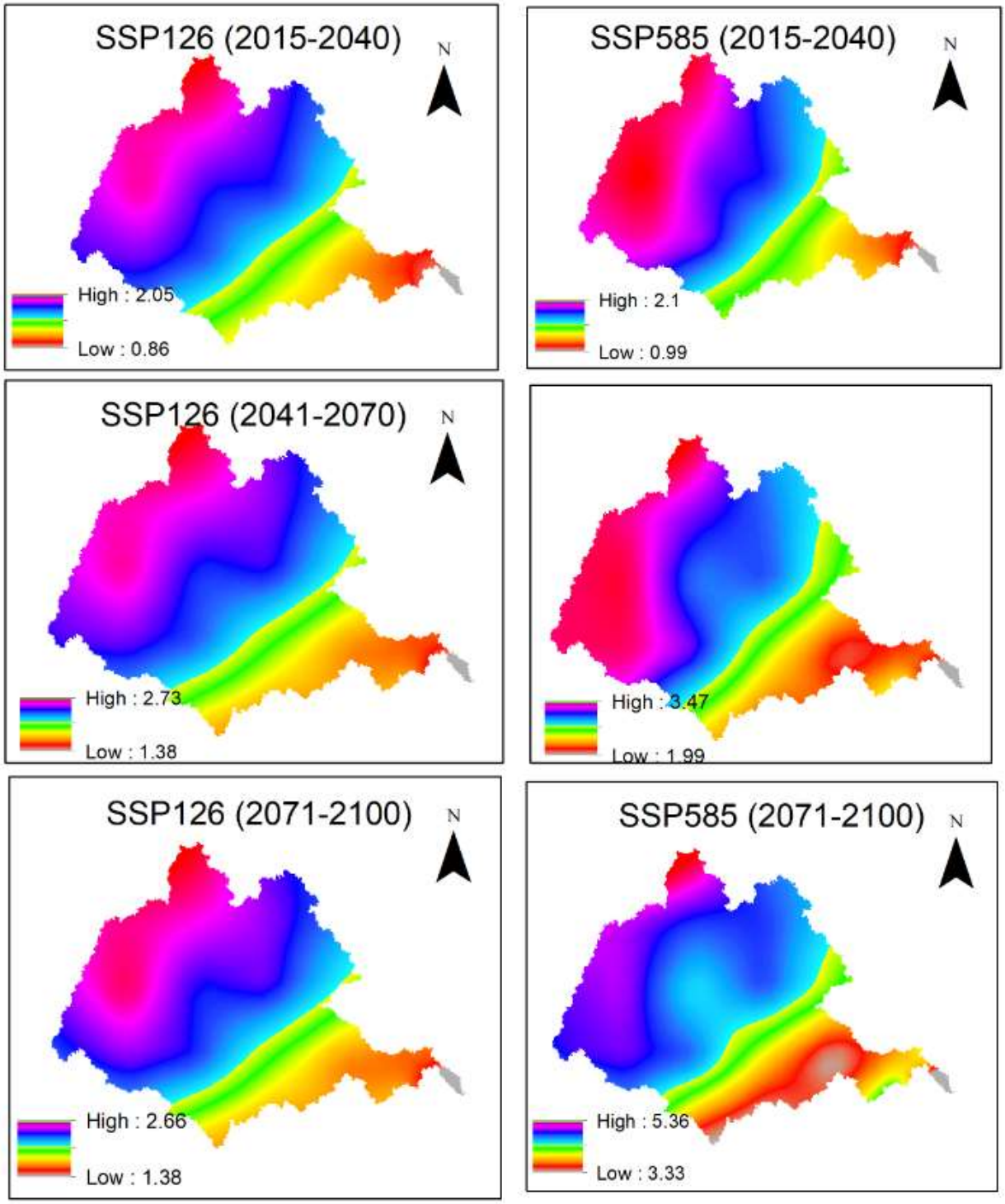

Figure A5.12: Increase projected for future winter (October to January) minimum temperature (°C) over the Mahanadi basin. The increase is higher for the SSP585 scenario than the SSP126 scenario.

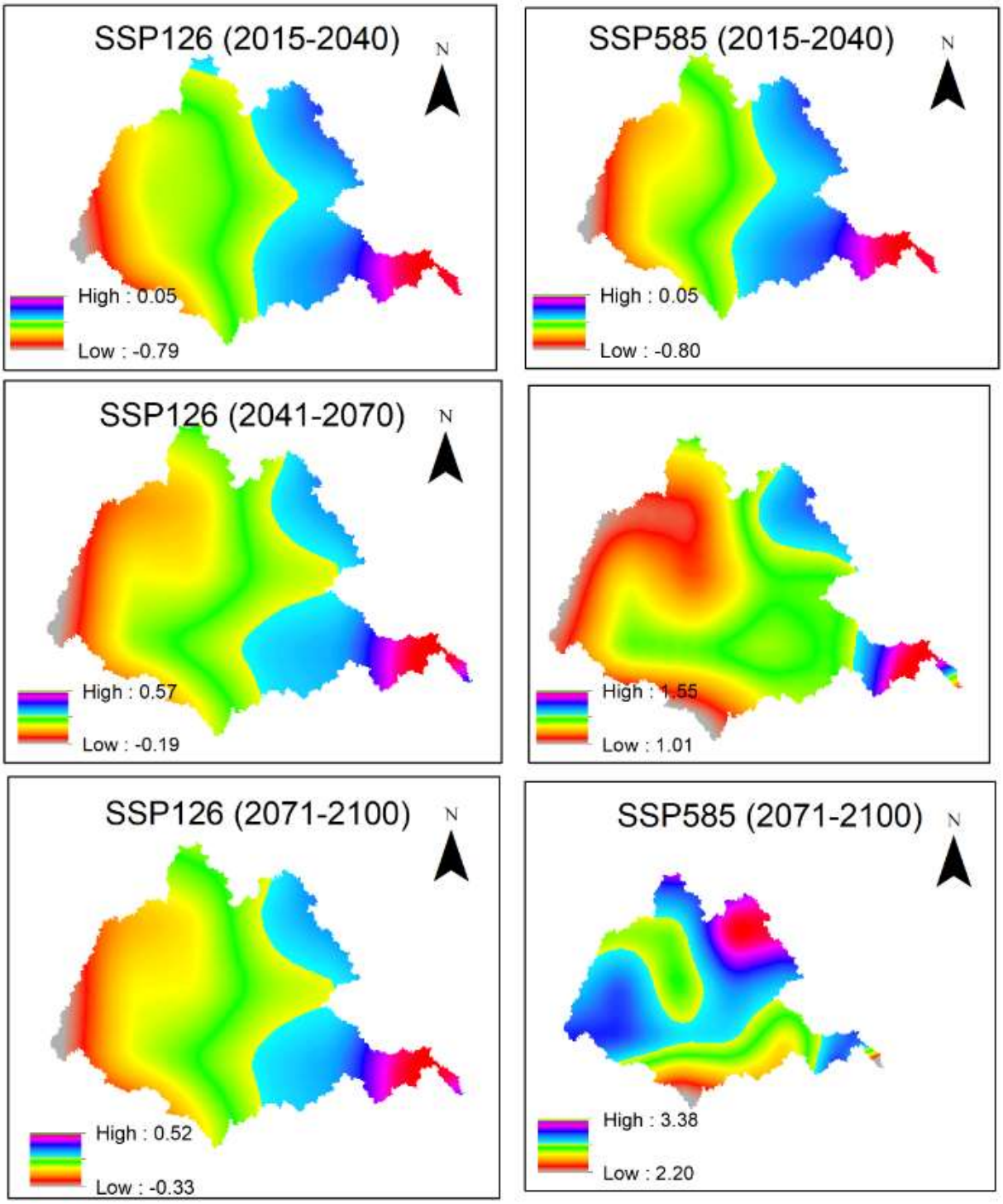

Figure A5.13: Projected future changes in minimum temperature (°C) over the Mahanadi basin for the summer season (considered as February to May). The minimum temperature is projected to (i) drop over the left part of the basin and increase over the right part of the basin for the SSP 126 scenario during 2015-2100 and for SSP585 during 2015-2040, and (ii) increase over the entire basin for SSP 585 scenario). The increase is higher for the SSP585 scenario than for the SSP126 scenario (except for the near future window, where the changes are small).

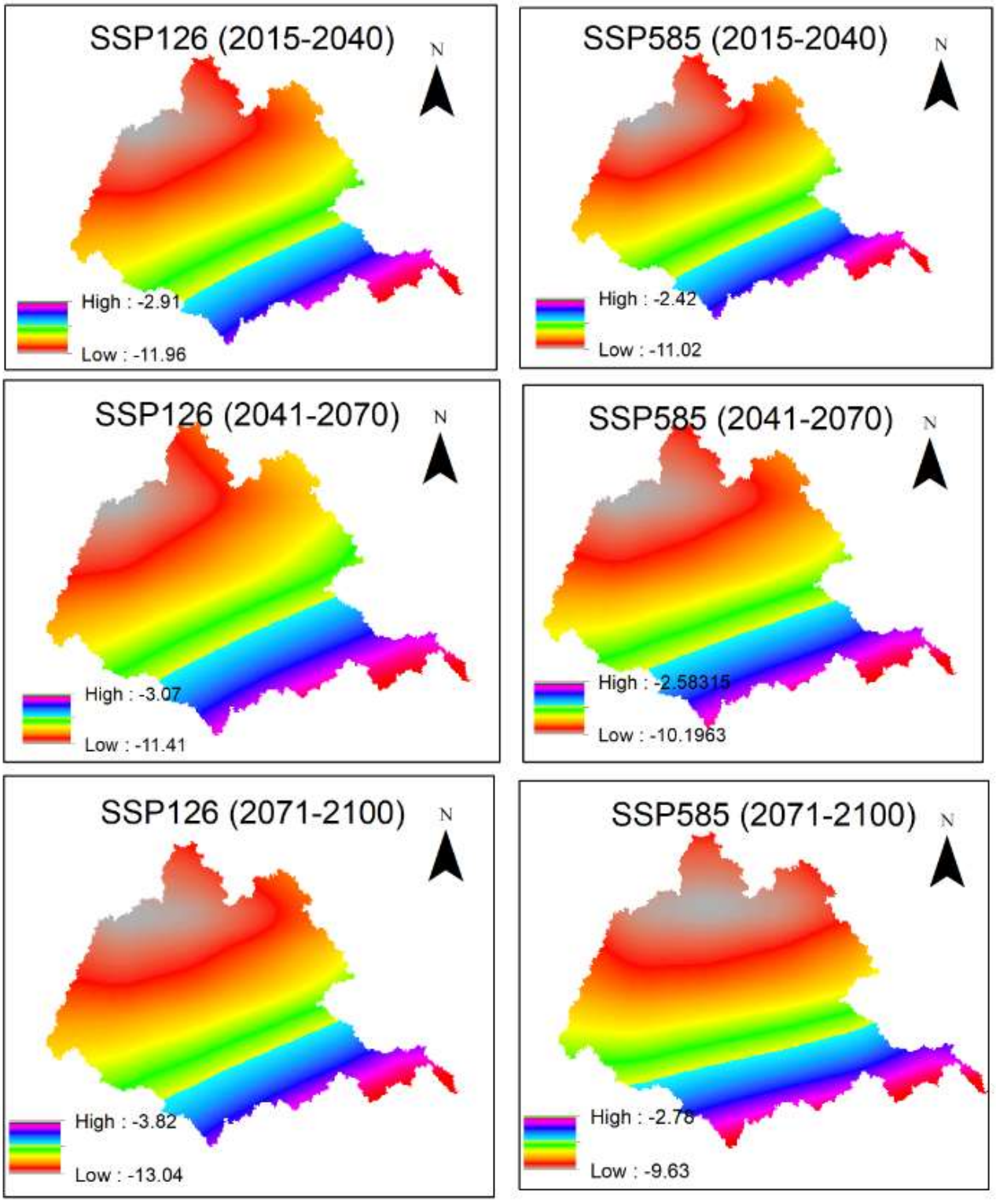

Figure A5.14: Projected future changes in humidity (%) over the Mahanadi basin for the monsoon season (June-September). There is a drop in humidity, and a higher drop is evident for the SSP126 scenario than the SSP585 scenario.

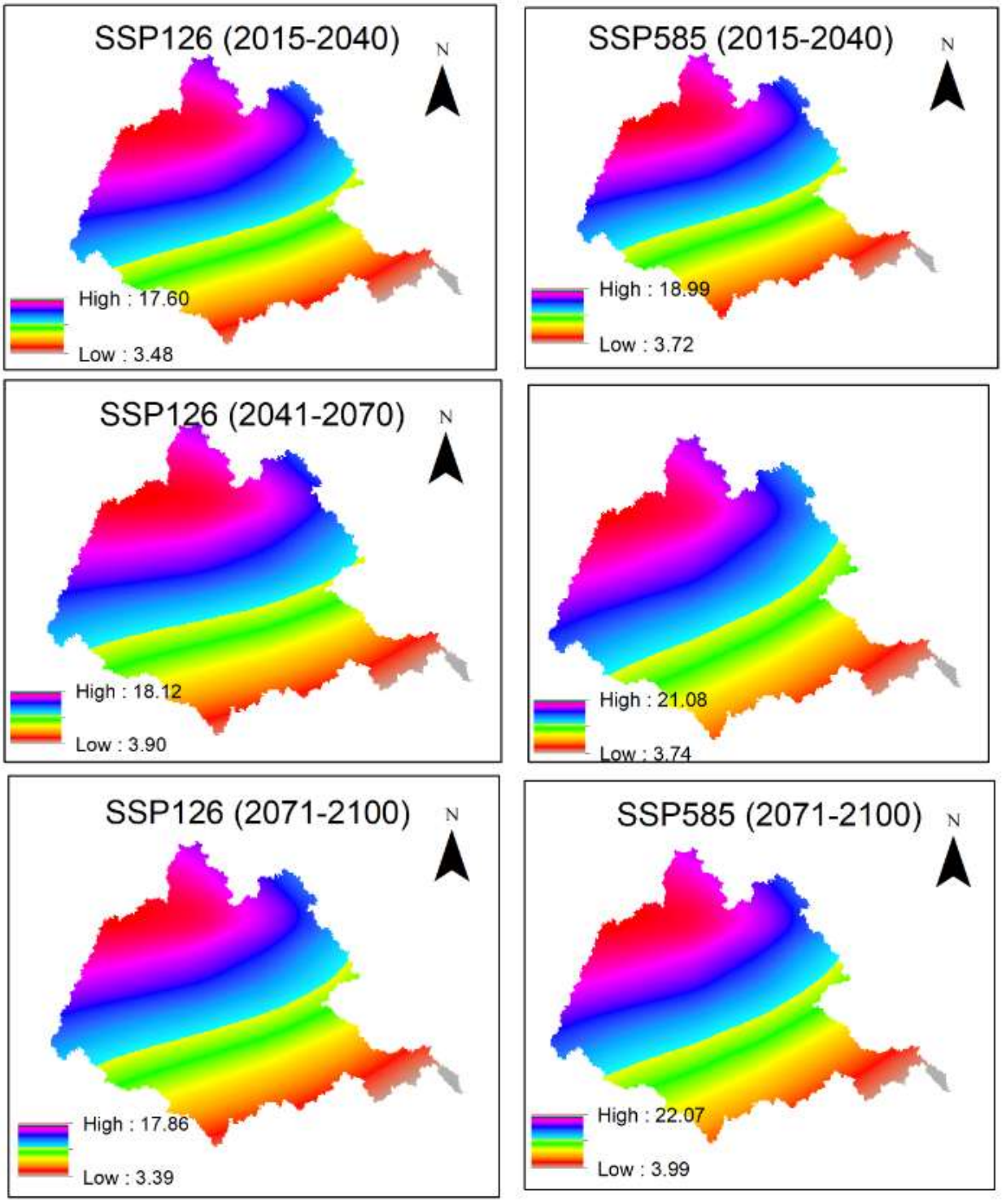

Figure A5.15: Projected future changes in humidity (%) over the Mahanadi basin for the winter season (considered as October to January). There is an increase in humidity, and a higher increment is primarily evident for the SSP585 scenario.

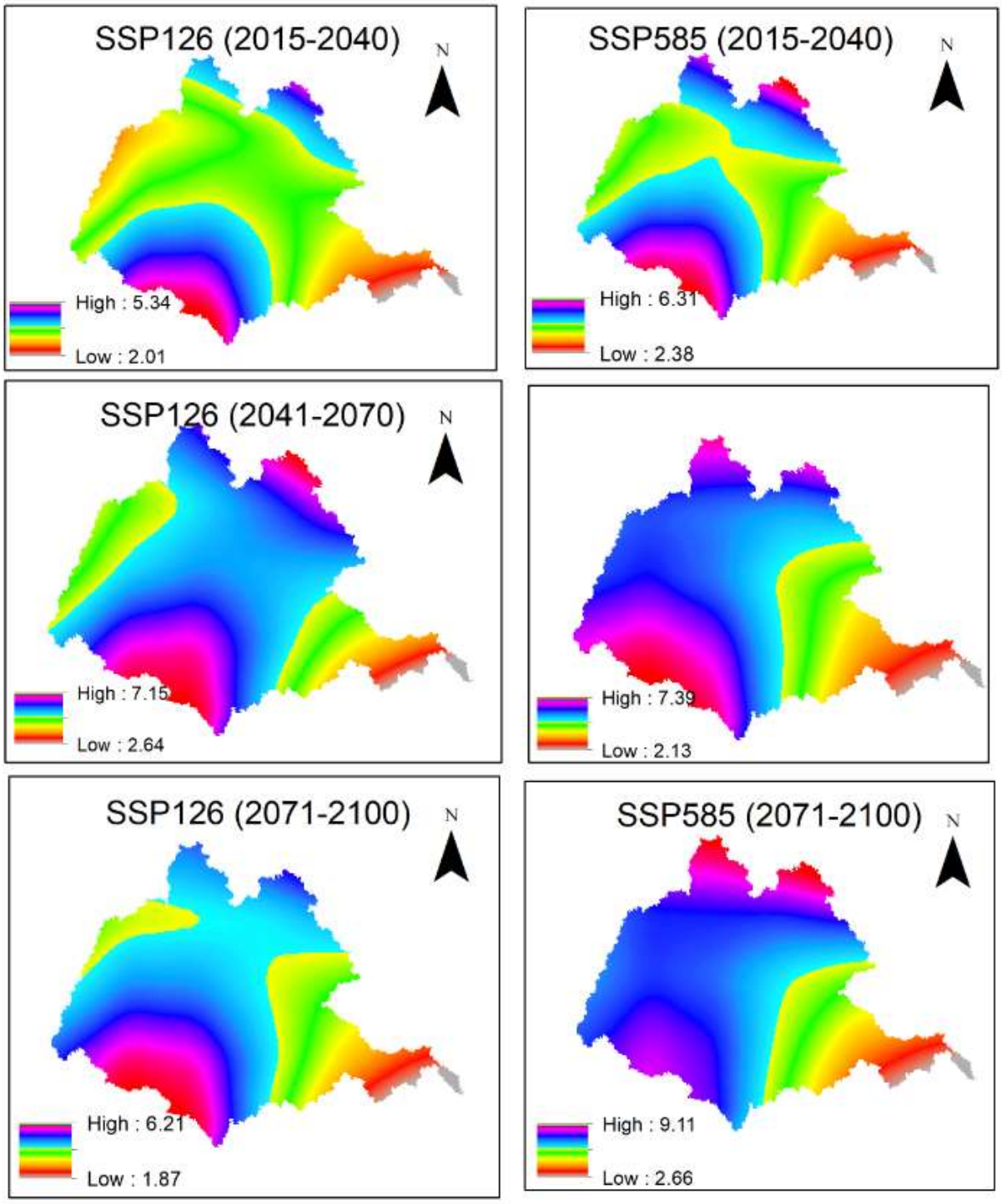

Figure A5.16: Projected future changes in humidity (%) over the Mahanadi basin for the summer season (considered as February to May). There is an increase in humidity, and a higher increment is primarily evident for the SSP585 scenario.

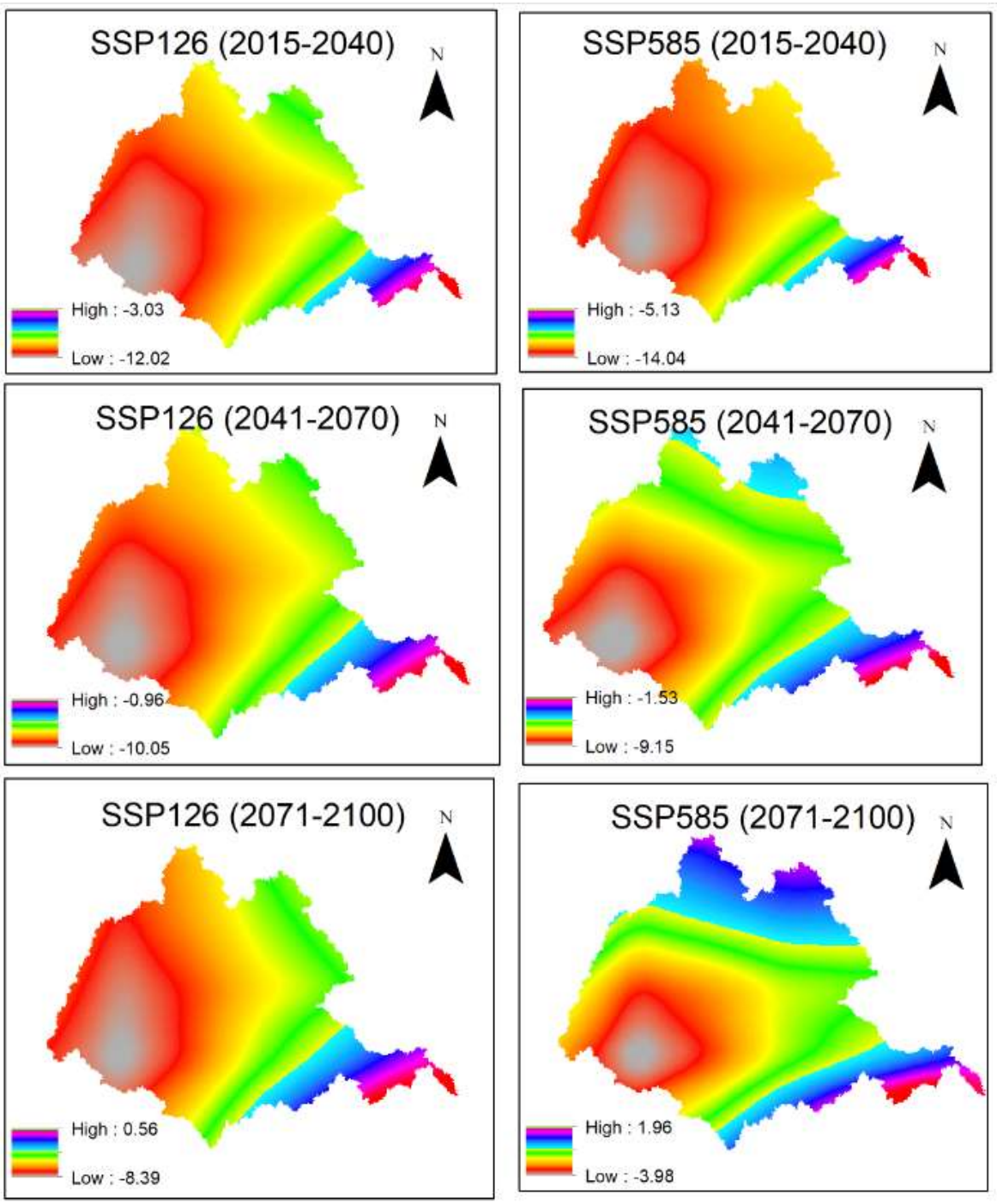

Figure A5.17: Projected future changes in net solar radiation (W/m^2) over the Mahanadi basin for the monsoon season (June-September). Overall, a drop in net solar radiation is projected for the entire basin up to 2070 and for a major part of the basin in the far future (2071-2100).

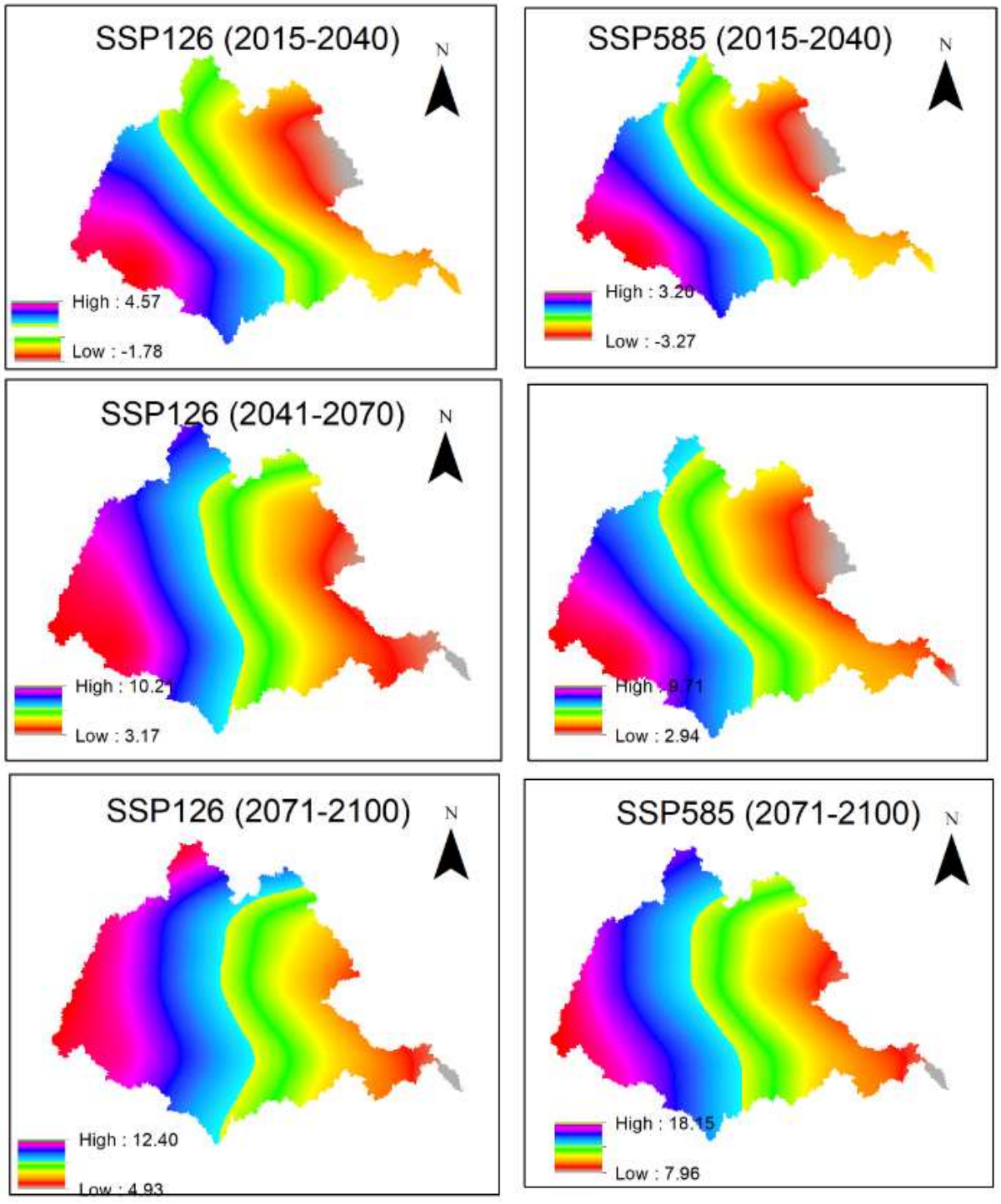

Figure A5.18: Projected future changes in net solar radiation (W/m^2) over the Mahanadi basin for the winter season (considered as October to January). There is an increase projected for the entire basin over the period 2041-2100. An increase in the left part of the basin and a drop in the right part is projected for the near-future period (2015-2040).

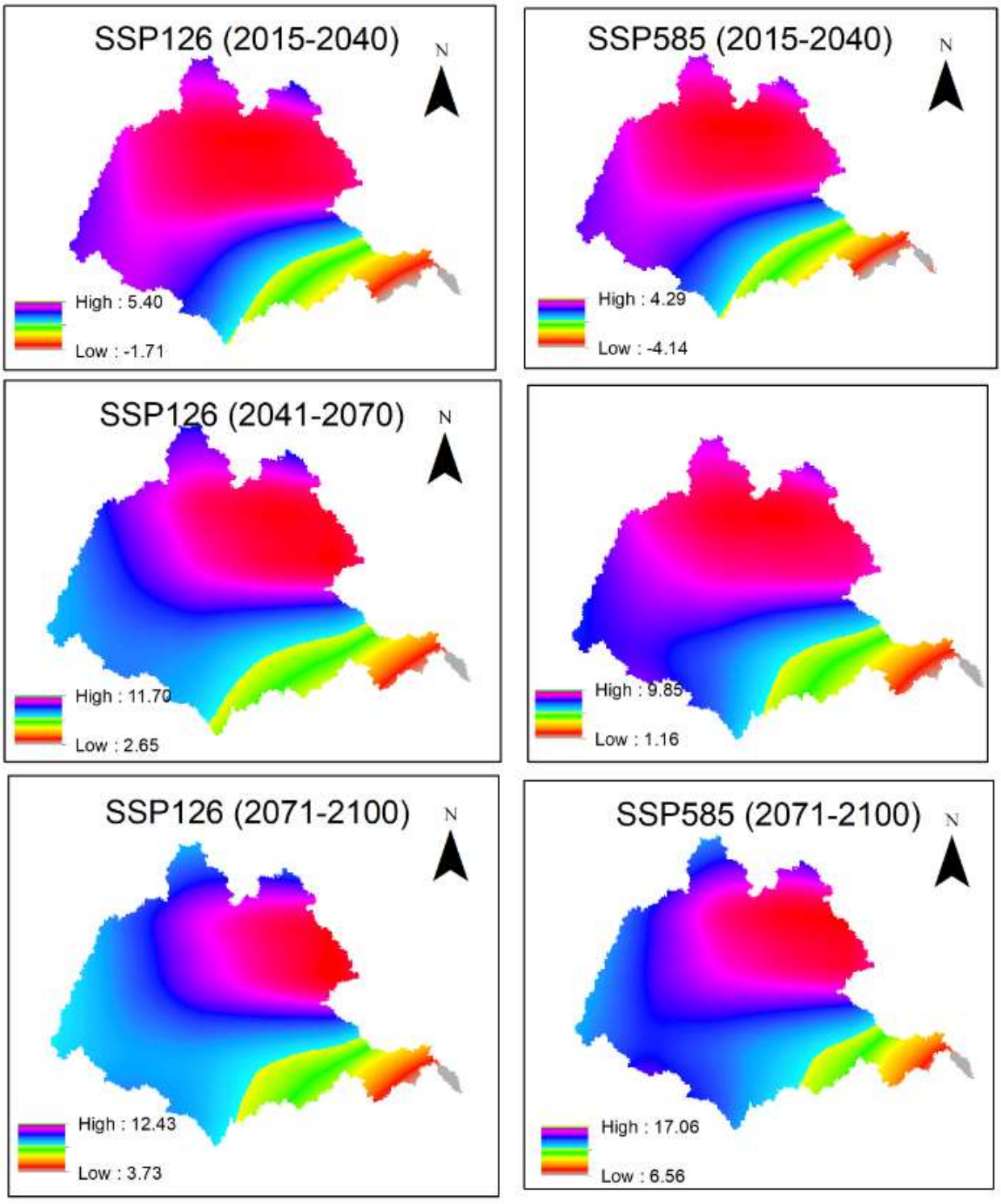

Figure A5.19: Projected future changes in net solar radiation (W/m^2) over the Mahanadi basin for the summer season (considered as February to May). There is an increase projected for (i) the entire basin over the period 2041-2100, and (ii) a major part of the basin for the near-future period (2015-2040), except areas adjoining the coastline.

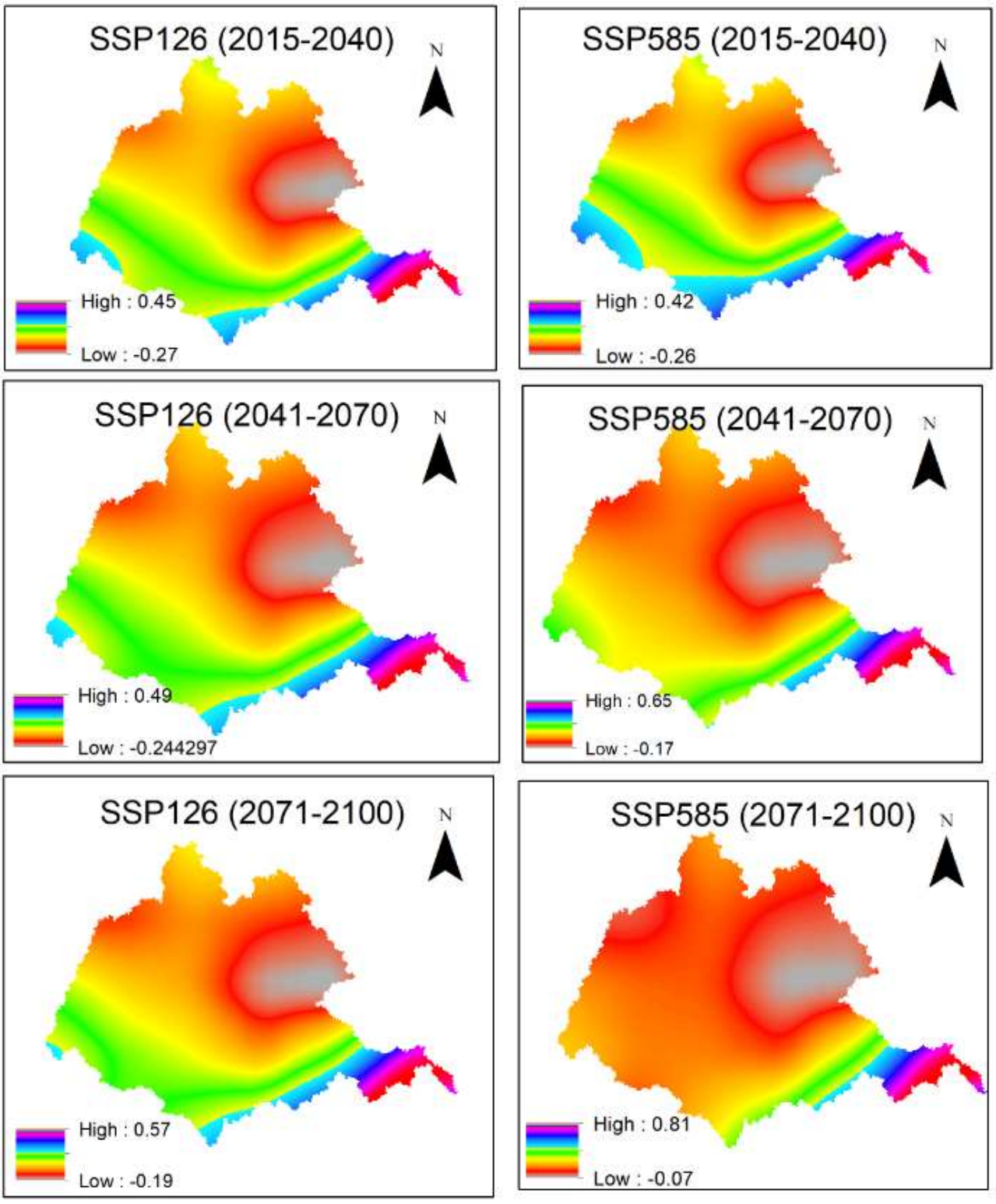

Figure A5.20: Projected future changes in wind speed (m/s) over the Mahanadi basin for the monsoon season (June-September). There is a decrease in wind speed projections over a major part of the basin.

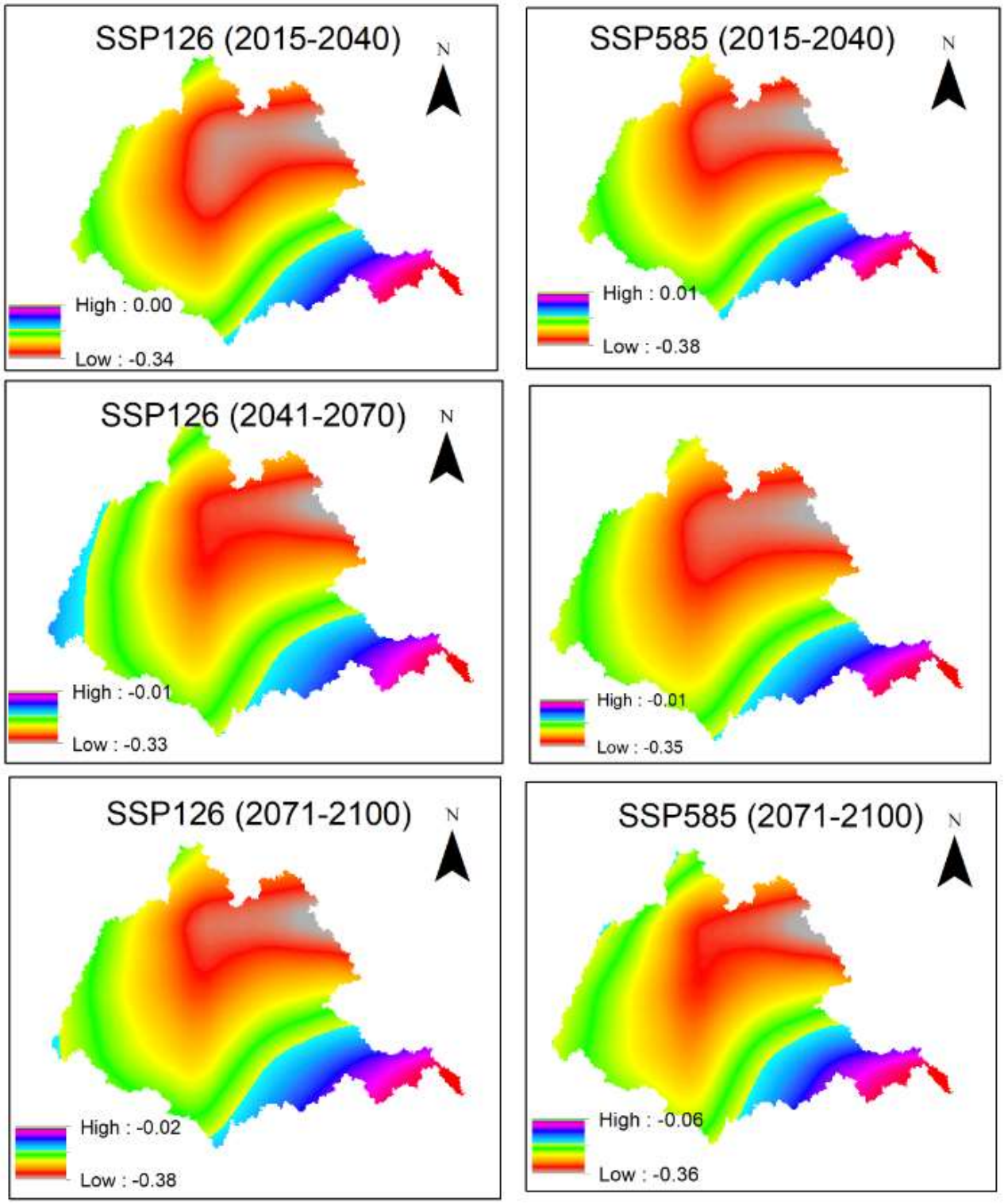

Figure A5.21: Projected future changes in wind speed (m/s) over the Mahanadi basin for the winter season (October to January). There is a decrease in wind speed projections over (i) a major part of the basin in the near future (2015-2040) and (ii) the entire basin over the period 2041-2100.

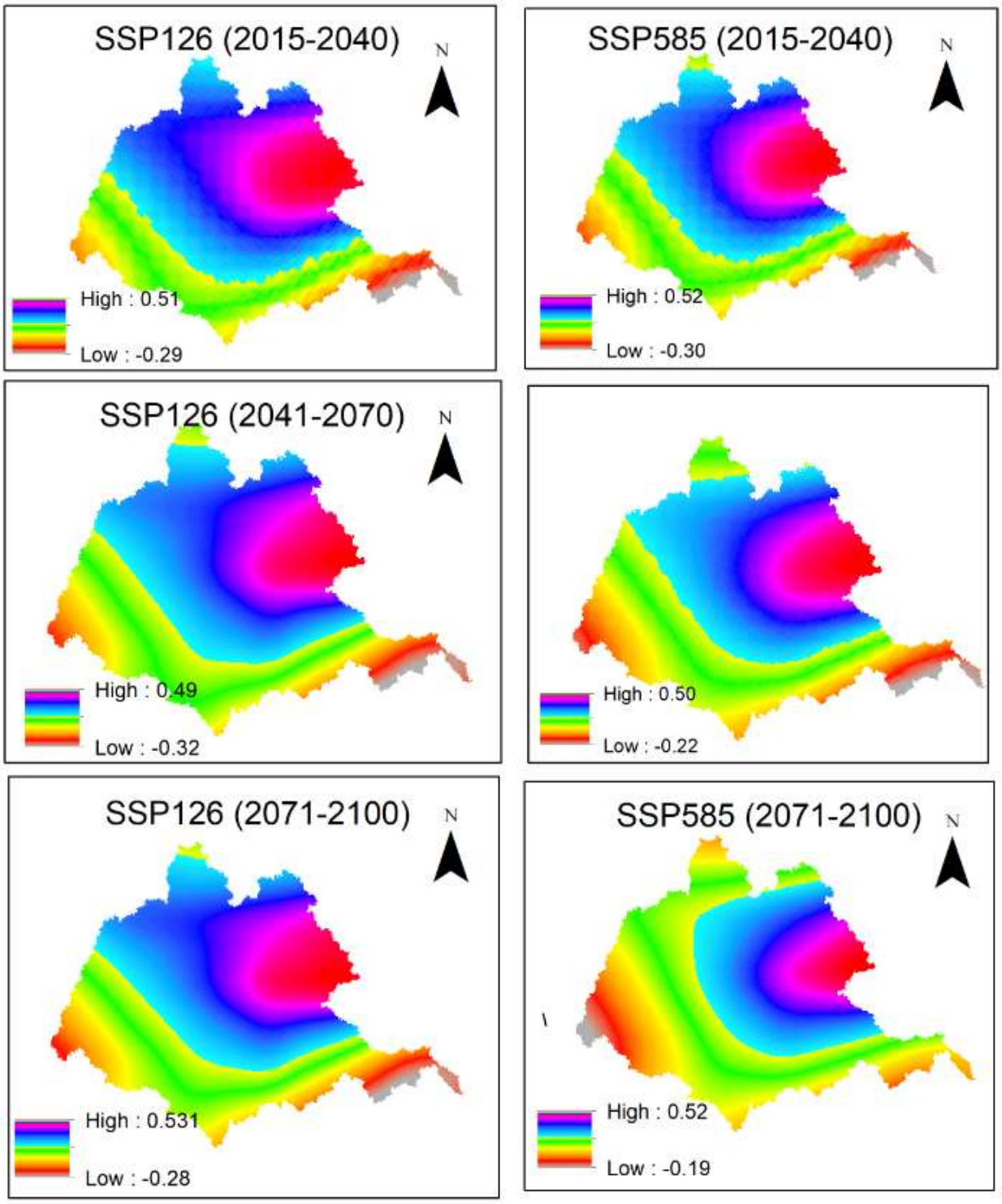

Figure A5.22: Projected future changes in wind speed (m/s) over the Mahanadi basin for the summer season (considered as February to May).

Section 6

Identification of hydrological extremes based on the baseline data

Mahanadi basin is frequently prone to floods. Major floods were witnessed in 1855, 1933, 1937, 1955, 1980, 1982, 2001, 2003, 2006, 2008, 2011, and 2013 (e.g., Parhi et al., 2012; Jena et al., 2014; Odisha State Disaster Management Authority, OSDMA) causing substantial loss to life, property, agricultural crops, and health hazard. The frequency of the worst observed floods is projected to rise under the projected future climate (Pandey et al., 2022), and this is attributed to an increase in extreme rainfall in the middle reaches of the basin (Jena et al., 2014). Approaches that are commonly used for statistical analysis of hydrological extremes could be broadly classified as those based on (i) Annual Maximum Series (AMS) or Block Maxima (BM), and (ii) Partial Duration Series (PDS) or Peaks Over Threshold (POT) series. The AMS approach involves the extraction of annual maxima (i.e., block-maxima) values from the available records, whereas the PDS approach considers values exceeding a predetermined high threshold.

An unresolved problem in statistical analysis of hydrological extremes (e.g., storms, floods) using the POT model is the identification of optimal threshold. There are various issues affecting the performance of different methods available for threshold selection (TS). A novel Mahalanobis distance-based automatic TS method (MDM) has been developed to overcome those issues. The method involves the use of a proposed transformation to map the Generalized Pareto distributed random variable (depicting peaks over tentative thresholds) from the original space to the standard exponential distributed random variable in a non-dimensional space. The optimal threshold is identified as that which minimizes Mahalanobis distance between *L*-moments of the transformed random variable and those of the population (i.e., standard exponential distribution) in the non-dimensional space. A variant of the proposed method based on analytical formulations is referred to as MDM-A, whereas that based on Monte Carlo simulations (MCS) is referred to as MDM-M. The effectiveness of the variants is demonstrated over four existing automatic TS methods through Monte-Carlo simulation experiments and case studies over rainfall and streamflow datasets chosen from India (including the Mahanadi basin) and elsewhere in the world. The four automatic TS methods include (i) a recent *L*-moment ratio diagram based method (LMM; Lomba,

& Alves, 2020), whose potential is unexplored in hydrology, and (ii) three based on goodness of fit (GoF) test statistics based methods namely Anderson-Darling GoF test-based method (ADM; Choulakian & Stephens, 2001, Solari et al., 2017), and two Hill-assumption based methods namely Jackson kernel method (JKM) and Lewis kernel method (LKM) (Goegebeur et al., 2008).

Investigations were carried out to gain insight into the properties and effectiveness of the four TS methods, which is scanty in the literature. Results indicate that there is inconsistency in the performance of GoF test-based methods across datasets exhibiting fat and thin tail behaviour, owing to their theoretical assumptions and uncertainty associated with the sampling distribution of test statistics. Issues affecting the performance of the *L*-moment ratio diagram-based TS method are also identified. The proposed method (MDM) overcomes those issues and appears promising for hydrologic applications. Cumulative distribution functions (CDFs) of peak flows (also called growth curves) that show quantile estimates corresponding to various return periods were constructed for extreme rainfall and floods at various stations. The curves prepared for floods at Basantpur station are shown in Figure 6.1, for brevity.

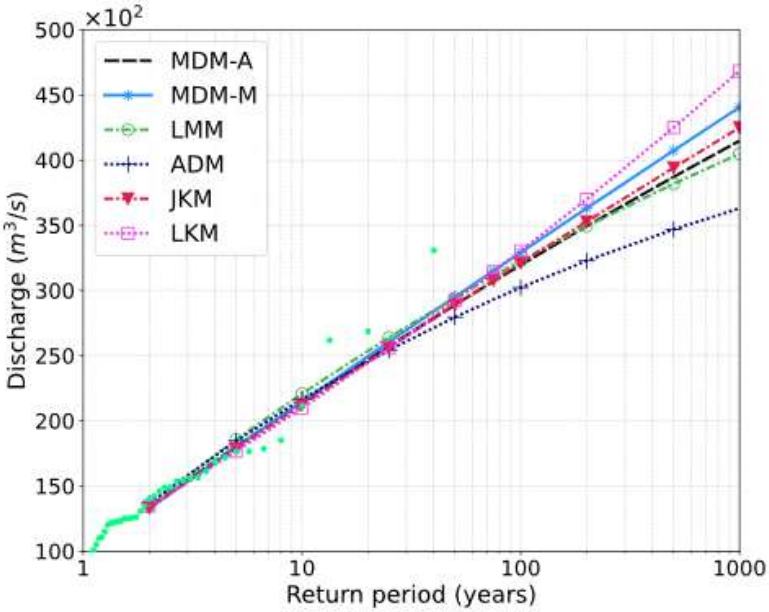

Figure 6.1: Growth (quantile) curves prepared based on analysis with different threshold selection methods, which show quantile estimates corresponding to various return periods for floods at Basantpur station on the Mahanadi river in India. Green dots show the empirical return periods of the observed data.

It can be noted from Figure 6.1 that the curve depicting JKM has a marginal difference with respect to curves corresponding to MDM-A, MDM-M, and LMM in the case of the Basantpur station, whereas ADM yielded lower quantile estimates for higher return periods. Finer details on the contributed method can be found in Kiran and Srinivas (2021a).

CDFs of peak flows are constructed for each streamflow gauging site considered in the Mahanadi basin based on analysis with AMS and PDS. The PDS is extracted corresponding to each site by identifying the optimal threshold for the site using the Mahalanobis distance-based analytical threshold selection method (MDM-A, Kiran & Srinivas 2021a). In analysis with PDS, GPD was considered as the at-site frequency distribution to fit the peak flows. On the other hand, in analysis with AMS, appropriate frequency distributions were identified using the *L*-moment-based goodness-of-fit (GOF) test (Hosking and Wallis, 1997), considering a 90% confidence level. Among generalized logistic (GLO), generalized extreme value (GEV), Gumbel (Extreme Value Type-1), generalized Pareto (GPA), generalized normal (GNO), and Pearson type III (PE3) distributions, the one for which GOF measure was sufficiently close to zero was selected for quantile estimation. Practitioners consider five parameter Wakeby distribution when none of the aforementioned distributions is found appropriate. Details of the best-fit distribution selected for the sites considered in the Mahanadi basin are provided in Table 6.1, and the constructed CDFs are presented in Figure 6.2. It can be noted that the best-fit frequency distributions differ across the sites in analysis with AMS (Table 6.1), and the quantile estimates determined in analysis with AMS and PDS differ across different return periods (Figure 6.2). For the majority of sites, PDS-based flood quantile estimates are marginally higher for lower return periods (T<10 years) and considerably lower for higher return periods when compared to the corresponding estimates determined in analysis with AMS. The PDS-based estimates are consistently higher than AMS-based estimates across all return periods for Jondhra, Kotni, and Rajim sites. Thus, at the majority of sites, the design of civil infrastructure (e.g., bridges) based on PDS analysis is likely to be economical. Several studies (Cunnane, 1973, Wang, 1991, Madsen et al., 1997, Caires, 2009) have shown through Monte Carlo simulations and real-world applications that the PDS approach is more effective in using information from the available records and variance of quantile estimates based on PDS approach is smaller than that based on AMS approach. The constructed CDFs find use in univariate risk analysis of civil infrastructure nearby the sites considered in the Mahanadi basin.

Table 6.1: The best-fit frequency distributions identified in analysis with AMS and PDS for fitting peak flows at the sites considered in the Mahanadi basin and details of their estimated parameters.

Stations	Selected Distribution (AMS)	Parameters			Selected Distribution (PDS)	Parameters		
		Location	Scale	Shape		Threshold	Scale	Shape
Andhiyarkore	GLO	259.29	96.84	-0.30	GPA	42.77	111.33	-0.15
Bamnidihi	PE3	3195.65	2625.73	1.81	GPA	1671.54	1942.52	-0.03
Baronda	PE3	2165.16	2133.78	1.88	GPA	1941.42	3548.00	0.64
Basantpur	GLO	12695.21	3358.93	-0.12	GPA	9116.00	5364.99	0.04
Ghatora	GLO	515.34	198.65	-0.37	GPA	190.00	258.56	-0.19
Jondhra	GLO	4680.87	1215.70	-0.20	GPA	3737.27	1752.95	-0.07
Kantamal	PE3	8458.08	5214.95	0.22	GPA	10885.00	2337.80	-0.07
Kesinga	PE3	7056.59	5798.72	1.54	GPA	8143.00	5430.94	0.11
Kotni	Gumbel	1420.96	1055.20	NA	GPA	1713.00	1158.98	0.00
Kurubhata	PE3	1494.28	505.69	-0.56	GPA	1909.77	130.73	0.15
Manendragarh	GNO	218.38	169.74	-1.33	GPA	49.15	80.38	-0.43
Pathardhi	GNO	1014.30	482.54	-0.05	GPA	373.56	835.39	0.45
Rajim	PE3	3693.10	3052.64	0.98	GPA	401.40	1683.44	-0.20
Rampur	PE3	1927.37	1589.36	1.65	GPA	370.08	1024.67	-0.07
Salebhata	GLO	1932.00	887.69	-0.36	GPA	576.00	1136.29	-0.20
Seorinarayan	PE3	10845.75	5570.89	-0.01	GPA	7188.00	6255.20	0.31
Simga	Gumbel	3370.72	2046.37	NA	GPA	1972.05	2806.95	0.16
Sundargarh	GEV	1396.19	634.86	-0.47	GPA	2000.30	1819.98	-0.09
Tikarapara	GEV	19205.06	8369.39	0.44	GPA	11000.00	14864.65	0.59
Pandigaon	GEV	1856.23	1407.73	0.44	GPA	647.50	1517.67	0.28
Sukma	PE3	793.81	733.58	1.62	GPA	264.36	425.72	-0.16

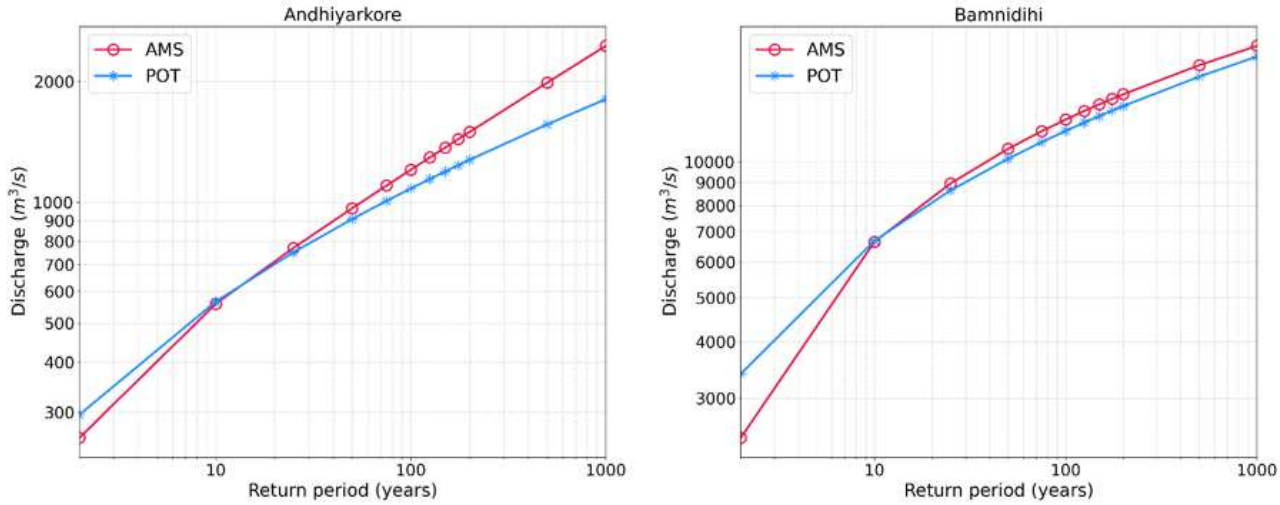

Figure 6.2: Growth (quantile) curves constructed for CWC gauging sites in the Mahanadi basin in analysis with AMS and PDS.

Figure 6.2 (continued…)

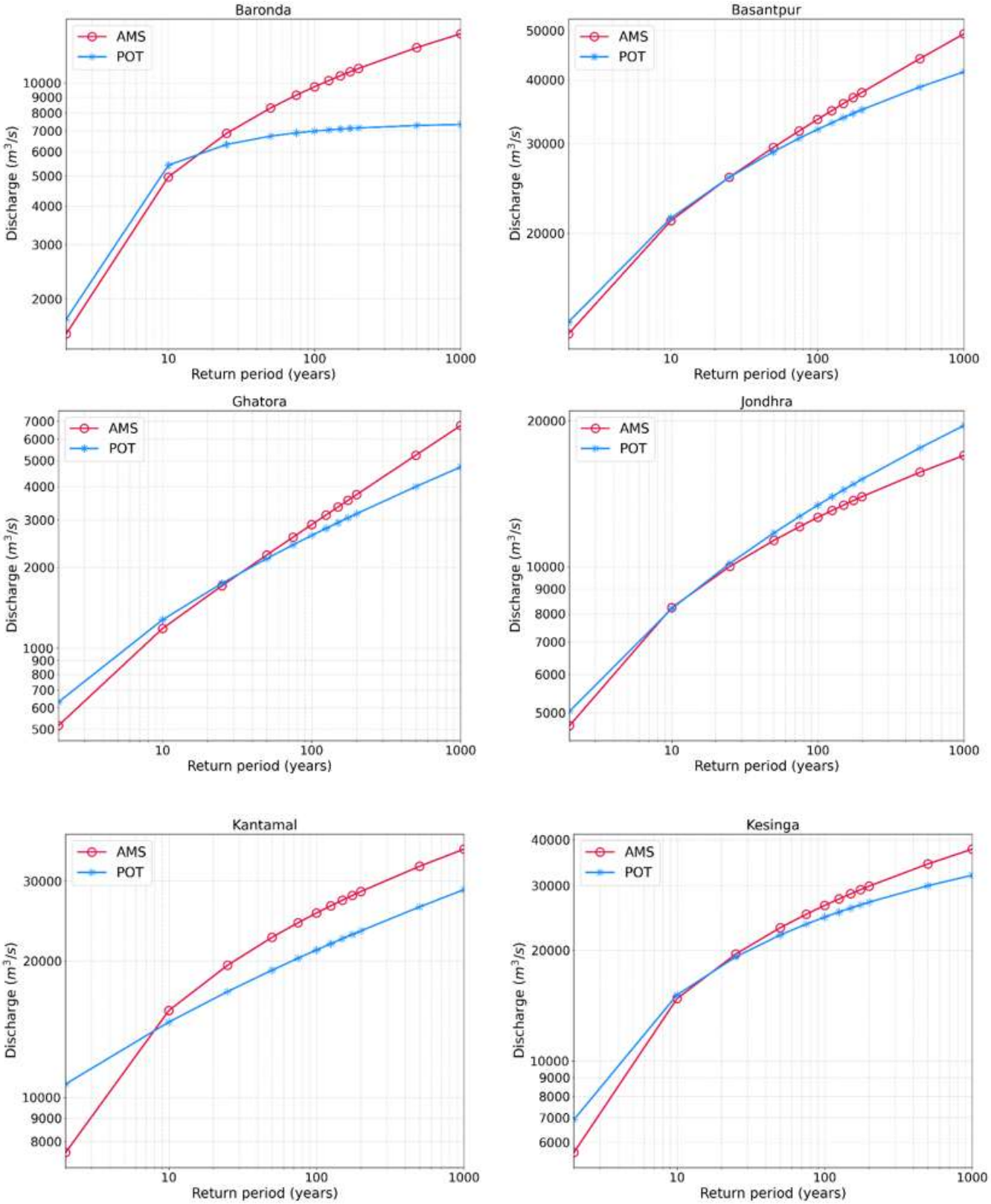

Figure 6.2 (continued…)

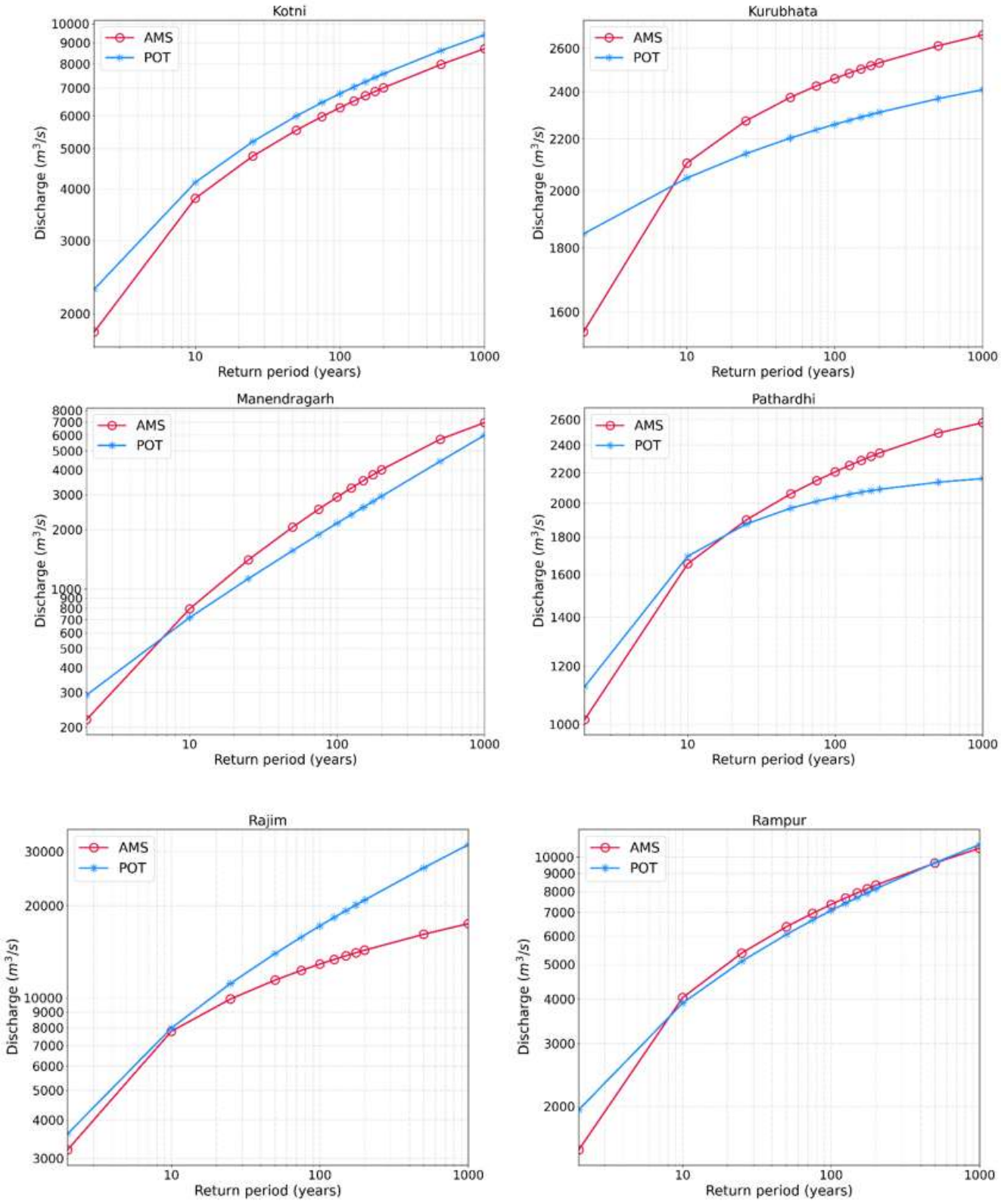

Figure 6.2 (continued…)

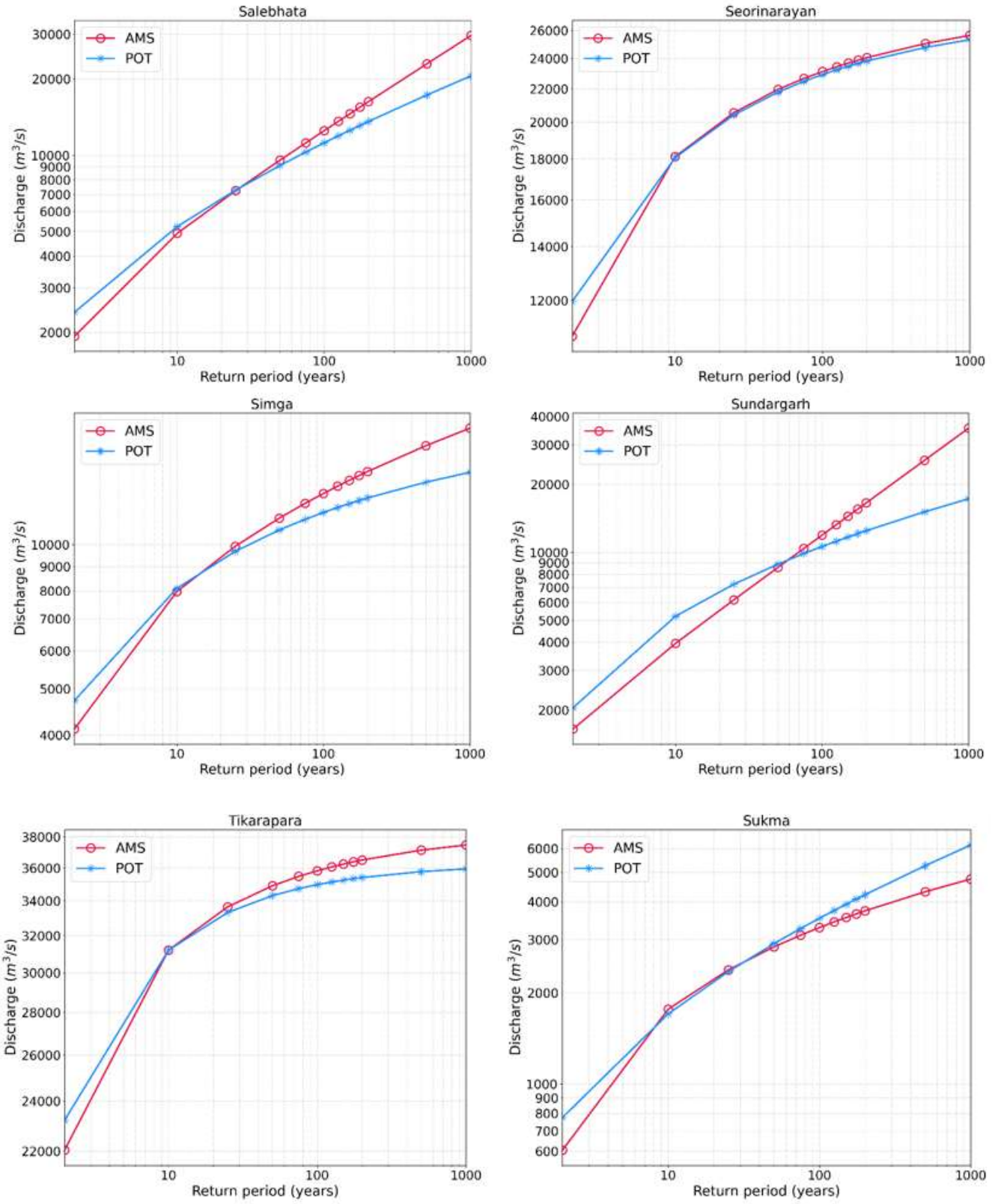

For use in arriving at design flood hydrographs at hotspots (including ungauged/sparsely gauged locations) in the Mahanadi basin, equivalent Geomorphological Instantaneous Unit Hydrographs (E-GIUHs) were developed in our earlier study considering the concept of self-similarity hypothesis of stream networks (Chavan and Srinivas, 2015). The E-GIUHs are useful to arrive at unit hydrographs (pulse response functions) for the catchment of a target location corresponding to any specified rainfall duration. Convolution of the response function with a specified design storm event yields flood hydrograph from the catchment.

In a previous study (CWC, 1983), the Indian subcontinent was delineated into 7 zones containing 26 contiguous sub-zones (Figure 6.3). The sub-zones are widely used by practitioners in India for flood estimation by considering them to be homogeneous. The Mahanadi basin falls in sub-zone 3(d). The sub-zone is evaluated for statistical homogeneity by using the regional homogeneity test (Hosking & Wallis, 1997) on annual maximum daily flows at 31 CWC gauges in the sub-zone. The test provides three heterogeneity measures: (i) H_1 in the one-dimensional space of coefficient of L-variation (L-CV), (ii) H_2 in the two-dimensional space of L-CV and L-skew, and (iii) H_3 in the two-dimensional space of L-skew and L-kurtosis. A region is considered acceptably homogeneous if the value of a heterogeneity measure $H < 1$, possibly heterogeneous if $1 \leq H < 2$, and definitely heterogeneous if $H \geq 2$.

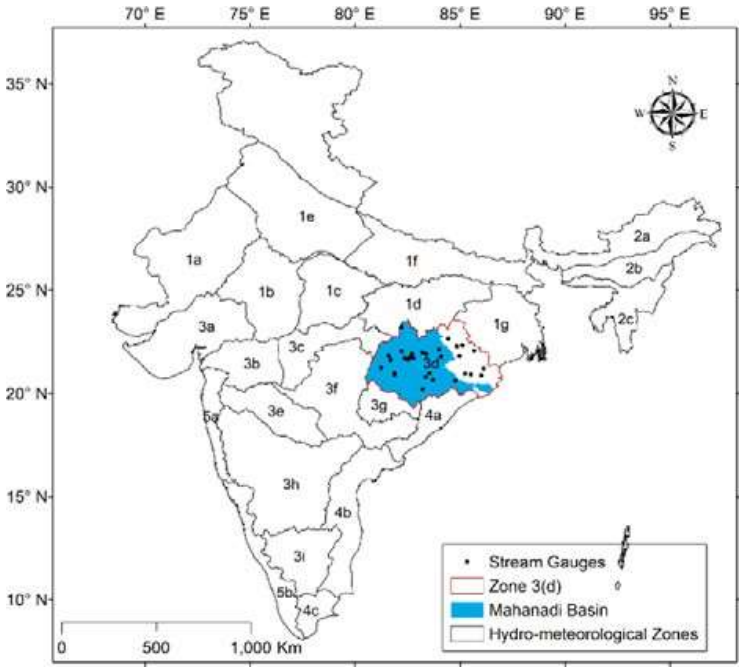

Figure 6.3: Location of zone 3(d) representing Mahanadi basin and stream gauges in the sub-zone.

Results obtained based on the *L*-moment homogeneity test (H_1=7.8, H_2=7.4, and H_3=*6.2*) indicated that the sub-zone 3(d) containing the Mahanadi basin is highly heterogeneous. Similar inferences were drawn for various other sub-zones located in peninsular India. The use of information from such a heterogeneous region/subzone has implications on flood quantiles estimated at target locations (hotspots) in the basin. Hence, there is a need to delineate new homogeneous zones.

In water resources engineering, practitioners consider various regionalization approaches to delineate watersheds in an area into homogeneous groups/regions for Regional Flood Frequency Analysis (RFFA). The RFFA involves the pooling of flood-related information from the region(s) comprising sites resembling the target site for use in flood risk assessment at ungauged or data-sparse locations. Each regionalization approach differs in the underlying assumptions and strategy and yields regions that differ in composition. There is ambiguity in the choice of approaches, as none is established to be universally superior in yielding true regions that are unknown. To address this, a novel Fuzzy Ensemble Clustering (FEC) approach is developed to deal with uncertainty in the composition of regions obtained using different regionalization approaches. It forms fuzzy meta-regions by integrating information on similarities in watershed groupings found in an ensemble of regions derived using several regionalization approaches. The FEC approach's potential to form effective regions (than those found in the ensemble) and their utility in regional flood frequency analysis (RFFA) to predict flood quantiles at ungauged sites is demonstrated through Monte-Carlo simulation (MCS) experiments and a case study on 89 watersheds from peninsular India covering 12 major river basins (Godavari, Krishna, Cauvery, Mahanadi, Narmada, Tapi, Sabarmati, Subernarekha, Mahi, Tadri, Brahmani, and Pennar) and a few west flowing small rivers between Kanyakumari and Tadri (Figure 6.4a). An ensemble of regions for use with FEC is formed using the Region of Influence (ROI) approach, Clustering Approach (CA) based on the Gaussian Mixture Model (GMM), and a Hybrid Approach (HA), which combines canonical correlation analysis (CCA) with GMM based clustering. For this purpose, twelve watershed-related attributes were considered, which included drainage area, perimeter, slope, length of longest flow path, drainage density, basin elongation, circularity ratio, mean annual precipitation, baseflow index, average bulk density of soil up to 30cm depth, latitude, and longitude.

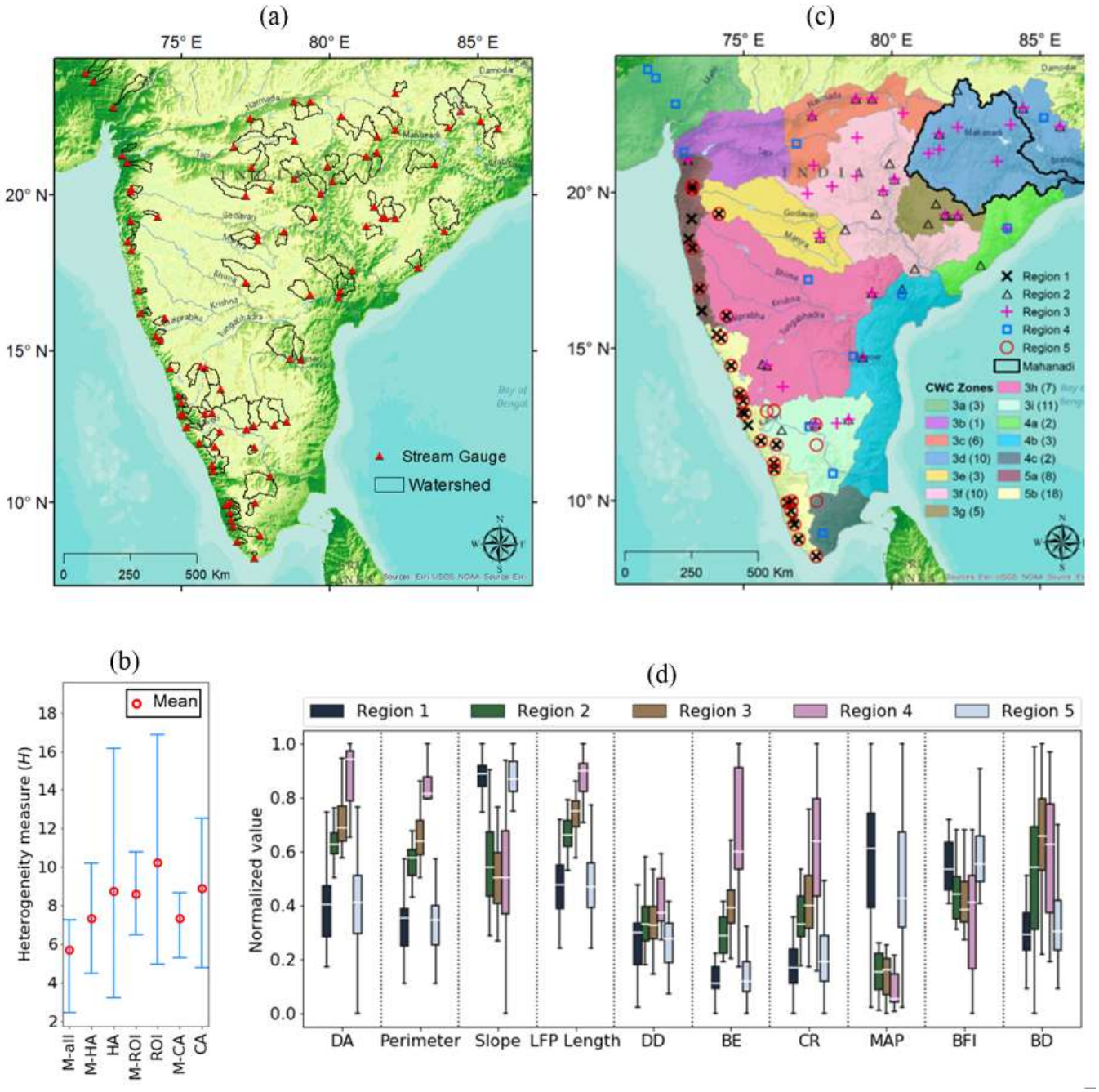

Figure 6.4: (a) Study area showing locations of the 89 watersheds considered in the study and stream gauges at their outlets, (b) Mean and range of heterogeneity index *H* values for seven sets of regions formed in the case study, (c) location of fuzzy meta-regions M-all formed using proposed FEC approach, and (d) variation in the normalized values of watershed related attributes for each of the regions shown in (c). An attribute's value is normalized by subtracting its minimum value and then dividing by its range across all the watersheds in the study area. The acronyms shown in (d) as horizontal axis labels are: DA - Drainage area; LFP - Longest flow path; DD - Drainage density; BE - Basin elongation; CR - Circularity ratio; MAP - Mean annual precipitation; BFI - Baseflow index; BD - Average bulk density of soil.

The FEC is found to be effective in grouping similar watersheds even when the ensemble comprises regions having some improperly/wrongly grouped watersheds (Kiran and Srinivas, 2021b). Five watershed regions were determined using the FEC approach in the area encompassing more than 12 river basins (Figure 6.4c). It can be noted that the Mahanadi basin area falls in the newly formed fuzzy Region 3, and the watersheds in that region resemble watersheds in other regions, several of which are far apart in geographical space. The practice of forming regions comprising watersheds that are not necessarily geographically contiguous gained wide recognition in the hydrology community since the proposal of the region-of-influence approach (Burn, 1990 a,b). It makes sense, as watersheds in different river basins can resemble each other in terms of various attributes influencing floods.

The effectiveness of the newly delineated regions in arriving at flood quantile estimates at ungauged sites was evaluated through a Leave-one-out cross-validation (LOOCV) experiment. Growth curves (non-dimensional cumulative distribution functions) corresponding to each of the newly formed regions were constructed (Figure 6.3) using the index-flood method (Dalrymple, 1960). The curves can be scaled to predict flood quantiles at ungauged or sparsely-gauged sites in the river basin. This has significance since the civil infrastructure is often planned at ungauged locations. Finer details on this contribution can be found in Kiran and Srinivas (2021b).

Multivariate Regional Frequency Analysis (MRFA) using the proposed Conditional Multivariate Extreme Values (CMEV) Approach

Floods can be characterized by various correlated variables such as peak flow, flood volume, duration, and time to peak. Hence, flood risk can be better assessed by frequency analysis in a multivariate framework. However, multivariate approaches involve sophisticated analyses that require considerably more data than univariate approaches. As mentioned earlier, RFFA is widely used for flood risk assessment at ungauged or data-sparse locations in a univariate framework. It involves the pooling of data from a region comprising a homogeneous group of sites resembling the target site. However, RFFA has received little attention in the multivariate framework. The available literature recommends the use of the Index Flood Approach (IFA), even though it has theoretical shortcomings (Basu and Srinivas, 2013). Furthermore, conventionally used multivariate models are not suitable for describing the dependence structure of extremes in the

regions of the support of the joint distribution where only some variables exhibit extreme behavior. A Conditional Extreme Values Approach (CEA) is contributed for use in multivariate RFA (MRFA) to address this issue. It uses the Conditional Multivariate Extreme Values (CMEV) model that involves transforming all the flood-related variables to a non-dimensional space where each of them follows Laplace distribution (Keef et al., 2013). The dependence structure of the Laplace distributed variables is modeled by conditioning their joint distribution on a subset of the variables exhibiting extreme behavior (i.e., large values). The CMEV model is flexible and can capture a broad range of asymptotic independence and dependence structures, even if the sign (positive/negative) of dependence is different between different pairs of variables (Keef et al., 2013). The proposed approach (CEA) is useful for assessing risk at sparsely gauged and ungauged locations based on the predicted joint distribution of multiple flood-related variables. The effectiveness of the approach was investigated through Monte-Carlo simulation experiments and application to watersheds in the Mahanadi basin. For MRFA in the Mahanadi basin, flood-related information was pooled from a region/group comprising ten watersheds that are unaffected by any major water control structures. The watersheds lie in the hydrometeorological sub-zone 3g (CWC, 1983). Critical flood events at each site were identified as those whose peaks exceeded an optimal threshold identified using Mahalanobis distance-based method (Kiran & Srinivas, 2021), and flood hydrographs corresponding to those events were extracted. The times corresponding to the rise of a flood hydrograph and its return to the baseflow were identified following a procedure described in Yue (1999). Flood volumes were then computed corresponding to each event. Table 6.2 provides details of the drainage area and extreme event-related characteristics for the chosen watersheds.

The homogeneity of the region comprising the N (=10) watersheds in the Mahanadi basin was assessed using a nonparametric L-comoment-based homogeneity test (Masselot et al., 2017). The test involved estimating the regional dispersion measure $V_{\|\cdot\|}$ as,

$$V_{\|\cdot\|} = \left(\frac{\sum_{i=1}^{N} n_i \left\| \Lambda_2^{(i)} - \bar{\Lambda}_2 \right\|^2}{\sum_{i=1}^{N} n_i} \right)^{1/2} \tag{6.1}$$

where $\|\cdot\|$ is the spectral norm, $\Lambda_2^{(i)}$ is the matrix of L-covariation between peak flow and flood volume at site i, and $\bar{\Lambda}_2 = \left(\sum_{i=1}^{N} n_i \Lambda_2^{(i)} \right) \Big/ \sum_{i=1}^{N} n_i$ is the weighted average of L-covariation matrices of all the sites. Herein, the weights are considered to be proportional to the number of data points or events extracted for the sites. The distribution of $V_{\|\|}$ under the null hypothesis of homogeneity is obtained by simulating N_{sim}(=10,000) synthetic regions and computing $V_{\|\|}$ corresponding to each of those regions. In a synthetic region, a sample of size n_i was generated for site i by randomly resampling (with replacement) data points from a bivariate sample comprising pooled information on flood-related characteristics of sites in the region. The p-value of the hypothesis test was estimated as the probability of exceedance of the estimated $V_{\|\|}$ for the region. $V_{\|\|}$ was estimated to be 0.254, and the corresponding p-value was 0.631, which indicated that the regional was homogeneous.

Table 6.2: Information on stream gauges considered in the case study and flood-related characteristics/variables (flood peak and volume) at those gauges.

Stream gauge	Drainage area (km^2)	Period of records	Threshold peak flow value identified for extraction of extreme events (m^3/s)	Number of flood events extracted	Mean peak flow (m^3/s)	Mean flood volume (Million m^3/day)
Andhiyarkore	2210	1977-2019	43.0	143	166.2	31.1
Champua	1710	1980-2019	72.8	18	529.9	1581.5
Ghatora	3035	1978-2019	735.0	11	1235.9	251.5
Jaraikela	9160	1972-2019	1023.7	95	2513.5	497.8
Kotni	6990	1977-2019	950.0	55	2196.2	461.4
Manendragarh	1100	1987-2019	49.1	93	190.4	29.9
Pathardhi	2511	1987-2019	393.4	50	945.5	224.5
Salebhata	4650	1971-2019	1146.6	56	2803.9	468.9
Sundargarh	5870	1977-2019	2000.3	20	4096.0	641.6
Tilga	3160	1978-2019	483.5	67	961.3	194.1

The performance of the proposed approach (CEA) in arriving at the reliable bivariate joint distribution of random variables (and thus bivariate quantile estimates) for ungauged sites in the Mahanadi basin

was assessed through leave-one-out cross-validation (LOOCV). It involved considering one site i (=1,…,N) at a time to be ungauged (in the realization) and using the CEA (Appendix 6.2) to predict a bivariate sample $\hat{\mathbf{Q}}^{(i)}$ corresponding to the ungauged site. In analysis with CEA, marginal distributions corresponding to peak flow and flood volume were considered as generalized Pareto and generalized extreme value (GEV), respectively. The GEV distribution was found adequate to fit the flood volume data of all the sites based on the Anderson-Darling goodness of fit test at a 5% significance level. As the true population of an ungauged site is unknown in the real-world scenario, a large sample comprising a thousand data points was generated from the CMEV model fitted to at-site data of the (pseudo) ungauged site, and it was considered as an at-site population. Furthermore, in analysis with IFA for ungauged site i, the index-flood value of each marginal variable (required for the prediction of samples) was assumed to be equal to the arithmetic mean of the variable.

Three error measures, namely Kullback-Leibler divergence (KLD), normalized Friedman-Rafsky statistic (NFRS), and maximum mean discrepancy (MMD), were computed for each site, and their variation across all the sites was visualized as boxplots (Figure 6.5a). Low values for all these measures indicate that the joint distributions of $\hat{\mathbf{Q}}^{(i)}$ and $\mathbf{Q}^{(i)}$ closely resemble. The boxplots indicate that the CEA approach performs better than IFA. The magnitude of estimates obtained for the regional parameters $\hat{\alpha}_{2|1}$ and $\hat{\rho}$ in the analysis indicates that flood volume has a strong dependence on peak flow in the Mahanadi basin (Figure 6.5b). Furthermore, the parameter $\hat{\beta}_{2|1}$ indicates that the variance of flood volume increases with peak flow, but not considerably.

To assess the performances of the CEA and IFA approaches in quantile estimation, empirical bivariate CDF was constructed for each site based on a bivariate sample $\hat{\mathbf{Q}}^{(i)}$ predicted for the site using each approach. Contour plots derived from the CDFs for different non-exceedance probabilities were compared with the corresponding plots constructed from analysis on the at-site population $\mathbf{Q}^{(i)}$ (derived by fitting the CMEV model to at-site data) for all the sites (Figure 6.6). The empirical bivariate CDF of the population derived for the site i can be expressed as,

$$\hat{G}\left(q_1^{(i)}, q_2^{(i)}\right) = \frac{1}{(n+1)} \sum_{\forall\left(q_1^{(i)}, q_2^{(i)}\right) \in \mathbf{Q}^{(i)}} H\left(q_1, q_2\right) \tag{6.2}$$

where $q_1^{(i)}$ and $q_2^{(i)}$ are predicted values corresponding to the flood-related random variables, (q_1, q_2) is a datapoint in the at-site population $\mathbf{Q}^{(i)}$, n represents the number of datapoints in the population, $H(\cdot)$ is the Heaviside's unit step function which attains a value 1 if $q_1 \leq q_1^{(i)}$ and $q_2 \leq q_2^{(i)}$, and zero otherwise. The CDF of a predicted sample can be determined using the above equation by considering $\hat{\mathbf{Q}}^{(i)}$ in place of $\mathbf{Q}^{(i)}$. The contour plots depicting bivariate quantile estimates obtained using CEA for ungauged sites were found to be closer to the corresponding contours derived from the at-site population for various values specified for non-exceedance probability F (Figure 6.6). In contrast, considerable bias was evident between contours corresponding to IFA and at-site population. These observations are consistent with the estimates obtained for error measures and indicate that the proposed CEA approach can effectively capture the regional dependence structure between flood-related variables and predict their joint distribution at ungauged/sparsely gauged locations reliably. The constructed CDFs (Figure 6.6) find use in multivariate risk analysis of civil infrastructure nearby the sites considered in the Mahanadi basin.

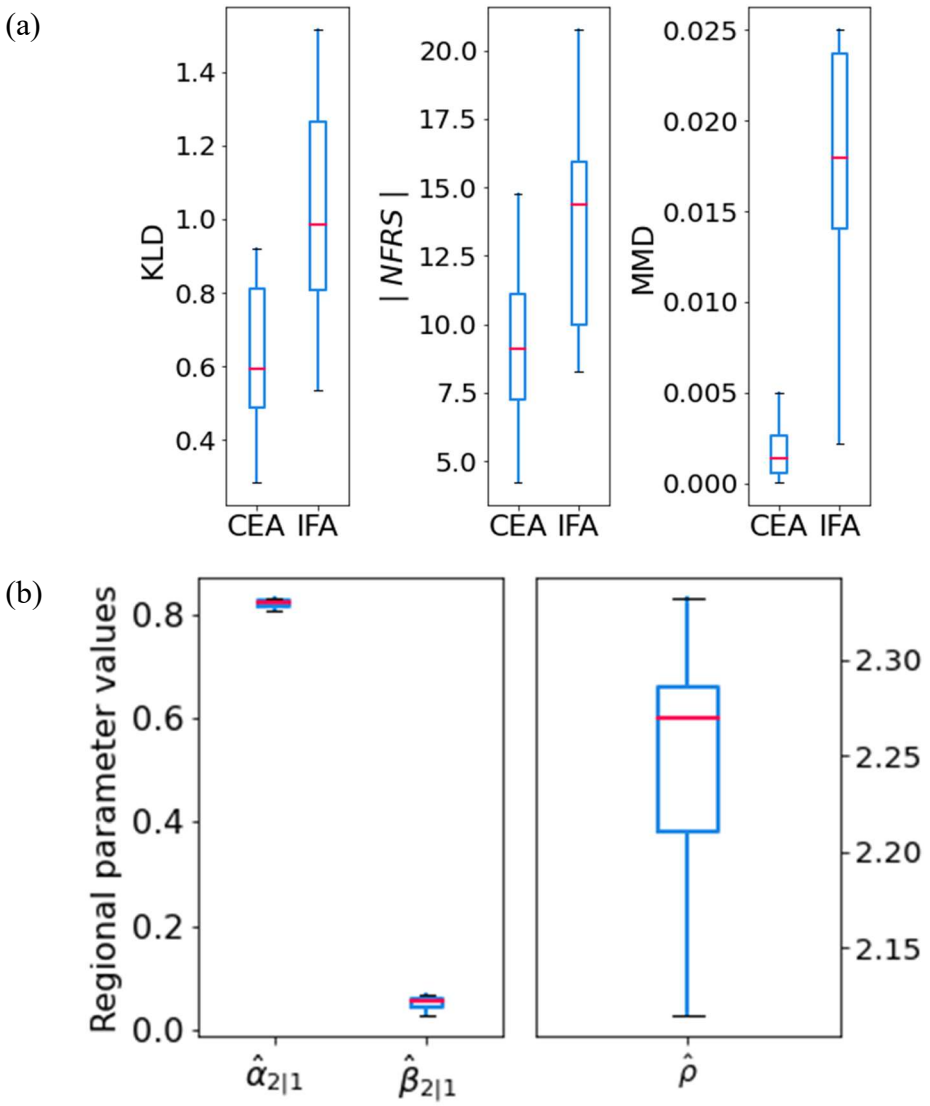

Figure 6.5: Variation in (a) estimates of error measures (KLD, Absolute value of NFRS, and MMD) and (b) regional estimates of parameters obtained in LOOCV with CEA and IFA in the case study on ten watersheds in the Mahanadi basin. CEA: Conditional extreme values approach; IFA: Index-flood approach.

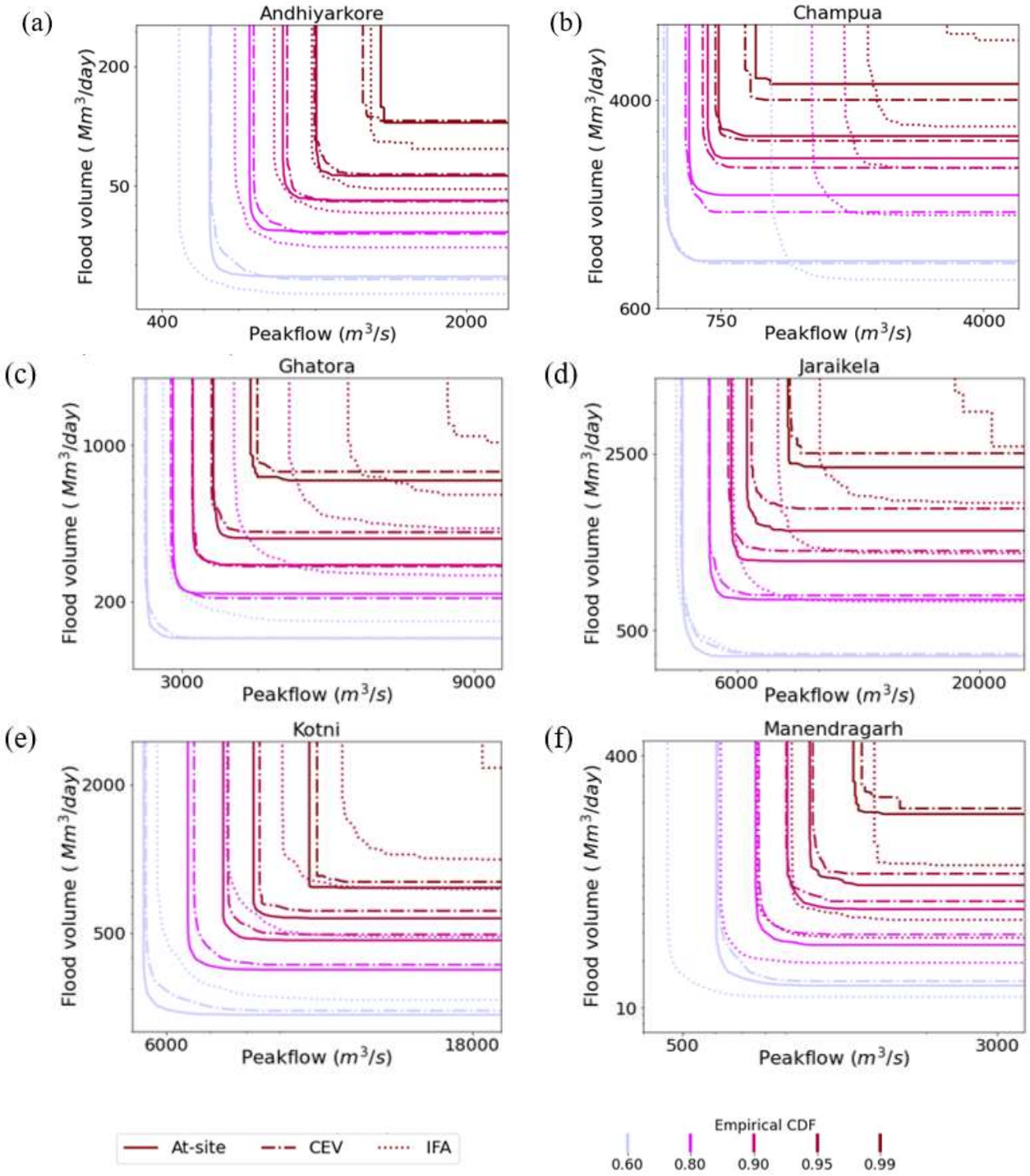

Figure 6.6: Contour plots of bivariate empirical cumulative distribution function obtained from at-site frequency analysis and regional frequency analysis with CEA and IFA for all the sites considered in the case study. CEA: Conditional extreme values approach; IFA: Index-flood approach.

Figure 6.6 (continued…)

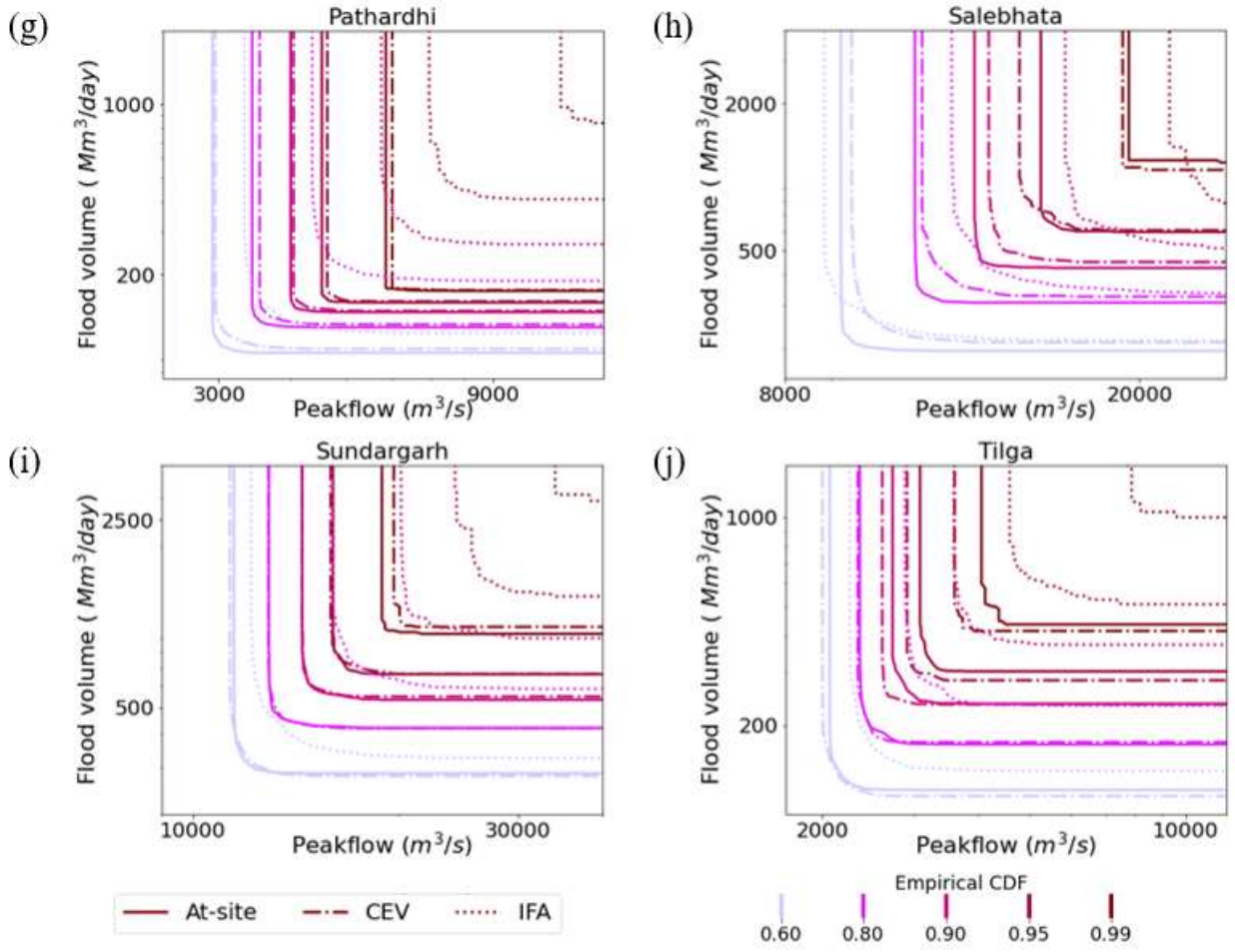

Appendices

A6.1. Proposed Mahalanobis Distance-based Threshold Selection Methodology

Let there be a sample/record of the hydrological variable (e.g., rainfall, streamflow) whose extremes are to be analyzed. A novel Mahalanobis distance (MD) based methodology (MDM) is proposed for threshold selection and extraction of peaks (i.e., extremes values) over the threshold from the record for use in frequency analysis. Various steps involved in the methodology are as follows.

1) Identify independent peaks in the time series using a moving window. The window length (L_w) depends on the characteristics of the process depicting the variable being analyzed. It could be considered as $2s+1$ to ensure the independence of peaks, where s is the minimum separation time between events in the time series. In analysis with daily rainfall, s could be considered as 1 or 2 days (e.g., Coles, 1993), whereas in analysis with streamflows, one could consider $s \geq 5 + \ln(DA)$ with DA as drainage area of the catchment in square miles (e.g., Lang et al., 1999). As the window moves through the time series, the maximum value within the window is chosen as an independent peak if it coincides with the window's center. For streamflows, an additional criterion is applied to ensure the independence of events causing the peaks. The criterion suggests that if the flows observed between two consecutive peaks do not drop below 0.75 times the magnitude of the lower peak among the two, then the lower peak value is to be discarded (Lang et al., 1999).
2) Let n_p be the number of independent peaks chosen. Arrange them in ascending order of their magnitude, so that the ordered sample appears as $Q_{1:n_p} \leq Q_{2:n_p} \leq \cdots \leq Q_{n_p:n_p}$, where Q_{in_p} is i-th smallest independent peak. Following this, define a set of possible thresholds $\boldsymbol{\Xi} = \left\{Q_{1:n_s}, Q_{2:n_s}, \ldots, Q_{n_s:n_s}\right\}$ from the identified n_p peaks by excluding repeated values, such that $n_s \leq n_p$. It is to be noted that considering all the n_p peaks as candidates in $\boldsymbol{\Xi}$ is neither efficient nor necessary. The choice of candidates in $\boldsymbol{\Xi}$ depends on the available data, and it is left to the discretion of the modeler.
3) Choose one possible threshold at a time from the set $\boldsymbol{\Xi}$ and perform the following analysis using it.
   (i) determine the set of excesses $\boldsymbol{Y}$ by deducting the threshold from independent peaks exceeding it. Fit GPD to $\boldsymbol{Y}$ and obtain a sample estimate of the distribution's scale parameter α and

shape parameter k using the method of *L*-moments. One could choose any other effective method for parameter estimation.

(ii) Transform or map $\boldsymbol{Y}$ to $\boldsymbol{Z}$ as, $\boldsymbol{Z} = -\frac{1}{k}\log\left(1 - k\frac{\boldsymbol{Y}}{\alpha}\right)$ (A6.1)

The true population of the random variable $\boldsymbol{Z}$ (depicting the transformed values) is known to be Exp(1) distribution if $\boldsymbol{Y}$ follows GPD (Kiran and Srinivas, 2021a). The advantage of transformation is that it enables representing the true population of $\boldsymbol{Z}$ as a point in the *L*-moment space (irrespective of the number of moments considered), which is not the case with the true population of $\boldsymbol{Y}$. This facilitates the computation of MD in the *L*-moment space.

(iii) Estimate MD between sample *L*-statistics (first *L*-moment l_1, and *L*-skew t_3) of $\boldsymbol{Z}$ and *L*-moments (first *L*-moment λ_1^E , and *L*-skew τ_3^E) of Exp(1) distribution in the transformed space using Equation (A6.2). As λ_1^E and τ_3^E are fixed values for the Exp(1) distribution, they do not have an associated distribution. Hence, the expected values and standard deviations of the sampling distributions of *L*-statistics (l_1^E and t_3^E) computed for samples from the Exp(1) distribution are considered.

$$\text{MD} = \left[\frac{1}{1-\rho^2}\left\{\frac{\left(l_1 - \mu_{l_1^E}\right)^2}{\sigma_{l_1^E}^2} - \frac{2\rho\left(l_1 - \mu_{l_1^E}\right)\left(t_3 - \mu_{t_3^E}\right)}{\sigma_{l_1^E}\sigma_{t_3^E}} + \frac{\left(t_3 - \mu_{t_3^E}\right)^2}{\sigma_{t_3^E}^2}\right\}\right]^{\frac{1}{2}} \quad \text{(A6.2)}$$

where, $\mu_{l_1^E}$ and $\mu_{t_3^E}$ denote the mean, and $\sigma_{l_1^E}$ and $\sigma_{t_3^E}$ represent the standard deviation of the sampling distribution of l_1^E and t_3^E respectively, and ρ is the coefficient of correlation between l_1^E and t_3^E . These statistics can be estimated by MCS, which involves generating several (e.g., 1000) samples from Exp(1) distribution having the same size as that of the transformed sample (obtained in step(ii)). The square of MD is equal to Hotelling's T^2 statistic (Hotelling, 1931), which has a χ^2 distribution with 2 degrees of freedom. Further details on this are provided in the following Section A6.2.

It is to be noted that l_1^E is an unbiased statistic for the expected value of a distribution. Thus for Exp(1) distribution, $\mu_{l_1^E} = 1$ and $\sigma_{l_1^E} = 1/\sqrt{n}$ following the central limit theorem. An

alternative to using MCS is to consider these exact values of $\mu_{l_1^E}$ and $\sigma_{l_1^E}$ together with $\rho=0$ (by Basu's Theorem (Basu, 1955)), and estimate $\mu_{t_3^E}$ and $\sigma_{t_3^E}$ using approximate expressions relating them to sample size n (Equations A6.3-A6.4). Analysis based on this alternative option is referred to as MDM-A, whereas that based on MCS is referred to as MDM-M.

$$\mu_{t_3^E} = \frac{1}{3} - 0.307n^{-1.076} \tag{A6.3}$$

$$\sigma_{t_3^E} = \frac{166.507n + 102.384}{347.652n^{1.498} - 43.041n - 575.098} \tag{A6.4}$$

The details of the derivation of the above equations are provided in the following Section A6.3. The use of these equations would reduce the computation time considerably, as MCS is averted.

For the computation of MD, (λ_1, τ_3) space is preferred to conventionally used τ_3 (L-skew) versus τ_4 (L-kurtosis) space. This is motivated by the fact that the set of possible alternate distributions for $\boldsymbol{Z}$ (obtained using Equation A6.1) are limited to standardized forms of distribution of $\boldsymbol{Y}$ (Hosking, 1994). In (λ_1, τ_3) space, the point $(1, 1/3)$ is unique to Exp(1) distribution. However, in (τ_3, τ_4) space $\tau_4 = 1/6$ is not unique to that distribution, as the value of τ_4 is the same even for standard logistic distribution. Further, sample estimates of the higher-order moment-related L-statistic τ_4 are known to be biased when compared to those of the lower-order moment λ_1 (Hosking & Wallis, 1997). Hence λ_1 is preferred to τ_4.

4) From the set $\boldsymbol{\Xi}$, identify the optimal threshold for which the estimate of MD is minimum. The excesses corresponding to the identified threshold denote the required PDS or POT series.

A6.2. Determination of the joint distribution of the first *L*-moment and *L*-skew of Exp(1) distribution

The exact joint distribution of l_1^E and t_3^E of Exp(1) distribution is unknown. Visual inspection of scatter plots (Figure A6.1 (a)-(d)) of the two *L*-statistics estimated from several samples indicates that the distribution could be assumed to be bivariate normal. This assumption is investigated through a GoF test based on a measure of kurtosis $M_{kurtosis}$ (Mardia, 1970), henceforth referred to as the Mardia test statistic.

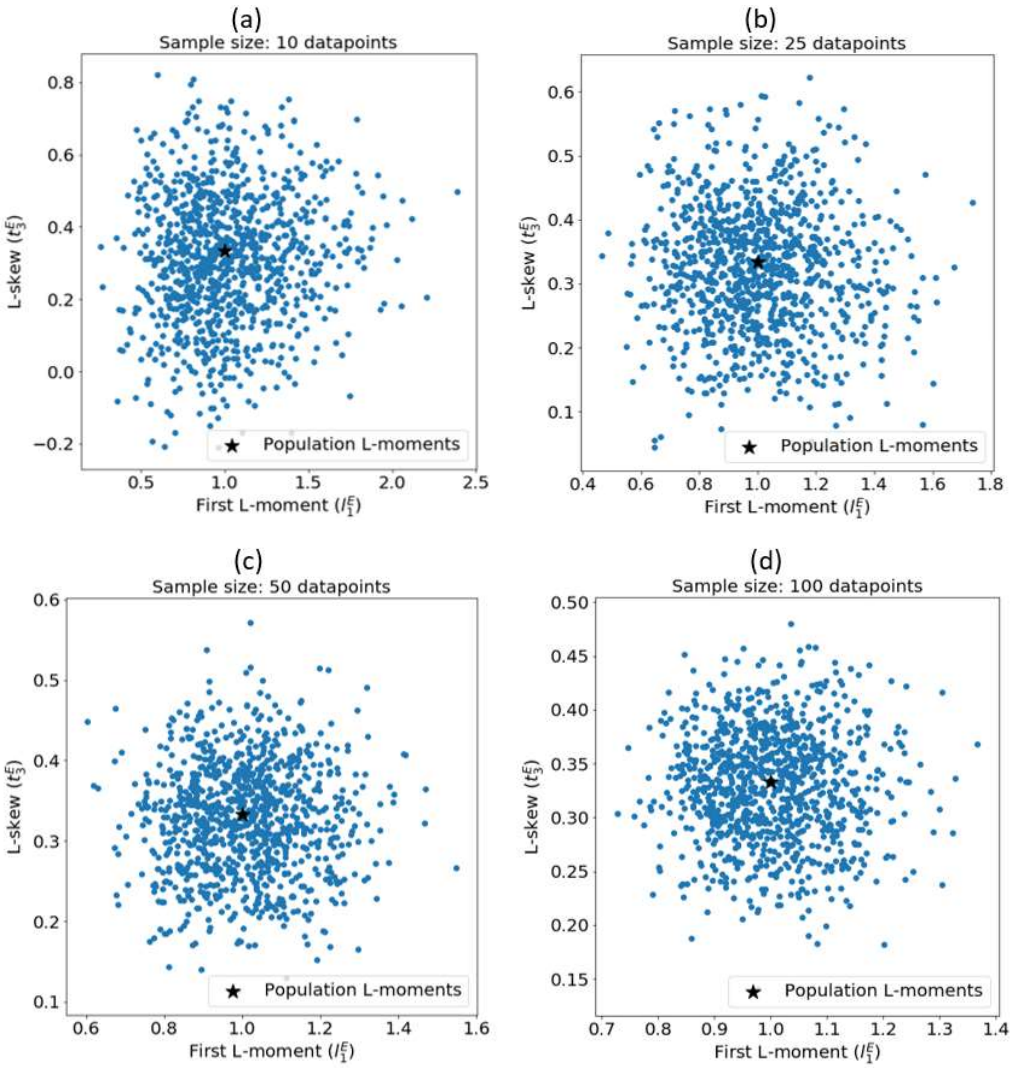

Figure A6.1: Scatter plots between the estimates of the first *L*-moment and *L*-skew obtained for one-thousand samples of different sizes generated from Exp(1) distribution ((a)-(d)). Boxplots showing variation in 500 Mardia test statistic values for different sample sizes (e).

Figure A6.1 (Continued…)

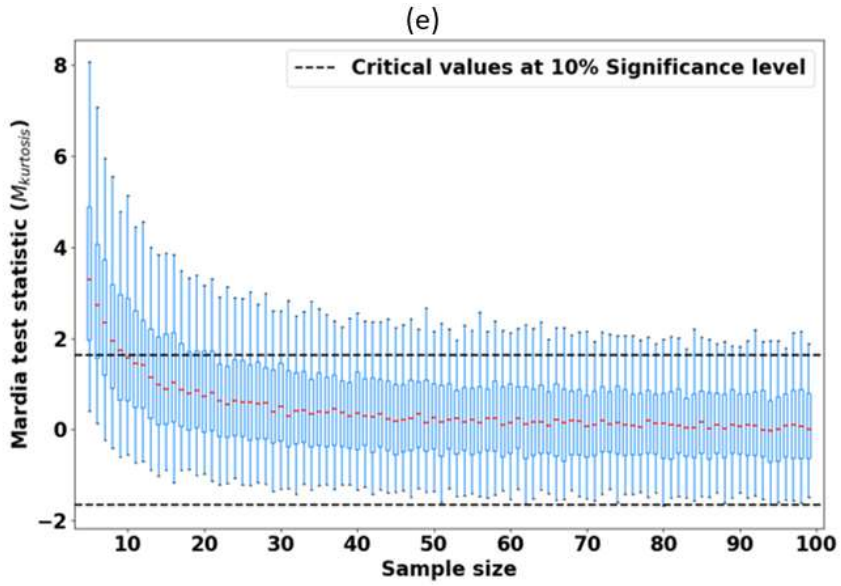

Experiments were performed by considering different sample sizes. In each experiment, N_{sim} (=1000) samples of size *n* were generated from Exp(1) distribution, and estimates of (l_1^E, t_3^E) corresponding to the N_{sim} samples were used to compute $M_{kurtosis}$. This was repeated 500 times to obtain 500 values of $M_{kurtosis}$ for the chosen sample size. Boxplots showing the variation in those $M_{kurtosis}$ values were prepared for different sample sizes (Figure A6.1 (e)). They indicate that the assumption of bivariate normality is valid (at a 10% significance level) for sample sizes greater than nine. Thus, even in analysis with small samples usually encountered in a real-world scenario, the assumption of bivariate normality could be considered valid.

When the distribution of l_1^E and t_3^E is bivariate normal, the square of MD between the *L*-statistics (l_1, t_3) of a sample and the corresponding *L*-moments of the Exp(1) population is the same as Hotelling's T^2 statistic (Hotelling, 1931), which is used for testing the equality of mean vector of a sample with that of a normal/Gaussian population in multivariate analysis. The sampling distribution of T^2 statistic in the bivariate case can be accurately approximated by χ^2 distribution with 2 degrees of freedom if GPD parameters used for the transformation of $\boldsymbol{Y}$ to $\boldsymbol{Z}$ are given/known *a priori*. This would allow assigning a *p*-value to estimate of MD. However, when the parameters are unknown and

are estimated from a sample, the distribution of l_1^E and t_3^E is not necessarily bivariate normal. Then, the square of the MD will not follow a χ^2 distribution. One could nevertheless associate a *p*-value or a significance level to the estimate of MD using MCS. It enables testing the hypothesis of exponentiality of $\boldsymbol{Z}$ based on the *L*-statistics in the transformed space. Thus, thresholds that yield samples that are not exponentially distributed in the transformed space can be rejected (at a specified significance level), as they will not be GP distributed in the original space. The option of rejecting samples is only possible in methods like MDM and ADM, which can associate a significance level to the estimated test statistic. This is not possible with distance-based methods (e.g., LMM) and GoF test-based methods such as Jackson and Lewis kernel methods (Goegebeur et al., 2008) which do not associate a significance level to the estimated test statistic. An advantage of associating *p*-value with chosen thresholds is that the modeler has the flexibility to opt for the least threshold value that meets a pre-specified significance/confidence level, as can be noted from Durocher et al. (2018), which considers ADM. The proposed methodology is thus simple like LMM, as it avoids making assumptions on SDTS. At the same time, it offers the advantage of GoF test-based methods like ADM, which allows associating a significance level to the identified threshold.

A6.3. Derivation of Equations (A6.3) and (A6.4)

To derive the expressions N_{sim} (=1000) simulations were performed. Each simulation involved generating one-thousand samples of size *n* from Exp(1) distribution and the use of *L*-statistics (l_1^E and t_3^E) of those samples to arrive at estimates for $\mu_{t_3^E}$ and $\sigma_{t_3^E}$. Variation in N_{sim} sample estimates of each of those latter statistics is visualized in the form of a boxplot for each sample size $\left(n = 5, 6, \ldots, 1000\right)$(Figure A6.2). The Equation for the approximate values of each statistic (i.e., $\mu_{t_3^E}$ and $\sigma_{t_3^E}$) was determined as that of the best-fit line connecting means of the boxplots corresponding to different sample sizes. Plots provided as insets in Figures A6.2(a)-(b) show boxplots along with the best-fit line connecting their means.

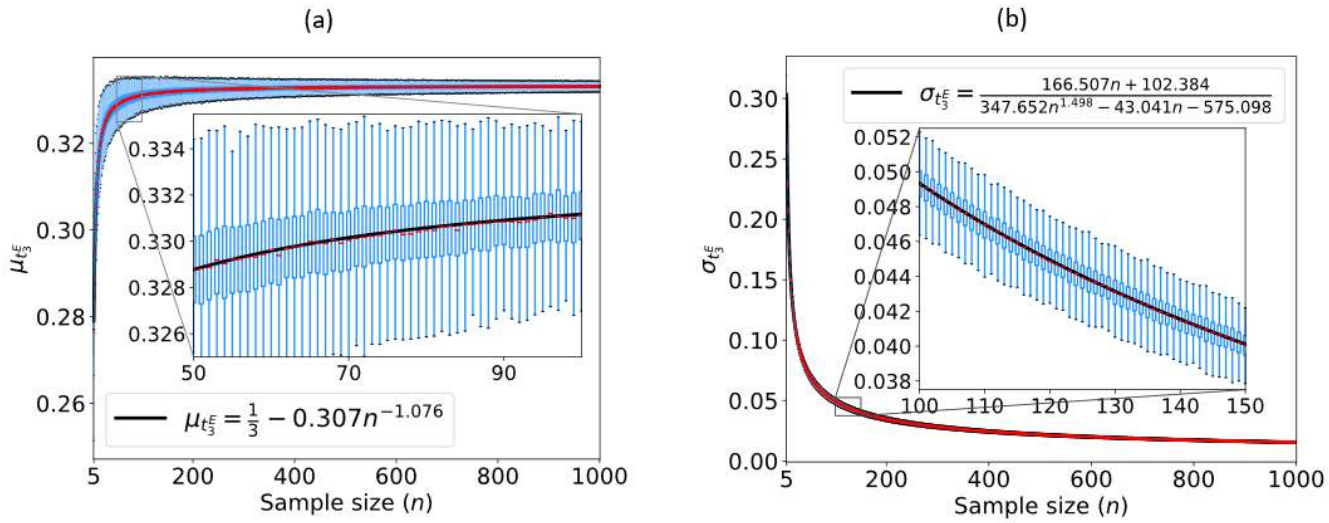

Figure A6.2: Variation in N_{sim} estimates of (a) $\mu_{t_3^E}$ and (b) $\sigma_{t_3^E}$ for samples from Exp(1) distribution.

A6.4. Theoretical Background of the CMEV model

This section provides the theoretical background of the CMEV model (Heffernan & Tawn, 2004). Let $\mathbf{Q}=[Q_1,\ldots,Q_m]$ be a vector containing m random variables (e.g., flood peak, volume, and duration) related to the natural hazard (flood) being analyzed. The dependence structure of variables in $\mathbf{Q}$ can be effectively analyzed by mapping them to $\mathbf{Y}=[Y_1,\ldots,Y_m]$ in a non-dimensional space, where the form of marginal distributions of $Y_1,\ldots,Y_m$ is the same. Heffernan & Tawn (2004) considered the relationship $\left\{Y_j=-\log\left[-\log F_j\left(Q_j\right)\right],\ j=1,\ldots,m\right\}$ for mapping such that marginal distribution becomes Gumbel in the non-dimensional space. Herein, $F_j(\cdot)$ is the cumulative distribution function (CDF) of Q_j. Keef et al. (2013) brought out the limitations of this mapping strategy (due to the asymmetry of the Gumbel distribution) in cases where marginals in $\mathbf{Q}$ have contrasting (positive and negative) dependences. To alleviate this issue, mapping of the marginals in $\mathbf{Q}$ to Laplace distributed random variables (using Equation A6.5) was suggested, as Laplace distribution has symmetry and exponential tails.

$$Y_j=\begin{cases}\ln\left[2F_j\left(Q_j\right)\right] & \text{for } F_j\left(Q_j\right)\le 0.5\\ -\ln\left\{2\left[1-F_j\left(Q_j\right)\right]\right\} & \text{for } F_j\left(Q_j\right)\ge 0.5\end{cases}\qquad j=1,\ldots,m \tag{A6.5}$$

Prior studies explored different options for the choice of $F_j(\cdot)$. Heffernan and Tawn (2004) suggested considering $F_j(\cdot)$ as CDF of (i) Generalized Pareto Distribution (GPD) for data points of Q_j exceeding an appropriate threshold, and (ii) an empirical distribution based on ranks for the remaining data points of Q_j. The strategy considered for mapping data points above the threshold would translate the measurement errors in Q_j and estimation errors in GPD parameters into Y_j. To avoid this, the entire sample of Q_j may be transformed using an empirical distribution based on ranks of the samples' data points (e.g., Keef et al., 2009a).

In the CMEV model, the joint distributions of marginal variables in $\mathbf{Y}$ are conditioned on the distribution of the primary variable Y_k (in $\mathbf{Y}$) when its corresponding Q_k exhibits extreme behavior. The basic assumptions and the asymptotic theory underlying the approach are described in detail by Heffernan and Tawn (2004). For the sake of simplicity, the approach is first described for the bivariate case and then extended for the scenario with more than two variables.

Consider two Laplace-distributed random variables $Y_1 = \{y_{1,1}, \ldots, y_{1,n}\}$ and $Y_2 = \{y_{2,1}, \ldots, y_{2,n}\}$ (obtained using Equation A6.5) whose joint distribution is to be modeled when Y_1 exceeds a prespecified threshold u. The CMEV model describes the behavior of $Y_2 \mid Y_1$ as,

$$Y_2 = \alpha_{2|1} Y_1 + Y_1^{\beta_{2|1}} Z_{2|1} \;:\; Y_1 > u \tag{A6.6}$$

where $Z_{2|1}$ is an independent and identically distributed random variable (with a non-zero mean) representing the standardized residuals; $\alpha_{2|1} \in [-1,1]$ depicts the strength and type of the dependence of Y_2 on Y_1, such that a higher positive (negative) value indicates strong positive (negative) dependence; $\beta_{2|1} \in (-\infty, 1)$ describes the nature of change in dependence of Y_2 on Y_1 with a change in Y_1. A higher positive value for $\beta_{2|1}$ indicates that the variance of $Y_2 \mid Y_1$ increases as $Y_1 > u$ increases (Keef et al., 2009b). The parameters $\alpha_{2|1}$ and $\beta_{2|1}$ can be estimated by numerical maximization of the following log-likelihood function.

$$\mathcal{L} = -\sum_{\forall t: y_{1,t} > u} \left[\log\left(\sigma_{2|1}\left(y_{1,t}\right)\right) + \frac{1}{2}\left\{ \frac{y_{2,t} + \mu_{2|1}\left(y_{1,t}\right)}{\sigma_{2|1}\left(y_{1,t}\right)} \right\}^2 \right] \tag{A6.7}$$

where, $\mu_{2|1}\left(y_{1,t}\right)=\hat{\alpha}_{2|1}y_{1,t}+\mu\left(\hat{z}_{2|1}\right)y_{1,t}^{\hat{\beta}_{2|1}}$ and $\sigma_{2|1}\left(y_{1,t}\right)=\sigma\left(\hat{z}_{2|1}\right)y_{1,t}^{\hat{\beta}_{2|1}}$ such that $\mu\left(\hat{z}_{2|1}\right)$ and $\sigma\left(\hat{z}_{2|1}\right)$ denote the mean and standard deviation of $\hat{z}_{2|1}$ respectively. The threshold u is chosen sufficiently high such that Y_1 and $Z_{2|1}$ can be considered to be independent of each other, and there are enough data points to arrive at reliable estimates of the dependence parameters ($\hat{\alpha}_{2|1}$, $\hat{\beta}_{2|1}$). The standardized residuals can be obtained as,

$$\hat{z}_{2|1}\left(t\right)=\frac{y_{2,t}-\hat{\alpha}_{2|1}y_{1,t}}{y_{1,t}^{\hat{\beta}_{2|1}}}\quad\forall\, y_{1,t}>u \tag{A6.8}$$

The fitted CMEV model is then used to simulate N_{sim} synthetic events using the following steps:

(i) Generate N_{sim} values of $\hat{y}_1$ such that $\hat{y}_1>u$ and $\hat{y}_1-u$ follows a standard exponential distribution. Corresponding to each $\hat{y}_1$ value, randomly sample a $\hat{z}_{2|1}$ value (with replacement) from the standardized residuals obtained using Equation (A6.8), as the form of distribution of $Z_{2|1}$ is unknown. Then estimate $\hat{y}_2$ corresponding to $\hat{y}_1$ using Equation (A6.6) by considering $\hat{\alpha}_{2|1}$, $\hat{y}_1$, $\hat{\beta}_{2|1}$ and $\hat{z}_{2|1}$ in place of $\alpha_{2|1}$, Y_1, $\beta_{2|1}$ and $Z_{2|1}$.

(ii) Inverse transform the N_{sim} simulated pairs of ($\hat{y}_1$, $\hat{y}_2$) values using Equation (A6.9) (which is based on Equation A6.5) to arrive at data points of the corresponding marginal variables Q_1 and Q_2 in the original space.

$$\hat{Q}_j=\begin{cases}F_j^{-1}\left[\dfrac{e^{\hat{y}_j}}{2}\right] & \text{for } \hat{y}_j\le 0\\ F_j^{-1}\left[1-\dfrac{e^{-\hat{y}_j}}{2}\right] & \text{for } \hat{y}_j\ge 0\end{cases}\qquad j=1,2 \tag{A6.9}$$

For the case involving more than two variables (i.e., m > 2), Equation (A6.6) can be extended to Equation (A6.10) by replacing Y_2 with the vector $\mathbf{Y}_{-k}$ (i.e., $\mathbf{Y}$ without k-th component Y_k), Y_1 with Y_k, $Z_{2|1}$ with $m-1$ dimensional random vector of standardized residuals $\mathbf{Z}_{|k}$, and the parameters $\alpha_{2|1}$ and $\beta_{2|1}$ with their respective $m-1$ dimensional vectors $\boldsymbol{\alpha}_{|k}\in[-1,1]^{m-1}$ and $\boldsymbol{\beta}_{|k}\in(-\infty,1)^{m-1}$.

$$\mathbf{Y}_{-k}=\boldsymbol{\alpha}_{|k}Y_k+Y_k^{\boldsymbol{\beta}_{|k}}\mathbf{Z}_{|k} \tag{A6.10}$$

In the above equation, vector algebra is interpreted componentwise. Each element of the parameter vectors $\boldsymbol{\alpha}_{|k}$ and $\boldsymbol{\beta}_{|k}$ corresponds to a marginal in $\mathbf{Y}_{-k}$. They are estimated using the log-likelihood function of the bivariate model (Equation A6.7) by considering the chosen marginal (from $\mathbf{Y}_{-k}$) as Y_2, and Y_k as Y_1. Thus, the dependence of each marginal of $\mathbf{Y}_{-k}$ on Y_k is modeled explicitly. The residual dependence structure among the marginals of $\mathbf{Y}_{-k}$ is expected to be captured by sampling from the standardized multivariate residual vector $\mathbf{Z}_{|k}$.

5.3. Proposed Approach for Multivariate Regional Frequency Analysis (MRFA)

This section presents the conditional extreme values approach (CEA) proposed for MRFA. It is developed by adapting the CMEV model (Heffernan and Tawn, 2004; Keef et al., 2013). It is useful to arrive at the joint distribution of multiple flood-related variables/characteristics (e.g., flood peak, volume) at sparsely gauged and ungauged locations. Let $\mathbf{Q}^{(i)} = \left[Q_1^{(i)}, \ldots, Q_m^{(i)} \right]$ denote a matrix containing *m* characteristics of independent peak flow events recorded at *i*-th among *N* sites in a given region. Further, suppose $Q_j^{(i)} = \left[q_{j,1}^{(i)}, \ldots, q_{j,n_i}^{(i)} \right]^{\mathrm{T}}$ is a vector containing n_i observations of the *j*-th variable. The steps involved in MRFA are as follows:

1) At each site $i \in (1, \ldots, N)$, transform the observed sample of each variable $Q_j^{(i)}; j \in (1, \ldots, m)$ independently using Equation (A6.5) to obtain $\mathbf{Y}^{(i)} = \left[Y_1^{(i)}, \ldots, Y_m^{(i)} \right]$. The empirical distribution of observations (based on their ranks) of each variable could be used for mapping it to non-dimensional space. It could be based on Weibull plotting position $F_j\left(q_{j,l}^{(i)}\right) = 1 - r_l / (n_i + 1)$, where r_l is the rank of *l*-th observation $q_{j,l}^{(i)}$ at site *i* that is determined after sorting values of $Q_j^{(i)}$ in ascending order of their magnitude.
2) Pool the transformed samples of all the sites in the region (i.e., $\left\{ \mathbf{Y}^{(i)}; i = 1, \ldots, N \right\}$) to obtain the regional sample $\mathbf{Y}$. Select an appropriate threshold $u > 0$ for the primary variable of interest Y_k (e.g., flood peak) in the transformed domain, such that Y_k is independent of $\mathbf{Z}_{|k}$ for all the values of $Y_k > u$. For this purpose, consider Y_k as Y_1 and select one of the *m*-1 variables from $\mathbf{Y}_{-k}$ at a

time and refer to it as Y_2. Sort Y_1 values in ascending order of their magnitude and perform the following steps.

(i) Choose each positive value of Y_1 (in the sorted values) as a threshold u and estimate the dependence parameters $\alpha_{2|1}$ and $\beta_{2|1}$ by numerically maximizing the log-likelihood function (Equation 5.3).

(ii) Obtain the residuals $Z_{2|1}\big|Y_1 > u$ using Equation (A6.8) and test the hypothesis of independence between $Y_1 > u$ and $Z_{2|1}\big|Y_1 > u$ using Hilbert-Schmidt independence criterion (Gretton et al., 2007) and obtain the corresponding *p*-value.

3) Repeat steps 2(i) and 2(ii) for each of the *m*-1 variables in $\mathbf{Y}_{-k}$ and identify the optimal value of the threshold u (referred to as u_o) as the least value of Y_1 (i.e., Y_k) for which the null hypothesis of independence cannot be rejected for all variables in $\mathbf{Y}_{-k}$ at a prespecified significance level (say 10%).

4) For each variable Y_j in $\mathbf{Y}_{-k}$, obtain estimates of regional parameters ($\hat{\alpha}_{j|k}$ and $\hat{\beta}_{j|k}$) depicting its dependence on the primary variable Y_k by numerically maximizing the log-likelihood function (Equation A6.3) conditional on values of Y_k exceeding the optimal threshold u_o. The estimated parameters corresponding to all the variables in $\mathbf{Y}_{-k}$ are used to form the regional parameter vectors $\hat{\boldsymbol{\alpha}}_{|k}$ and $\hat{\boldsymbol{\beta}}_{|k}$.

5) Obtain the set of standardized residuals using the following equation by interpreting vector algebra componentwise.

$$\hat{\mathbf{Z}}_{|k} = \frac{\mathbf{Y}_{-k} - \hat{\boldsymbol{\alpha}}_{|k} y_{k,t}}{y_{k,t}^{\hat{\boldsymbol{\beta}}_{|k}}} \quad \forall\, y_{k,t} > u_o \tag{A6.11}$$

6) Simulate n_E (say 1000) synthetic events for the region in the transformed domain. For this purpose, generate values of $\hat{y}_k$ such that $\hat{y}_k > u_o$ and $\hat{y}_k - u_o$ follows a standard exponential distribution. Corresponding to each $\hat{y}_k$ value, randomly sample a vector from the set $\hat{\mathbf{Z}}_{|k}$ obtained in Step (5), then estimate $\hat{\mathbf{Y}}_{-k}$ corresponding to $\hat{y}_k$ using Equation (A6.10), considering $\hat{\boldsymbol{\alpha}}_{|k}$ for $\boldsymbol{\alpha}_{|k}$, $\hat{\boldsymbol{\beta}}_{|k}$ for

$\boldsymbol{\beta}_{|k}$, $\hat{y}_k$ for Y_k, and $\hat{\mathbf{Z}}_{|k}$ for $\mathbf{Z}_{|k}$. Inverse transform the simulated vector $\hat{\mathbf{Y}}_{-k}$ along with its corresponding $\hat{y}_k$ using Equation (A6.12) to arrive at data points of the corresponding marginal variables $\hat{\mathbf{Q}}^{(i)} = \left[\hat{Q}_1^{(i)}, \ldots, \hat{Q}_m^{(i)}\right]$ for the target site *i* in the original space.

$$\hat{Q}_{i,j} = \begin{cases} F_{i,j}^{-1}\left[\dfrac{e^{\hat{y}_j}}{2}\right] & \text{for } \hat{y}_j \le 0 \\ F_{i,j}^{-1}\left[1-\dfrac{e^{-\hat{y}_j}}{2}\right] & \text{for } \hat{y}_j \ge 0 \end{cases} \qquad i = 1,\ldots,N;\ j = 1,\ldots,m \tag{A6.12}$$

where $F_{i,j}^{-1}(\cdot)$ is the quantile function of the *j*-th variable corresponding to the target site *i*. Form of $F_{i,j}(\cdot)$ and its parameters can be estimated reliably using at-site observations if adequate data are available at the target site. However, if the target site is ungauged or has inadequate data, the form of $F_{i,j}(\cdot)$ could be considered to be the same as that of a majority of gauged sites in the region. Furthermore, the parameters can be estimated based on regional information using various strategies. One strategy is to use regression relationships developed between each of the parameters and site-specific attributes which influence the variable being analyzed. To facilitate this, the site-specific attributes are chosen such that they are available even for ungauged locations. In applications where the spatial extent of the study area is large, one can delineate the area into homogeneous regions using any effective procedure (e.g., Kiran & Srinivas, 2021b) and apply the proposed methodology to each of the delineated regions.

Section 7

Impacts on meteorological/hydrologic droughts

7.1. Introduction

The Mahanadi basin receives uneven rainfall, and erratic southwest monsoons can cause droughts. It is more prone to floods and cyclones on the eastern coast, and drought-prone areas are found in the central part of the basin covering about 14 (5 of Chhattisgarh and 9 of Odisha) of 45 districts encompassing the basin. In Chattisgarh state, located in the upstream part of Mahanadi, the total number of climatological drought years varied from 53 to 66 years during 1901-2010 (Mahesh et al., 2018), and drought frequency has increased in recent decades. The majority of witnessed droughts events could be classified as mild, whereas severe/disastrous droughts events are very rare. Mahasamund, Dhamtari, and Raigarh districts and more prone to droughts, and Bilaspur and Janjgir districts are relatively less drought-prone (Mahesh et al., 2018). Recent droughts in Odisha state (located in the downstream part of Mahanadi) were witnessed in 2015 and 2018. The majority of about nine districts affected by the 2018 droughts are located in western Odisha, adjoining Chattisgarh state. The spatial extent of the 2015 droughts was much larger, affecting at least 25 of the 30 districts.

Droughts are the most complex natural hazards whose onset is often followed by a trail of impacts on society, ecology, the environment, and the economy. The spatial-temporal characteristics of droughts differ significantly across different regions in the world (Herrera-Estrada et al., 2017). The complexity of drought characterization increases due to the difficulty in formulating the proper definition of drought (Soľáková et al., 2014). In general, the onset of meteorological drought occurs due to adverse meteorological situations (e.g., a deficit of precipitation and humidity and an increase in temperature). Persistence of meteorological drought, anywhere from (i) 1 month to 6 months, impacts agricultural productivity causing agricultural drought, (ii) about 6 months to 24 months or more could lead to hydrological drought through a deficit in both surface and groundwaters (WMO, 2012), causing a reduction in the availability of water for drinking, irrigation, industrial needs, and hydropower production. Subsequently, it leads to socio-economic drought.

Recent decades witnessed interest in developing different methodologies and indices to analyze droughts due to an increase in their frequency/intensity and associated losses (e.g., Kao and

Govindaraju, 2010; Mishra and Singh, 2010; Li et al., 2015; Asadi Zarch et al., 2015; Mallya et al., 2013). Examples include the Standardized Precipitation Index (SPI; Mckee et al., 1993), Standardized Precipitation Evapotranspiration Index (SPEI; Vicente-Serrano et al., 2010), Reconnaissance Drought Index (RDI; Tsakiris and Vangelis, 2005), and Standardized Deficit Distance Index (SDDI; Vergni et al., 2021) for meteorological droughts, Standardized Runoff Index (SRI; Shukla and Wood, 2008) and Standardized Hydrological Index (SHI; Sharma and Panu, 2010) for hydrological droughts, Palmer Drought Severity Index (PDSI; Palmer, 1965), Standardized Soil Moisture Index (SSI; Hao and AghaKouchak 2013), and Agricultural Standardized Precipitation Index (aSPI; Tigkas et al., 2019) for agricultural droughts. Mishra and Singh (2010) demonstrated applications of copula-based models for multivariate drought characterization.

Multivariate standardized drought indices (MSDIs), such as SPEI, RDI, and SDDI, which consider the information of both precipitation and ET_0, are deemed more effective than univariate indices like SPI (which depends only on precipitation) in characterizing, monitoring, and forecasting drought events over various spatial-temporal scales. The PET accounts for different hydrometeorological variables (e.g., temperatures, wind speed, relative humidity, solar radiation) affecting droughts. Globally, the loss of approximately 60% of land surface precipitation water from river basins is attributable to evapotranspiration. An increase in potential/reference evapotranspiration can intensify dry conditions in arid and semi-arid regions of the world where water resources are limited (Masanta and Srinivas, 2022).

7.2. Theoretical background

Estimates of drought intensity corresponding to different Accumulation Periods (APs) were obtained using the Standardized Precipitation Evapotranspiration Index (SPEI).

Let $P_{\upsilon,\tau}$ and $\mathrm{PET}_{\upsilon,\tau}$ denote the precipitation and potential evapotranspiration corresponding to month τ (=1,…,12) in the year υ (=1,…, N). The water surplus or deficit (i.e., climate water balance) corresponding to the AP of M months is calculated at a month τ in the year υ as,

$$d_{\upsilon,\tau}^{M} = \sum_{t=13-M+\tau}^{12} \left(P_{\upsilon-1,t} - \mathrm{PET}_{\upsilon-1,t}\right) + \sum_{t=1}^{\tau} \left(P_{\upsilon,t} - \mathrm{PET}_{\upsilon,t}\right) \quad \text{if } \tau < M$$

$$d_{\upsilon,\tau}^{M} = \sum_{t=\tau-M+1}^{\tau} \left(P_{\upsilon,t} - \mathrm{PET}_{\upsilon,t}\right) \quad \text{if } \tau \geq M \qquad (1)$$

The time series obtained for $d_{\upsilon,\tau}^{M}$ was subdivided into subseries d_{τ}^{M} corresponding to each month τ. Then a Generalised extreme value (GEV) distribution was fitted to each subseries d_{τ}^{M}. The non-exceedance probability corresponding to d_{τ}^{M} was then transformed to a standard normal variable (i.e., SPEI) using the approximate transformation. Based on the SPEI value, months were classified into seven intensity levels: extreme wet ($\mathrm{SPEI}>2$), severe wet ($1.5<\mathrm{SPEI}\leq 2$), moderate wet ($1<\mathrm{SPEI}\leq 1.5$), normal ($-1<\mathrm{SPEI}\leq 1$), moderate dry ($-1.5<\mathrm{SPEI}\leq -1$), severe dry ($-2<\mathrm{SPEI}\leq -1.5$), and extreme dry ($\mathrm{SPEI}\leq -2$).

Various drought characteristics were analyzed to assess the impacts and changes in drought events for various SSP-FS with respect to the historical period. The MFD characteristics considered include (i) relative frequency/probability of occurrence, (ii) mean critical severity, and (iii) mean annual duration. The relative frequency is defined as the ratio of the number of moderate, severe, or extreme drought months to the total number of months considered in the period analyzed. The mean annual drought duration is determined as the mean of the total number of months in a year experiencing droughts (i.e., $\mathrm{SPEI}\leq -1$). The mean annual critical severity of a drought event is defined as the mean of annual minimum SPEI values less than -1.

7.3. Results and discussion

Future projections of the ensemble mean time series of PET and precipitation derived at 0.25° resolution from three GCMs (CanESM5 (2.7906°×2.8125°), INM-CM4-8 (1.5°×2°), and INM-CM5-0 (1.5°×2°)) were used to arrive at future projections of SPEI for near-future (2015-2040) and distant future (2041-2100) periods corresponding to 1-, 3- and 6-months accumulation periods. The SPEI values were subsequently used to identify moderate, severe, and extreme dry months and determine projected changes in relative frequency (RF), mean annual critical severity, and mean annual duration of droughts.

The RF of occurrence was highest for moderate drought events and least for extreme drought events in the case of both historical and future climate change scenarios. The RF is found to be increasing for future climate change scenarios when compared to the historical period. The highest increase in RF is found for SSP5-8.5, and the lowest is found for the SSP1-2.6 scenario. When compared to the far future (2041-2100), the near future (2015-2040) is projected to experience the highest RF of moderate

and severe droughts events. For SSP3-7.0 and SSP5-8.5 scenarios, the RFs of moderate drought events are projected to increase with the accumulation period (AP), and they are found to be highest for SSP5-8.5 scenario with 6-month AP.

The mean annual critical severity of droughts is found to be increasing with projected future climate change scenarios for all durations. For the historical period, the highest critical severity for 1-month AP is experienced in the lower reaches of the Mahanadi basin, whereas that of 3-month AP is found in the upper reaches of the basin. When compared to the far future (2041-2100), the near future (2015-2040) is projected to experience the highest mean annual critical severity of droughts events. The mean annual critical severity of droughts is found to be decreasing with an increase in AP. Hence the lowest critical severity is found for the drought events computed for 6 months AP for the far future for all SSP forcing scenarios. The critical severity is found to be higher for the SSP5-8.5 scenario, and it is relatively lower but comparable for SSP1-2.6, SSP2-4.8, and SSP3-7.0 scenarios in the case of the near-future period. Whereas in the case of the far future, it is found to be lowest for SSP5-8.5 and highest for the SSP1-2.6 scenario.

The mean annual drought duration is found to be increasing for all SSP future climate projections when compared to the historical period. Across all the APs considered, the mean annual duration of droughts for the historical period is approximately 1-month. Similar to RF and mean annual critical severity, mean annual drought duration is also highest for the near future when compared to the far future. In the case of the near future, the highest mean annual duration of droughts is found to be rising with an increase in AP. Across all the SSP scenarios considered, droughts events computed considering 6-month AP for SSP5-8.5 showed the highest mean annual drought duration.

Relative Frequency (RF) of droughts

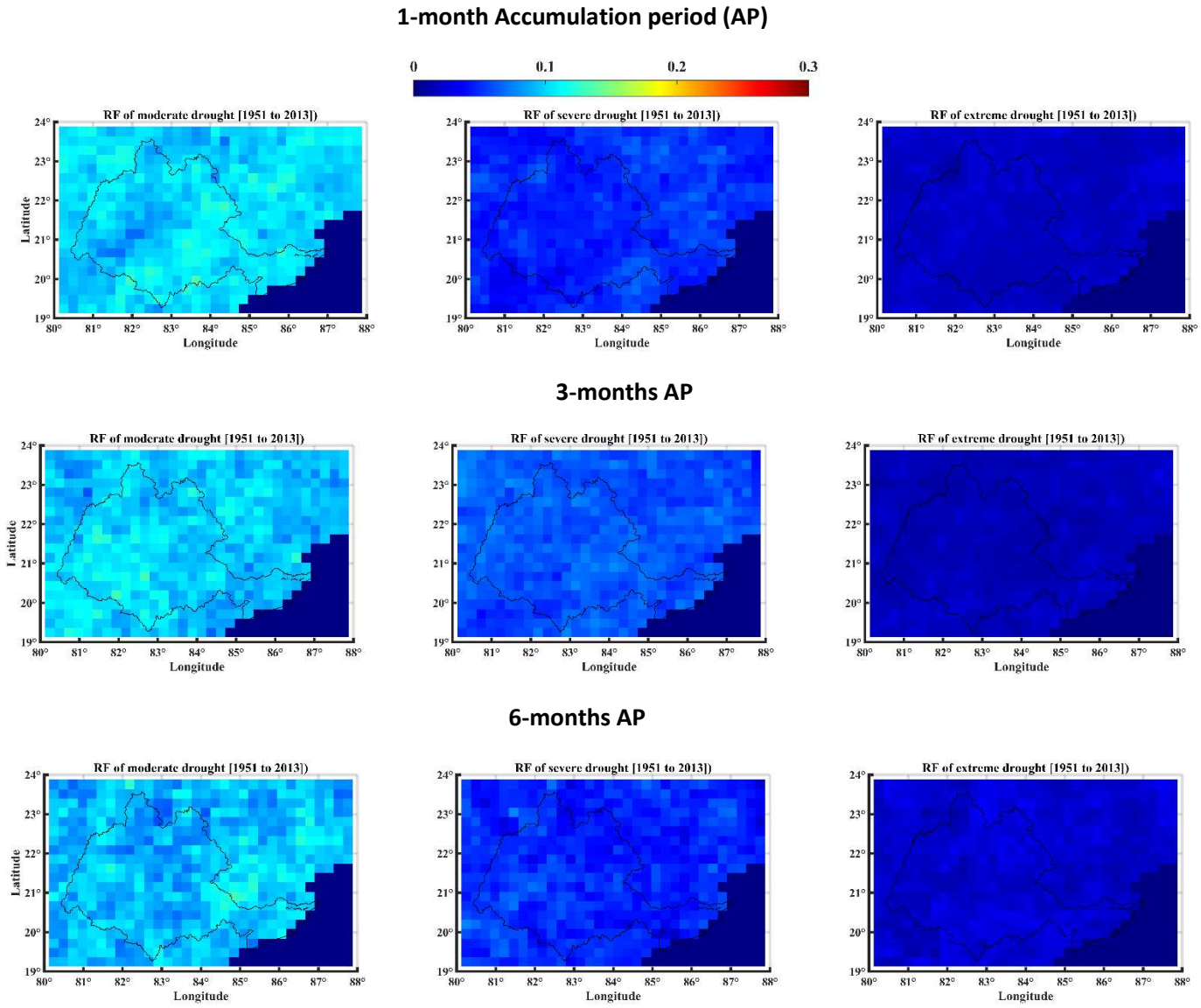

Figure 7.1: Historical Relative Frequency (RF) of droughts in Mahanadi basin.

Scenario: SSP1-2.6; **Accumulation period:** 1-month

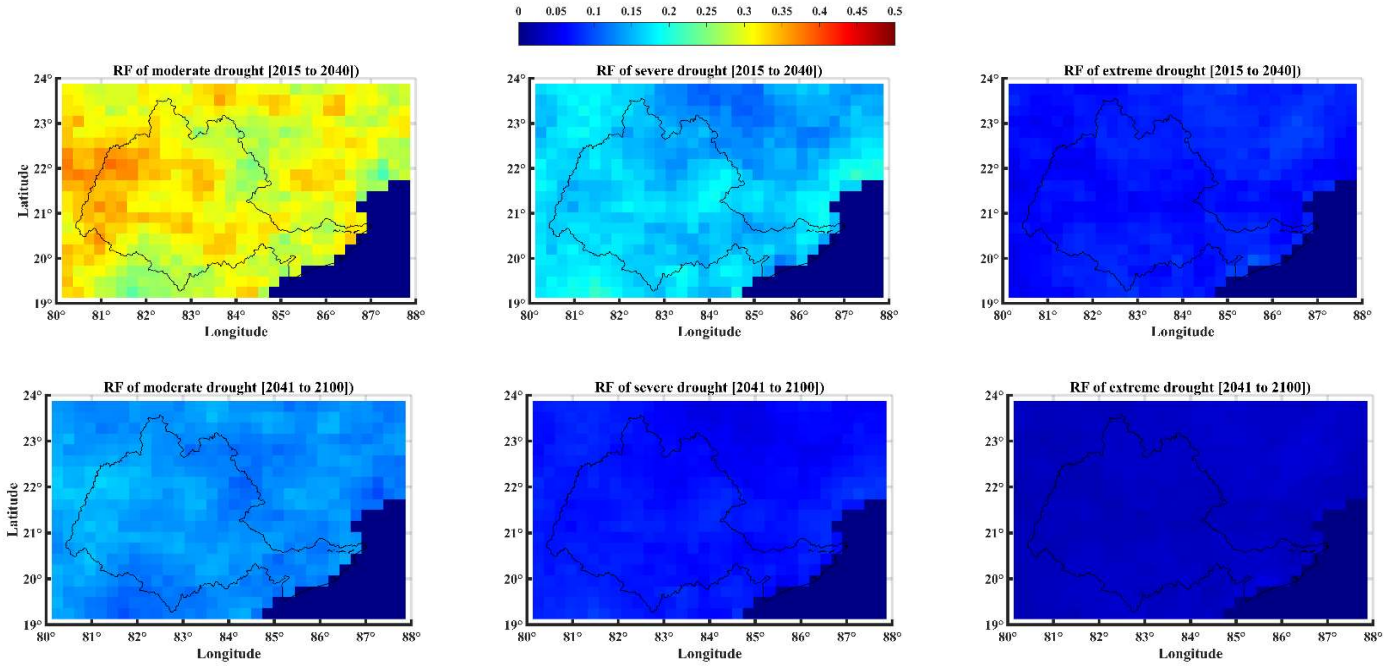

Scenario: SSP1-2.6; **Accumulation period:** 3 months

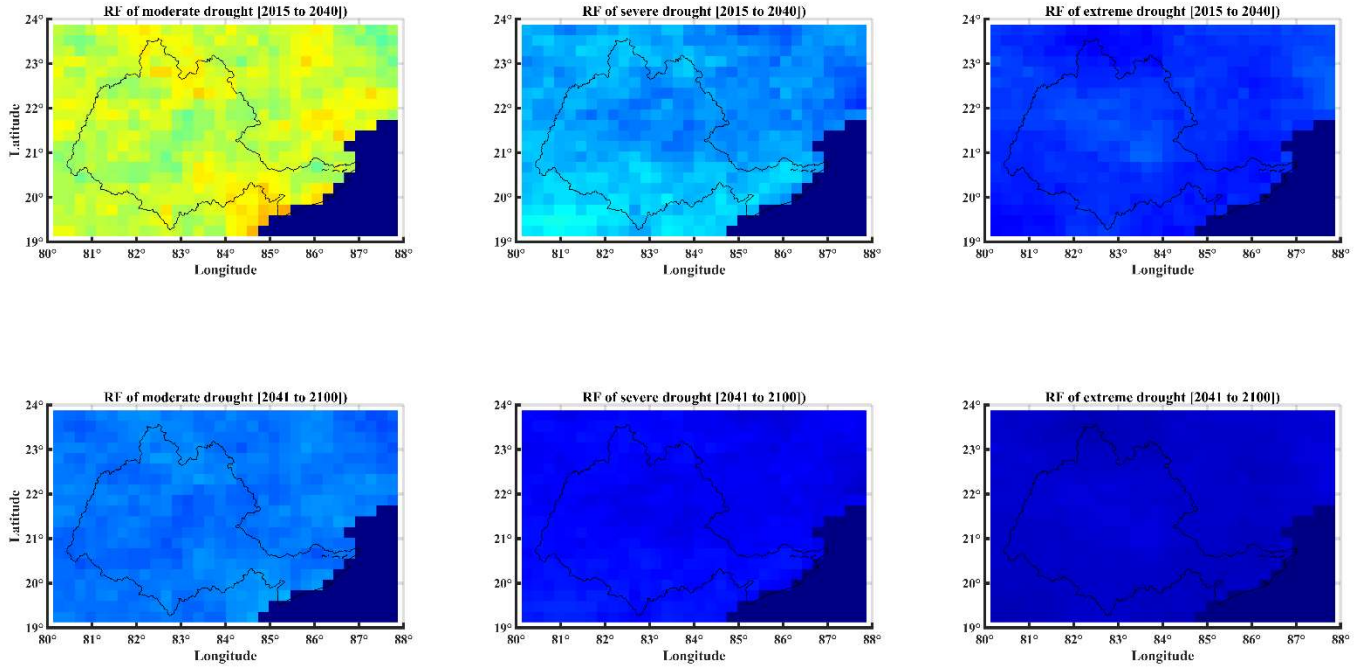

Figure 7.2: Future projections for Relative Frequency (RF) of droughts in the Mahanadi basin obtained corresponding to 1-, 3- and 6- months accumulation periods and four SSP scenarios (SSP1-2.6, SSP2-4.8, SSP3-7.0, and SSP5-8.5) for near-future (2015-2040) and distant future (2041-2100) periods.

Figure 7.2 (continued…)

Scenario: SSP1-2.6; **Accumulation period:** 6 months

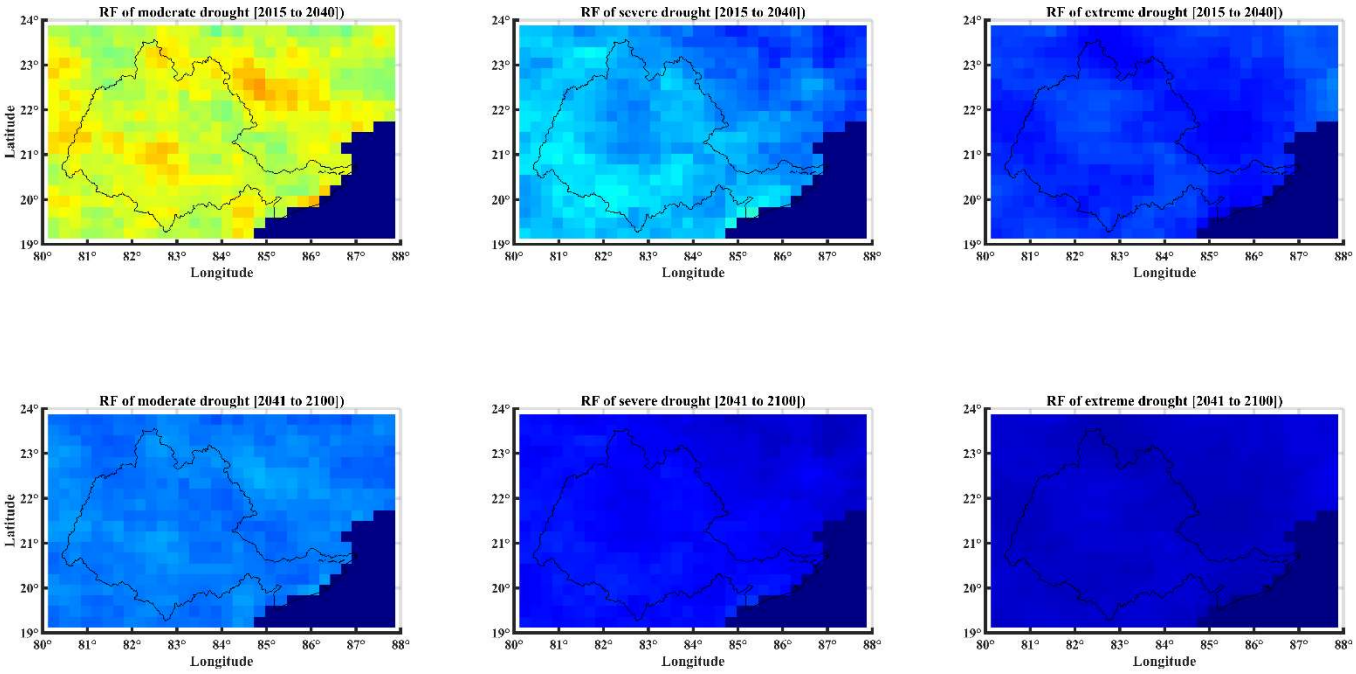

Scenario: SSP2-4.8; **Accumulation period:** 1 month

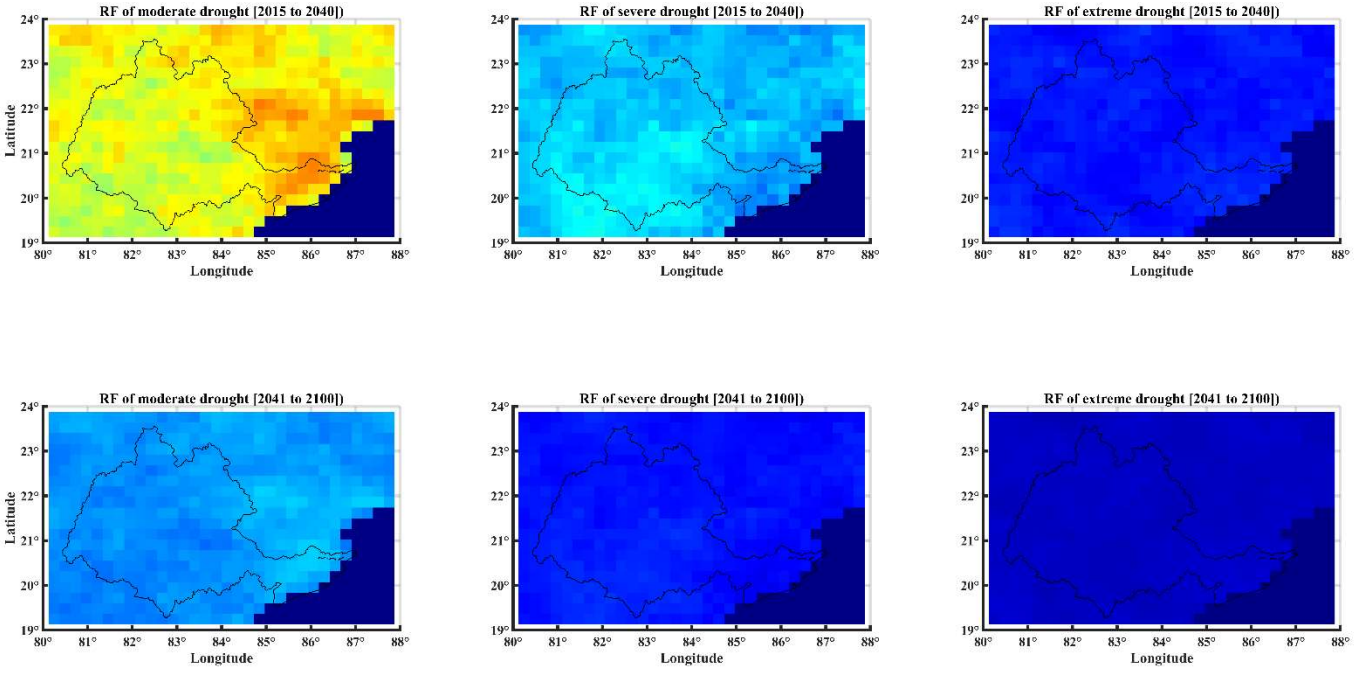

Figure 7.2 (continued…)

Scenario: SSP2-4.8; **Accumulation period:** 3 months

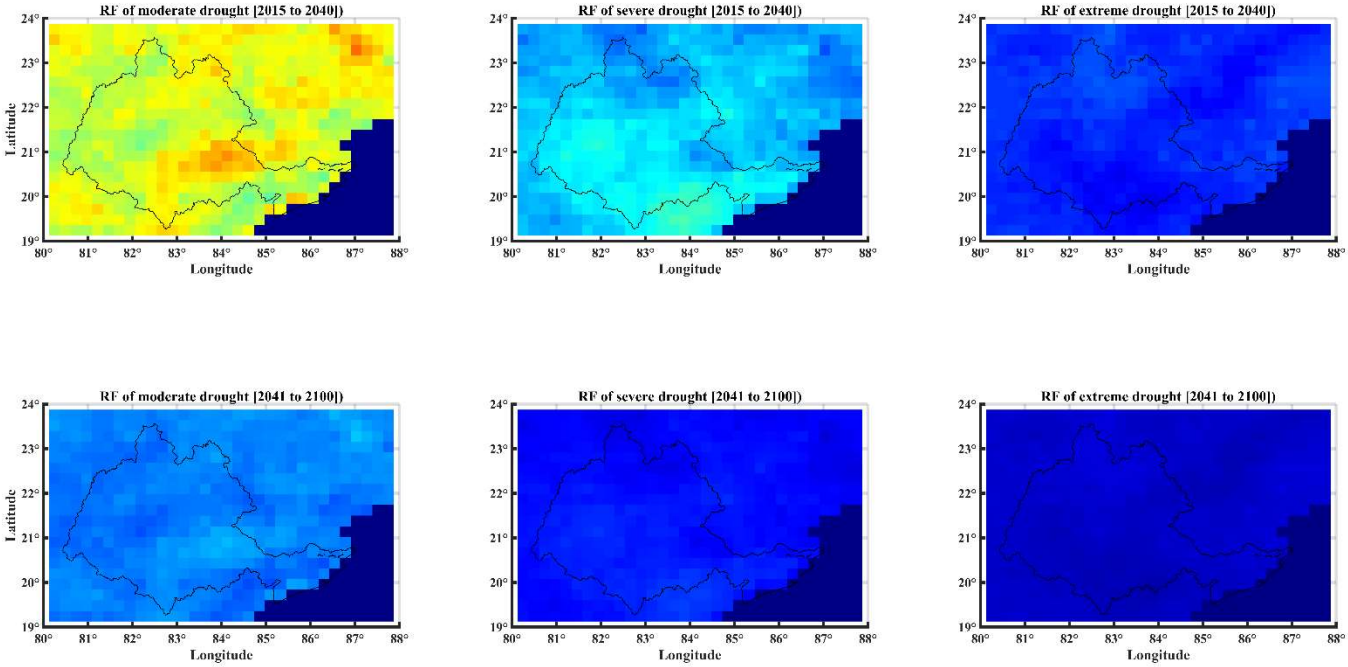

Scenario: SSP2-4.8; **Accumulation period:** 6 months

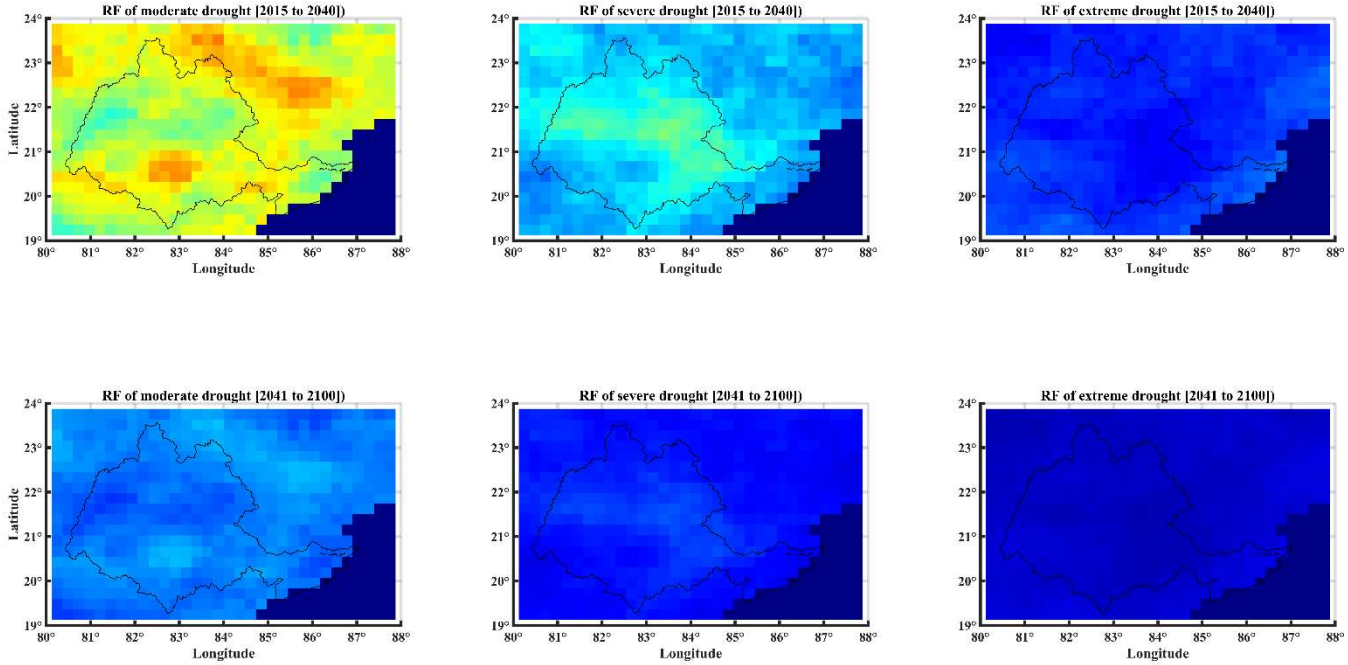

Figure 7.2 (continued…)

Scenario: SSP3-7.0; **Accumulation period:** 1 month

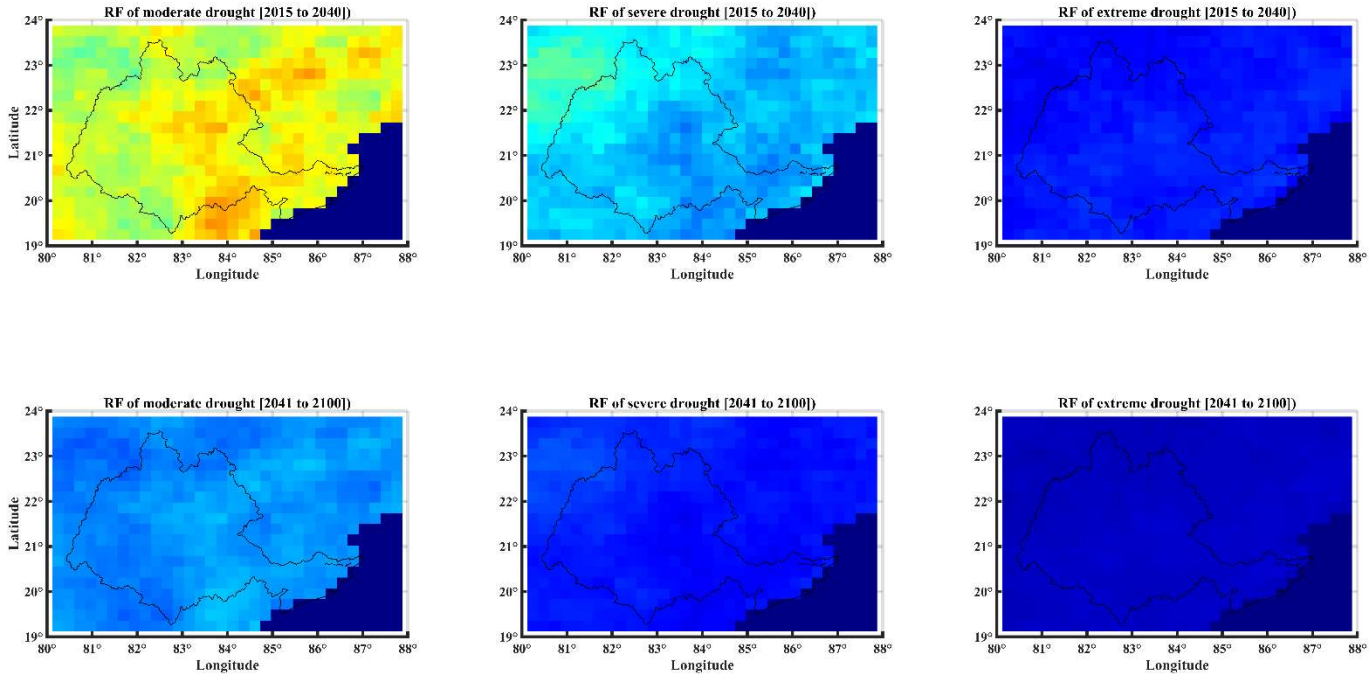

Scenario: SSP3-7.0; **Accumulation period:** 3 months

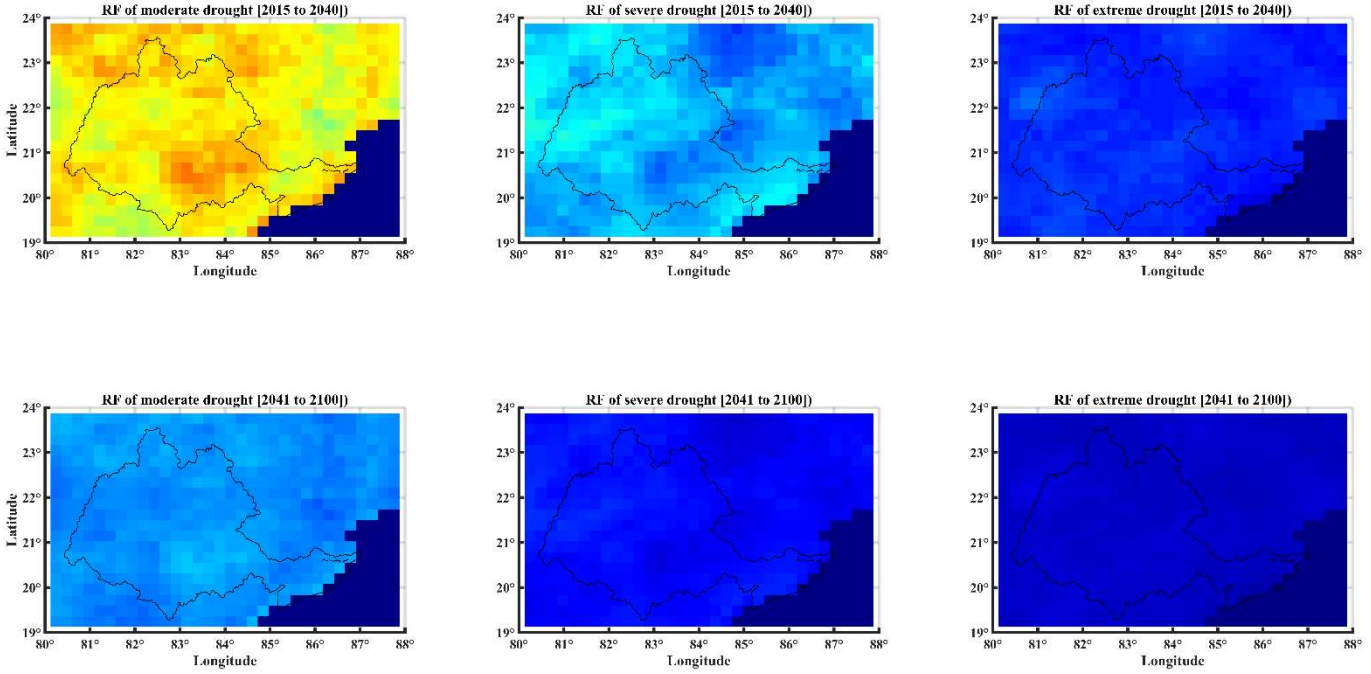

Figure 7.2 (continued…)

Scenario: SSP3-7.0; **Accumulation period:** 6 months

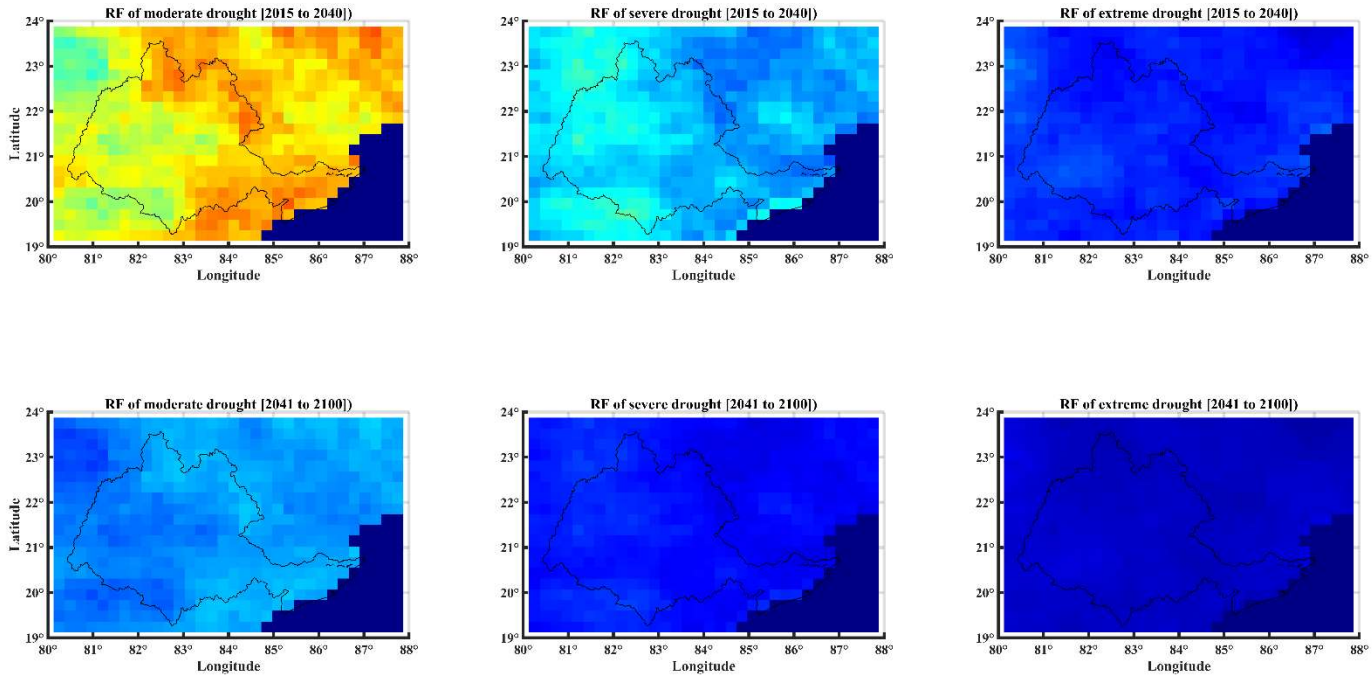

Scenario: SSP5-8.5; **Accumulation period:** 1 month

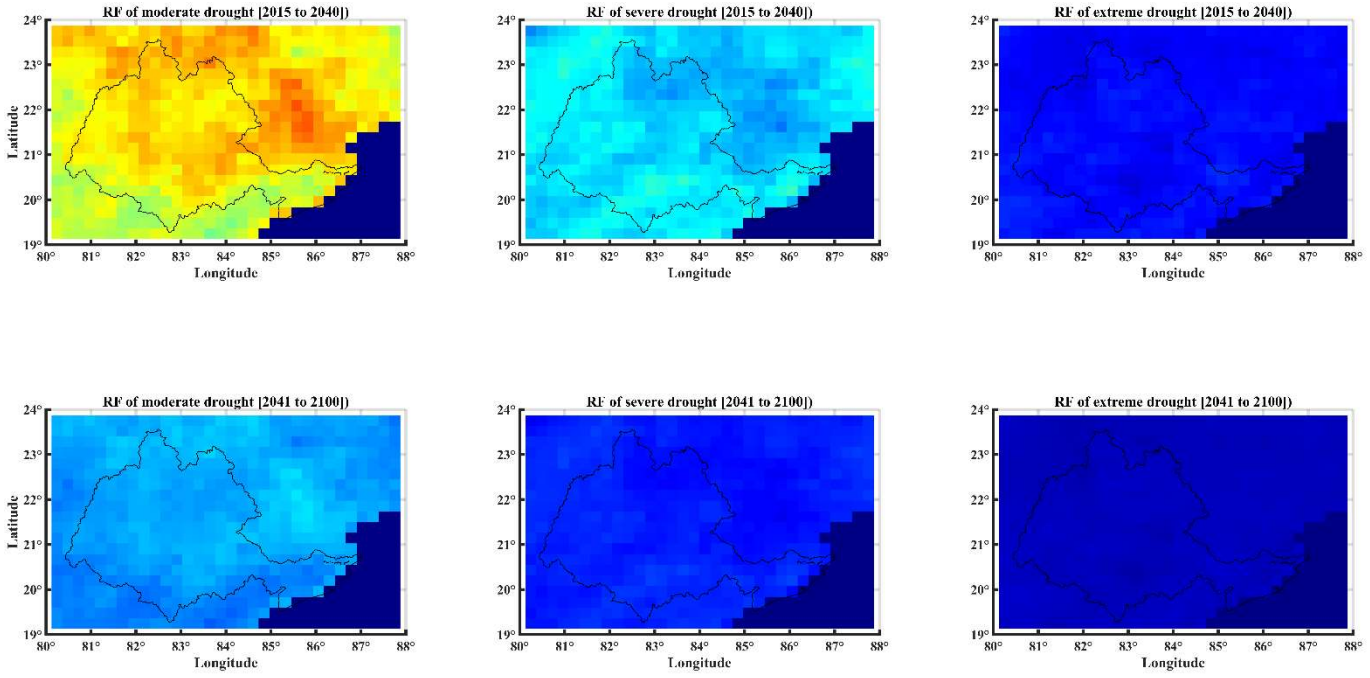

Figure 7.2 (continued…)

Scenario: SSP5-8.5; **Accumulation period:** 3 months

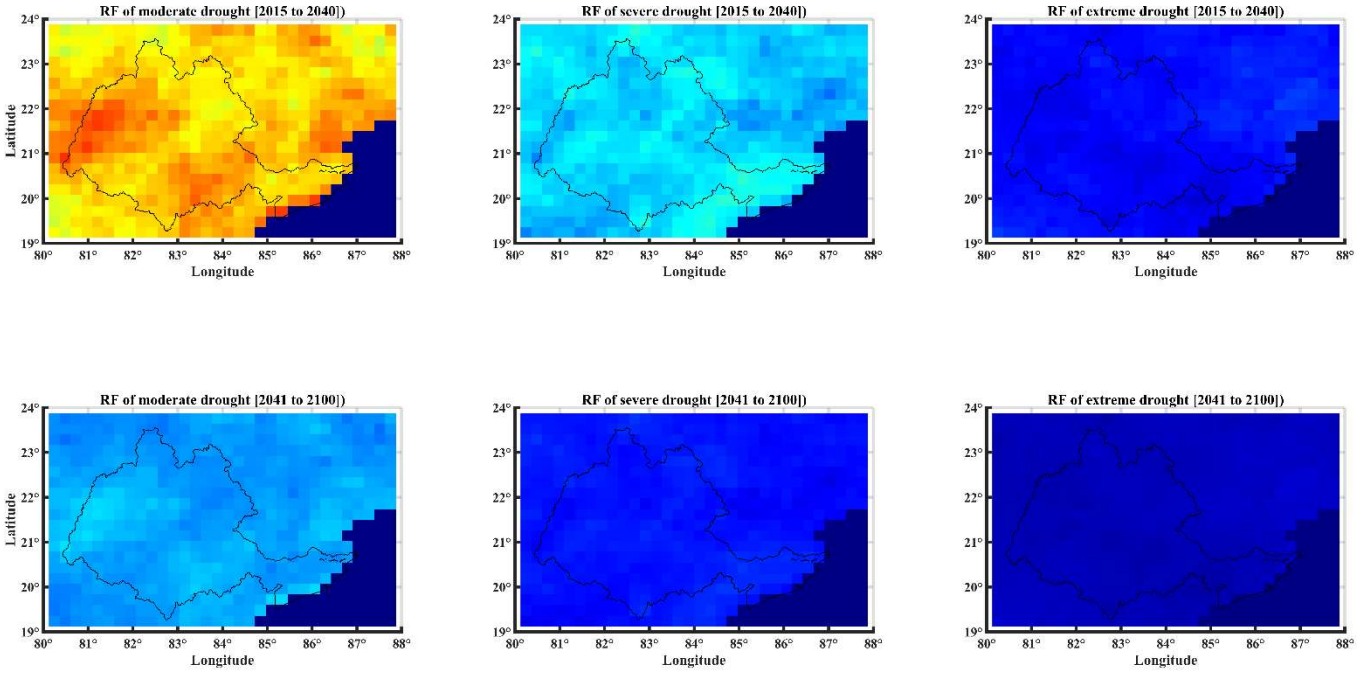

Scenario: SSP5-8.5; **Accumulation period:** 6 months

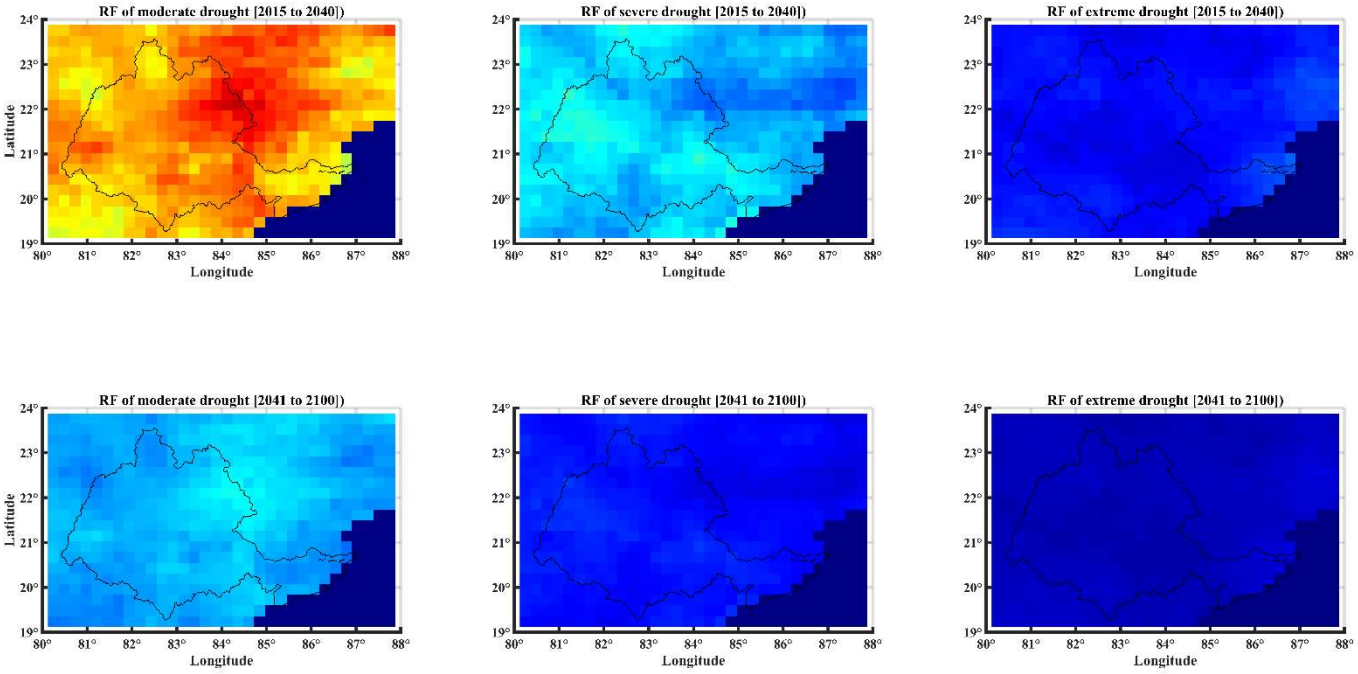

Mean annual critical severity of droughts

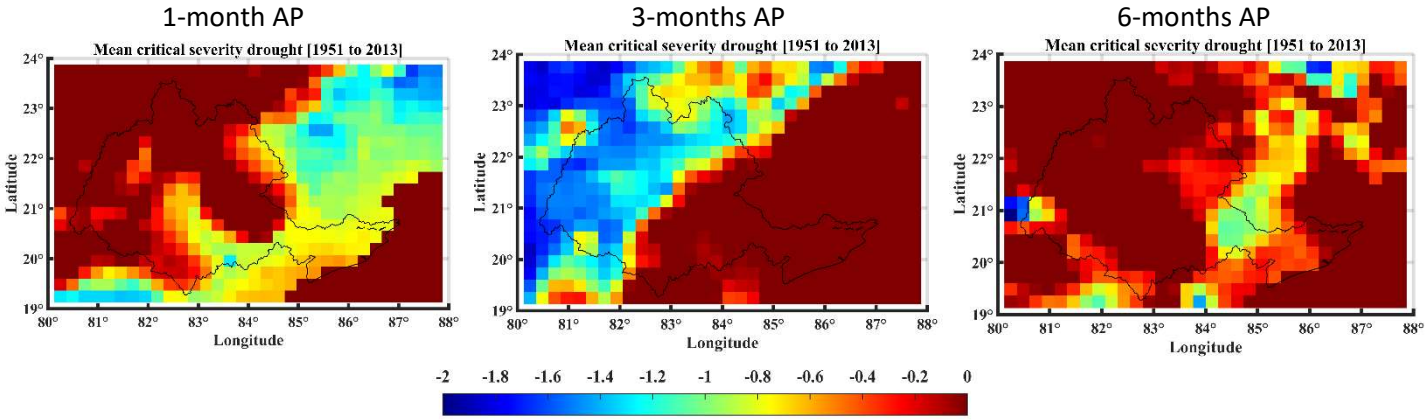

Figure 7.3: Mean annual critical severity of droughts in Mahanadi basin corresponding to 1, 3, and 6 months Accumulation Periods (APs) over the historical period.

Scenario: SSP1-2.6**; Accumulation period:** 1-month

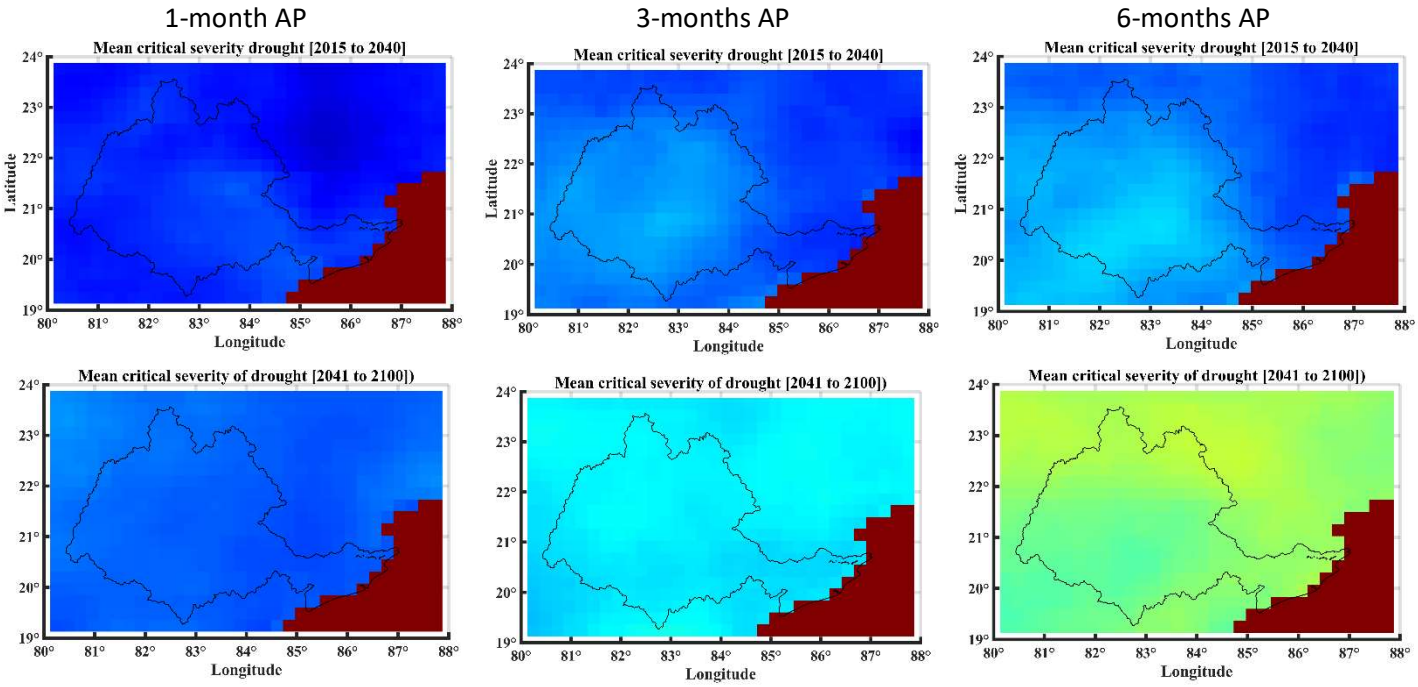

Figure 7.4: Future projections for mean annual critical severity of droughts in Mahanadi basin corresponding to 1, 3, and 6 months Accumulation Periods (APs). Plots are shown for SSP1-2.6, SSP2-4.8, SSP3-7.0, and SSP5-8.5 scenarios and for near-future (2015-2040) and distant future (2040-2100) periods.

Figure 7.4 (continued…)

Scenario: SSP2-4.8

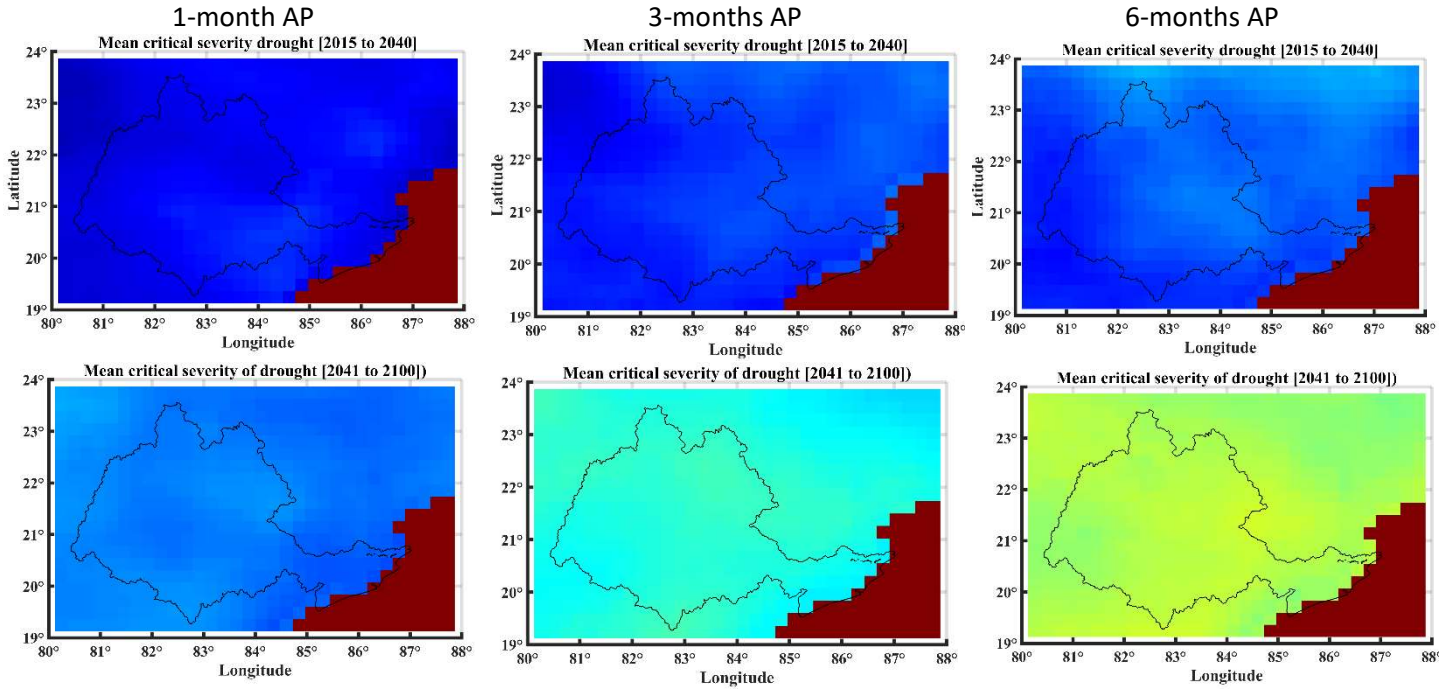

Scenario: SSP3-7.0

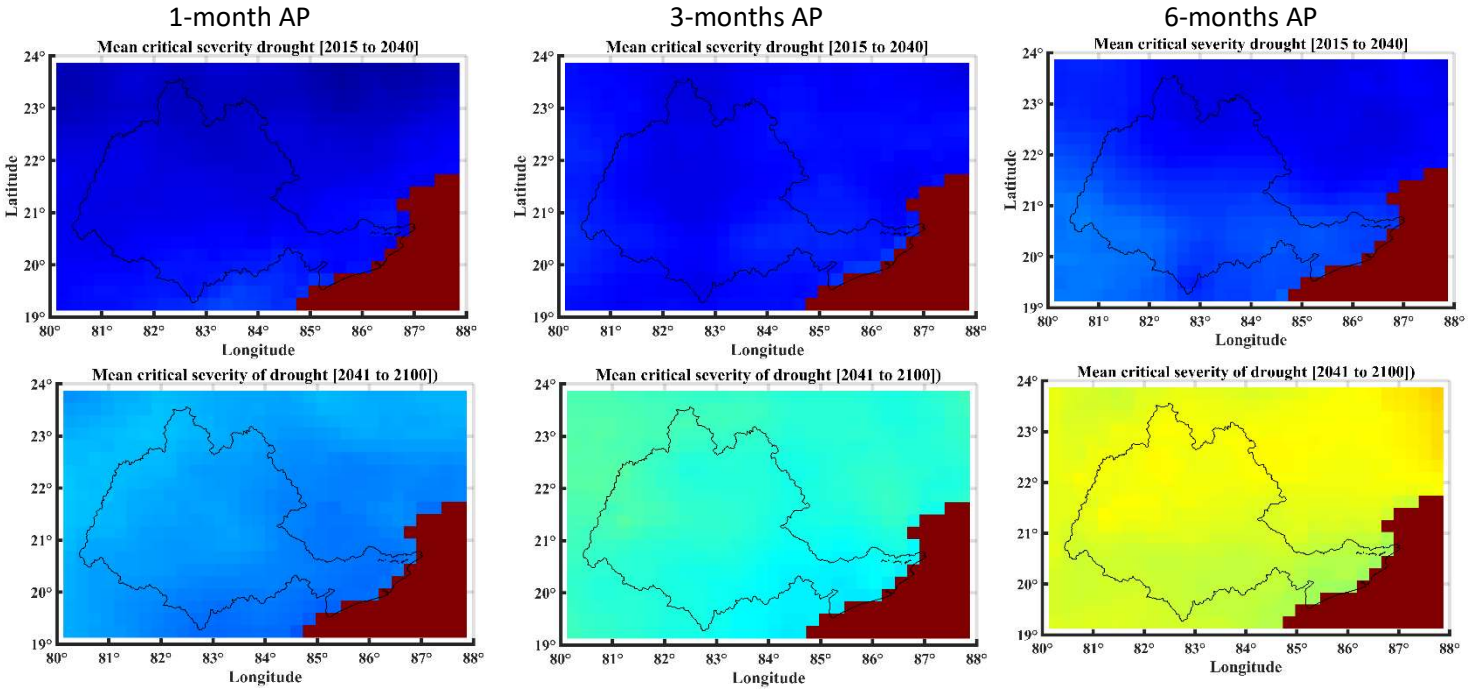

Figure 7.4 (continued…)

Scenario: SSP5-8.5

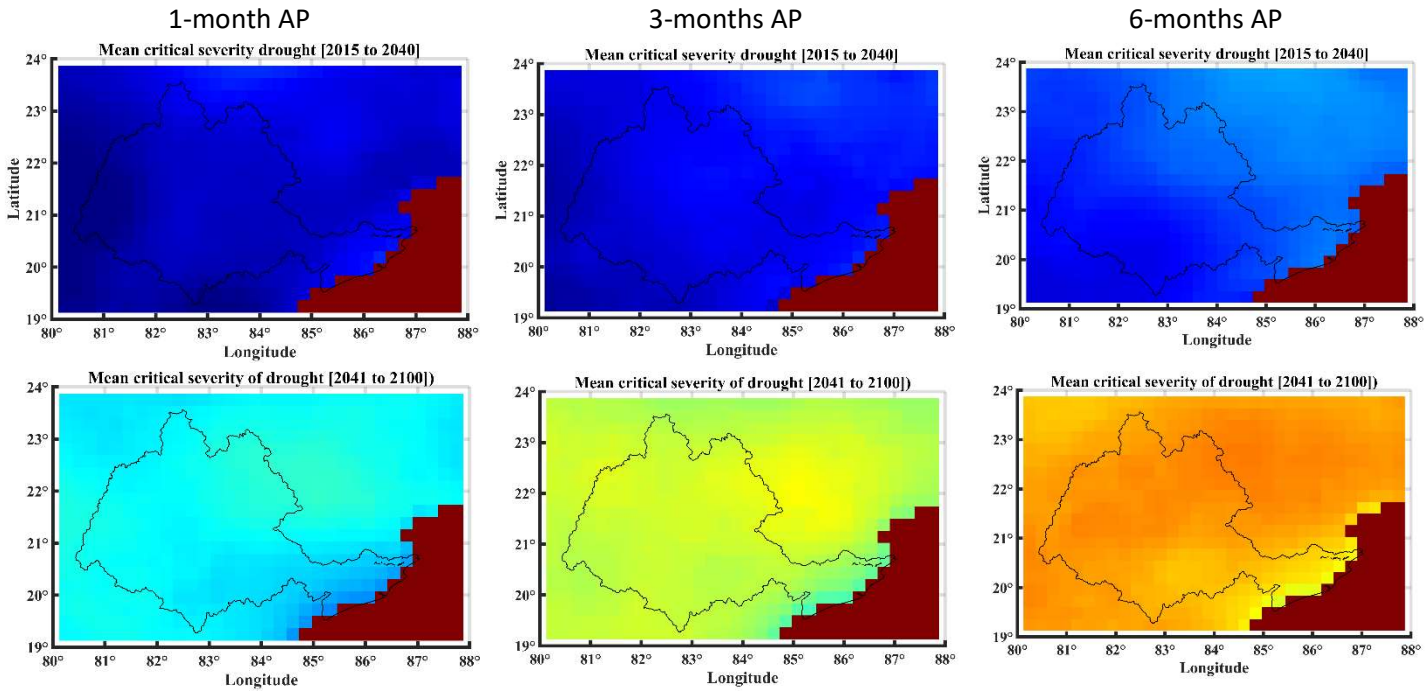

Mean annual duration of droughts

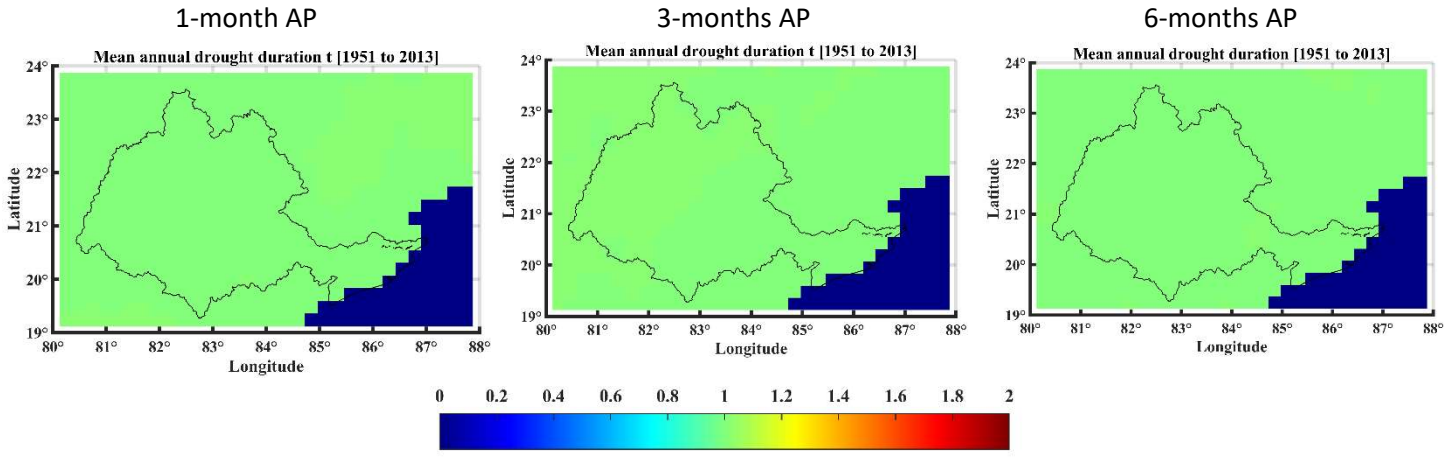

Figure 7.5: Mean annual duration of droughts in Mahanadi basin corresponding to 1, 3, and 6 months Accumulation Periods (APs) over the historical period.

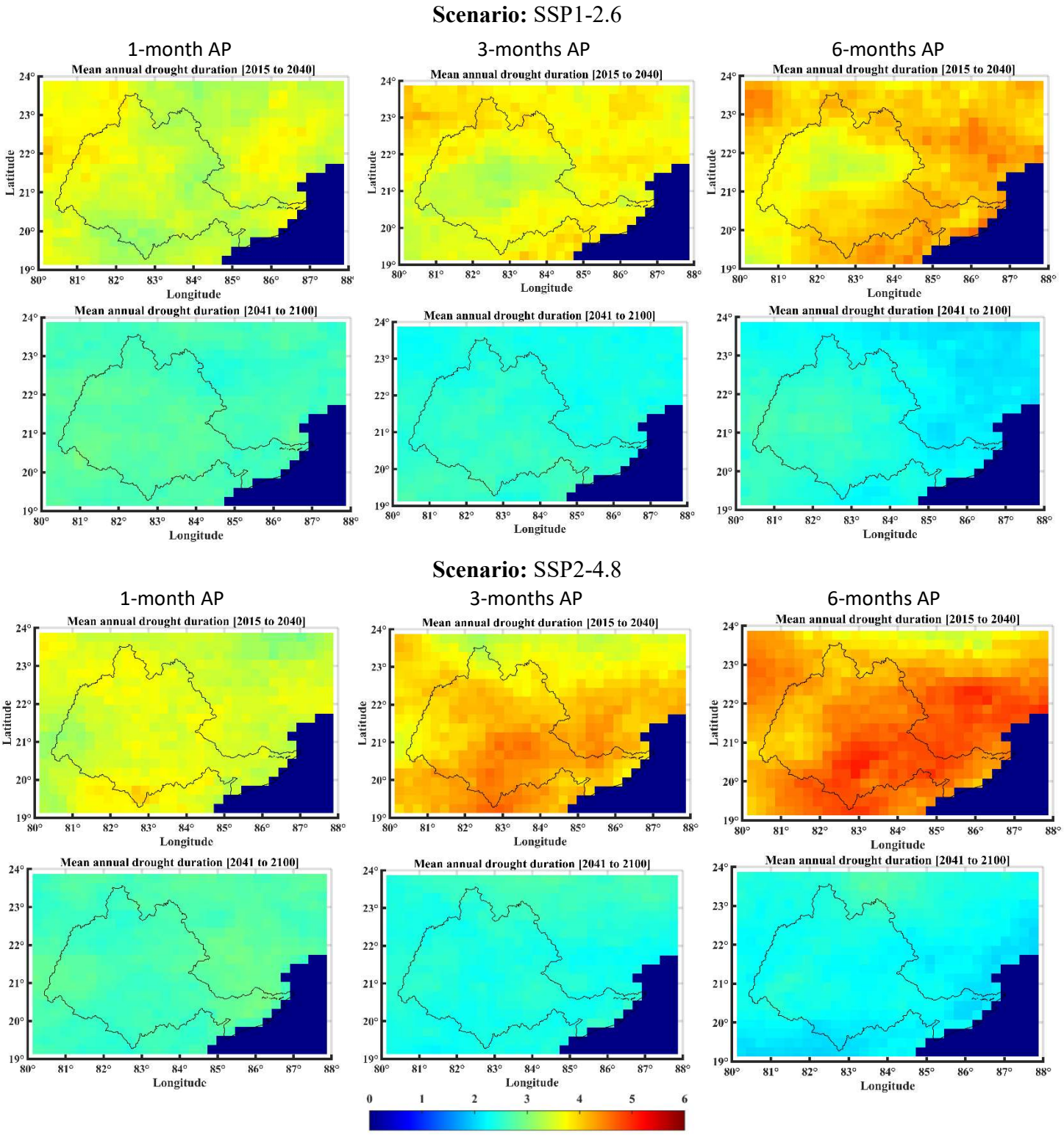

Figure 7.6: Future projections for the mean annual duration of droughts in the Mahanadi basin corresponding to 1, 3, and 6 months Accumulation Periods (APs). Plots are shown for SSP1-2.6, SSP2-4.8, SSP3-7.0, and SSP5-8.5 scenarios and for near-future (2015-2040) and distant future (2040-2100) periods.

Figure 7.6 (continued…)

Scenario: SSP3-7.0

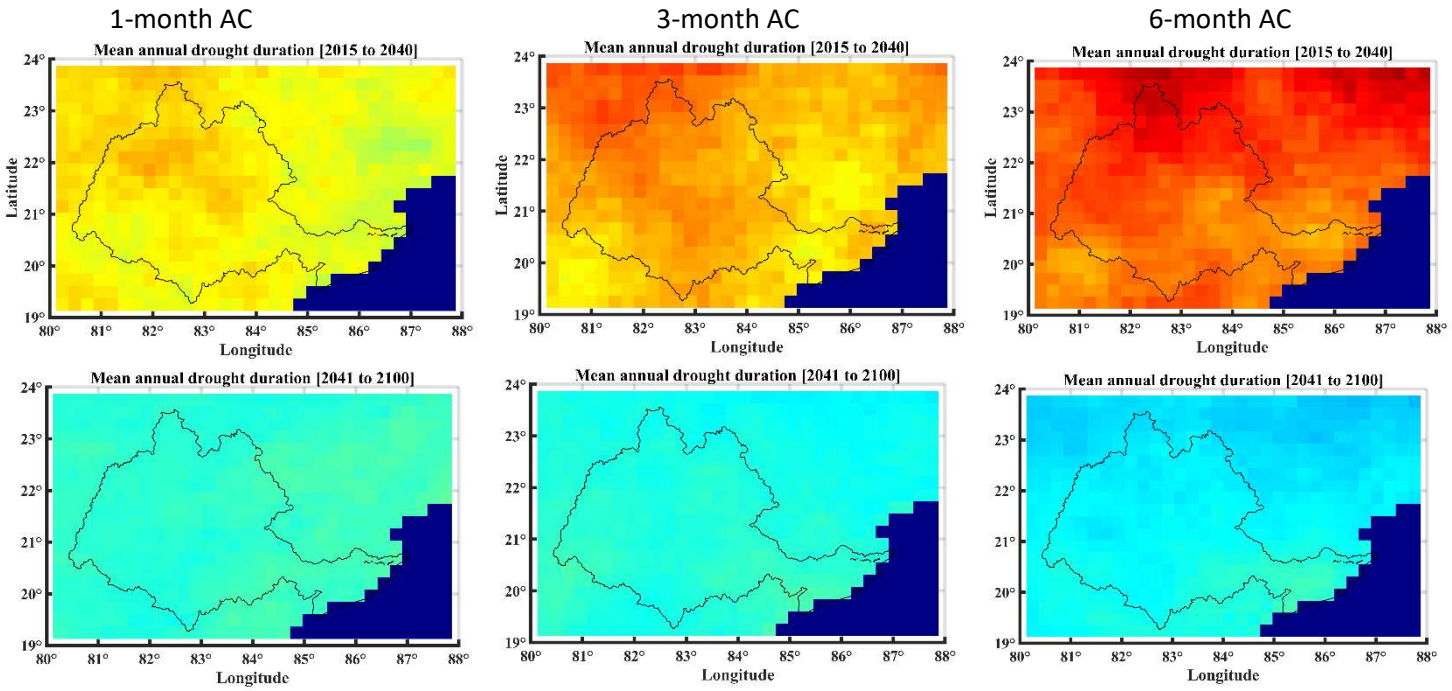

Scenario: SSP5-8.5

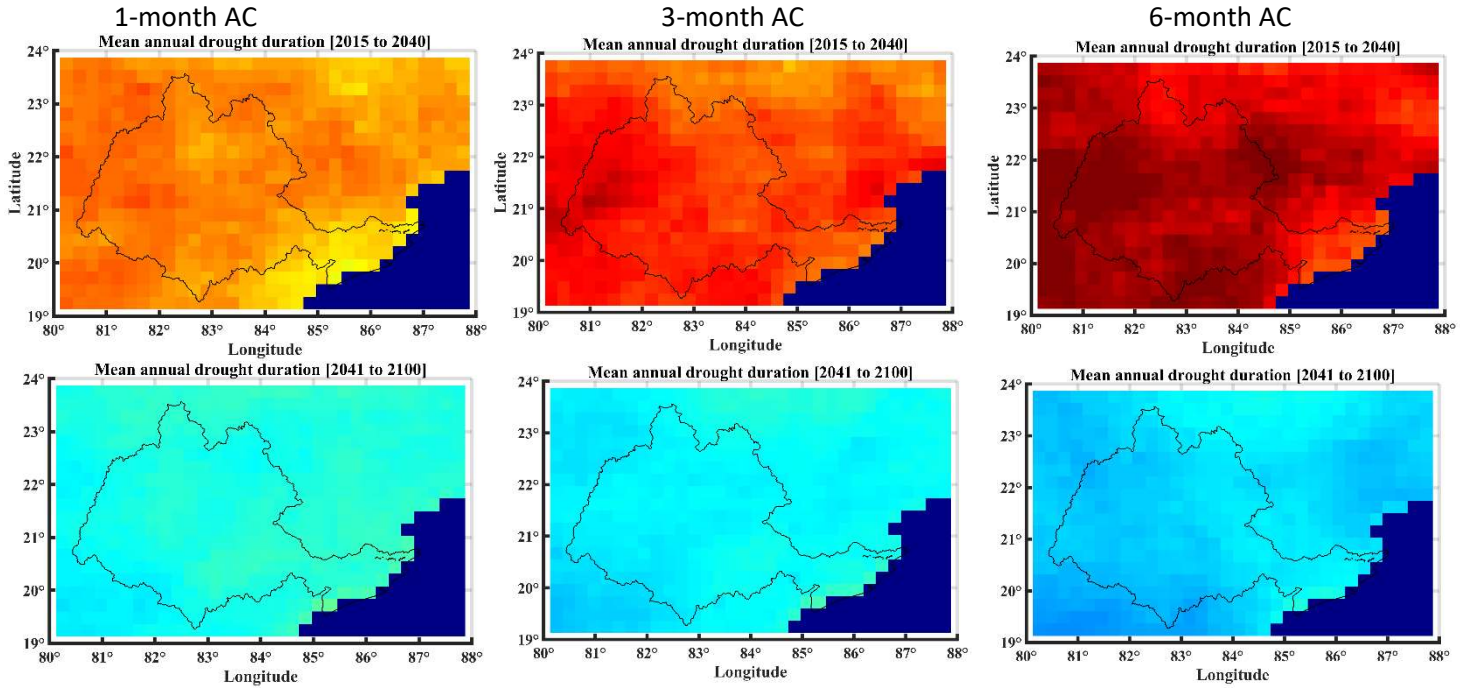

8. Recommendations for adaptation measures/options

The following recommendations are made for the Mahanadi basin based on the investigations carried out in this study.

1) To alleviate ill-effects associated with projected increase in future flows (corresponding to different exceedance probabilities) at majority of stations in the basin under different climate change scenarios, initiatives be taken for (i) identification and mapping of floodplains corresponding to the different scenarios, (ii) reducing flood-related vulnerability by devising cost effective and sustainable flood mitigation strategies/policies (in upstream catchments and along the river network in downstream areas), which are compatible with long-term economic and social goals. These may include dredging of lakes and construction of check dams for detaining flood waters and controlling sediment movement in catchments, (iii) developing and improving effective probabilistic long-term riverine flood forecasting systems/models, such as the presented HEFS, for different catchments in the basin, (iv) improving flood warning dissemination process and preparedness, and (v) promoting use of remote sensing, Internet of Things (IoT), and artificial intelligence tools/techniques for real-time monitoring of floods and precise mapping of vulnerable areas for devising effective evacuation process.

2) Conventional storage rule curves be replaced by fuzzified rule curves for optimal operation of reservoirs in the basin (as demonstrated in this report), as they help the reservoir managers to gradually vary the releases with respect to change in initial storage, thus reducing the likely risk of large deficits during the droughts. This is of significance, as in the near future (2015-2040) the Mahanadi basin is projected to experience droughts with highest relative frequency, highest mean annual duration and mean annual critical severity under different climate change scenarios. In addition, fresh water availability per capita in the basin is also projected to decrease significantly for the SSP-370 scenario due to high population.

3) For flood risk assessment at hotspots in the basin, multivariate regional frequency analysis approaches (such as the proposed multivariate extreme values approach, CEA), be opted in conjunction with partial duration series (PDS) of floods (extracted using effective methods such as the proposed Mahalanobis distance-based automatic threshold selection method). This is because PDS based approach has been (i) established to be effective than conventional annual maximum

series (AMS) based approach, and (ii) found to yield flood quantiles that are considerably lower for higher return periods (T>10 years) when compared to the corresponding estimates determined in analysis with AMS for the Mahanadi basin.

4) Initiatives be taken for validating the sub-zones (currently in use by practitioners especially under the Dam Rehabilitation and Improvement Project, GoI) for their homogeneity in flood generation mechanism, as many of the sub-zones (including sub-zone 3(d) containing the Mahanadi basin) are suspected to be heterogeneous. There is a need to account for dynamically evolving rainfall-runoff relationships (accounting for changes to climate and landuse/landcover patterns) to arrive at effective sub-zones.

5) Hydrometric monitoring network in the basin be improved/upgraded to get precise observations, as large part of the basin is found to be sparsely gauged. For this purpose, the proposed fuzzy entropy-based methodology could be adopted in conjunction with remote sensing options (e.g., Sreeparvathy and Srinivas, 2022), or adapted to account for increased variability and changes in spatiotemporal pattern of different hydrometeorological variables and the associated extreme events (e.g., floods, droughts) under climate change scenario to arrive at effective monitoring network designs.

6) Better methods/strategies be considered for determining suspended sediment load at gauged and ungauged locations

   (i) The suspended sediment load at any gauged station in the river basin be calculated using an alternative and effective approach of linear mixed effects modeling rather than conventional sediment rating curves.

   (ii) The suspended sediment load for an ungauged site in the river basin be determined using the proposed empirical model adopting remotely observed physical variables.

   (iii) Bagnold's bed load formula be used for calculating the bed sediment load across the river basin.

7) Non-structural approaches such as soil bioengineering and biotechnical engineering be explored for flood mitigation. For example, anchored plantings along streambanks to protect slopes against surficial erosion and shallow mass movement.

Section 9
Additional deliverables

9.1. Homogeneous evapotranspiration (ET) regions for India

A new regionalization approach is developed in the fuzzy framework to delineate homogeneous evapotranspiration (ET) regions. For regions formed in the Mahanadi basin using the approach, the effect of climate variables on ET and long-term (annual) surface runoff changes is quantified. Furthermore, new relevance vector regression relationships are developed for the regions to arrive at FAO Penman-Monteith estimate of ET from limited climate variables in data sparse areas.

9.2. Mahalanobis distance-based automatic threshold selection method for extraction of peak flows for flood frequency analysis

Novel Mahalanobis distance-based automatic threshold selection method is contributed for analysis of extreme hydrological/hydrometeorological variables (e.g., extreme rainfall, floods) in a river basin using peaks over threshold model. It is used for the construction of flood quantile functions at various sites within the Mahanadi basin. The contribution is published in the following paper.

Kiran K. G. and Srinivas V. V. (2021a) A Mahalanobis distance based automatic threshold selection method for Peaks Over Threshold (POT) model, Water Resources Research, American Geophysical Union & Wiley, Vol. 57, Issue 1, January 2021, e2020WR027534, https://doi: 10.1029/2020WR027534

9.3. Fuzzy entropy-based methodology for optimal design and performance assessment of hydrometric monitoring networks

Fuzzy entropy-based methodology is developed for optimal design and performance assessment of hydrometric monitoring networks. It potential is demonstrated through application to the Mahanadi river basin. The work is published in the following paper.

Sreeparvathy, V., Srinivas, V. V., (2020), A fuzzy entropy approach for design of hydrometric monitoring networks. Journal of Hydrology, Elsevier, Netherlands, Vol. 586, pp.1-18, July 2020, 124797. https://doi.org/10.1016/j.jhydrol.2020.124797

Brief details: In the past few decades, there is growth in evidence of intensification of the global

hydrologic cycle due to climate change associated with anthropogenic forcing. In this perspective, there is a need for effective and efficient hydrometric network for monitoring water quantity- and quality- related parameters in different subsystems of the hydrologic cycle. This is because timely availability of data is useful for various purposes such as, (i) water resources planning/assessment to upkeep human and ecosystem needs, (ii) forecasting extreme hydrologic events and assessing the associated risk, and (iii) assessment of the effects of flow regime alterations and related flow-ecology interactions. Often stream gauge stations tend to be spatially clustered and short-lived because most of the data collection is reliant on development projects. Enormous loss in hydrometric monitoring networks has been observed in the past few decades in both developed and developing countries due to economic constraints and changing government priorities (Pilon et al., 1996; Lanfear and Hirsch, 1999; Spence et al., 2007, Mishra and Coulibaly, 2009; Ruhi et al., 2018). Against this backdrop, investigations were carried out to assess the adequacy of the stream gauge network in the Mahanadi basin. Stream gauge deficient zones in the basin were identified by analyzing the spatial variability of the Shannon mutual information index (Figure 9.1a). For use in this analysis, estimates of fuzzy mutual information index (FMII) marginal entropy were obtained for all the existing stations in the river basin using the proposed fuzzy entropy based method. Subsequently, spatial interpolation was carried out using the FMII) values of each station using the spline method. Based on the FMII values, a river basin can be classified into five zones, namely highly deficit ($0 \leq FMII \leq 0.2$), deficit ($0.2 < FMII \leq 0.4$), average ($0.4 < FMII \leq 0.6$), above average ($0.6 < FMII \leq 0.8$), or excess ($0.8 < FMII \leq 1.0$) in terms of stream gauges. The spatial variability of the FMII over the Mahanadi basin indicates that a considerable part of the basin could be classified as belonging to a highly deficit zone. Therefore, the expansion of the hydrometric network in the basin is necessary. Similar results obtained for various other river basins in peninsular India can be found in Sreeparvathy and Srinivas (2020). Investigations were carried out to identify optimal locations to set up additional stream gauges in the Mahanadi basin (Figure 9.1b). The details can be found in Sreeparvathy and Srinivas (2020).

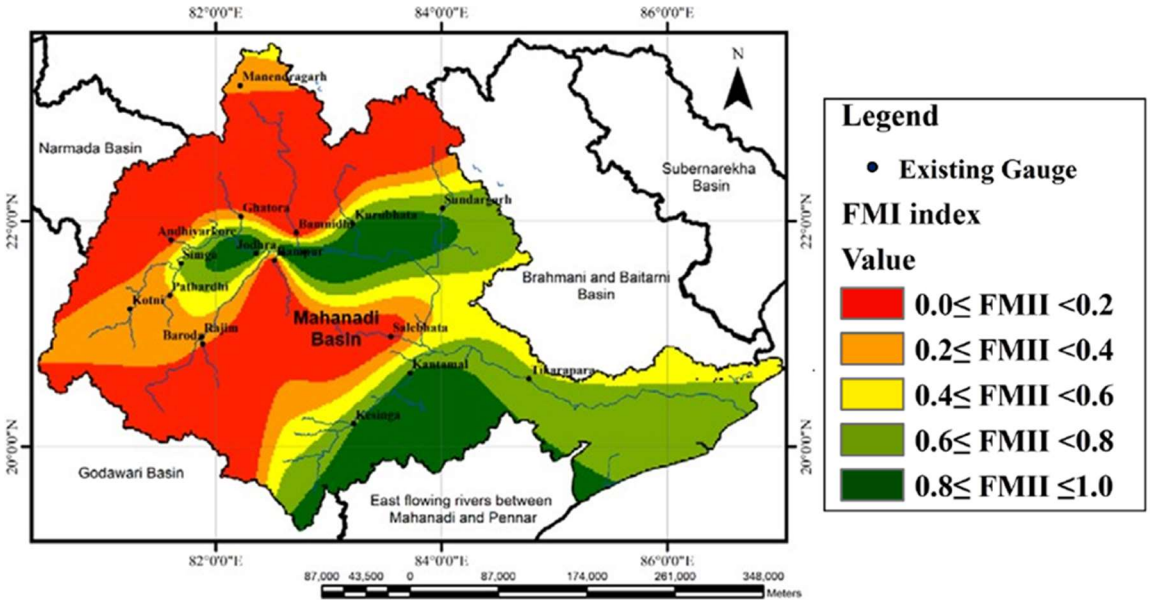

Figure 9.1a: Spatial variability of Fuzzy mutual information index (FMII) for the Mahanadi basin.

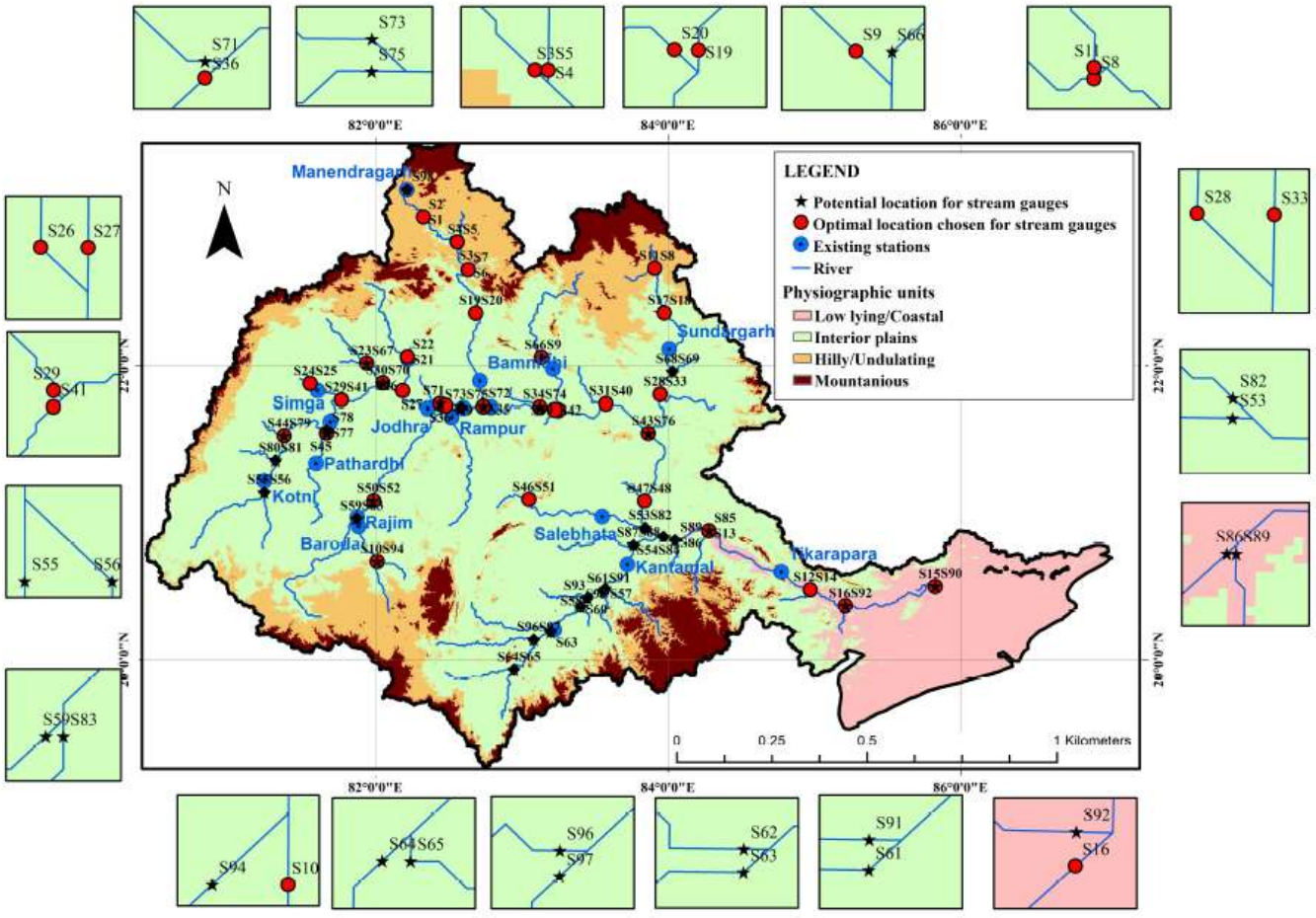

Figure 9.1b: The optimised hydrometric network in the Mahanadi basin.

9.4. Operating policies are developed for the Hirakud reservoir using two hedging models

Conventionally, multipurpose reservoir operation is guided by storage rule curves, which divide the reservoir storage into different zones for different purposes. Although such operation may be acceptable during normal years, it might lead to significant deficits for one or more purposes during droughts. Hedging policies are aimed at storing the water in the reservoir during the periods of impending drought by accepting smaller deficits (hedging) and using it to reduce the likely risk of large deficits during the drought. Starting with Tu et al. (2003) many researchers (Chang et al. 2005; Tu et al. 2008; Guo et al. 2013; Taghian et al. 2014; Adeloye et al. 2016) have formulated hedging policies for multipurpose reservoir operation by coupling the storage rule curves with hedging factors, wherein, the rule curves define the storages that will act as the hedging triggers, while the hedging factors regulate the amount of rationing to be done depending on the hedging zone in which the initial storage falls. Ahmadianfar et al. (2016) fuzzified the rule curves, by introducing transition rule curves around the original storage rule curves, wherein the hedging factors are varied linearly which allows for the continuous variation of the releases with respect to storage. Herein, due to continuous hedging, the performance of the system is reported to have improved considerably over the conventional rule curve-based hedging, which has been confirmed by Shiau et al. (2018) through more detailed investigations done in a multi- objective framework. In this study, the aforesaid two hedging models are coupled with Borg-MOEA (Hadka and Reed 2013), a multi-objective evolutionary algorithm to derive an optimal hedging policy for the operation of Hirakud reservoir.

Methodology

1. Rule-curve based hedging (RCH) Rule:

   Tu et al. (2003) proposed rule curve based hedging rule for multipurpose reservoir operation, by coupling the storage rule curves and hedging factors. In case of RCH (Fig. 14), the reservoir is divided into several storage zones by means of rule curves, and the releases are curtailed by means of hedging factors, α and β. In other words, if the storage at the beginning of the i^{th} period falls under zone two, then the releases are obtained by multiplying the respective demands with respective hedging factors specified for zone 2. A drawback associated with this rule is that the releases will be sharply changing as the initial storage shifts from one zone to another (Figure 9.2).

The decision variables to be optimized in this rule are the periodic storage rule curves and the periodic hedging factors.

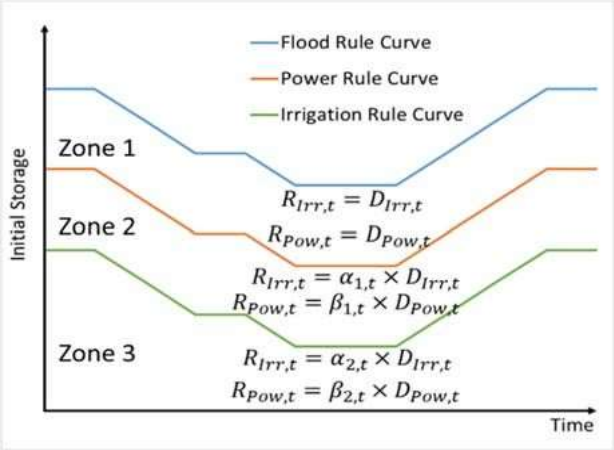

Figure 9.2: Representation of Rule curve based hedging rule. R_{Irr} and R_{Pow} are releases and D_{Irr} and D_{Pow} are demands corresponding to irrigation and hydro-power generation respectively.

2. Fuzzified Rule-curve based hedging FRCH rule:

Fuzzified Rule-curve based hedging rule proposed by Ahmadianfar et al. (2016) improves upon the RCH by fuzzy conditioning the hedging factors on the transition rule curves provided around the original rule curves. This fuzzy conditioning ensures the hedging factors to linearly vary within the transition zones as shown in Figure 9.3. This helps the reservoir manager to gradually vary the releases with respect to change in initial storage. In other words, this rule is a piecewise linear function between the releases and initial storage. The decision variables to be optimized in this rule are the periodic transition rule curves and the periodic hedging factors.

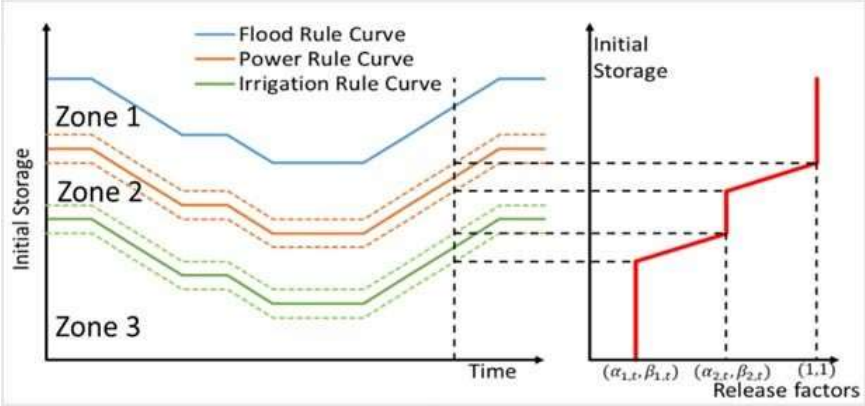

Figure 9.3: Representation of Fuzzified Rule curve based hedging rule

3. Parameterization-simulation-optimization aka. Direct policy search

In this study, the optimal release policies for each of the above rules are obtained, by coupling them to Borg-MOEA (Hadka and Reed 2013), a multi objective evolution algorithm in a direct policy search framework. Two parameterization schemes are adopted: (1) within year varying hedging parameters, and (2) within- and over-year varying hedging parameters to reduce the number of decision variables.

In case of within year varying hedging parameters, the hedging parameters are allowed to vary within the months, but enforced to remain constant across the years. In case of over year hedging parameters, firstly, each year in the operation horizon is classified into one of the three inflow scenarios: *dry-, normal-* and *wet- Years* depending upon the expected inflows during that year. Secondly, for each hedging rule, three different parameter sets representing the *three scenarios* were considered to define the release policy. In this study, Modified Shortage Indices (MSI) (Hsu and Cheng 2002; Taghian et al. 2014) calculated for power releases and irrigation releases are considered as the two objective functions to drive the optimization model. MSI is defined as follow:

$$MSI = \frac{100}{NP} \times \sum_{t=1}^{NP} \left(\frac{Deficit_t}{Demand_t} \right)^2$$

Owing to its formulation, MSI represents both the long-term (by of summing the deficit characteristics) and short-term (by giving differential weightage for the deficits) reservoir performances.

Results

The above models are evaluated and their performance is compared with regard to Hirakud reservoir. Out of the 35 years of inflow data available, first 25 years of data is considered for calibration of the release policy (i.e., by obtaining the optimal decision variables through Direct policy search (DPS) framework) and later 10 years of data is considered for validating the release policy (i.e., simulating the release policy obtained a priori with the last 10 years of data). Since the *Benchmark Releases* are not available to validate, the DPS framework is employed with last 10 years alone, so as to get the best possible releases for the last 10 years. Out of the three objective function settings considered, the results corresponding to MSI as objective function are discussed in detail

as the behaviour of the results is similar.

Comparison of hedging rules considering within year variability of hedging parameters

The Pareto-optimal fronts obtained with each of the hedging rules during calibration period are plotted in Figure 9.4. It can be seen that the FRCH is performing relatively better than the RCH, which is in agreeement with earlier literature. During validation (Figure 9.5) as well, the simulated solutions corresponding to FRCH are nearer to the cosrresponding pareto-front when compared to that of the RCH, indicating that FRCH is adopting better to the non- stationarity of inflows.

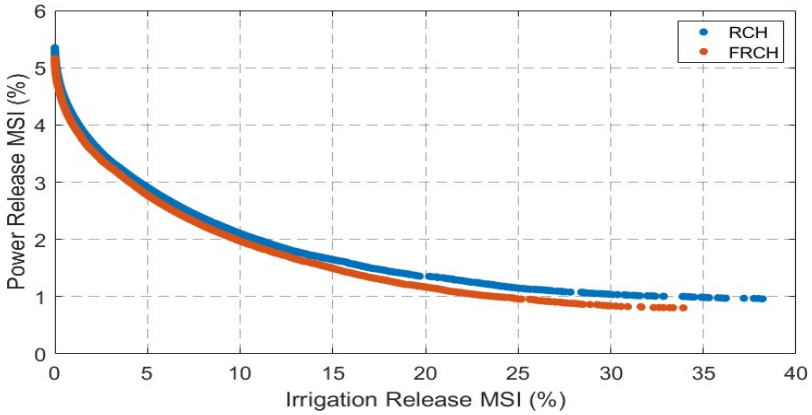

Figure 9.4: Comparision of hedging rules during calibration period considering within year hedging parameters.

An important observation in Figure 9.5 is that the Pareto-optimal fronts corresponding to the calibration period are significantly inferior compared to that of validation period. This is attributed to the severe drought period extending for over two years between 7^{th} to 9^{th} year in the inflow series. As no such severe deficit years are seen in the validating period, the Pareto- optimal fronts corresponding to validation period are better. For the same reason, the validated solutions are also better compared to that of Pareto-optimal solutions obtained for calibration period.

Comparison of hedging rules considering withinyear and overyear variability of hedging parameters

The Pareto-optimal fronts obtained with each of the hedging rules during calibration period by considering withinyear and overyear variability of hedging parameters are plotted in Figure 9.6. Like the previous case, here also FRCH is performing better than the RCH during calibration. Figure 9.7 represents the comparision between the two parameterization schemes for each of the

four hedging rules apart from facilitating the comparision across the four hedging rules. It can be seen that during calibration period, both the rules have gained with overyear parameterization sceme. However, this improvement is only marginal, indicating that both the rules are not able to capture the overyear variability in inflows. Further, the simulated solutions during validation period, are also not following any smooth trend as have been the case in the previous parameterization scheme. A plausible reason for this might be that the FRCH and RCH are overfitted during calibration, and thus not able to properly handle the different inflows during validation. Investigations are underway to assess performance of current operating policies for various future climate change scenarios and to develop new policies (if necessary).

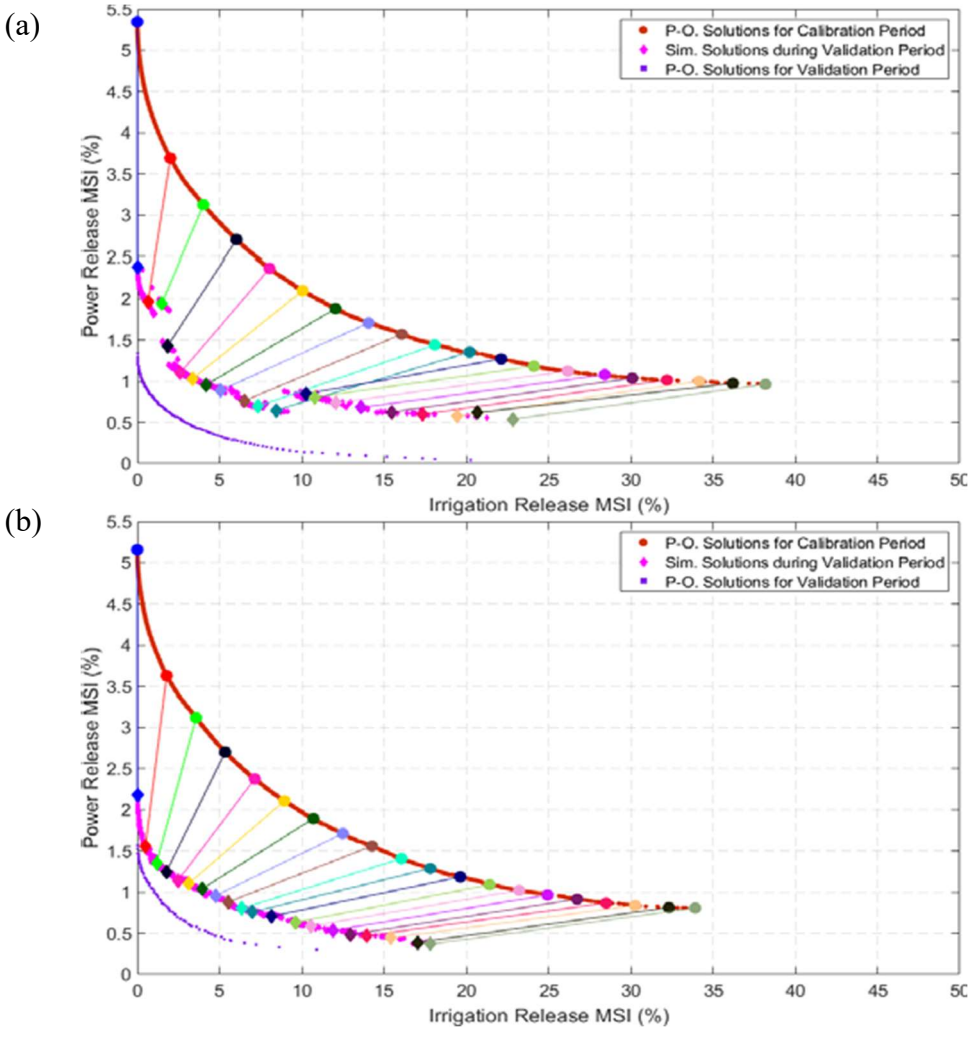

Figure 9.5: Comparison between Pareto-Optimal solutions for calibration and validation periods obtained corresponding to (a) RCH and (b) FRCH by considering within year hedging parameters. Simulated solutions obtained during validation period are also shown.

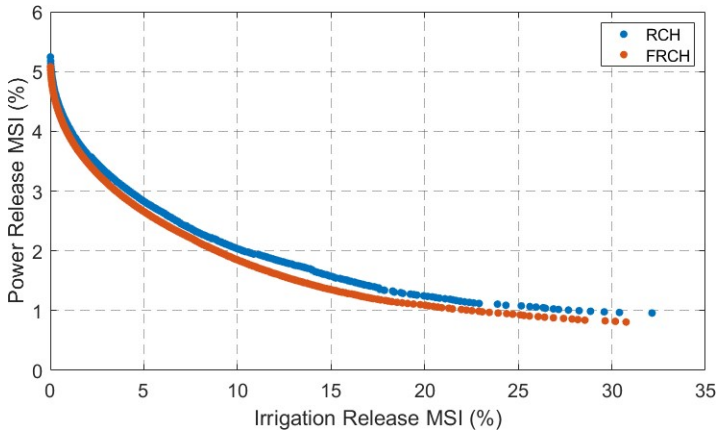

Figure 9.6: Comparision of hedging rules during calibration period considering within year and overyear hedging parameters.

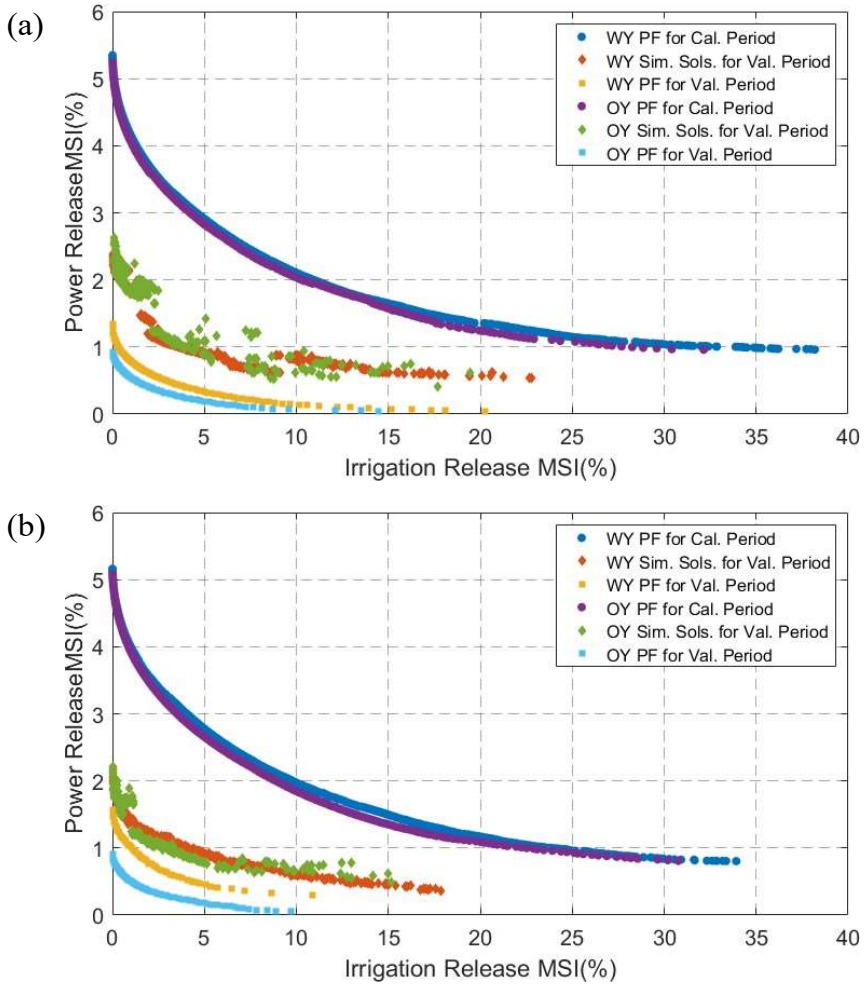

Figure 9.7: Comparison between Validated solutions with corresponding Pareto-Optimal solutions for (a) RCH, and (b) FRCH considering within year and overyear hedging parameters.

9.5. Research on various objectives related to sediment yield in Mahanadi basin (from Partner Institute, IIT Bhubaneswar)

9.5.1 Introduction

Literature review on modelling sediment yield in river basins is presented in Section 1.2 of this report. The objectives of the present study with regard to the Mahanadi River basin (MRB) are (i) to detect and quantify the presence of trends and abrupt change points from the latest observed annual runoff and sediment data (1973-2017) for the MRB, (ii) to recognize proper attributes defining observed trends or change points, (iii) to quantitatively explore the deltaic response due to the change in basin sediment yield, (iv) to relate the change in sediment discharge and the delta evolution in terms of anthropogenic influences over the basin, (v) to identify the hysteresis behavior of the SRC for gauging stations throughout the monsoon during 2007-2017, (vi) to develop a simplified model considering the hysteresis pattern to determine the SSC for gauged stations in the MRB, (vii) to develop a basin specific fixed effect rating model using various environmental controls, (viii) to explore the efficacy of the proposed rating model in estimating the monthly SSC of a few ungauged sub-catchments within the basin, (ix) to develop a reasonable method for predicting the ungauged bed load concentration (BLC_u) of the MRB when only the SSC and hydraulic variables for a hydrological station are accessible and (x) to determine the future sediment load at selected stations of the basin based on the future projection of meteorological variables and (xi) to assess implication of future sediment load on capacity of Hirakud reservoir.

9.5.2. Study area

The Mahanadi River basin is the eighth largest basin in India, having a broad basin area of 139681.5 km^2, i.e., roughly 4.3% of the entire terrestrial area of the country (CWC, 2014). It is the second-largest east-flowing peninsular river, which covers a distance of 851 km before it discharges into the Bay of Bengal. The basin terrain covers from 80°28'E to 86°43'E longitude and 19°08'N to 23°32'N latitude. Originating in the Dhamtari district of Chhattisgarh, approximately at the height of 442 m over sea level, it covers an area of 75,136 km^2 in Chattisgarh, 65,580 km^2 in Odisha, 635 km^2 in Bihar, and 238 km^2 in Maharashtra. The entire basin has three major dams: the Ravishankar Sagar dam located at the most upstream of the main Mahanadi River, the Minimato Bango dam situated at the Hasdeo tributary, and the Hirakud dam situated at the downstream main Mahanadi River. Seven major

tributaries join the upstream of the Hirakud reservoir. The Seonath, the Hasdeo, the Mand, and the Ib meet the left side of the river flow direction while the other three that join the right part of the flow direction are the Pairi, the Sukha, and the Jonk.

Moreover, the Tel and the Ong tributaries meet the mainstream downstream of the Hirakud reservoir. The river Brahmani (in the northeast) and the Chilika Lake (in the southwest) confine the deltaic region of the basin. Tropical monsoon climate with an average annual precipitation of 1350 mm mostly prevails in the basin and above 80% of yearly discharge during monsoons. The mean annual runoff of the Mahanadi is 66,900 MCM (CWC, 2014). The river branches into several distributaries before discharging into the Bay of Bengal, ultimately forming a coastal delta.

The agricultural land area covers 54.3% of the total basin area, which also adds firmly to the economy of India. The remaining 32% includes forest, and 14% have wastelands, water bodies, and built-up areas. Medium textured soil covers 51.3% of the area, followed by fine-textured soil with almost 42% coverage (CWC, 2014). The upstream geology of the basin is mainly dominated by the hard rock of the Eastern Ghats from Precambrian time. In contrast, the deltaic alluvium of the river predominates in the downstream region. Moreover, bed sediments are generally coarse-grained compared to suspended sediments (Chakrapani and Subramanian, 1990a). However, the entire river basin deposits the maximum silt compared to all other Indian rivers (Mahalik, 2000).

9.5.3. Data sources

In this study, the long-term mean water level (in m), Q (in m^3/s), SSC (in g/l) and transverse bed-surface profiles for sixteen hydro-observation stations were collected from the Central Water Commission, Government of India (CWC). The daily average depth of flow (h_a, in m) at all sub-basin outlet stations was obtained by subtracting a station's zero-gauge level (given by CWC) from the daily mean water stage of the same station during the entire study period. The daily cross-sectional area (A, in m^2) and flow width (FW, in m) of a station were deduced using the transverse bed surface profiles and the daily average flow depth. Further, the average daily flow velocity (v_a, in m/s) was computed as discharge divided by the daily cross-sectional area at any station. The spatial details of all the gauging stations in the basin are shown in Figure 9.8. Since the monsoon rain (June to October) conveys a significant share of the basin's yearly sediment load, the sediment monitoring time was daily in the monsoons while weekly during non-monsoon (November-May). Similarly, the rainfall of the same period was acquired from high resolution ($0.25^o \times 0.25^o$) gridded rainfall data of the India Meteorological Department (IMD).

Additionally, topographic data of 30 m spatial resolution in the form of Cartosat-1 digital elevation models (CartoDEM), archived by the Indian Space Research Organisation (ISRO), was utilized in this study. The basin's dominant soil information was collected from the soil map (1999) of scale 1:500000 by the National Bureau of Soil Survey and Land Use Planning (NBSS and LUP), Nagpur, India. However, the particle size information for the individual dominant soil taxonomy was obtained from the Water Technology Centre for Eastern Region (Singh et al. 2009). The detailed information related to catchment characteristics and hydrological (observation/ gauging) stations are shown in Table 9.1. Topographic data in the form of ASTER (30 m) and SRTM (90 m) DEMs, archived by the United States Geological Survey (USGS) and National Aeronautics and Space Administration (NASA) (https://earthexplorer.usgs.gov/, https://search.earthdata.nasa.gov/) were utilized in this study for the Geomorphic Change Detection (GCD) of coastal landforms. The information of large dams in the basin was collected from the National Register of Large Dams (NRLD, 2018). The data on seasonal water allocation for irrigation and hydropower from the Hirakud dam was obtained from the Department of Water Resources, Government of Orissa (DoWR, 2014). The water allocations and installed thermal power capacity data for thermal power plants of Chattisgarh and Odisha were obtained from the Ministry of Environment and Forests (MoEF, 2016).

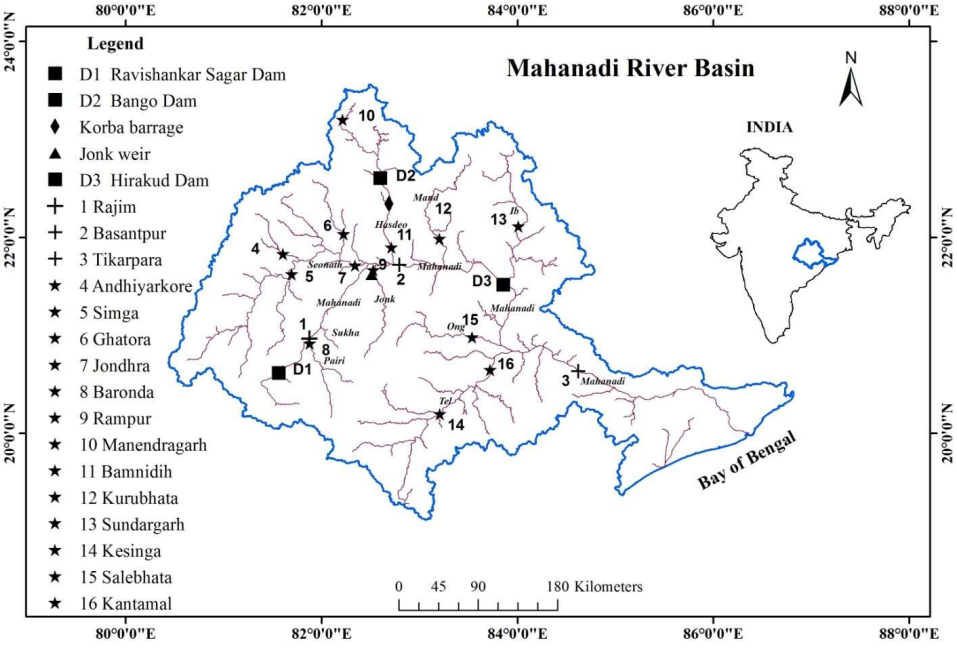

Figure 9.8: A map of the study area

9.5.4. Methodology

9.5.4.1 Trend analysis

Numerous statistical methods are available for detecting trends within a time series. Although there are different trend analysis methods (Sonali and Kumar, 2013), main focus was on determining the magnitude and statistical significance of the trend and evaluating the specific form of the trend using the rank-based statistical nonparametric techniques, namely, the Mann-Kendall (MK) (Mann, 1945; Kendall, 1975), Sen's slope estimator (M) (Sen, 1968) and the Pettitt test (Pettittt, 1979). These methods are used to identify a monotonic trend and a sudden shift in hydrological time series. The presence of autocorrelation can affect the trend recognition in time series analysis (Yue et al., 2003). The Modified Mann-Kendall (MMK) (Hamed and Rao, 1998) method was used for auto-correlated data. The MK test statistics and variance were used to compute the MK standardized test statistic (Z_s). An increasing or decreasing trend was designated by the corresponding positive or negative values of Z_s. Further, for a time series, the rate of change of the linear trend was evaluated non-parametrically. The value of Sen's estimator specifies the magnitude of the slope, and the sign (positive or negative) of the estimator indicates the corresponding trends (increasing or decreasing).

Table 9.1: Details of Hydrological stations of the Mahanadi River basin

Hydrological stations	Latitude (°)	Longitude (°)	Data Interval	Altitude (m.a.s.l)	Drainage area (km^2)	Tributary/ Sub-tributary
Andhiyarkore	21.83	81.61	1981-	252	2210	Seonath
Simga	21.63	81.69	1973-	244	30,761	Seonath
Baronda	20.91	81.89	1980-	283	3225	Pairi
Rajim	20.97	81.88	1973-	275	8760	Mahanadi
Manendragarh	23.20	82.22	1994-	411	1100	Hasdeo
Ghatora	22.06	82.22	2001-	246	3035	Seonath
Jondhra	21.73	82.35	1981-	219	29,645	Seonath
Rampur	21.65	82.52	1977-	219	2920	Jonk
Bamnidih	21.90	82.72	1973-	223	9730	Hasdeo
Basantpur	21.73	82.79	1973-	206	57,780	Mahanadi
Kurubhata	21.99	83.20	1980-	215	4625	Mand
Sundargarh	22.12	84.01	1980-	214	5870	Ib
Salebhata	20.98	83.54	1973-	130	4650	Ong
Kesinga	20.20	83.23	2007-	166	11,960	Tel
Kantamal	20.65	83.73	1977-	118	19,600	Tel
Tikarpara	22.63	84.62	1973-	50	124,450	Mahanadi

9.5.4.2 Change point analysis

The probable leap (or abrupt change) in the variation of the trend was explored for the analysis of the hydrological series. The leap often indicates the parallel rise or drop of the statistical characteristics of hydrological series (commonly taken as the arithmetic mean of the series) before and after the abrupt change point, which may occur due to human or natural factors. For the identification of probable leap, initially, the abrupt change point was determined. Then a significance test was carried out on the abrupt change in the hydrological series before and after the abrupt change point. Out of the various methods that exist to detect the shift in the time sequence, the nonparametric Pettitt test (Pettit, 1979) was applied in the present study. It is used to identify a sudden single shift in the mean of the distribution at any point in time.

9.5.4.3 Volumetric change analysis of the delta

The DEM data were utilized through a sequence of orderly geo-processing procedures in the ArcGIS 10.2 platform for the volumetric change analysis of coastal morphology in the Mahanadi delta. The Geomorphic change detection (GCD) study was conducted using the DEM datasets through the DEM of Difference (DoD) method. This method was precisely used to assess the volumetric change analysis of coastal morphology from 2000 to 2011. This algorithm measures the difference in pixel values of DEM's of two successive years. The output DEM presents the change of sediment depth due to erosion and accretion over time. For the present analysis, the ASTER DEM of October 2011 was considered the DEM of the later period, and the SRTM DEM of February 2000 was considered for the earlier period. However, the DEM datasets have different spatial resolutions for the volumetric change analysis.

Consequently, the SRTM 90 m data was resampled to 30 m resolution using the cubic convolution resampling algorithm. Upon applying the DoD method, the positive and negative pixel values indicate accretion and erosion, respectively. However, the outcome of DoD may generate and escalate specific errors that need to be recognized and reduced (Wood, 1996). These uncertainties from the resultant DEM were addressed by quantifying the individual DEM errors using the equation by Wheaton et al. (2010). The Google Earth (GE) elevation could be considered as reference data for general investigation and preliminary analysis (El-Ashmawy, 2016). Therefore, the uncertainty analysis establishes the accuracy of the volumetric change assessment (Wheaton et al., 2010). It is recognized that most of the geomorphic features like a sandy beach, delta, mangrove, estuary, mudflat, spits,

aquaculture and salt pans, and inundated coasts along the Odisha coastline lies within 500 m (Kumar et al., 2010; Kankara et al., 2018) and 85 m to 120 m of the coast (Monalisha and Panda, 2018). Hence, a buffer of 500 m from the coastline is considered a coastal zone for assessing volumetric change detection, as it was assumed that marked deltaic response to the change in sediment load from the entire catchment would not extend beyond 500 m distance from the coastline.

9.5.4.4 Double mass curve analysis

Variability in sediment load measured at a gauging station arises when the morphology around the gauging station changes significantly throughout the observation period. The changes in the relation between sediment load and runoff were estimated using the double Mass Curve (DMC) technique. The mean yearly runoff was considered the base data corresponding to a gauging station in the present study. The DMC method was further used to understand the role of anthropogenic activities in the deviations in sediment load (Walling and Fang, 2003; Wang et al., 2007; Zhongbao et al., 2015). The mean yearly sediment load and runoff data of a station were arranged in normal time chronological order (i.e. the oldest record as the first entry and the latest record as the last entry in the list) for the DMC method analysis. The cumulative mean yearly sediment load (CSL) at a station and its corresponding mean annual runoff (CR) were then calculated starting from the oldest record and plotted as CSL versus CR. The shift in the sediment regime concerning previous times of a particular station is displayed by the distinct break in slope of the developed plot (Figure 9.9). The break-in slope was considered significant when it continued for greater than five years (Subramanya, 2013).

With the above DMC technique, the relative contribution of human interference on the sediment load of the gauging station was evaluated quantitatively concerning the mean yearly runoff throughout the study period. The deviations of the subsequent breakpoints in the curve were calculated from the extrapolated points of the period before the first breakpoint (estimated from the regression equation, Fig. 9.9). The period before the first breakpoint was considered as the reference of change. The percentage change of individual observed mean yearly sediment load from the estimated one was then calculated, and the average percentage contribution of the human interference for the breakpoint was determined.

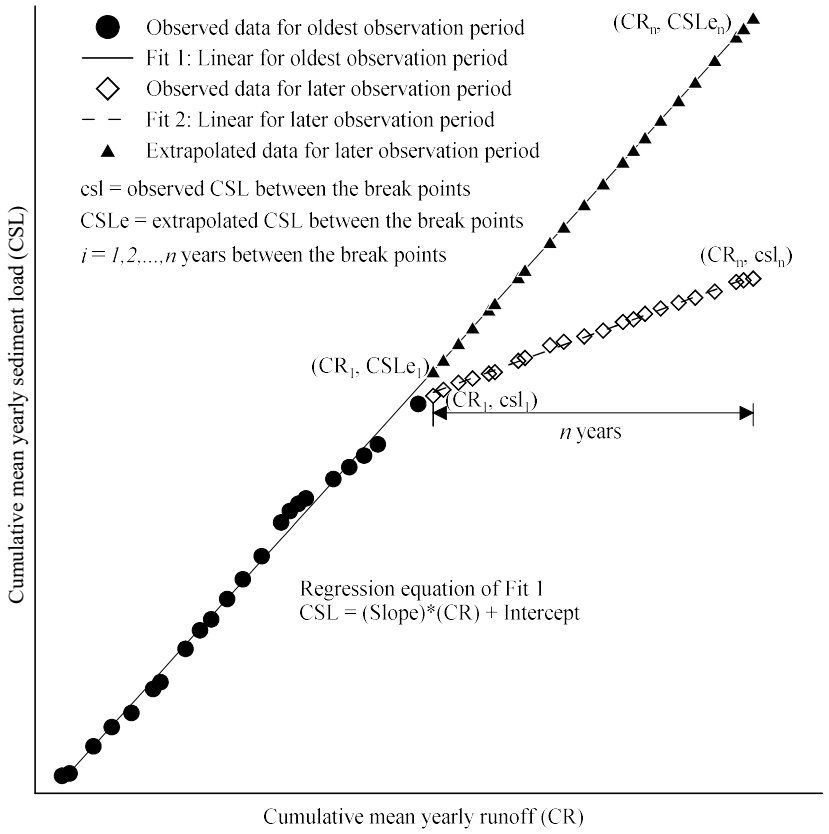

Figure 9.9: Schematic representation of the double mass curve

9.5.4.5 Characterization of SRC hysteresis

The hysteresis of the SRC was evaluated at Tikarpara for each monsoon month throughout the study period. Only the data from the last observation station was used to study the hysteresis pattern in SRC, as it was assumed to represent the hydrological response of the entire basin. The SRC hysteresis analysis for the specified timescale was calculated using Andrea et al. (2006) and Sadeghi et al. (2019). The hysteresis behaviour of SSC was defined using two factors, namely ΔC and ΔR, and compared for the monsoon months across years. ΔC represented the changes in SSC. In contrast, the magnitude and direction of hysteresis were represented by ΔR. These factors were used to understand the dynamics of hysteretic loops and provide data on sediment behaviour in response to changes in discharge. ΔC and ΔR are therefore defined as

$$\Delta C\ (\%) = \left(\frac{C_s - C_b}{C_{\max}} \right) \times 100 \qquad (9.2)$$

$$\Delta R\ (\%) = (A_h \times R) \times 100 \quad (9.3)$$

where C_s is the SSC at peak discharge, C_b is the SSC at discharge, C_{max} is the maximum SSC during the period under consideration, A_h is the area of the SRC hysteresis, and R is the rotational pattern of the hysteresis loops. The area under the hysteresis loop (A_h) was calculated after normalizing discharges and suspended sediment concentrations to a unit scale by their peak values. As a result, A_h assumes a value between 0 and 1, with values closer to 0 indicating linearity and no significant fluctuation in SSC across different hydrological settings. On the other hand, even with comparable discharge, A_h values closer to 1 show substantial variation in SSC. Factor ΔC varies from -100% to 100%, with positive (negative) values indicating flushing (dilution) conditions. R can be -1,1, or 0 for anticlockwise, clockwise, or complicated (unclear/non-specific) SRC hysteresis loops, respectively. The discharge peak occurs before the peak of the SSC in the case of anticlockwise loops and vice-versa. Accordingly, the factor ΔR also varies from -100% to 100%.

The characteristics of the hysteresis pattern of SRC was evaluated from the ΔC versus ΔR representation, where four quadrants of the graph are defined based on the flushing or dilution condition of SSC. The areas above (below) the horizontal axis represent flushing (diluting) conditions, whilst the areas to the right (left) of the vertical axis represent clockwise (anticlockwise) loops.

9.5.4.6 Linear mixed-effects modelling (LMM)

For the prevailing climatic conditions, an SRC can only be considered typical for a particular gauging station when the interrelation between SSC and Q is homogeneous for the entire study period (Asselman 2000). Hence, the homogeneity of the data was evaluated using the double mass curve (DMC) technique. Except for Rampur and Bamnidih, the DMC confirms data homogeneity for all hydrological stations. As a result, the Rampur and Bamnidih datasets were not chosen for further analysis. Also, Yadav et al. (2021) made a similar point, especially regarding the poor performance of sediment prediction at Bamnidih.

Initially, an exploratory investigation of the Q and SSC was carried out to identify the possible data classes (months, weeks, hydrological season, etc.) required for mixed-effects modelling. It was then categorized to incorporate two stages of variation for the observed data. The first stage of variation was considered for a particular month across years. The variables (SSC and Q) within each month correspond to the second level of variation. Five linear mixed-effects models (LMM) were developed for the current study, considering each for a particular month of monsoon (June to October) across all

years (2007-2017) of the hydrological observations. In LMM, the fixed effect parameters were predicted every month. In contrast, considering the hysteresis effects, the random effect parameters were permitted to differ between years for a specific month.

The LMM was developed with sets of equations for two stages of embedded data. The following equation depicts the first stage of variation:

$$b_{jk} = \delta_{0k} + \delta_{1k} a_{jk} + \varepsilon_{jk} \quad (9.4)$$

where $b_{jk} = \log_{10}(SSC_{jk} + 1)$, $a_{jk} = \log_{10}(Q_{jk} + 1)$ for jth observation in the year k, δ_{0k} = intercept, δ_{1k} = slope corresponding to the rating parameters of the power rating equation, and ε_{jk} = random error. The logarithmic transformation of data was done to confirm the normality of the residuals. As the logarithmic transformation may result in erroneous value in the presence of any observations of zero value, therefore +1 is added in a_{jk} , and b_{jk} equations. However, ε_{jk} characterizes the intra-month variance.

The second stage of variation is given by

$$\delta_{0k} = \delta_0 + d_{0k}, \ \delta_{1k} = \delta_1 + d_{1k} \quad (9.5)$$

where δ_{0k} and δ_{1k} are assumed to be distributed normally with a mean (fixed effect parameters) of (δ_0 and δ_1). Its variance-covariance form describes inter-year variance and covariance for $\begin{bmatrix} d_{0k} \\ d_{1k} \end{bmatrix}$, which defines the monthly variation of SRC across years. The ultimate equation of the LMM after incorporating equation (2) is as follows:

$$b_{jk} = \delta_0 + d_{0k} + \delta_1 a_{jk} + d_{1k} a_{jk} + \varepsilon_{jk} \quad (9.6)$$

The restricted maximum likelihood method was used to estimate the variance-covariance matrix components as it does not produce any biases compared to other estimating methods (Corbeil and Searle 1976). The LMM efficiency was evaluated by comparing it with the ordinary least square regression (using the power rating curve). The Akaike information criterion (AIC) (Webster and McBratney 1989) was used to measure the model's goodness of fit. The fixed effect rating parameter was further used for the regression modelling of SSC for the ungauged catchments.

9.5.4.7 Environmental control parameters for regression modelling

Eleven environmental control parameters (ECPs) that mainly cover hydrological, soil, topographic, and meteorological categories were used to develop the regression model. The eleven parameters

include the following: fixed effect intercept (δ_0) and slope (δ_1), mean discharge (Q+1), mean suspended sediment concentration (SSC+1), catchment area (A), soil erodibility factor (K), relief ratio (RR), time of concentration (T_c), elongation ratio (ER), drainage density (D_d) and mean areal precipitation (MAP).

The soil erodibility factor (K) evaluates soil vulnerability to erosion by runoff and precipitation (Renard et al. 1997). The factors influencing soil erodibility include the soil texture, soil structure, soil permeability, and proportion of organic matter. The following equation of K established by Wischmeier et al. (1958) was used for each gauging station of the basin.

$$K = 0.1317 \times \left[2.1 \times 10^{-6} m^{1.14} (12 - a) + 0.0325(b - 2) + 0.025(c - 3) \right] \quad (9.7)$$

where m = P_{silt} (100 – P_{clay}), P_{silt} = percentage silt (%), P_{clay} = percentage clay (%), a = percentage of organic matter (%) = 2% (assumed), b = soil structure index (Table 9.2), c = soil infiltration index (Table 9.3). A similar classification of soil structure index and infiltration index was done by Huang et al. (2012). The above equation used the 0.1317 factor to convert K from US customary units to SI units $\left(\frac{t \times ha}{ha \times N} \right)$, as given by Foster et al. (1981). The particle size diameter, d_{50} (mm), was calculated as a weighted mean of the standard soil particle sizes of sand (0.075 to 4.75 mm), silt (0.002 to 0.075 mm), and clay (0 to 0.002 mm) given by the Indian Standard Soil Classification System, using the equation below

$$d_{50} = \left(P_{sand} \times S_{avg} \right) + \left(P_{silt} \times M_{avg} \right) + \left(P_{clay} \times C_{avg} \right) \quad (9.8)$$

where P_{sand} = percentage sand (%), S_{avg} = average sand size diameter = 2.412 mm, M_{avg} = average silt size diameter = 0.038 mm, C_{avg} = average clay size diameter = 0.001 mm, d_{50} = particle size (mm).

Table 9.2: Classification of the soil structure index

Structure classification (*b*)	Soil structure	Particle size, d_{50} (mm)
1	Very fine particles	<1.000
2	Fine particles	1.000~2.000
3	Medium or coarse particles	2.000~10.000
4	Blocks, shales, or coarse particles	>10.000

Table 9.3: Classification of soil infiltration index

Infiltration classification (c)	Soil infiltration
1	Excessively drained
2	Somewhat excessively drained
3	Well-drained
4	Moderately well-drained
5	Imperfectly drained
6	Poorly drained

The catchment relief (R) is the vertical distance between the highest and the lowest levels of a catchment (Horton 1945). However, the relief ratio (RR) is defined as the ratio of catchment relief to the catchment length (Schumm 1956). The RR corresponding to each sub-catchment in the study area was calculated from CartoDEM using ArcGIS 10.2. The time of concentration (t_c) value was calculated using the widely used Kirpich equation (Chow et al. 1988), which uses the maximum length of travel of water and the catchment slope. The t_c is given by

$$t_c = 0.01947C^{0.77} \tag{9.9}$$

where $C = \sqrt{\frac{L^3}{R}}$, t_c = time of concentration (minutes), L = maximum length of travel of water (m), R = catchment relief. The ratio of the diameter of a circle of the same area as of the catchment and maximum catchment length is called the elongation ratio (ER) (Schumm 1956). ER calculates the shape of the river basin, where it gets influenced by the geological and climatic types. Obi Reddy et al. (2004) found that low ER values are categorized by high vulnerability to erosion and sediment load, whereas higher values indicate low infiltration capacity and runoff. It is given by

$$ER = \frac{\sqrt{A/\pi}}{L_c} \tag{9.10}$$

where A = area of the catchment (km^2), L_c = catchment length (km), $\pi = 3.14$. The ratio of the total stream length to the catchment area is called the drainage density (D_d) (Horton 1945). The D_d is given by

$$D_d = \frac{L_s}{A} \tag{9.11}$$

where L_s = total stream length (km), D_d = drainage density ($km.km^{-2}$). The Thiessen polygon method is widely used to precisely assess the spatial distribution of precipitation over a catchment (Theissen 1911). The MAP was calculated using the gridded rainfall data using ArcGIS 10.2. The weighted mean precipitation is calculated by

$$MAP = \frac{\sum_{i=1}^{n} P_i A_i}{\sum_{i=1}^{n} A_i} \tag{9.12}$$

where A_i = area of each Theissen polygon (km^2), P_i = precipitation in each polygon (mm), MAP = mean areal precipitation (mm)

9.5.4.8 Development of a sediment rating regression model

The proportionate strength of the relationship between all ECPs and the rating coefficients were established using principal component analysis (PCA). Based on the correlation matrix, the ECPs were reduced to principal components that correlate well with the rating parameters (δ_0 and δ_1). The PCA assumes the reduced principal components with higher eigenvalues (variance) best characterize the system's functioning, as Halim et al. (2007) mentioned. Henceforth, only principal components with eigenvalues greater than or equal to one were further employed in this study (Golshan et al. 2020). The results of PCA include matrices of unrotated component, communality, and orthogonal (rotated) solution. Syvitski (2010) discussed that the unrotated component loadings signify the degree to which each parameter imparts to the individual component and can be understood as correlation coefficients. The communality matrix explains the total variance predicted from a single component using squared multiple correlations. The results of PCA were subjected to varimax rotation (orthogonal), where each rotated component describe a specific group of correlated variables. The varimax rotation typically increases the correlations among the associated parameters and decreases the correlation among the unrelated parameters.

Stepwise multiple linear regression (SMLR) on log-transformed data was carried out using the sets of parameters reduced from eleven ECPs to model the rating parameters and, consequently, the SSC. The rating model was developed considering the data of ten stations, namely Simga, Baronda, Rajim, Ghatora, Basantpur, Kurubhata, Sundargarh, Salebhata, Kantamal, and Tikarpara. However, all the log-transformed parameters were normalized before the development of the model, as given by Choubin et al. (2017).

$$V^* = \frac{v - v_{\min}}{v_{\max} - v_{\min}} \tag{9.13}$$

where ν = original parameter, ν_{min} = minimum value of the original parameter, ν_{max} = maximum value of the original parameter, V* = normalized parameter. However, merely converting estimates from a log-regression equation back into the original units of *y* yields a median estimate of SSC rather than a mean estimate. Ferguson (1986) pointed out that applying the median or rating curve estimate for SSC would underestimate the mean up to 50%. As a result, the smearing estimate of Duan (1983) was used to compensate for the median estimate of SSC bias. It assumes that the residuals are homoscedastic and independent. This method re-expresses the residuals from the log-log equation into the original units and computes the mean. This mean represents the bias-correction factor (CFs) to be multiplied by the median estimate of SSC for every x_0. It is the most widely applicable technique since it is resistant to residual distributions. The smearing estimator is likewise applicable to any transformation. If $Y = f(y)$, where *y* is the response variable in its original units and *f* is the transformation function, then the bias-correction factor is given by

$$CF_s = \frac{\sum_{i=1}^{n} f^{-1}(e_i)}{n} \tag{9.14}$$

where e_i are the residuals ($Y_i = b_0 + b_1x_0 + e_i$), b_0 and b_1 are the fitted regression coefficients, and f^{-1} is the inverse of the selected transformation (e.g., $\log_{10}$ in our case), and x_0 is the specific value of x for which we want to estimate y.

The predictive functional equations of the regression model were further used to evaluate the degree of the explained variance of the SSC for the hydrological stations that were not considered for the development of the model, namely Andhiyarkore, Manendragarh, Jondhra and Kesinga (2007-2017). Hereafter, these stations were assumed as ungauged stations to test the developed model. The performance of the model was therefore evaluated using frequently used statistical metrics. The metrics used were namely coefficient of determination (R^2), Nash-Sutcliffe efficiency (NSE), observed standard deviation ratio (RSR), and per cent bias (PBIAS) as proposed by Moriasi et al. (2015). The R^2 is defined by equation (12). It varies between 0 and 1, which establishes the amount of variance in the observed data described by the predicted model, with higher values representing less error variance.

Further, Moriasi et al. (2015) advised that the regression line gradient and intercept should also be reported when R^2 is employed as a performance metric. The intercept should be near zero, and the gradient should be close to one for an excellent agreement (Krause et al., 2005). Again, the NSE is a standardized statistic that determines the amount of the residual variance in comparison to the variance of the observed data. It denotes how closely the observed versus predicted data plot fits the 1:1 line and was calculated by equation (13). Another statistic introduced by Moriasi et al. (2007), named observations standard deviation ratio (RSR), was also employed to measure the error-index of the developed model and computed using equations (14) (Moriasi et al., 2015). A lower RSR score implies that the model prediction performed better. It was suggested to provide RSR over the root mean square error (RMSE), as it provides a normalized number for comparing model performance across studies (Moriasi et al., 2007). The R^2 offers a sense of the sediment dynamics; nevertheless, it may not accurately represent the order of magnitude. As a result, the per cent bias (PBIAS) statistic was also calculated, which quantifies the average propensity of the predicted data to be greater or smaller than observed ones (Gupta et al. 1999). It quantifies bias overestimation and underestimation and expresses it as a percentage given by equation (15) (Moriasi et al., 2015). Positive values imply model underestimation bias, whereas negative values suggest model overestimation bias. The metrics R^2 and NSE have ideal values of 1.0, but RSR and PBIAS have optimal values of 0.0.

Moriasi et al. (2015) provide the performance evaluation criteria for a catchment scale sediment model using R^2, NSE and PBIAS (%). For a monthly scale sediment model, $R^2 > 0.4$, NSE > 0.45 and PBIAS $\leq \pm 20\%$ is considered as satisfactory. However, the acceptable level of RSR for a monthly time step model is taken as ≤ 0.7 (Moriasi et al., 2007).

$$R^2 = \left[\frac{\sum_{i=1}^{n}(O_i - O_m)(P_i - P_m)}{\sqrt{\sum_{i=1}^{n}(O_i - O_m)^2}\sqrt{\sum_{i=1}^{n}(P_i - P_m)^2}} \right]^2, 0 \leq R^2 \leq 1 \tag{9.15}$$

$$NSE = \left[1 - \frac{\sum_{i=1}^{n}(O_i - P_i)^2}{\sum_{i=1}^{n}(O_i - O_m)^2} \right], -\infty \leq NSE \leq 1 \tag{9.16}$$

$$RSR = \left[\frac{\sqrt{\sum_{i=1}^{n}(O_i - P_i)^2}}{\sqrt{\sum_{i=1}^{n}(O_i - P_m)^2}} \right], 0 \leq RSR \leq \infty \tag{9.17}$$

$$PBIAS(\%) = \left[\frac{\sum_{i=1}^{n} (O_i - P_i)}{\sum_{i=1}^{n} (O_i)} \times 100 \right], -\infty \leq PBIAS \leq +\infty \quad (9.18)$$

where O_i = ith observed data, O_m = mean of the observed data, P_i = ith predicted data, P_m = mean of the predicted data and *n* = number of observations considered under study.

9.5.4.9 Estimation of bedload transport

Multiple bedload transport equations were developed using various techniques. The BLC_u for the MRB was estimated by applying 7 established bedload functions developed by Shields (1936), Schoklitsch (1962), Bagnold (1980), Roorkee (1984), Julien (2002), Huang (2010) and Recking (2013). The details of the above formulae are given in Table 9.4. These models were decided based on concepts of bed shear stress, discharge, stream power, suitability in sand-bed streams, and firm performance in rivers with unlimited sediment supply.

The BLC_u determined using the bedload functions were compared and analyzed with the bedload classification of the Maddocks approach (Vanoni, 2006). The Maddocks classification was based on suspended sediment concentrations (SSC_g) and mean particle size of sediments (d_{50}) as tabulated in Table 9.5. The appropriateness of the bedload functions for the estimation of BLC_u was therefore established based on the reference percentage of bed load given by Maddock's classification.

Table 9.4: Bed load functions incorporated in the present study.

Bed load functions (Approaches involved)	Functional equations	Parameters involved
Shields, 1936 (Shear stress)	$\frac{q_b\gamma_s}{q\gamma S_a} = 10\frac{\tau-\tau_c}{(\gamma_s-\gamma)d_{50}}$ $\tau = \gamma h_a S_a$ $\tau_c = \theta_c(s-1)\gamma d_{50}$ $\theta_c = 0.1414 S_*^{-0.23}, S_* \le 6.61$ $\theta_c = \frac{\left[1+(0.0223S_*)^{2.84}\right]^{0.35}}{3.09S_*^{0.68}}, 6.61 < S_* < 282.84$ $\theta_c = 0.045, S_* \ge 282.84$ $S_* = \frac{d_{50}\sqrt{(s-1)gd_{50}}}{\upsilon}$	q_b = bedload transport rate [(m^3/s)/m] q = unit flow discharge [(m^3/s)/m] γ_s = specific weight of sediment [KN/m^3] γ = specific weight of water [KN/m^3] S_a = average longitudinal bed slope [m/m] τ = bed shear stress [KN/m^2] τ_c = critical shear stress [KN/m^2] d_{50} = particle size [mm] h_a = mean flow depth [m] θ_c = critical shields stress given by Cao et al. (2006) s = specific gravity of sediment = 2.65 υ = kinematic viscosity of water [m^2/s] g = acceleration due to gravity = 9.81 [m/s^2]
Schoklitsch, 1962 (Unit flow discharge)	$q_c = \frac{1.944\times10^{-5}}{S_a^{4/3}}$ $q_b = \frac{7000\times S_a^{1.5}\times(q_w-q_c)}{d_{50}^{0.5}}$	q_b = bedload transport rate [(kg/s)/m] q_w = unit flow discharge [(m^3/s)/m] q_c = unit critical flow discharge [(m^3/s)/m] d_{50} = particle size (mm) S_a = average longitudinal bed slope (m/m)
Bagnold, 1980 (Stream power)	$\frac{i_b}{i_b^*} = \frac{(W-W_0)^{1.5}}{(W-W_0)^*}\left(\frac{Y}{Y^*}\right)^{-2/3}\left(\frac{D}{D^*}\right)^{-0.5}$ $W_0 = 290\times D^{1.5}\log\left(\frac{12Y}{D}\right)$	i_b = bedload transport rate [(kg/s)/m] i_b^* = 0.1 [(kg/s)/m] W = stream power [(kg/s)/m] W_0 = threshold stream power [(kg/s)/m] Y = mean flow depth (m) $D = d_{50}$ = particle size (m) $(W\text{-}W_0)^*$ = 0.5 [(kg/s)/m] Y^* = 0.1 (m) D^* = 1.1×10^{-3} (m)

Table 9.4 (Continued…)

Bed load functions (Approaches involved)	Functional equations	Parameters involved
Roorkee, 1984 (Shear stress)	$\phi_b = 4.6\times10^{7}\,\tau_*^{'8}, \tau_*^{'} \le 0.065$ $\phi_b = \dfrac{8.5\tau_*^{'1.8}}{\left(1+5.95\times10^{-6}\,\tau_*^{'-4.7}\right)^{1.43}}, \tau_*^{'} > 0.065.$ $\tau_*^{'} = \dfrac{R_b S_a}{(s-1)d_{50}}, R_b = \left(\dfrac{v_a}{K_b\sqrt{S_a}}\right)^{1.5}$ $K_b = \dfrac{KK_w(FW)^{2/3}}{\left[(FW)K_w^{1.5} + 2h_a\left(K_w^{1.5} - K^{1.5}\right)\right]^{2/3}}$ $K = \dfrac{25.8}{\left(2d_{90}\right)^{1/6}}$ $K_w = \dfrac{1}{0.009}$ $\phi_b = \dfrac{q_b}{d_{50}\sqrt{(s-1)gd_{50}}}$	ϕ_b = non dimensional bedload transport rate $\tau_*^{'}$ = non dimensional grain shear stress R_b = hydraulic radius of bed region (m) S_a = average longitudinal bed slope (m/m) s = specific gravity of sediment = 2.65 d_{50} = particle size (m) v_a = average flow velocity (m/s) K_b = resistance coefficient of bed K = general resistance coefficient K_w = resistance coefficient of channel walls FW = flow width (m) d_{90} = particle size at which 90% of the sediment is finer by weight (m) q_b = unit bedload transport [(m^3/s)/m]
Julien, 2002 (Shear stress)	$q_b = 18\sqrt{g}\,d_{50}^{1.5}\tau_*^2$ $\tau_* = \dfrac{h_a S_a}{(s-1)d_{50}}$	q_b = unit bedload transport [(m^3/s)/m] g = 9.81 m/s^2 d_{50} = particle size (m) τ_* = Shields parameter h_a = mean flow depth (m) S_a = average longitudinal bed slope (m/m) s = specific gravity of sediment = 2.65

Table 9.4 (Continued…)

Bed load functions (Approaches involved)	Functional equations	Parameters involved
Huang, 2010 [Modified Meyer-Peter and Muller, 1948] (Shear stress)	$\phi = 6\left(\eta\tau_b^* - 0.047\right)^{5/3}$ $\eta = 0.9997\left(\frac{K_b}{K_s}\right)^{1.1981}$ $K_b = \frac{KK_w(FW)^{2/3}}{\left[(FW)K_w^{1.5} + 2h_a\left(K_w^{1.5} - K^{1.5}\right)\right]^{2/3}}$ $K_s = \frac{25.8}{\left(2d_{90}\right)^{1/6}}$ $K_w = \frac{1}{0.009}$ $\tau_b^* = \frac{R_b S_a}{(s-1)d_{50}}, R_b = \left(\frac{v_a}{K_b\sqrt{S_a}}\right)^{1.5}$	ϕ_b = non dimensional bedload transport rate η = bedform correction τ_b^* = non dimensional bed shear stress R_b = hydraulic radius of bed region (m) S_a = average longitudinal bed slope (m/m) s = specific gravity of sediment = 2.65 d_{50} = particle size (m) v_a = average flow velocity (m/s) K_b = resistance coefficient of bed K_s = general resistance coefficient for skin friction K_w = resistance coefficient of channel walls FW = flow width (m) d_{90} = particle size at which 90% of the sediment is finer by weight (m) q_b = unit bedload transport [(m^3/s)/m]
Recking, 2013 (Shear stress)	$\phi = \frac{14\tau_{84}^{*2.5}}{1 + \left(\tau_m^* / \tau_{84}^*\right)^4}$ $\tau_m^* = 0.045$ for sand $\tau_{84}^* = \frac{S_a}{(s-1)d_{84} \times \left[\left(2/FW\right) + 74p^{2.6}\left(gS_a\right)^p q^{-2p} d_{84}^{3p-1}\right]}$ where $p = 0.23$ when $\frac{q}{\sqrt{gS_a d_{84}^3}} < 100$ and $p = 0.3$ otherwise $q = Q/FW$	ϕ = Einstein non dimensional bedload transport rate $\phi = \frac{q_b}{\sqrt{(s-1)gd_{84}^3}}$ q_b = unit bedload transport [(m^3/s)/m] g = 9.81 m/s^2 d_{84} = particle size at which 84% of the sediment is finer by weight (m) τ_{84}^* = Shields stress for d_{84} τ_m^* = mobility shear stress S_a = average longitudinal bed slope (m/m) s = specific gravity of sediment = 2.65 FW = flow width (m)

Table 9.5: Maddocks classification of ungauged bed load concentration

Suspended sediment concentration (ppm)	Bed material class	Texture of suspended sediment	Percentage of suspended load as ungauged bed load
< 1000	Sand	Similar to bed material	25 to 150
< 1000	Gravel, rock or consolidated clay	Small amount of sand	5 to 12
1000 to 7500	Sand	Similar to bed material	10 to 35
1000 to 7500	Gravel, rock or consolidated clay	25% sand or less	5 to 12
> 7500	Sand	Similar to bed material	5 to 15
> 7500	Gravel, rock or consolidated clay	25% sand or less	2 to 8

9.5.4.10 Estimation of future sediment load and capacity of Hirakud reservoir

The Hirakud reservoir has an incoming sediment load from 3 streams: the Main Mahanadi, the Mand tributary, and the Ib tributary. As a result, the sum data of 3 gauging stations, i.e., Basantpur, Kurubhata and Sundargarh, at the outlet of these streams were considered to analyze the reservoir capacity in the historical (1980-2018) and future (2018-2100) climatic scenarios. The historical period's rainfall-runoff model (M1) was generated by developing a power regression between the total mean areal average precipitation versus total runoff to the Hirakud reservoir. Eventually, the runoff-sediment model (M2) for the same period was designed using power regression between the total runoff versus total sediment load to the Hirakud reservoir. The M2 model was checked for consistency using the double mass curve method, as discussed in Fig.2. Further, the sediment load was corrected concerning the latest sediment regime, and the corrected runoff sediment model (M2C) was further used. The projected precipitation for the future period was taken from the study of Regional Climate Projections in India with Statistical Downscaling by Salvi et al. (2013) and Kannan and Ghosh (2013). The data was obtained for bias-corrected downscaled rainfall from CCCMA CanESM2 global circulation model (GCM) for RCP 8.5 climatic scenarios prescribed by the Intergovernmental Panel on Climate Change (IPCC). The projected runoff was modelled using the developed M1 model incorporating projected precipitation, and ultimately, the projected sediment load entering the Hirakud reservoir was generated using the M2 model. The entire analysis was done on an annual basis for the monsoon period. The reservoir capacity for the future period was then estimated using Brune's curve developed for the Hirakud reservoir (Dutta and Sen, 2016).

9.5.5. Results and Discussion

The results and discussions of the different analyses performed in the present study are mentioned in the following subsections:

9.5.5.1 Variations of normalized runoff and sediment load

The hydrological stations' mean yearly runoff and sediment load is normalized by its drainage area to allow comparisons among basins with different basin sizes. The primary statistical summary of the normalized yearly runoff (mm/yr) and sediment load (tons/km^2/yr) throughout the study interval in the Mahanadi River and its principal tributaries is presented in Fig. 9.10. The significant difference in the normalized runoff is the consequence of the variation in the drainage area of the various stations upstream of Tikarpara. The variation in the normalized yearly runoff at different stations is more pronounced in the upstream part of the basin than in the downstream stations. The normalized mean yearly runoff to the sea decreases marginally around 1.7% from 382 mm/yr to 375.4 mm/yr during the first (1973-1983) and the last decades (2007-2017) of the study period. The data shows that almost 77% to 92% of total yearly runoff takes place during monsoons (June-September) at different hydrological stations of the basin, as shown in Fig. 9.11, confirming significant seasonal variations. It is, however, found to be nearly independent of the different observation years for various hydrological stations.

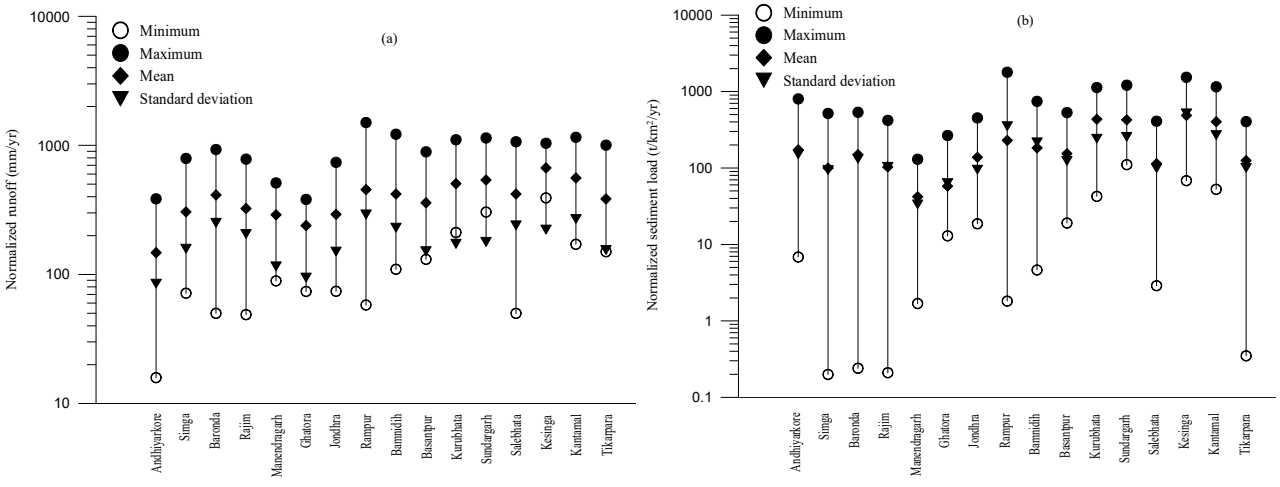

Figure 9.10: Statistical summary of normalized yearly (a) Runoff and (b) Sediment load

Further, there is a wide spatiotemporal fluctuation in the normalized yearly sediment load of the observed data (Fig. 9.10b). The spatial variation in normalized sediment load is predominantly attributed to the variability in relief between the upstream and downstream watershed areas. Moreover,

the accumulated sedimentary deposits at the upstream portion of the basin resulted in reduced sediment yield in contrast to the downstream region, which is composed of igneous and metamorphic rocks confined by thick soil layers. The Tel tributary deposits the maximum normalized mean yearly sediment load to the main channel with Seonath, Ib, Mand, Jonk, Hasdeo and Pairi following it, respectively.

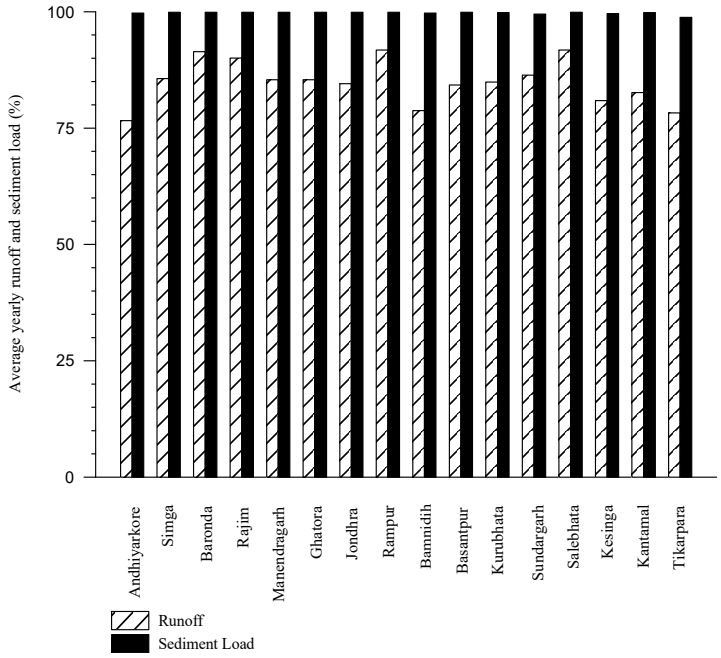

Figure 9.11: Average percentage of yearly runoff and sediment load for all gauging stations during monsoon.

Normalized yearly sediment load discharging into the Bay of Bengal varies from 0.35 t/km^2/yr (2009-2010) to 403.9 t/km^2/yr (1994-1995) with an arithmetic mean of 125.1±100.2 t/km^2/yr (1973-2017). Furthermore, the normalized mean yearly sediment load varies from 233.3±102.9 t/km^2/yr in the first ten years (1973-1983) to 48.7±24.5 t/km^2/yr in the last ten years (2007-2017) of the available data period at the final gauging station, computing to approximately 79% decline in normalized mean yearly sediment load between the two periods. The global normalized mean yearly sediment load was found to be 150 t/km^2/yr, as reported by Milliman and Meade (1983).

In contrast, the normalized mean yearly load of the Mahanadi River basin is computed as 207.6±145.3 t/km^2/yr, which is more than the world average. The sediment load throughout monsoons in the basin is relatively constant for all gauging stations indicating that monsoon sediment load is the major contributor to yearly sediment discharge irrespective of different observation years of the different

hydrological stations (Fig. 9.11). It also shows a significant impact of runoff on the sediment load. Fig. 9.12 shows the deviation in yearly runoff and sediment load at the last gauging station Tikarpara, where the sediment load decreases for a given runoff over time. Also, significant variations in different periods are evident, but no periodicity in runoff is noticeable.

Moreover, a peak in the yearly runoff is observed for 1994-1995. It is due to a major flood event in Odisha during that time, hitting almost 25 districts of the Mahanadi river basin as per the report of major flood occurrences (DoWR, 2009). Further, the minimum value observed in 1979-1980 is attributed to the drought year in the basin (Chakrapani and Subramanian, 1990b). However, a significant decreasing pattern was observed in the yearly sediment load from 1995-1996 onwards compared to runoff. Consequently, the yearly sediment load becomes zero in 2009-2010 due to the steady decrease in annual runoff from 2006-2007 (Fig. 9.12). Moreover, this also suggests that most of the runoff is stored in the reservoirs during those periods.

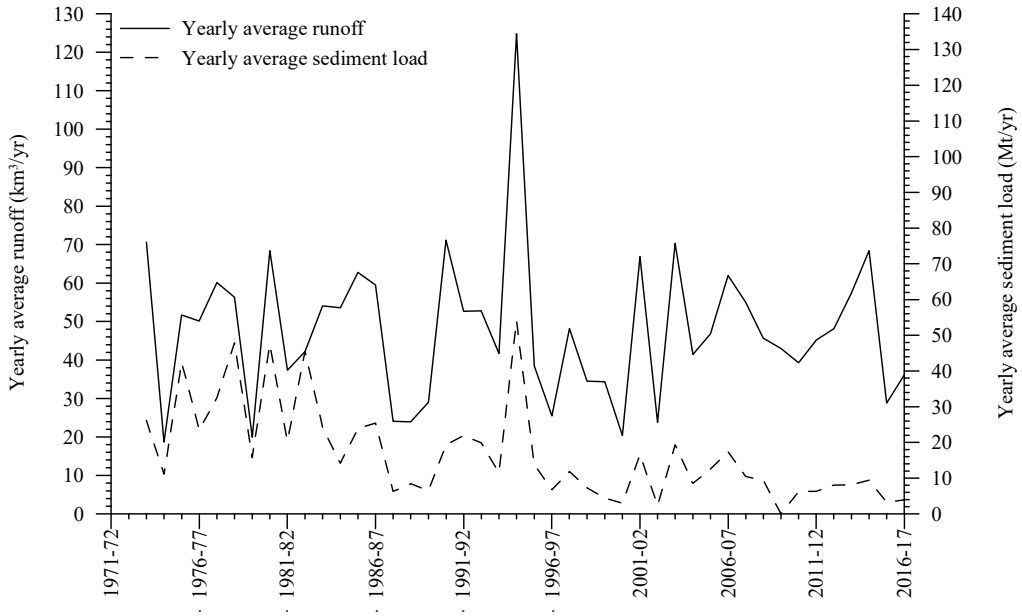

Figure 9.12. Yearly average runoff and sediment load variation at Tikarpara

9.5.5.2 Sediment rating curve

For the present study, the power function between the sediment load and runoff is considered for the determination of SRC. Strong positive correlations (R^2 = 0.5 to 1) are obtained for SRC for most stations, with Rajim, where the most upstream station of the Mahanadi mainstream, shows the maximum value of the coefficient of determination (R^2) as 0.7. The linear correlation of the SRC decreases from the Rajim to the Tikarpara (R^2 = 0.4) of the Mahanadi river. This drop-in R^2 is due to

the confluence of the Ong tributary showing a very weak correlation ($R^2 = 0.3$) with the mainstream of the Mahanadi river before Tikarpara. Nordin (1985) discussed that sediment flux is greatly influenced by the material supplied for transport rather than the flow capacity to transport it. Eventually, the temporal and spatial variations in SRC is assumed to be due to the increasing extent of human activities in the basin for the last decades. It is further established in the subsequent section 5.6.

The steepness of SRC is considered a suitable attribute of the erodible nature of the soil and the erosive power of a stream (Asselman, 2000). Hence, the SRC of all the hydrological stations is plotted to understand the changes in SRC parameters (Fig. 9.13). Most of the hydrological stations situated on the basin's tributaries show the maximum steepness of SRC compared to the mainstream stations, with the upstream Andhiyarkore being the steepest of all. The existence of weirs also increases the steepness of the SRC as the sedimentation occurs behind it due to low runoff during non-monsoon, which washes out due to excess runoff during monsoons. It is explained by the steepness of SRC of the Bamnidih station, situated immediately downstream of the Korba barrage. A similar observation is seen from the steepness of SRC of the Rampur station at the immediate downstream of Jonk weir. The flatness of the SRC is taken as the evidence of channel with sediments being conveyed at all discharges. As a result, the flattest SRC is found at Tikarpara, having the largest drainage area.

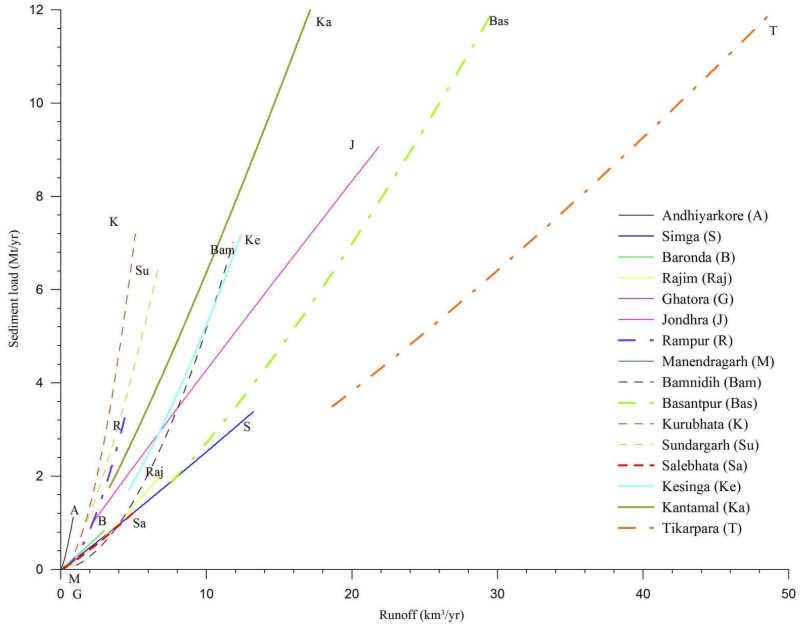

Figure 9.13: Variation of yearly SRC for all hydrological stations of the basin fitted using power law

Moreover, to establish that steeper SRC is evidence of larger transport of sediments at higher runoff, the sediment transport mechanism of the Mahanadi River basin is additionally analyzed. Table 9.6, therefore, explains the impact of high and low runoff on the sediment transport of the Mahanadi River basin. It shows the significance of high runoff in transporting sediments in tributaries compared to a river's mainstream stations.

Table 9.6: Impact of high and low runoff on the sediment transport of the Mahanadi River basin

Hydrological stations	$q_{avg.}$	$q_{avg.\ \%}$	$q_{savg.\ \%}$	$q_{10\%}$	$q_{s10\%}$
Andhiyarkore	0.66	66	11	2.0	60
Simga	15.5	48	26	34.2	38
Baronda	2.6	65	16	4.9	60
Rajim	6.9	53	24	16.9	39
Manendragarh	0.6	26	13	1.1	35
Ghatora	2.6	77	17	12.1	65
Jondhra	18.8	49	17	44.7	46
Rampur	2.0	57	17	6.2	24
Bamnidih	3.8	70	34	9.0	45
Basantpur	32.9	52	23	79.0	46
Kurubhata	7.6	48	11	19.1	61
Sundargarh	9.3	49	9	18.6	62
Salebhata	2.5	59	11	7.3	49
Kesinga	13.0	52	18	29.6	49
Kantamal	20.3	62	20	52.0	54
Tikarpara	84.3	53	22	215.2	40

Note: $q_{avg.}$ is the yearly mean runoff in km^3/yr, $q_{avg.\ \%}$ is the percentage of time when runoff is less than $q_{avg.}$, $q_{savg.\%}$ is the percentage of total yearly sediment load conveyed at runoff below $q_{avg.}$, $q_{10\%}$ is the runoff that exceeded 10% of the time (km^3/yr), $q_{s10\%}$ is the percentage of total yearly sediment load conveyed at runoff greater than $q_{10\%}$

9.5.5.3 Trend analysis

The results of the trend analysis are shown in Fig. 9.14. Out of 16 hydrological stations in the basin, only 2 stations (or 12.5% of the total stations) showed a significant decreasing trend with a magnitude of 0.01 km^3/yr (Manendragarh) and 0.07 km^3/yr (Bamnidih) during 1973-2017. The decreasing trend in mean yearly runoff at Bamnidih accounts for the large volume of water being stored in the Minimato Bango reservoir for various competing demands during dry monsoon periods. Moreover, the yearly sediment load showed a significant decreasing trend (at a 5% level of significance) for all but 5 stations

(or 31.3% of the total stations), namely, Ghatora and Jondhra of Seonath tributary; Kesinga and Kantamal of Tel tributary and Salebhata of Ong tributary during 1973-2017. The decreasing slope was more drastic in the main channel than the tributaries, where the sediment load of the left bank tributaries is significantly less in relation to those of the right banks. This decline in yearly sediment load to the Bay of Bengal is noteworthy in contrast with the non-significant trend in the annual runoff. Also, this illustrates that the natural process in the form of change in precipitation is perhaps not the foremost basis for the drastic decreasing trend observed for suspended sediment load. However, the number of dams or reservoirs in the MRB had progressively increased many folds in recent years (CWC, 2014) compared to only 70 dams functioning before 1980, which also resulted in the decreasing trend of sediment discharge. Chakrapani and Subramanian (1990b) also mentioned that 65% of the sediment load of the Mahanadi river is sequestered by storage structures built along the direction of the river. Following this, it is seen that after completion of the Minimato Bango dam in the Hasdeo tributary in 1990, there is a 78% decrease in mean yearly sediment load (3.4 to 0.7 Mt/yr). Similarly, a significant reduction of around 65% in mean yearly sediment load (2.0 to 0.7 Mt/yr) is observed after the construction of the Ravishankar Sagar dam of the Mahanadi River basin in 1979. Moreover, as per the latest CWC data on the reservoir module, it was observed that the total storage capacity of the Hirakud dam reduced by 60% in the period of 01-01-2005 to 17-05-2018 (absolute value decreased from 3900 MCM to 1500 MCM). It shows the influence of human-induced activities in the form of a reservoir that has resulted in noteworthy entrapment of sediments and thus reduced the total storage capacity of reservoirs.

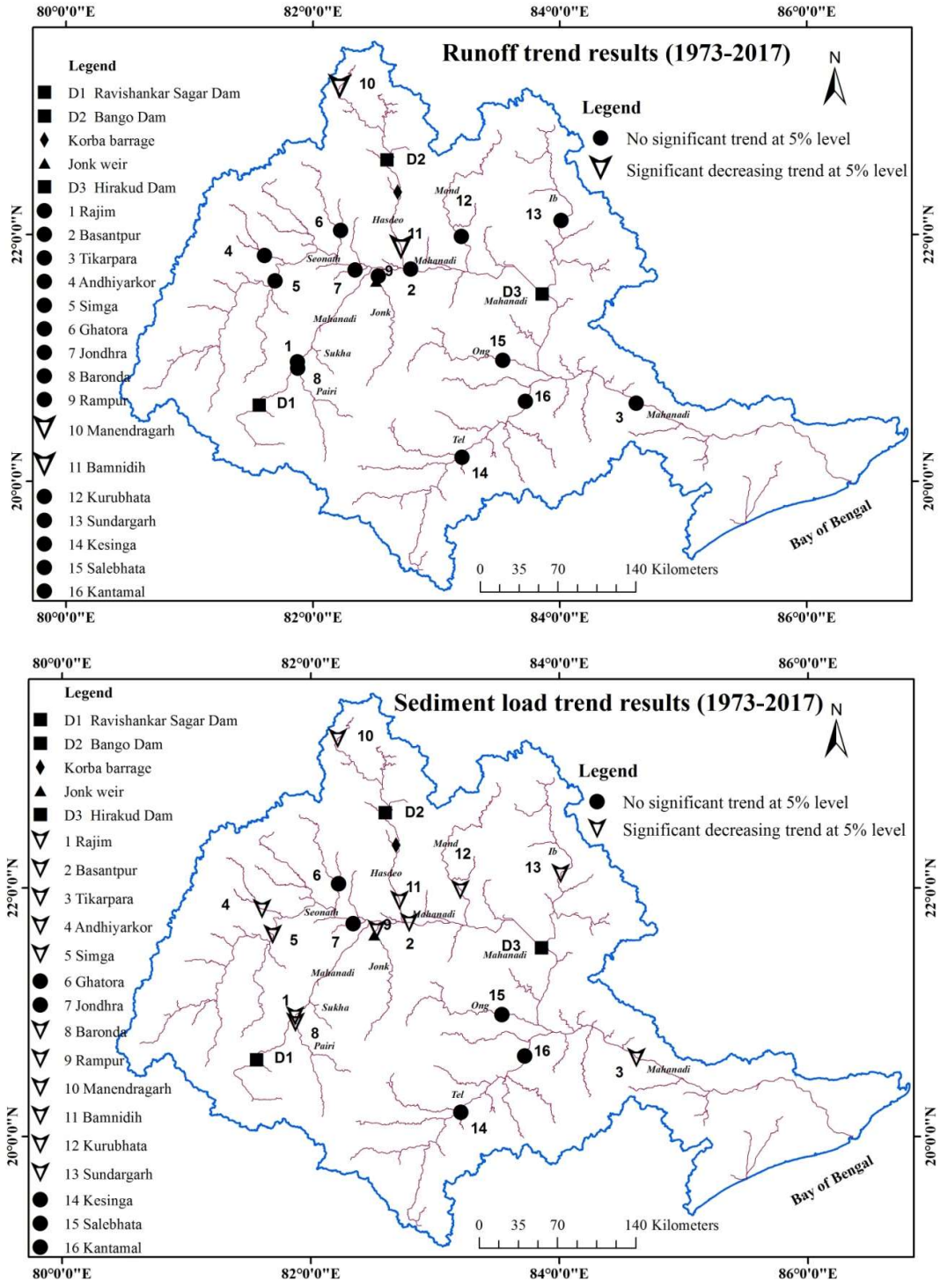

Figure 9.14: Trend analysis results of (a) runoff and (b) sediment load across the basin.

9.5.5.4 Change point analysis

The breakpoints for the stations at Mahanadi tributaries did not arise simultaneously as the tributaries encountered significant disturbances in terms of runoff and human activities (Table 9.7). However, the change points occur nearly simultaneously for Basantpur and Tikarpara station along the mainstream of the Mahanadi River. Variations of runoff across all stations do not show any significant change points except at Bamnidih of the Hasdeo basin, where it is significantly changing during the year 2005-2006. The table shows a decrease of 51% in the mean yearly runoff before and after 2005-2006. The reason for this shift in the year 2005-2006 is attributed to the significant reduction in mean yearly yield (at 75% dependability) at the Hasdeo barrage (just upstream of Bamnidih station) from 3536 MCM (1959-1999) to 1851 MCM (2005-2015), which was associated to the falling rainfall in that region (Dsouza et al., 2017). However, the significant change points in the sediment load are identified at ten stations: Andhiyarkore, Simga, Manendragarh, Rampur, Bamnidih, Basantpur, Kurubhata, Sundargarh, Salebhata, and Tikarpara. The time of shift in sediment load is observed to be the same (1994-1995) for both Bamnidih and Basantpur station, commonly on account of Minimato Bango reservoir operation, which began late of 1990; however, the filling of the reservoir took place during 1994-1995 (Dsouza et al., 2017). It subsequently results in significant sediment trapping, reducing the mean yearly sediment load of approximately 89% at Bamnidih and 68% at Basantpur station after the change period. The yearly sediment load from the basin to the Bay of Bengal is 22.7 Mt/yr averaged for the time 1973-1974 to 1995-1996 and reduced to 7.7 Mt/yr averaged for the time of 1996-1997 to 2016-2017 as evident from the change point detection analysis (Fig. 9.15c). This decreasing trend of sediment load may also impact coastal morphology. Fig. 9.15 shows all the observed significant change marks in runoff and sediment load across some of the gauging stations of the Mahanadi River basin.

Table 9.7: Change point analysis of yearly runoff and sediment load

Stations	Runoff	Sediment load
Andhiyakore	No	2005-06
Simga	No	1997-98
Baronda	No	No
Rajim	No	No
Manendragarh	No	2003-04
Ghatora	No	No
Jondhra	No	No
Rampur	No	2008-09

Stations	Runoff	Sediment load
Bamnidih	2005-06	1994-95
Basantpur	No	1994-95
Kurubhata	No	1999-00
Sundargarh	No	1998-99
Salebhata	No	1986-87
Kesinga	No	No
Kantamal	No	No
Tikarpara	No	1995-96

Note: "No" means no change point detected at 5% significance level

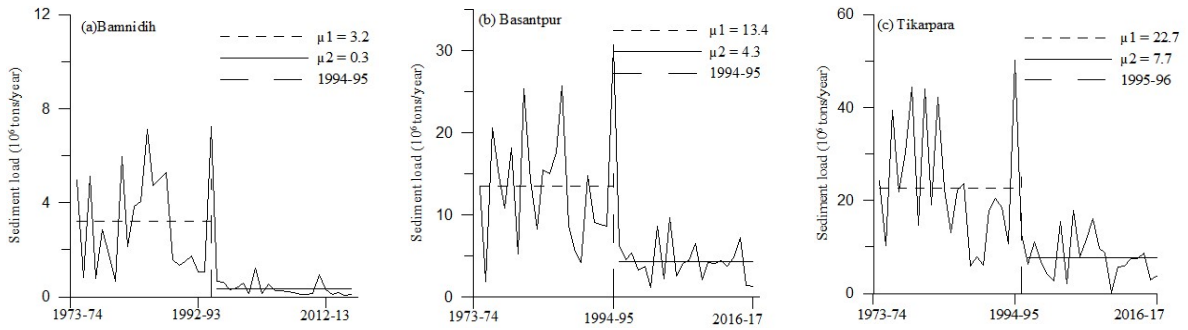

Figure 9.15: Sudden change point years in trend (at the significance level of 0.05) of sediment load, where μ1 and μ2 indicate arithmetic mean before and after the change point, respectively.

9.5.5.5 Volumetric change estimation of the Mahanadi delta

To further understand the consequence of the significant decrease in yearly sediment load, an attempt is made to determine its impact on the Mahanadi delta from 2000 to 2011. The study was conducted over a total area of nearly 115 km^2, where the cumulative area of erosion and accretion is found to be 20 km^2 and 88 km^2, respectively. However, around 7 km^2 area persisted in either being stable or conserving equilibrium between erosion and accretion processes. Further, the equivalent volumetric attribute of the delta shows that the total volume of erosion and accretion as 0.1 km^3 and 0.5 km^3, respectively. Therefore, it results in a vertical average yearly erosion and accretion of 29 cm and 48 cm, respectively. For eleven years, these quantitative figures of morphological changes (land lost and land gain) demonstrate that the coastal landforms susceptible to erosion are highly vulnerable. It is perceived by the 65% increase in the percentage of vertical accretion (with respect to vertical erosion) when the corresponding areal accretion is increased remarkably by 340% compared to areal erosion. This volumetric coastal loss is attributed to the heavy rainfall causing flash floods in 2011 resulting

from the abrupt opening of gates of Hirakud dam, thereby leading to substantial monetary and environmental damages to the coastal delta (Panda et al., 2013). In this context, it is pertinent to mention that Le Nguyen and Vo Luong (2019) reported an average vertical erosion and accretion of 20 cm and 40 cm, respectively, at the Vietnam coast.

Moreover, these significant volumetric changes are also related to the spatial differences of sediment load due to various coastal and alluvial processes and other human activities over the catchment. Fig. 9.16 shows the maps highlighting the zones of significant erosion and accretion distributed spatially along the coastal belt of the Mahanadi delta during 2000-2011. It is observed that the accretion of delta plays a vital role between the mouth of the Rushikulya River to the mouth of Chilika Lake (Fig. 9.16a). This stretch of the delta is an ecologically important habitat zone, also classified as a Gahirmatha marine wildlife sanctuary, the world's largest nesting beach for Olive Ridley Turtles, and a few other habitable zones with major district roads near Chilika Lake.

Further, it is seen that there is some vertical erosion at the mouth of Chilika Lake. The picture changes in the next section, from the stretch of Chilika Lake to the mouth of the Dhaudia river (Fig. 9.16b). Significant erosion is observed near the mouth of the Dhaudia river, which matched well with the study of Mukhopadhyay et al. (2018) for the years 1990-2015. However, looking into the next stretch from the mouth of the Dhaudia river to the NuaNai river, the scenario completely reverses. This entire coastal stretch is mainly subjected to erosion, where lies the Puri, a densely populated tourist pilgrimage place, and some areas of other commercial establishments (Fig. 9.16c). The situation is almost the same in the next stretch between the mouth of the NuaNai river and the Kadua river (Fig. 9.16d). This stretch has got mainly the Balukhand-Konark Wildlife Sanctuary and the Puri-Konark marine drive, where erosion is dominant. Next, the deposition takes over erosion, mostly near the mouth of the Kadua river. The same observation was reported by Mishra and Panda (2016) for the year 1972-2014. The last stretch of the delta from the mouth of the Devi river to the Mahanadi river is dominated by accretion (Fig. 9.16e). Few spots of erosion are also observed on the right bank at the mouth of the Devi river. Also, the accretion around the Paradip seaport is controlled mainly by constructing coastal structures in that area. Overall, the areal extent of accretion is more considerable than erosion; however, the major cities and tourist places are subjected to significant land loss. Consequently, it is a state of concern for being considered one of India's most populous deltas (Census, 2011). Therefore, the analysis visualizes the strong influence of sediment starvation from the catchment, which leads to accelerated coastal erosion at various locations along the Mahanadi coast.

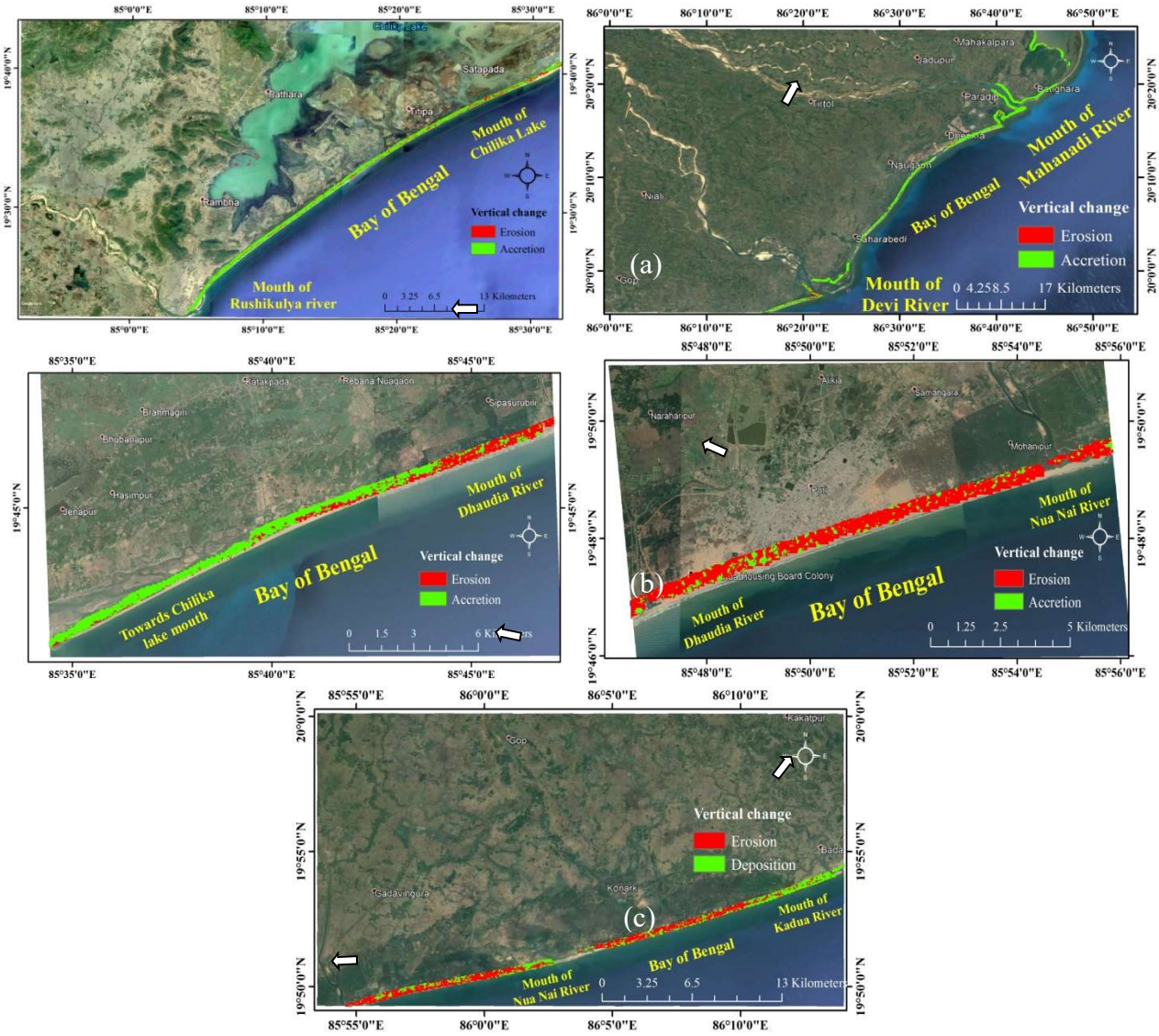

Figure 9.16: Maps showing areas of significant erosion and accretion along the coastal belt from (a) Mouth of Rushikulya River to Chilika Lake (b) Mouth of Devi River to Mahanadi river (c) Mouth of Chilika Lake to Dhaudia River (d) Mouth of Dhaudia River to Nua Nai River and (e) Mouth of Nua Nai River to Kadua River, during 2000-2011

The outcome of the volumetric change estimation is validated using the specified four hundred number of ground control points derived from Google Earth (GE) (taken as a reference). The elevation values for these control points were retrieved from SRTM and ASTER DEM's. It is noticed that the average difference between the GE control points and DEM's observed points is (-2.0 m). The uncertainty, therefore, seems sensible for accepting the volumetric change estimation of the delta.

9.5.5.6 Effects of anthropogenic stresses on sediment supply to the Mahanadi delta

5.6.1 Effect of building large dams in the basin

To understand the influence of major anthropogenic activities in the catchment influencing the sediment transport rate to the ocean, the effect of building large dams in the Mahanadi River basin is studied at the decadal scale (Fig. 9.17). A compelling inverse relationship is noticed between the increase in the number of large dams in the basin during the last four decades (1977-2017) with the drop in yearly sediment load recorded at the Tikarpara. Fig. 9.17 thus illustrates a substantial consequence of human activities in large dam constructions on the decadal response of yearly sediment load transported across the basin.

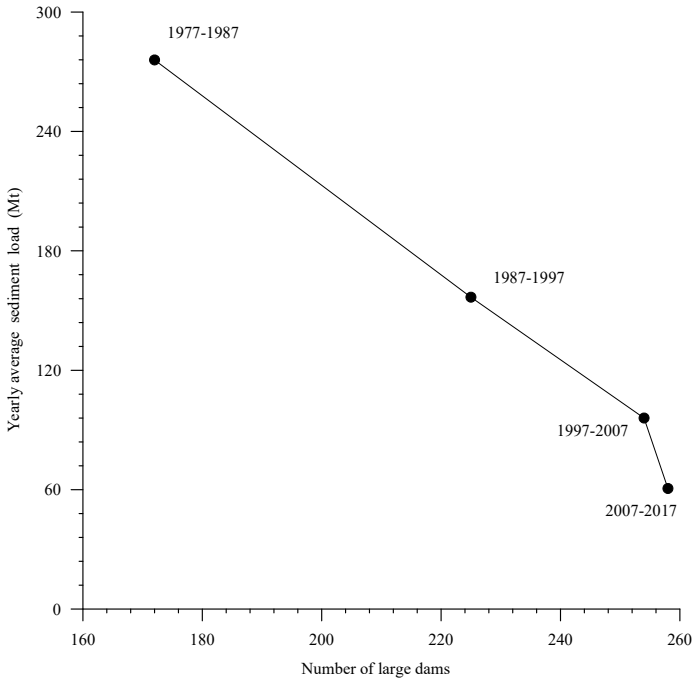

Figure 9.17: Decadal variation of sediment load at Tikarpara versus number of large dams

5.6.2 Effect of dam impoundment

Fig. 9.18 illustrates the variation of yearly sediment load at the next downstream station Rajim of the Ravishankar Sagar dam before and after the impoundment in 1979. The variation in yearly runoff explains more than 95% ($R^2 = 0.96$) of the change in sediment load before the dam impoundment. However, it drops drastically to 40% ($R^2 = 0.40$) after the impoundment in 1979. Likewise, Fig. 9.18 also displays the fluctuations of yearly sediment load at the downstream station Bamnidih next to the Minimato Bango dam before and after the construction in 1990. The yearly runoff-sediment load

variability decreases from 65% to 46% (R^2 = 0.65 to 0.46) after the dam's impoundment in 1990. The reason for which the variation in yearly runoff explained 95% of the change in sediment load at Rajim before the dam impoundment is due to the construction of the Ravishankar Sagar dam in one of the headwater streams of where the main Mahanadi originates. Also, it results in minor inconsistency in the relation between runoff and sediment load before impoundment of the Ravishankar Sagar dam in contrast to the explained variation at Bamnidih located in the mid-Mahanadi basin. It further demonstrates the consequence of dam operations with an enormous quantity of sediments being sequestered by those reservoirs, thus resulting in a remarkable fall of sediment load to the Bay of Bengal over the years.

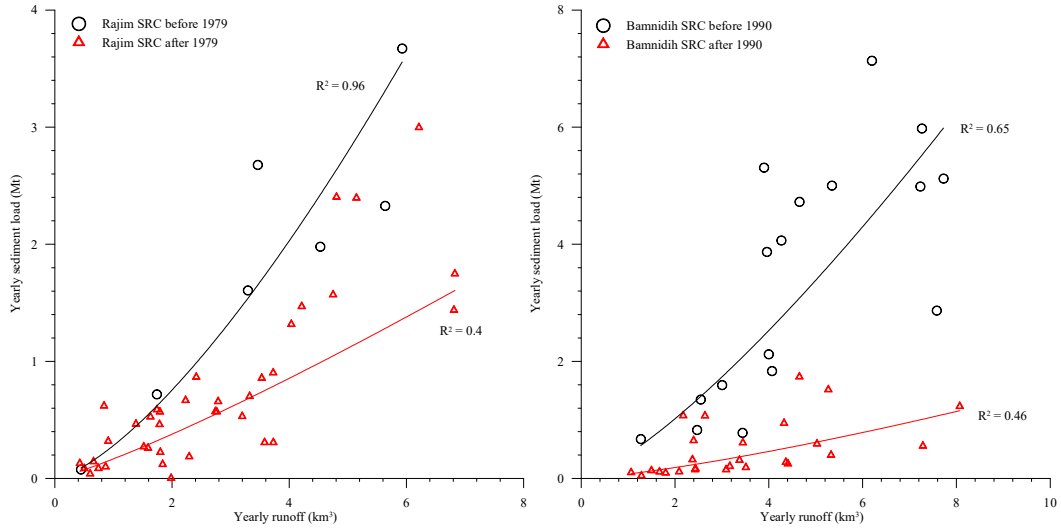

Figure 9.18: Variation of yearly sediment load vs. runoff at Rajim & Bamnidih station before and after the construction of Ravishankar Sagar (1979) & Minimato Bango dam (1991)

5.6.3 Relative contributions of various human interferences in the basin

Figure 9.19 show the double mass curve plot of cumulative mean yearly sediment load versus cumulative mean yearly runoff at the Rajim, Basantpur, and Tikarpara stations, respectively, during 1973-2017. A good correlation is observed for all the three observation stations between cumulative mean yearly sediment load and cumulative mean yearly runoff (Table 9.8). The break-in slope for 1980-1981 (at Rajim) is associated with the impoundment of the Ravishankar Sagar dam (1979) in one headwater stream, just upstream of Rajim station. The relative contribution of human interference for the first deviation (1980-1981) is found out to be 24.9% and subsequently increased for the second deviation (2010-2011) to 37.9%. This greater relative change for the year 2010-2011 compared to 1980-1981 is attributed to the shift in water allocation priorities in the state of Chattisgarh within the

basin (Dsouza et al., 2017). This increase in water allocation was due to the rampant rise in industrialization, where most of the region's large industries are gathered in small pockets around the storage structures, nearby Rajim station. The sudden increase in water utilization was so high that 87% of the projected water requirement for industries in 2040 was already supplied in 2010-2011. Therefore, this rapid growth in water demand for industrial sectors results in a substantial deviation of the mean annual sediment load.

Similarly, a single breakpoint is observed for Basantpur station during 1994-1995 (same as Pettitt test), for which the role of human activities is quantified to be 21.6%. This turning point is attributed to the operation and impoundment of the Minimato Bango dam in the Hasdeo basin at the immediate upstream of Basantpur station. The proportionate human contribution is assessed to be 15.2% and 33% for 1986-1987 and 1995-1996, respectively for Tikarpara. The first turning point in 1986-1987 is ascribed to the soil conservation measures adopted in the Hirakud catchment as verified by Kumar (1989). The next change point in the year 1995-1996 is due to the effect of Minimato Bango reservoir operations in 1990.

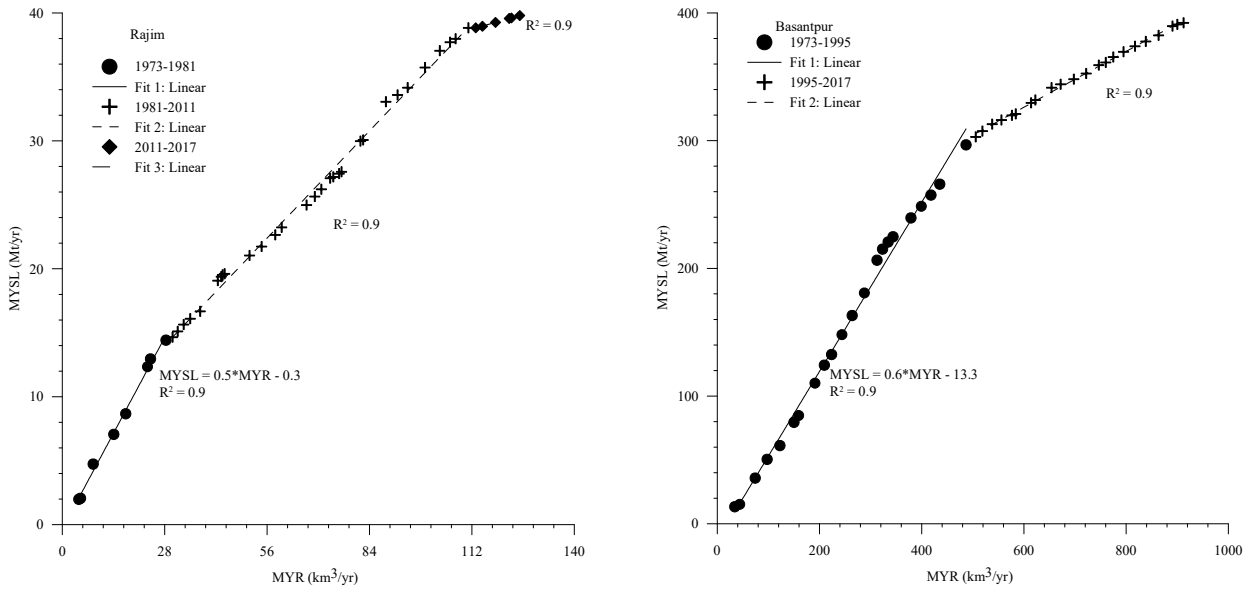

Figure 9.19: Influence of human interference on sediment load at Rajim, Basantpur & Tikarpara estimated using DMC.

Figure 9.19 (continued…)

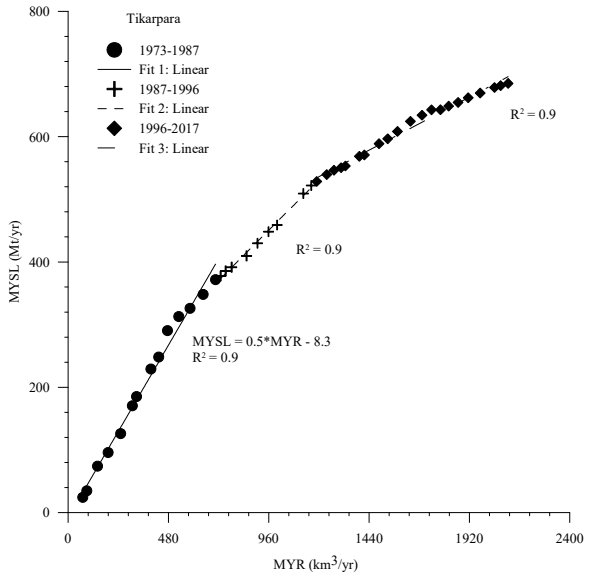

5.6.4 Changes in the parameters of the SRC

Anthropogenic activities like constructing dams and soil conservation measures in a basin decrease the natural supply of sediments (rating parameter *a*) and thereby increase the erosive capacity (rating parameter *b*), as understood from Table 9.9. The rating parameter *a* at Basantpur decreases steadily from 0.3 (1973-1995) to 0.09 (1995-2017), whereas the rating parameter *b* increases from 1.2 to 1.3 for the same time. The same fluctuation in rating parameters is observed at Tikarpara, where *b* increases from 0.8 (1973-1979) to 1 (1979-1996) till 1.4 (1996-2017). However, *a* decreases from 0.9 to 0.4 till 0.03 for the respective periods.

The rating parameter *b* at Rajim seems not to vary much from 1.21 (1973-2011) to 1.2 (2011-2017). But the rating parameter *a* decreases considerably from 0.4 (1973-1981) to 0.2 (1981-2011) till 0.03 (2011-2017). The insignificant variation of *b* at Rajim (the most upstream station) is due to the lower deviation in discharge compared to the other downstream stations of the basin. This entire analysis further supports the DMC interpretation that human interferences have a long term influence on the morphological changes of the river basin.

Table 9.8: Quantitative percentage contribution of human interference to the decrease in sediment load.

Stations	Break year	R^2	Percentage of human interference
Rajim	1973-1981	0.9	-
	1981-2011	0.9	24.9
	2011-2017	0.9	37.9
Basantpur	1973-1995	0.9	-
	1995-2017	0.9	21.6
Tikarpara	1973-1987	0.9	-
	1987-1996	0.9	15.1
	1996-2017	0.9	33

Table 9.9: Sediment rating parameters (*a* and *b*) for different periods at Rajim, Basantpur, and Tikarpara.

Stations	Break year	*a*	*b*
Rajim	1973-1981	0.4	1.21
	1981-2011	0.2	1.21
	2011-2017	0.03	1.2
Basantpur	1973-1995	0.3	1.2
	1995-2017	0.09	1.3
Tikarpara	1973-1987	0.9	0.8
	1987-1996	0.4	1
	1996-2017	0.03	1.4

5.6.5 Effect of water allocations and their use in the basin

Further, to support the claim of the long-term influence of human interferences on the trend of yearly flow from the entire basin, the yearly runoff is separated seasonally (Fig. 9.20). A notable decrease in the monsoon runoff trend is observed compared to the increase in non-monsoon runoff. It is due to the rise of storage in reservoirs during the monsoon that is discharged in non-monsoon. Additionally, to justify the increase in human consumption of water from the reservoir over the years, the variation of seasonal allocation of water for irrigation from the world's longest man-made dam-Hirakud is plotted in Fig. 9.21a. It is observed that there is a steep rise in the water distribution for irrigation purposes during non-monsoon relative to the monsoon period. Besides that, Fig. 9.21b shows a more steep rise in water allocation for hydropower during monsoon than in the non-monsoon period. The trends also establish that the installed hydropower capacity had steadily increased during the period, which ultimately increased the monsoon allocation compared to the non-monsoon allocation post-1995.

Additionally, the industrial development of thermal power plants over the Chattisgarh region of the basin is surged up to 400% since 2005 (Fig. 9.22a). The figure shows that these thermal power plants had excess water allocation compared to their required quantity before 2005. In contrast, the allocation

is inadequate to fulfil the installed thermal capacity in the later period. However, in Odisha, it is observed that the allocation of water was marginally in excess before 2010. Still, the differences gained significantly later, with more allocated water remaining unused by the end of 2016 (Fig. 9.22b). On the other hand, in Odisha, the installed thermal power capacity jumped after 2007, much after Chattisgarh. Overall, the analysis shows the remarkable rise in the demand of industries and their corresponding water allocations in the last decade, which resulted in significant water diversions from the major storage structures of the river basin. The entire analysis presented in this section shows the increasing extent of human interference in the basin, which further influences the overall sediment flux discharged into the delta.

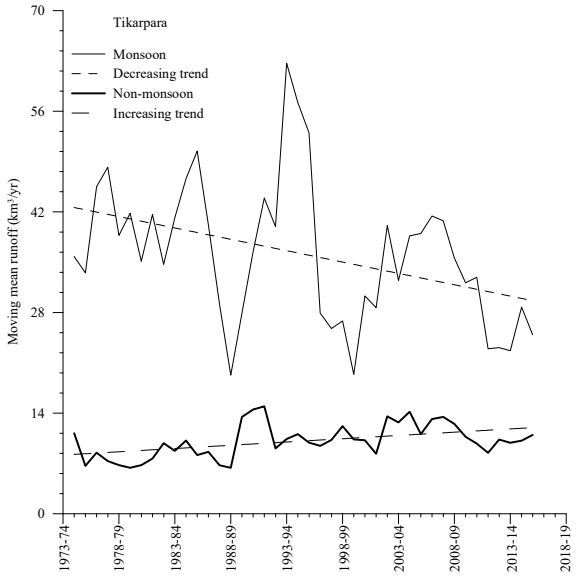

Figure 9.20: Seasonal variation of runoff at Tikarpara

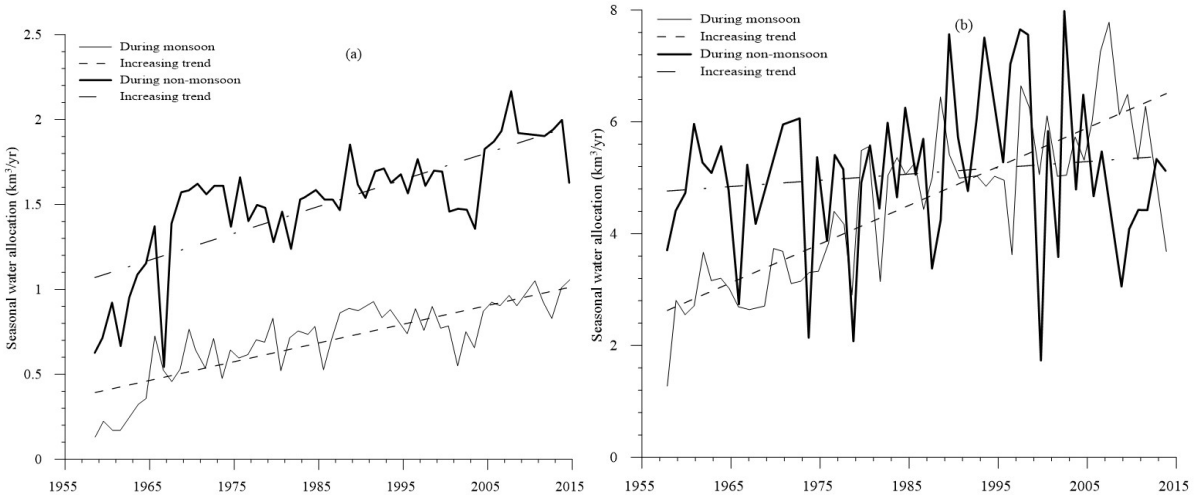

Figure 9.21: Seasonal variation of water allocation from Hirakud Reservoir for (a) Irrigation and (b) Hydro-Power

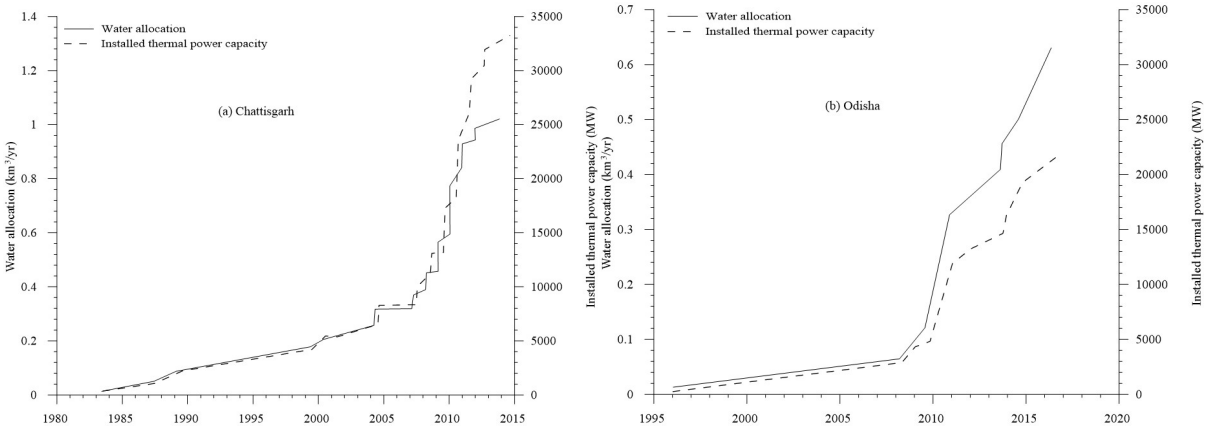

Figure 9.22: Variation of installed power capacity and corresponding water allocations to thermal power plants in the Mahanadi River basin.

9.5.5.6 Characteristics of SRC hysteresis

The examination of hysteretic patterns over time is recommended as a basic approach for evaluating heterogeneity in sediment source and behaviour at the watershed scale (Mao and Carrillo 2017). The plot of ΔR and ΔC for different hysteresis loops of June to October for different years of the study period at Tikarpara is shown in Fig. 9.23. The results for June (Fig. 9.23) across years show that with varying dilution and flushing conditions, the majority of the hysteresis loops take on more complex shapes on the onset of monsoons. The loops for June 2008, 2009, 2011, 2012, 2013 and 2014 reveal a complicated and ambiguous loop (ΔR = 0), which is impacted by numerous sediment sources in the watershed. Negative ΔC (dilution characteristic) in June 2008 further confirms that inadequate accessible eroded material was created due to vegetation and change in land cover and their impact on the interconnectivity of water and sediment dynamics. However, the hysteresis loops for June 2009, 2011, 2012, 2013 and 2014 display a complex-type structure with a flushing response, which may be due to periodic storm events, sand mining, and long-term summer dryness. The hysteresis loops for June 2015 and 2016 differ from other years, with a distinct counter-clockwise loop with the flushing and diluting conditions, respectively. The SSC variations indicate a trend, with lower oscillation from 2008 to 2009 due to the gradual increase of sediments supply from the upstream watershed. The hysteresis loops for 2007, 2010, and 2017 in zone A demonstrate a clockwise flushing pattern. Positive and higher ΔR in 2007 and 2010 also confirms wide loops. The availability of sediment on the rising limb of the hydrograph drove the clockwise and flushing behaviour for the years in question. The river bed and sides could induce it, other sources near the mouth, subsequent storms, land cover conditions, and human activities.

Similarly, Fig. 9.23 shows that the hysteresis loops for most of the years (2009, 2010, 2012, 2013, 2016 and 2017) in July acknowledge clockwise and flushing patterns, indicating excess availability of sediments with the increase in discharge during monsoons. It also illustrates the sediment supply from various sources across the whole basin. However, July 2011 shows clockwise hysteresis loops with positive ΔR and negative ΔC in zone B, indicating the diluting behaviour. Here, sediment sources are anticipated to be primarily situated on hillsides/ upstream rather than in the stream due to sediment depletion near Tikarpara. The hysteresis loops for July 2007, 2008 and 2014 had a mixed shape with flushing in SSC, suggesting the influence of consecutive storms and anthropogenic interferences. The same pattern is observed for 50% of the years (2009, 2010, 2013, 2014 and 2017) in August SRC (Fig. 16). But, the loops are anticlockwise for the remaining years with the same flushing behaviour. The loops for September (Fig. 9.23) exhibit similar trends to June, with most hysteresis loops (2007, 2008, 2011, 2013, 2015, and 2017) taking on more complicated forms with flushing conditions reflecting the start of the monsoon retreat. The hysteresis loops of September 2009 and 2010, on the other hand, follow clockwise and flushing patterns, implying increased sediment availability. The investigation of October loops in 2007, 2008 and 2010 are in zone C (Fig. 9.23). It indicates a decrease in SSC to a minimum for an increase in discharge up to its maximum. Similar unavailability of sediments was observed in October 2015 and September 2016 with complex loops. Few other complex type loops are obtained for October (in 2011, 2013, 2014, 2015 and 2017) with flushing conditions. The data for the year 2012 (in August, September and October) was missing and therefore not considered in the analysis. Overall, the behaviour of SSC is uneven when hysteresis loops for various months are compared across years. The hysteresis loops' distinct behaviour in these months might be attributable to several variables, including sediment sources, storm characteristics, and connectivity impacts on water and sediment dynamics. Due to the instability of the hysteresis loops, no precise hysteresis pattern for a given month could be applied across all years in the present study—this inter-year variability of hysteresis influences the parameters of the SRC. Hence, the intra-month and inter-year variability were considered for the developments of the LMM.

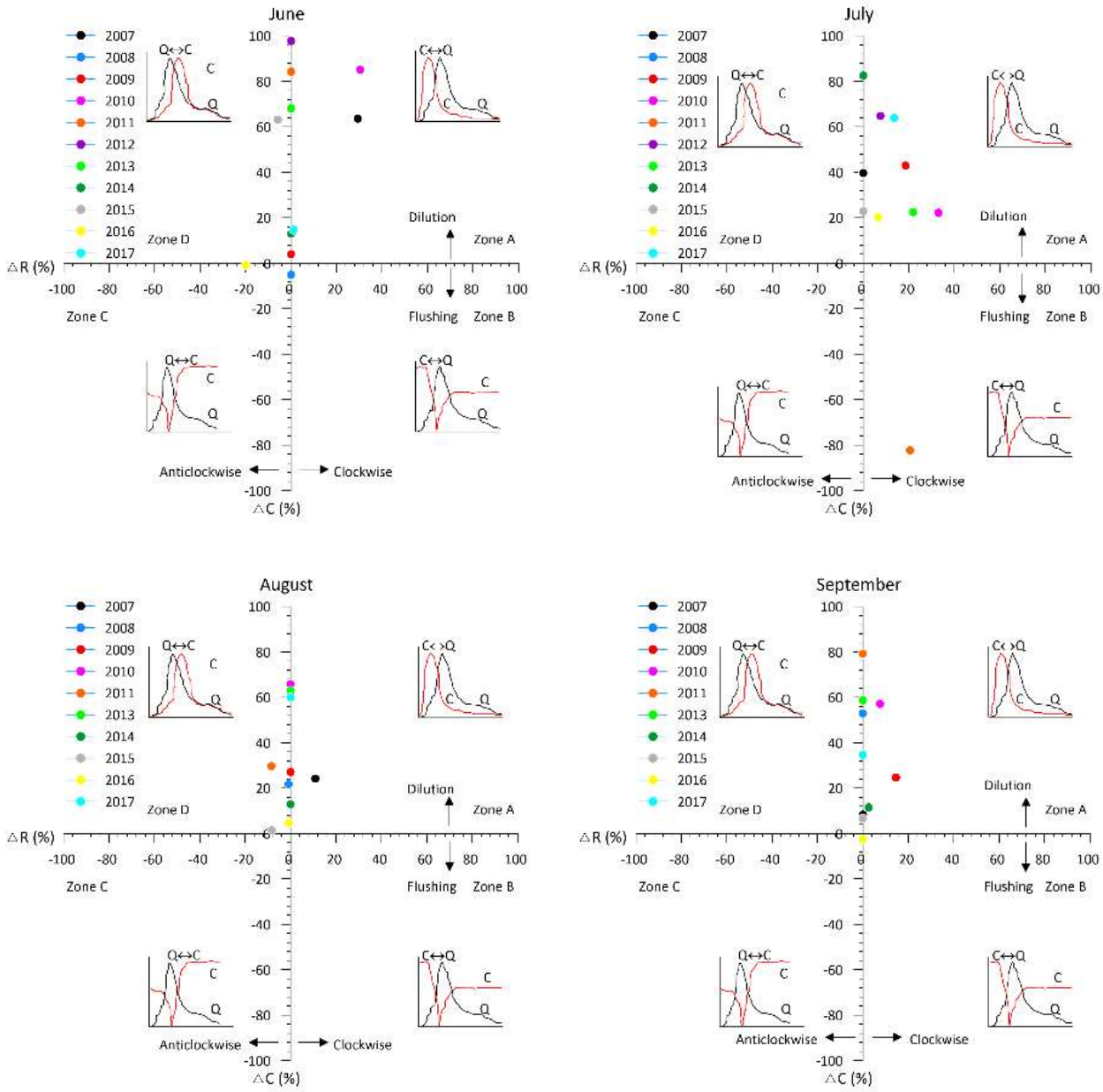

Fig. 9.23: Variation of ΔR and ΔC for different hysteresis loops of June to October for different years of the study period at Tikarpara.

Fig. 9.23 (Continued…)

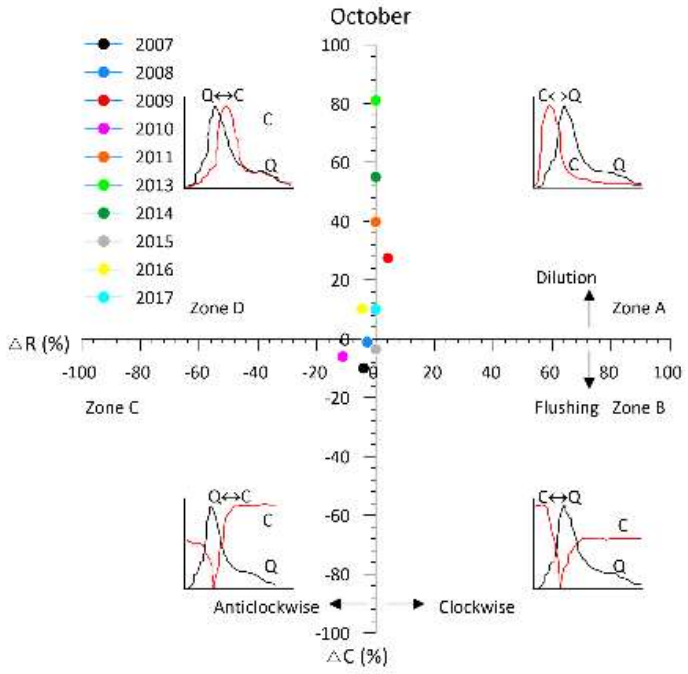

9.5.5.7 Linear mixed-effects modelling (LMM)

The variations in the δ_0 and δ_1 are attributed to the monthly seasonal fluctuations in the data. Also, the inter-yearly variation of intercept and slope of the monthly SRC is displayed by the standard deviations (STD) of random log intercepts and random log slope values. The goodness of fit for both models was evaluated using AIC values. The AIC of each month are compared, and lower AIC values represent the effectiveness of the goodness of fit. The LMM of each month across stations produced lower AIC values than the ordinary least square regression (OLM), as given in Table 9.10. A typical plot of observed versus model predicted SSC (for both the models) across a few stations is shown in Fig. 9.24 for the study period. The LMM displays overall limited scattering about the identity line (1:1 line) compared to the OLM across all stations. The low scattering, therefore, shows better goodness of fit.

Table 9.10: Listed AIC values for the two models across stations

Hydrological stations	Period (2007-2017)	OLM	LMM
Simga	June	-1582	-2159
	July	-1440	-1498
	August	-1349	-1619
	September	-1093	-1446
	October	-1629	-2237
Baronda	June	-587	-601
	July	-962	-1028
	August	-941	-976
	September	-971	-1051
	October	-1467	-1585
Rajim	June	-806	-939
	July	-1099	-1165
	August	-1348	-1456
	September	-1290	-1394
	October	-1545	-1599
Ghatora	June	-1710	-2797
	July	-1150	-1302
	August	-1080	-1214
	September	-1027	-1276
	October	-1479	-1767
Basantpur	June	-1671	-2066
	July	-1164	-1221
	August	-1356	-1353
	September	-1316	-1381
	October	-1451	-1617
Kurubhata	June	-1031	-1272
	July	-737	-926
	August	-803	-1140
	September	-738	-1030
	October	-1193	-1757
Sundargarh	June	-684	-851
	July	-719	-755
	August	-800	-861
	September	-649	-691
	October	-921	-1063
Salebhata	June	-649	-767
	July	-859	-1060
	August	-859	-1428
	September	-1274	-1452
	October	-1565	-1584

Table 9.10 (continued…)

Hydrological stations	Period (2007-2017)	OLM	LMM
Kantamal	June	-644	-1204
	July	-591	-1049
	August	-428	-705
	September	-477	-976
	October	-648	-1161
Tikarpara	June	-1380	-1464
	July	-1231	-1318
	August	-894	-1352
	September	-1076	-1452
	October	-1586	-1613

AIC: Akaike information criterion, OLM: Ordinary least square model, LMM: Linear mixed-effects model

Among the stations under consideration, the Salebhata has the most significant improvement in R^2 (200%), whilst Basantpur has the smallest gain (38.29%). An average improvement of 99.93% in R^2 is observed with LMM over OLM across all stations under study. It shows a significant improvement in the overall scatters around the identity line. Moreover, the gradient and intercept of the regression line of the LMM approach are more towards one and zero, respectively, indicating the efficacy of LMM over the OLM. The ordinary least square model produces a much lower R^2, which depicts that the traditional power rating form (SRC) is insufficient in estimating SSC. The average R^2 of 0.36 is obtained for all the gauging stations, which is not considered satisfactory because values greater than 0.5 are generally acceptable (Santhi et al. 2001). Moreover, for a majority of the stations, the ordinary least square regression yields a set of negative concentration values below the identity line, generally at observed SSC $\leq$ 0.05 g/l. However, Kurubhata and Sundargarh exhibit a set of negative predictions for SSC $\leq$ 0.3 g/l. It also demonstrates how difficult it is to match the low SSC with an OLM. Further, the predicted data deviates significantly from the 1:1 line, especially for higher sediment concentrations $\geq$ 1.5 g/l. Sundargarh has the broadest range of observed SSC, with a noticeable departure from the 1:1 line for SSC $\geq$ 6.5 g/l.

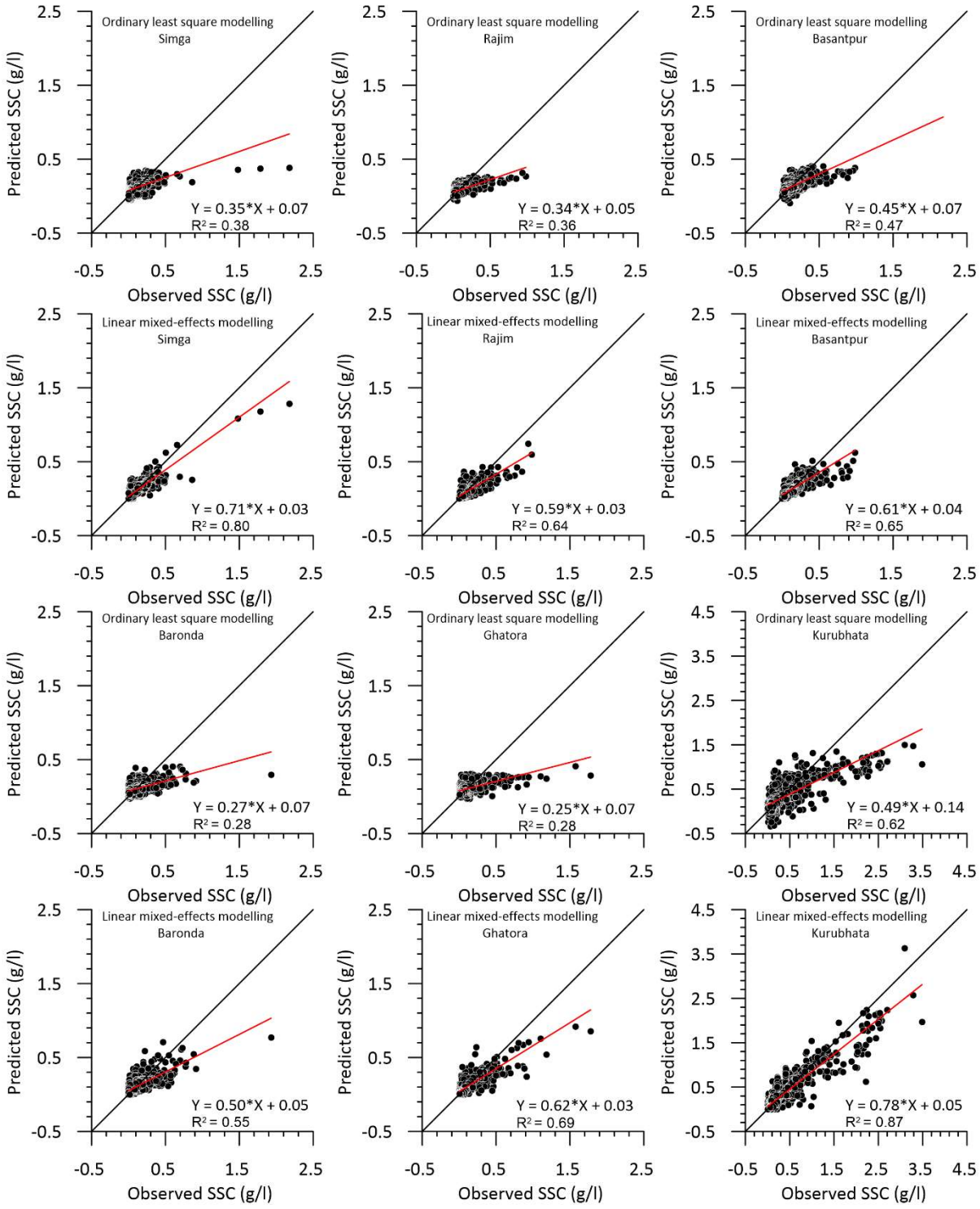

Fig. 9.24: Comparison of ordinary least square regression and linear mixed-effects modelling results at Simga, Baronda, Rajim, Ghatora, Basantpur and Kurubhata (2007-2017)(Red and black bold lines show the regression and 1:1 lines respectively).

A typical representation of the time series comparison is shown in Fig. 9.25 for the ultimate gauging station of the MRB. Both models appeared to reflect the time variation in general. The LMM, on the other hand, performs better for reflecting the overall pattern throughout the low-flow period, particularly in June and October. When comparing the fitted average curve of LMM to the traditional rating curve, the mixed-effects model illustrates less bias in capturing the SSC over the temporal scale of study. Even in the face of periods with occasional high levels of SSC, LMM performs significantly better at preserving the patterns in the data (Fig. 9.25).

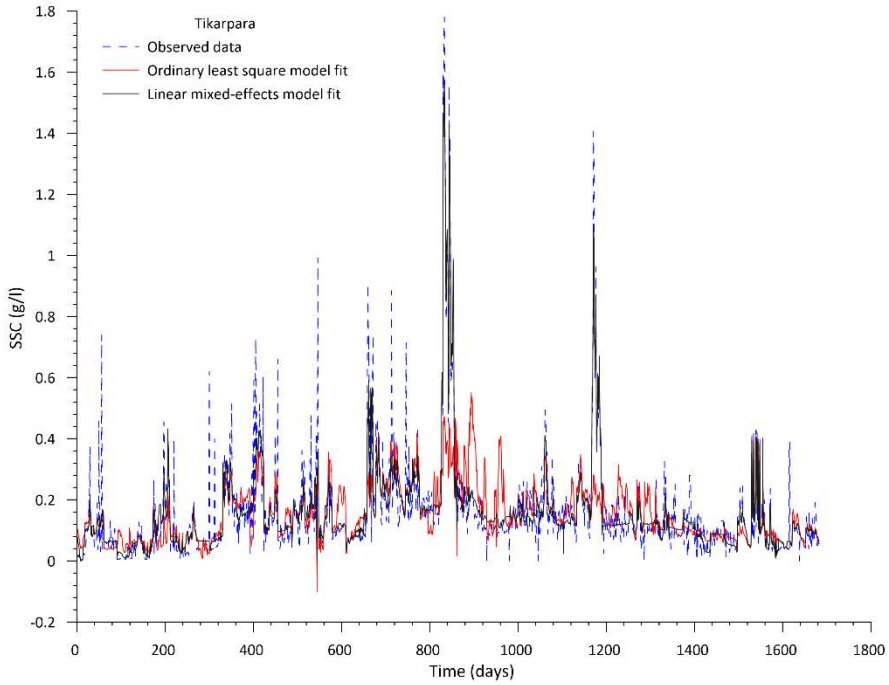

Fig. 9.25: Typical time series comparison of suspended sediment concentration (SSC) prediction using both the models at Tikarpara (2007-2017).

The error metrics of OLM and LMM are compared in Table 9.11. Based on the acceptability criteria set by Moriasi et al. (2015) for a daily scale of temporal data, the PBIAS (%) is considered satisfactory in the range of $\pm 15 \leq \text{PBIAS} \leq \pm 20$, suitable for $\pm 10 \leq \text{PBIAS} \leq \pm 15$ and very good for $\text{PBIAS} \leq \pm 10$.

However, the positive values of LMM across stations indicate model underestimation bias. In light of this, it can be observed that LMM has performed very good in 80% of stations, good in 10%, and poor at Sundargarh. The poor performance at Sundargarh is due to both negative and positive Yule-Kendall skewness in the observed data. However, PBIAS for LMM has fallen substantially relative to OLM

throughout stations, reaching a fall of up to 75% at Tikarpara. Although there are no such evaluation criteria set for NSE and RSR in a daily scale sediment model, the improvement of LMM for these metrics are also very substantial concerning OLM and therefore supports the enhanced efficiency in favour of LMM. So, overall, the LMM outperforms the OLM in characterizing the observed SSC distributions, which are otherwise ignored in traditional SRC. Eventually, the fixed effect parameters of the LMM were employed to develop a rating regression model and monthly SSC for the ungauged stations of the catchment.

Table 9.11: Comparison of error metrics between the two models across the Mahanadi River Basin

Hydrological stations	R^2		NSE		RSR		PBIAS (%)	
	OLM	LMM	OLM	LMM	OLM	LMM	OLM	LMM
Simga	0.38	0.80	0.38	0.79	0.44	0.34	7.52	2.46
Baronda	0.28	0.55	0.28	0.55	0.43	0.45	11.06	6.89
Rajim	0.36	0.64	0.36	0.64	0.44	0.43	6.61	3.71
Ghatora	0.28	0.69	0.28	0.68	0.40	0.40	12.41	5.35
Basantpur	0.47	0.65	0.47	0.65	0.48	0.44	4.84	3.22
Kurubhata	0.62	0.87	0.59	0.86	0.38	0.29	24.13	7.90
Sundargarh	0.31	0.57	0.30	0.54	0.38	0.37	50.09	32.75
Salebhata	0.26	0.78	0.26	0.77	0.38	0.37	20.68	6.19
Kantamal	0.34	0.77	0.32	0.77	0.40	0.39	35.15	11.73
Tikarpara	0.35	0.83	0.64	0.91	0.42	0.35	12.36	3.07

OLM: Ordinary least square model, LMM: Linear mixed-effects model

9.5.5.8 Selection of environmental control parameters (ECPs) for regression modelling

The significant variations in fixed-effect rating parameters of the SRC depict substantial spatial heterogeneity in the SRC. These log intercepts and slopes are plotted against each other in Fig. 9.26, which shows a strong inverse relationship. This degree of correlation ($R^2 = 0.93$) also indicates the role of the various environmental controls in maintaining the natural equilibrium between the two coefficients across the entire catchment.

The PCA results listed in Table 9.12 shows the total variance explained by the reduced components. It can be seen that 81% of the variance in data is defined by the first three components of the system, which are also having eigenvalues greater than one. The three components of the unrotated component matrix display the grouping of parameters with higher correlations. The unrotated component,

communality and rotated component matrix are shown in Table 9.12. The three orthogonal components are named as (i) sediment rating component with maximum loadings of δ_0 , δ_1 , *SSC*+1, *K*, and *MAP*, (ii) catchment response component with maximum loadings of *Q*+1*, A, RR, and* T_c, and (iii) morphometric component with maximum loadings of *RR, ER* and D_d. These components indicate the environmental variables which will provide robust multiple correlations for estimation of rating parameters.

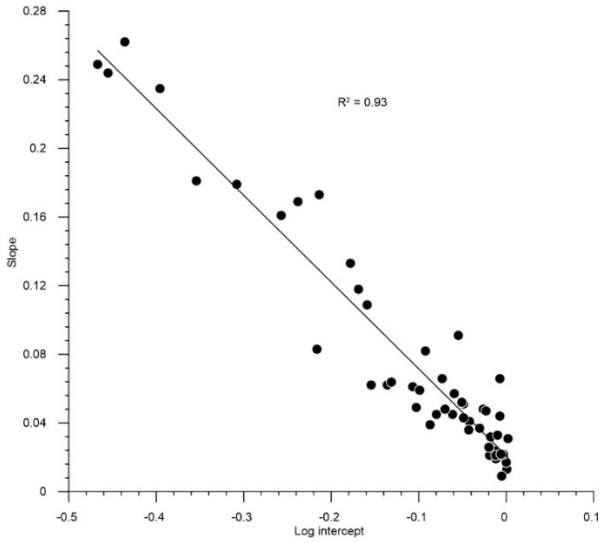

Fig. 9.26: Variation of the sediment rating parameters across the Mahanadi River basin (2007-2017).

Table 9.12: Total variance explained by the various components

Components	Initial Eigenvalues		
	Total	% of variance	Cumulative %
1	4.347	39.521	39.521
2	3.180	28.905	68.426
3	1.392	12.654	81.08
4	0.989	8.995	90.075
5	0.425	3.866	93.941
6	0.278	2.526	96.467
7	0.205	1.867	98.334
8	0.109	0.995	99.329
9	0.062	0.567	99.895
10	0.011	0.098	99.993
11	0.001	0.007	100

9.5.5.9 Determination of regression models and their performance in ungauged catchments

Using SMLR, two normalized rating regression models for each rating coefficient were developed based on PCA on log-transformed variables. The functional model relationship and the related coefficients determined for the two models using ECPs of ten gauging stations of the basin are listed in Table 9.13. The R^2 involved in each equation states the percentage of variance explained. Both the equations denote a reasonably good fit to the data, with 67-87% of the variance acknowledged. The remaining unexplained variance may be due to the sampling issues, hydrological variability and the influence of various anthropogenic regulations in the river basin that arise over time.

Table 9.13: Final model equations developed using stepwise multiple linear regression

Functional equation	$(\delta_0)^* = f\{(\log K)^*, (\log Q+1)^*, (\log ER)^*\}$
	$(\log \delta_1)^* = f\{(\log K)^*, (\log MAP)^*, (\log Q+1)^*, (\log ER)^*, (\log RR)^*\}$
Final form	$(\delta_0)^* = 0.471\times(\log ER)^* - 0.493\times(\log K)^* - 0.995\times(\log Q+1)^* + 1.206, \quad R^2 = 0.67$
	$(\log \delta_1)^* = 0.442\times(\log K)^* + 0.188\times(\log MAP)^* + 0.89\times(\log Q+1)^* - 0.383\times(\log ER)^* + 0.184\times(\log RR)^* - 0.118, R^2 = 0.87$

δ_0 and δ_1 = fixed effect rating parameters, Q = mean discharge, K = soil erodibility factor, RR = relief ratio, ER = elongation ratio, MAP = mean areal precipitation

Various error statistics are computed and shown in Table 9.14 to examine the performance of the model during validation at the aforementioned ungauged stations. The predicted monthly SSC across these stations is in close pact with the measured ones (Fig. 9.27). The metrics R^2, NSE, RSR, and PBIAS (%) are in the ranges of 0.44-0.83, 0.44-0.64, 0.59-0.74, and (-0.34) -(-0.003), respectively for all the four ungauged stations of the MRB. The coefficient of determination (R^2 = 0.44) between observed and estimated SSC is minimum at Andhiyarakore, while it varies from 0.70-0.83 for the remaining ungauged stations under study. Moriasi et al. (2015) stated that the coefficient of determination be regarded as satisfactory if R^2 is in the range of 0.4-0.65, good for R^2 in the range of 0.65-0.80 and very good if R^2 exceeds 0.80. The NSE ranges between 0.44-0.64. The low NSE (0.44) in Andhiyarakore shows that the model's performance is inadequate. The NSE of 0.82 and 0.83 for Jondhra and Kesinga, respectively, is closer to one, the maximum among all ungauged stations, demonstrating that model predictability is very good at Jondhra and Kesinga. Although, in the estimation of SSC at Manendragarh, the model performs satisfactorily (NSE = 0.70). Also, due to a

river check dam at the immediate upstream of Manendragarh, a much low overall sediment concentration was observed compared to other ungauged stations; however, the model performance is uncompromised. The per cent bias shows that the model slightly overestimated at all the ungauged stations; however, it is negligible with regard to the criteria set by Moriasi et al. (2015). Also, the RSR shows good performance at Manendragarh and Jondhra; and satisfactory at Kesinga as per Moriasi et al. (2007). However, it reveals an unsatisfactory performance at Andhiyarkore. As a result, it is believed that the proposed model would predict SSC at all stations except at Andhiyarakore. The proposed model results are closer to the 1:1 line in the scatter graphs (Fig. 9.27). The station data points are distributed about a 1:1 line except at Andhiyarkore, where the deviation between regression and the 1:1 line is most prominent. Throughout the validation, the consistency of all the metrics (R^2, NSE, RSR and PBIAS) revealed that the proposed model is broadly applicable.

Table 9.14: Final statistical performance of the proposed model in the Mahanadi River Basin

Ungauged stations	R^2	NSE	RSR	PBIAS (%)
Andhiyarkore	**0.44**	0.44	0.74	**-0.003**
Manendragarh	**0.70**	**0.64**	**0.59**	**-0.009**
Jondhra	**0.82**	**0.64**	**0.59**	**-0.33**
Kesinga	**0.83**	**0.58**	**0.64**	**-0.34**

Bold figures mean the values are acceptable.

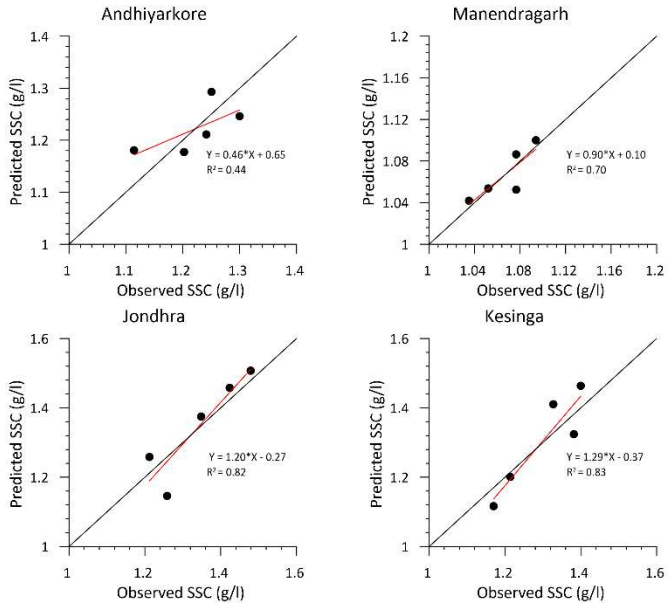

Fig. 9.27: Performance of the predicted monthly monsoon suspended sediment concentration (SSC) for the assumed ungauged stations of the basin (2007-2017) (Red and black bold lines show the regression and 1:1 lines respectively).

Furthermore, as demonstrated in Fig. 9.27, the proposed method is fairly capable of reflecting the low monthly SSC. It contrasts with the model established by Yadav et al. (2021), where modelling of low suspended sediment was shown to be inadequate. Additionally, the predicted monthly SSC exhibits less variation in all peaks and at low concentrations for all ungauged stations. The proposed model yielded the best statistics at Jondhra and Kesinga, which may be attributed to the maximum Q, SSC, A, and MAP values among all MRB ungauged stations. The underperformance of the proposed model in estimating SSC at Andhiyarkore can be ascribed to the dynamic interaction of different sediment yield regulating variables.

Besides, Andhiyarkore is amid limestone deposits that should result in low suspended sediments yield in contrast to Kesinga, which is underlain by igneous and metamorphic rocks (Panigrahy and Raymahashay 2005). However, Fig. 9.27 displays that the Andhiyarkore (a Seonath tributary), having a smaller catchment area, carries a comparable suspended material as that of Kesinga (Tel tributary). Hence, it is likely that the poor performance of the proposed model at Andhiyarkore may be related to the existing non-linear relationship between sediment transport and the catchment area; and other sampling issues. However, the proposed model well simulates the relatively low flows (of June/October) as well as high flows (of July/August) events in contrast to the study of Yadav et al. (2021). Because of the inclusion of different stations in the model construction and subsequent validation procedure across the wide river basin, the presented regression model has greater generalization potential than previously established models in the MRB. Therefore, the rating parameter model developed in this study help estimate the suspended sediment concentration for ungauged sub-catchments of the Mahanadi River basin.

9.5.5.10 Estimation of ungauged bed load concentration (BLC_u)

The details of the hydraulic variables concerning the hydrological stations employed in the prediction of bed load are listed in Table 9.15. Among the sub-basin stations, the tributaries Seonath, Jonk and Ib (i.e., at Jondhra, Rampur and Sundargarh) carried higher SSC than the other tributaries stations in the MRB. The unusually high SSC for Jondhra was attributed to the highest drainage area, while Rampur and Sundargarh were due to maximum longitudinal bed slope in contrast to other tributaries. The highest SSC at Tikarpara results from the penultimate gauging station of the MRB carrying the highest discharge. However, the tributaries at Baronda and Bamnidih can be considered a stream for absorbing higher SSC due to the presence of hydraulic structures upstream of these stations. It also

increases the maximum flow width downstream of the structures at Baronda and Bamnidih. The representative particle size calculated from equation (1) reveals that the sediments are generally medium sand as per ISSCS across the MRB. The average grain size class of bed sediments as medium sand was also established by Chakrapani and Subramanian (1990).

Table 9.15: Characteristics of different hydraulic variables at all major sub-basin stations of the basin.

Hydrological stations	h_a (m)		Q (m^3/s)		v_a (m/s)		FW (m)		SSC (ppm)		S_a (m/m)	d_{50} (mm)
	m	*M*	*m*	*M*	*m*	*M*	*m*	*M*	*m*	*M*		
Baronda	1.31	6.33	21.04	6593.79	0.20	6.07	203.17	907.35	1	3357	0.00175	0.789
Jondhra	1.52	11.57	23.57	12700	0.51	5.78	87.50	661.10	6	11748	0.00092	1.559
Rampur	1.70	7.57	33.40	3990.11	0.33	3.07	105.81	242.06	1	22000	0.00771	1.559
Bamnidih	1.61	5.88	33.6	12700	0.32	5.20	173.29	946.67	1	3975	0.00130	1.559
Kurubhata	0.90	5.07	16.70	2160	0.15	4.59	150.98	288.06	7	6584	0.00100	0.576
Sundargarh	3.08	8.53	32.81	10404	0.31	5.85	118.78	359.78	2	10012	0.00460	1.480
Salebhata	0.77	5.40	33.56	3864.40	0.31	3.93	151.03	416.26	1	4746	0.00177	1.435
Kantamal	1.60	13.54	30	16263	0.20	4.67	198.78	418.60	1	8200	0.00204	0.782
Tikarpara	3.98	20.64	101.25	30862.5	0.30	3.85	124.53	902.97	1	25173	0.00141	1.366

h_a = average depth of flow, Q = discharge, v_a = average flow velocity, FW = flow width, SSC = suspended sediment concentration, S_a = average longitudinal bed slope, d_{50} = mean particle diameter, m = minimum, M = maximum

The range of SSC differs across stations, and thereby, the Maddocks classification of the percentage of BLC_u based on SSC will also vary. Eventually, the proportion of BLC_u was determined considering the maximum SSC and representative particle size of bed sediments for each station. The BLC_u at Baronda, Bamnidih, Kurubhata, and Salebhata was identified to lie in the range of 10 to 35% of SSC. In contrast, the remaining 5 gauging stations carry around 5 to 15% of the SSC as BLC_u. However, the bed load functions used in the study resulted in different proportions of bed load concentrations to suspended sediment concentrations at each station. The proportion of BLC_u was finalized based on comparing the derived BLC_u using different bed load functions and Maddocks classification. The suitable bed load functions for each station was eventually decided based on the value of the percentage of calculated BLC_u to SSC closest to the range of Maddocks classification. Table 9.16 shows the estimated rate of BLC_u of each station with the suitable bed load functions applicable. The bed load functions of Bagnold (1980) and Huang (2010) seem to have provided an acceptable estimate of BLC_u throughout the MRB's investigated stations. However, Bagnold (1980) performed most

consistently in five out of nine basin stations. In this regard, Hoey and Sutherland (1991) demonstrated that when applied to degraded channels or reaches with supply-limited characteristics, the Bagnold (1980) equation yields the best predictions.

Table 9.16: Estimated percentage of bed sediment concentration.

Hydrological stations	Estimated percentage of bed sediment concentration to suspended load concentration (%)	Applicable bed load function
Baronda	23	Bagnold (1980)
Jondhra	7.40	Bagnold (1980)
Rampur	35	Huang (2010)
Bamnidih	10	Bagnold (1980)
Kurubhata	7.10	Bagnold (1980)
Sundargarh	24.60	Huang (2010)
Salebhata	39	Bagnold (1980)
Kantamal	21.50	Huang (2010)
Tikarpara	19.10	Huang (2010)

9.5.5.11 Estimation of future sediment load and capacity of Hirakud reservoir

The historical (1980-2018) rainfall-runoff model was plotted as monsoon areal average precipitation versus mean monsoon runoff for all the 3 stations together (Fig. 9.28a). It shows a high R^2 value of 0.84, which establishes that the model is capturing a perfect amount of variance in the mean monsoon runoff. Therefore, it is further utilized to get the projected runoff against the future precipitation generated from bias-corrected downscaled rainfall from CCCMA CanESM2 global circulation model (GCM) for RCP 8.5 climatic scenario (2018-2100). Similarly, as discussed, the runoff-sediment model (M2C) for the historical period is shown in Fig. 9.28b, attaining an R^2 value of 0.79. A bed load percentage of 18.85%, 7.10%, and 24.60% was considered for Basantpur, Kurubhata and Sundargarh, respectively, to calculate the total sediment load contributed by the river Mahanadi into the Hirakud reservoir. Hence, M2C is further applied to generate the projected incoming sediment load from the Mahanadi river to the Hirakud reservoir to evaluate its capacity for the future climatic scenario.

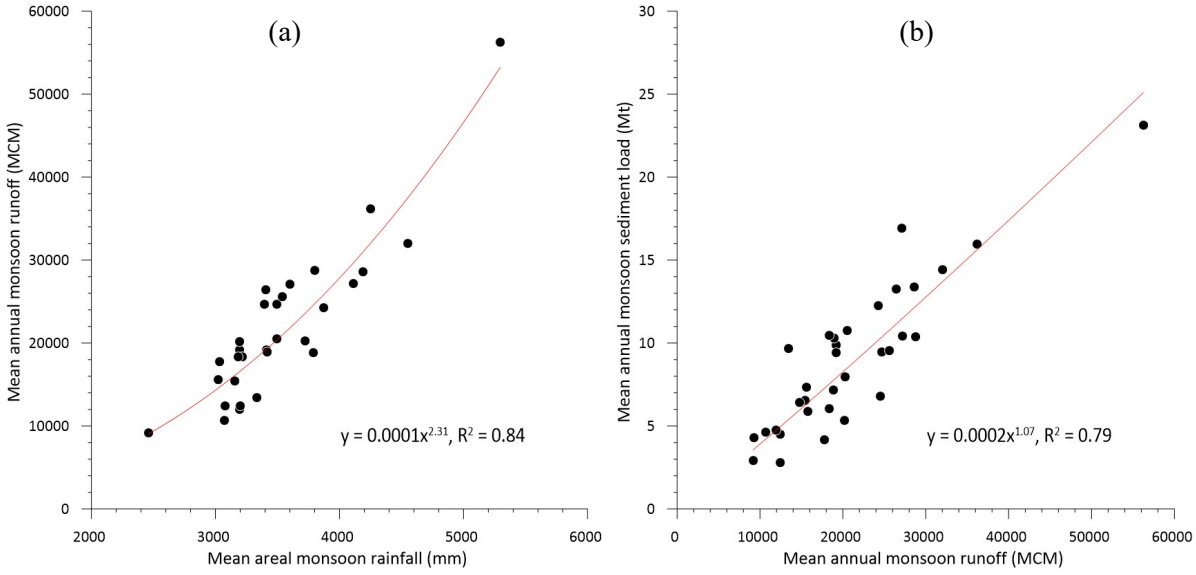

Fig. 9.28: Plot showing (a) Rainfall-runoff model (M1) and (b) Runoff-sediment model (M2C) for the historical period (1980-2018)

Using the Brune Method, Dutta and Sen (2016) reported the variation of the trap efficiency of the Hirakud Reservoir during the period from 1957 to 2110. This projected trap efficiency is further utilized to determine the projected deposition of the sediment load being contributed by the river Mahanadi into the Hirakud reservoir. The cumulative sediment deposited in the reservoir from the river Mahanadi is plotted in Fig. 9.29. It is observed that up to nearly 200 MCM of sediment load will get deposited in the reservoir by 2100, considering 2020 as the base year. Further, the decline in gross storage capacity was evaluated using the reservoir storage curve of Dutta and Sen (2016). It was noticed that there is a decline of 48 MCM of gross storage capacity of the reservoir on an annual basis. In addition, it is estimated that incoming sediments from the Mahanadi river provide an average of 5% of the reservoir's gross storage capacity.

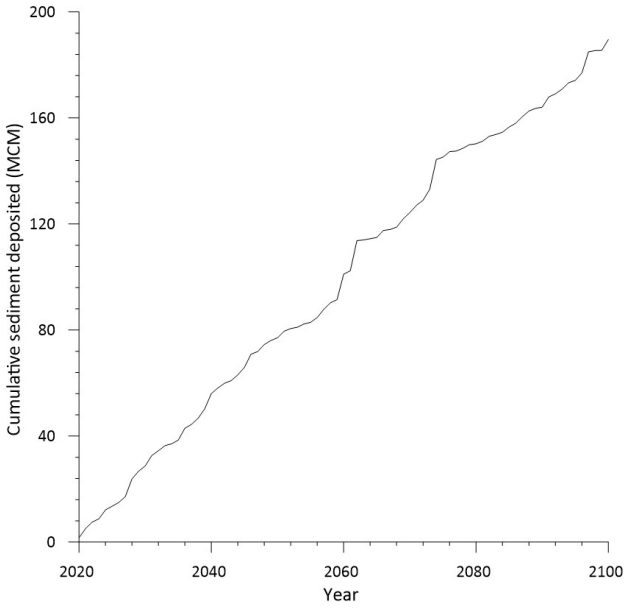

Fig. 9.29: Future variation of cumulative sediment deposited in the Hirakud reservoir from the Mahanadi river.

9.5.6. Conclusions

Following conclusions were made from the present study:

(a) 90% of the runoff takes place during monsoons, which is also consistent with the sediment load of the basin.

(b) The sediment load from the entire Mahanadi River basin has shown a significant decreasing trend over the past forty-four years compared to the non-significant trend in the yearly runoff.

(c) The quantitative role of various human interferences in reducing the yearly sediment load from the basin is touching nearly 40%.

(d) The significant anthropogenic stresses affecting the decrease of sediment delivery to the sea are identified as operations of large dams, increasing water allocation priorities for multiple industries, and diverse catchment soil conservation programs.

(e) The findings demonstrate the distinct roles of factors impacting hysteresis loops during monsoon months across years and confirm the instability of the sediment hysteresis loops.

(f) Linear mixed-effects models outperformed the traditional rating approach by increasing the mean covariance between observed and predicted data to nearly twice and significantly reducing the percentage bias across gauging stations.

(g) The developed rating model provides accurate estimates for the larger area sub-catchments within MRB and performs poorly in a station with a limited catchment area, non-linearity in sediment transport with catchment area, and other sampling problems.

(h) Bagnold (1980) bed load functions performed most consistently in five of nine basin stations. There is bed sediment of nearly 19% of suspended sediment concentration found at the last gauging station of the basin.

(i) The sediments entering the reservoir from the Mahanadi river account for approximately 5% of the Hirakud reservoir's gross storage capacity.

Publications based on the work

Journal papers

Kar, R., & Sarkar, A. (2021), Anthropogenic influences on the variation of runoff and sediment load of the Mahanadi River basin. Hydrological Sciences Journal, 66(12), 1820–1844. https://doi.org/10.1080/02626667.2021.1967957

Kar, R., & Sarkar, A. (2022), Potential predictability of suspended sediment concentration in the data constrained regions of the Mahanadi River basin, Eastern India. International Journal of River Basin Management, 1–45. https://doi.org/10.1080/15715124.2021.2016782

Kar, R., & Sarkar, A. (2023). Assessment of the fraction of bed load concentration towards the sediment transport of a large river basin of Eastern India. (In Press)

Book Chapters

Kar, R., & Sarkar, A (2022). Impact of Anthropocene on the Fluvial Sediment Supply: The Mahanadi River Basin Perspective. In: Pandey, M., Azamathulla, H., Jaan, H.P. (eds) River Dynamics and Flood Hazards: Studies on Risk and Mitigation. Disaster Resilience and Green Growth. Springer, Singapore. https://doi.org/ 10.1007/978-981-19-7100-6_14.

Patel, P., Kar, R., & Sarkar, A. (2022). Estimation of velocity index for flow calculation in open channels using geometric and hydraulic characteristics. Lecture Notes in Civil Engineering. Springer (Accepted)

Conference

Kar, R., & Sarkar, A. (2022). Geomorphic response of the mid-Mahanadi River towards inflowing runoff and sediment load variation. HYDRO 2022 International on December 22- 24, 2022, Chandigarh, India.

9.6. Probabilistic riverine flood forecasting in Tel river catchment using the Hydrologic Ensemble Forecast Service

Streamflow forecasts are very useful for a variety of applications such as flood warning, reservoir operation and water resources planning and management, especially in countries like India where streamflow can be highly variable. Methods available for streamflow forecasting can be broadly classified as process-driven and data-driven methods. Streamflow forecasts always have uncertainty associated with them due to limitations in modelling complex processes in the hydrologic system, and factors such as scarcity of data and measurement errors. It is important to quantify the forecast uncertainty for making informed decisions. Hydrologic Ensemble Prediction Systems (HEPS; Cloke et al., 2013), which use ensembles in process-driven approach for generating probabilistic forecasts which quantify forecast uncertainty are gaining popularity in the world. However, there is dearth of studies on application of HEPS for forecasting streamflows in Indian rivers. Recently, United States (US) National Weather Service developed a HEPS called Hydrologic Ensemble Forecast Service (HEFS; Demargne et al., 2014; Figure 9.30) to generate seamless probabilistic hydrologic forecasts from short to long lead times.

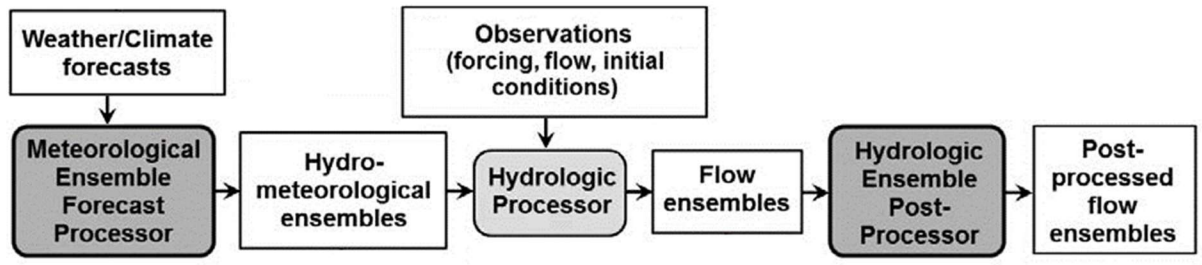

Figure 9.30: Schematic diagram of HEFS (modified from Demargne et al., 2014).

In HEFS, forecast uncertainty is decomposed into meteorological uncertainty and hydrologic uncertainty which are modelled separately and combined numerically. Meteorological uncertainty consists of uncertainty in meteorological forecasts. Hydrologic uncertainty includes uncertainties related to model structure, parameter estimates, basin initial conditions, flow regulation, and measurement of meteorological (forcing) variables and streamflow. The HEFS consists of three main components - (i) Meteorological Ensemble Forecast Processor (MEFP), (ii) Hydrologic Processor and (iii) Hydrologic Ensemble Postprocessor (EnsPost). MEFP accounts for meteorological uncertainty by generating bias corrected ensemble meteorological forecast which is subsequently propagated through

the Hydrologic Processor initialised with basin conditions. The resulting hydrologic ensemble forecast is input to EnsPost to generate postprocessed hydrologic ensemble forecast which reflects the total forecast uncertainty accounting for both meteorological and hydrologic uncertainties.

Research is in progress to assess potential of HEFS in generating skilful streamflow forecasts for Indian rivers, as there is no prior application of HEFS outside US. In this connection, case study was undertaken on Tel river (Figure 9.31), which is one of the tributaries of Mahanadi river that is frequently prone to floods. Forecasts of meteorological variables (precipitation and temperature) required as input to HEFS were obtained from Global Ensemble Forecast System reforecast dataset (GEFS; Hamill et al., 2013). A lumped rainfall-runoff model called GR4J (Perrin et al., 2003) was used as the Hydrologic Processor.

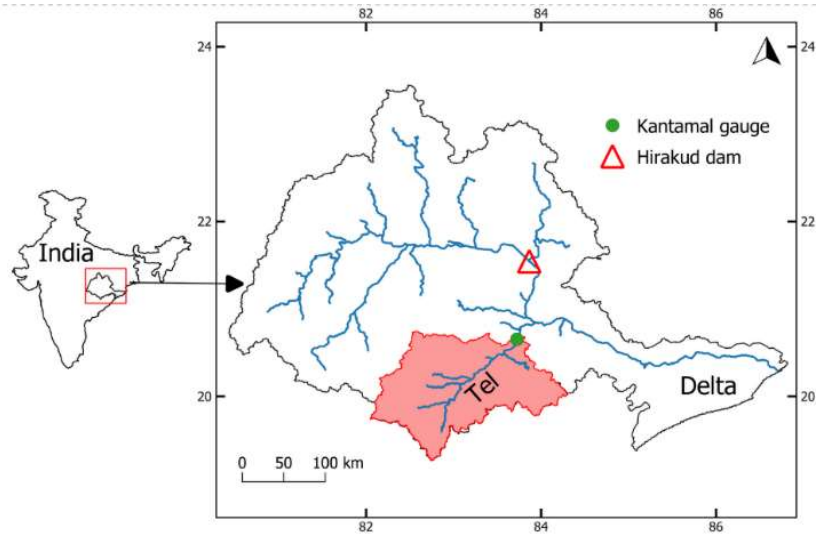

Figure 9.31: Catchment of Tel river (red) in Mahanadi basin contributing flow to the gauge at Kantamal where forecasts are generated.

A major flood event occurred in the Mahanadi river in September 2008 with major contribution of flow from the Tel river. HEFS forecast for Kantamal gauge initialised on 15th September is able to indicate possibility of flood on 18th and 19th September (Figure 9.32). However, magnitude of the flood is underestimated.

Retrospective daily streamflow forecasts for Tel river were generated using HEFS and verified against the corresponding observations for the wet season (June-October) during the period 2000-2011. The performance of the forecasts was evaluated through scatter plots and four metrics namely RME

(Relative Mean Error), correlation, MCRPS (Mean Continuous Ranked Probability Score) and CRPSS (Continuous Ranked Probability Skill Score). Streamflow forecasts generated by HEFS were found to have good skill at short lead times (1 to 3 days).

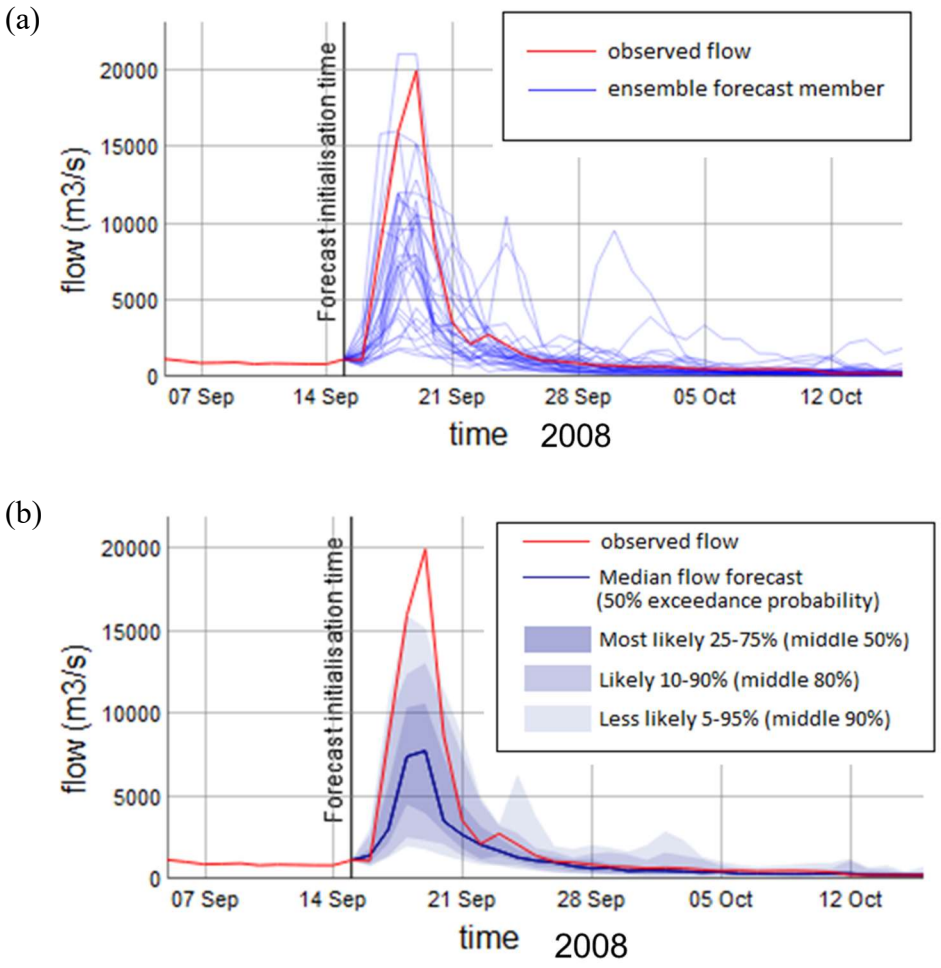

Figure 9.32: (a) Ensemble streamflow forecast (initialised on 15-09-2008) generated by HEFS and observed streamflow, and (b) median forecast along with prediction intervals (corresponding to different probabilities of occurrence) estimated from the distribution of values of ensemble members.

Most of the skill of the streamflow forecasts especially at short lead times is gained by accounting for basin initial conditions. Precipitation forecasts from GEFS were found to have low skill, and they added a small amount of skill to the streamflow forecasts. Hydrologic postprocessing contributed some more skill to the forecasts at shorter lead times by accounting for hydrologic uncertainty and persistence. Aggregated streamflow forecasts were found to have small amount of skill even at monthly time scale. Overall, streamflow forecasts generated by HEFS were found to be more skilful

than climatological forecasts and those generated by ARIMA model. The results are published in a recent conference (Sarath and Srinivas, 2019).

It is planned to extend the study to basins located in other parts of India to strengthen the conclusions drawn. Rainfall forecasts generated by regional agencies like IMD (India Meteorological Department) and National Centre for Medium Range Weather Forecasting (NCMRWF) can have higher skill than GEFS forecasts at short lead times. Incorporating these forecasts into HEFS may improve the skill of the streamflow forecasts. Also, there is scope for trying alternate hydrologic models in lieu of GR4J model in the Hydrologic Processor. The forecasts can be provided as input to hydraulic routing models (e.g., HEC-RAS) to determine the corresponding probabilistic inundation maps during floods.

Conference Publication based on the work

Sarath, M. and Srinivas, V. V., 2019. Short to medium range probabilistic streamflow forecasting for Tel river using the Hydrologic Ensemble Forecast Service. In proceedings of national conference on flood early warning for disaster risk reduction, Organised by NRSC, & CWC under National Hydrology Project, 30-31 May 2019, Hyderabad, pages 80-87.

References

Abbaspour, K. C., Johnson, C. A., and Van Genuchten, M. T. (2004). Estimating uncertain flow and transport parameters using a sequential uncertainty fitting procedure. *Vadose Zone Journal*, 3(4), 1340-1352.

Adamowski, K. (2000). Regional analysis of annual maximum and partial duration flood data by nonparametric and L-moment methods. *Journal of Hydrology*, 229(3-4), 219-231.

Adarsh, S., VishnuPriya, M. S., Narayanan, S., Smruthi, M. S., George, P. and Benjie, N. M., (2016). Trend analysis of sediment flux time series from tropical river basins in India using nonparametric tests and multiscale decomposition. *Modeling Earth Systems and Environment,* 2(4), 1-16. doi:10.1007/s40808-016-0245-0

Adeloye, A. J., Rustum, R., and Kariyama, I. D. (2011). Kohonen self-organizing map estimator for the reference crop evapotranspiration. *Water Resources Research* **47**(8). https://doi.org/10.1029/2011WR010690.

Adeyeri, O. E., Laux, P., Lawin, A. E., and Arnault, J., (2020). Assessing the impact of human activities and rainfall variability on the river discharge of Komadugu-Yobe Basin, Lake Chad Area. *Environmental Earth Sciences*, *79*(6). doi:10.1007/s12665-020-8875-y

Ahmadianfar, I., Adib, A., & Taghian, M. (2016). Optimization of fuzzified hedging rules for multipurpose and multireservoir systems. *Journal of Hydrologic Engineering*, 21(4), 05016003.

Allen, R. G., Pereira, L. S., Raes, D., and Smith, M. (1998). Crop evapotranspiration—guidelines for computing crop water requirements—FAO irrigation and drainage paper 56. *Irrigation and Drainage*, 34, 1–15. https://doi.org/10.1016/j.eja.2010.12.001.

Andrea, B., Francesc, G., Jérôme, L., Eusebi, V. and Francesc, S. (2006). Cross-site comparison of variability of DOC and nitrate c–q hysteresis during the autumn–winter period in three Mediterranean headwater streams: a synthetic approach. *Biogeochemistry*, *77*(3), pp.327-349. https://doi.org/10.1007/s10533-005-0711-7

Arkley, R.J. and Ulrich, R. (1962). The use of calculated actual and potential evapotranspiration for estimating potential plant growth. *Hilgardia* **32**(10): 443–469. https://doi.org/10.3733/hilg.v32n10p443.

Armijos, E., Merten, G. H., Groten, J. T., Ellison, C. A., and Lisiecki, L. U. (2021). Performance of Bedload Sediment Transport Formulas Applied to the Lower Minnesota River. *Journal of Hydrologic Engineering*, *26*(7), 05021014. https://doi.org/10.1061/(ASCE)HE.1943-5584.0002107

Asadi Zarch, M.A., Sivakumar, B. and Sharma, A., (2015). Droughts in a warming climate: A global assessment of Standardized precipitation index (SPI) and Reconnaissance drought index (RDI). *Journal of hydrology*, 526, pp.183-195. http://dx.doi.org/10.1016/j.jhydrol.2014.09.071

Asheghi, R., and Hosseini, S. A. (2020). Prediction of bed load sediments using different artificial neural network models. *Frontiers of Structural and Civil Engineering 2020 14:2*, *14*(2), 374–386. https://doi.org/10.1007/S11709-019-0600-0

Ashkar, F., El Jabi, N., & Issa, M. (1998). A bivariate analysis of the volume and duration of low-flow events. *Stochastic Hydrology and Hydraulics*, 12(2), 97-116.

Ashley, T. C., McElroy, B., Buscombe, D., Grams, P. E., and Kaplinski, M. (2020). Estimating Bedload From Suspended Load and Water Discharge in Sand Bed Rivers. *Water Resources Research*, *56*(2), e2019WR025883. https://doi.org/10.1029/2019WR025883

Asselman, N. E. M. (2000). Fitting and interpretation of sediment rating curves. *Journal of Hydrology*, *234*(3–4), 228–248.

Bagnold, R. A. (1980). "An empirical correlation of bedload transport rates in flumes and natural rivers." *Proc. R. Soc. London. Ser. A*. 372 (1751): 453–473. https://doi.org/10.1098/rspa.1980.0122

Bastia F. and Equeenuddin, S.M. (2016). Spatio-temporal variation of water flow and sediment discharge in the Mahanadi River, India. *Global and Planetary Change*, *144*, pp.51-66.

Basu, B. and Srinivas, V.V. (2014). Regional flood frequency analysis using kernel-based fuzzy clustering approach. *Water Resources Research* **50**(4): 3295–3316. https://doi.org/10.1002/2012WR012828.

Basu, B. and V. V. Srinivas (2013). Formulation of a mathematical approach to regional frequency analysis, *Water Resources. Research*, 49, 6810–6833.

Basu, D. (1955). On statistics independent of a complete sufficient statistic. In *Selected Works of Debabrata Basu* (pp. 223-226). Springer, New York, NY.

Berghuijs, W. R., Larsen, J. R., Van Emmerik, T. H., and Woods, R. A. (2017). A Global Assessment of Runoff Sensitivity to Changes in Precipitation, Potential Evaporation, and Other Factors. *Water Resources Research* **53**(10): 8475–8486. https://doi.org/10.1002/2017WR021593.

Bouchet, R.J. (1963). Evapotranspiration réelle et potentielle, signification climatique.

Brutsaert, W. and Parlange, M.B. (1998). Hydrologic cycle explains the evaporation paradox. *Nature* 396(6706), 30. https://doi.org/10.1038/23845.

Budyko, M.I. (1974). Climate and Life. *Academic Press*, New York.

Buishand, T. A. (1984). Bivariate extreme-value data and the station-year method. *Journal of Hydrology*, 69(1-4), 77-95.

Caires, S. (2009). A comparative simulation study of the annual maxima and the peaks-over-threshold methods. *Deltares report 1200264-002 for Rijkswaterstaat*, Waterdienst.

Cantalice, J. R. B., Cunha Filho, M., Stosic, B. D., Piscoya, V. C., Guerra, S. M. S., and Singh, V. P. (2013). Relationship between bedload and suspended sediment in the sand-bed Exu River, in the semi-arid region of Brazil. *Hydrological Sciences Journal*. https://doi.org/10.1080/02626667.2013.839875

Census(2011), Primary Census Abstract, Registrar General of India, Ministry of Home Affairs, Government of India.

Central Water Commission (CWC), (2012). Integrated hydrological data book. Hydrological data directorate, information systems organization, Water planning and projects wing, New Delhi, India.

Chakrapani G.J. and Subramanian V. (1990b). Factors controlling sediment discharge in the Mahanadi River Basin, India. *Journal of Hydrology*, *117*(1-4), pp.169-185.

Chakrapani, G. J. and Subramanian, V. (1990a). Preliminary studies on the geochemistry of the Mahanadi River basin, India. *Chemical Geology,* 81(3), 241-253. doi: 10.1016/0009-2541(90)90118-Q

Chang, F. J., Chen, L., and Chang, L. C. (2005). "Optimizing the reservoir operating rule curves by genetic algorithms." *Hydrological Processes*, 19(11), 2277–2289.

Chavan, S. R. and Srinivas, V. V. (2015). Effect of DEM source on equivalent Horton–Strahler ratio based GIUH for catchments in two Indian river basins. *Journal of Hydrology*, *528*, 463-489. https://doi.org/10.1016/j.jhydrol.2015.06.049

Chebana, F. and Ouarda, T. B. (2009). Index flood–based multivariate regional frequency analysis. *Water Resources Research*, 45(10), W10435.

Chebana, F. and Ouarda, T. B. (2011). Multivariate quantiles in hydrological frequency analysis. *Environmetrics*, 22(1), 63-78.

Chen, Y. and Wang, Y. (2019). Variations in Basin Sediment Yield and Channel Sediment Transport in the Upper Yangtze River and Influencing Factors. *Journal of Hydrologic Engineering,* 24(7). doi: 10.1061/(ASCE)HE.1943-5584.0001783

Choubin, B., Solaimani, K., Habibnejad Roshan, M., and Malekian, A. (2017). Watershed classification by remote sensing indices: A fuzzy c-means clustering approach. *Journal of Mountain Science*, *14*(10), 2053–2063. https://doi.org/10.1007/s11629-017-4357-4

Choudhury, B. (1999). Evaluation of an empirical equation for annual evaporation using field observations and results from a biophysical model. *Journal of Hydrology*. Elsevier Sci B.V. **216**(1–2): 99–110. https://doi.org/10.1016/S0022-1694(98)00293-5.

Choulakian, V. & Stephens, M. A. (2001). Goodness-of-fit tests for the generalized Pareto distribution. *Technometrics*, 43(4), 478-484.

Chow, V. T., Maidment, D. R., and Mays, L. W. (1988). *Applied Hydrology*. McGraw-Hill.

Cloke, H.L., Pappenberger, F., van Andel, S.J., Schaake, J., Thielen, J., Ramos, M.H., (2013). Hydrological ensemble prediction systems. *Hydrol. Process*. 27, 1–4. https://doi.org/10.1002/hyp.9679

Coles, S. G. (2001). An introduction to statistical modeling of extreme values. London: 756 Springer.

Coles, S.G. (1993). Regional modelling of extreme storms via max-stable processes. *Journal of the Royal Statistical Society: Series B (Methodological)*, 55(4), 797-816.

Cunnane, C. (1973). A particular comparison of annual maxima and partial duration series methods of flood frequency prediction. *Journal of hydrology*, 18(3-4), 257-271.

CWC (Central Water Commission), (1983). "Flood estimation report. Directorate of hydrology (small catchments)." New Delhi, India.

CWC, (2014). *Mahanadi Basin.* Ministry of Water Resources: Govt. of India

Dadhwal V.K., Aggarwal S.P. and Mishra N. (2010). Hydrological simulation of Mahanadi river basin and impact of land use/land cover change on surface runoff using a macro scale hydrological model. *na*

Dalrymple, T. (1960). *Flood-frequency analyses*, *US Geol. Surv. Water Supply Pap.*, 1543-A, 11–51.

Demargne, J., Wu, L., Regonda, S.K., Brown, J.D., Lee, H., He, M., Seo, D.J., Hartman, R., Herr, H.D., Fresch, M., Schaake, J., Zhu, Y. (2014). The science of NOAA's operational hydrologic ensemble forecast service. *Bull. Am. Meteorol. Soc.* 95, 79–98. https://doi.org/10.1175/BAMS-D-12-00081.1

Demaria, E. M. C., Palmer, R. N., and Roundy, J. K. (2016). Regional climate change projections of streamflow characteristics in the Northeast and Midwest U.S. *Journal of Hydrology: Regional Studies*, *5*, 309–323. https://doi.org/10.1016/j.ejrh.2015.11.007

Dooge, J. C. (1992). Sensitivity of runoff to climate change: a Hortonian approach. *Bulletin - American Meteorological Society* **73**(12): 2013–2024. https://doi.org/10.1175/1520-0477(1992)073<2013:SORTCC>2.0.CO;2.

DoWR, Government of Orissa (2014). *Flood report of the Hirakud dam.* Superintending Engineer, Hirakud Dam Circle, Burla, Government of Odisha

Dsouza C., Samuel A., Bhagat S. and Joy K.J. (2017) July. Water allocations and use in the Mahanadi River basin. In *Forum for Policy Dialogue on Water Conflicts in India, Pune*.

Duan, N. (1983). Smearing estimate: A nonparametric retransformation method. *Journal of the American Statistical Association*, *78*(383), 605–610. https://doi.org/10.1080/01621459.1983.10478017

Durocher, M., Burn, D. H., & Zadeh, S. M. (2018). A nationwide regional flood frequency analysis at ungauged sites using ROI/GLS with copulas and super regions. *Journal of Hydrology*, 567, 191-202.

D'urso, P. (2004) Fuzzy C-Means Clustering Models for Multivariate Time-Varying Data: Different Approaches. *International Journal of Uncertainty, Fuzziness and Knowledge-Based Systems* **12**(3): 287–326. https://doi.org/10.1142/S0218488504002849

Dutta, S., and Sen, D. (2016). Sediment distribution and its impacts on Hirakud Reservoir (India) storage capacity. *Lakes and Reservoirs: Research and Management*, 21(3), 245–263. https://doi.org/10.1111/lre.12144

El-Ashmawy, K. L. A., (2016). Investigation of the Accuracy of Google Earth Elevation Data. *Artificial Satellites*, *51*(3), 89–97. https://doi:10.1515/arsa-2016-0008

Ellison, C. A., Groten, J. T., Lorenz, D. L., & Koller, K. S. (2016). Application of dimensionless sediment rating curves to predict suspended-sediment concentrations, bedload, and annual sediment loads for rivers in Minnesota. *Scientific Investigations Report*, 1–68. https://doi.org/10.3133/SIR20165146

Favis-Mortlock, D. T., and Guerra, A. J. T. (1999). The implications of general circulation model estimates of rainfall for future erosion: A case study from Brazil. *Catena*, *37*(3–4), 329–354. https://doi.org/10.1016/S0341-8162(99)00025-9

Ferguson, R. I. (1986). River Loads Underestimated by Rating Curves. *Water Resources Research*, *22*(1), 74–76.

Ford, M. (2013). Shoreline changes interpreted from multi-temporal aerial photographs and high resolution satellite images: Wotje Atoll, Marshall Islands. *Remote Sensing of Environment,* 135, 130-140. https://doi:10.1016/j.rse.2013.03.027

Foster, G.R., Lane, L.J., Nowlin, J.D., Laflen, J.M. and Young, R.A. (1981). Estimating erosion and sediment yield on field-sized areas. *Transactions of the ASAE*, *24*(5), pp.1253-1262.

Fu, B. (1981). On the calculation of the evaporation from land surface [in Chinese], *Sci. Atmos. Sin*., 1(5), 23–31.

Ghosh S., Vittal H., Sharma, T., Karmakar S., Kasiviswanathan, K. S., Dhanesh Y., and Gunthe, S. S. (2016). Indian summer monsoon rainfall: implications of contrasting trends in the spatial variability of means and extremes. *PloS one*, *11*(7), e0158670. https://doi.org/10.1371/journal.pone.0158670

Goegebeur, Y., Beirlant, J. and de Wet, T. (2008). Linking Pareto-tail kernel goodness-of-fit statistics with tail index at optimal threshold and second order estimation. *REVSTAT–Statistical Journal*, 6(1), 51-69.

Golshan M., Kavian A., Esmali A. and Ziegler A.D. (2020). Runoff and sediment yield modeling in data-sparse catchments in the Garehsoo River basin, northern Iran. *Environmental Earth Sciences*, *79*(14), pp.1-18.

Gretton, A., Fukumizu, K., Teo, C. H., Song, L., Schölkopf, B., and Smola, A. J. (2007). A kernel statistical test of independence. *Nips*, 20, 585-592.

Gudmundsson, L., Gudmundsson, M. L. (2012). Package 'qmap'. *Methods*, 3383-3390.

Gunawardhana L.N., Al-Rawas, G.A. and Kazama, S. (2017). An alternative method for predicting relative humidity for climate change studies. *Meteorological Applications*, *24*(4), pp.551-559. https://doi.org/10.1002/met.1641

Guo, X., Hu, T., Zeng, X., and Li, X. (2013). "Extension of Parametric Rule with the Hedging Rule for Managing Multi-Reservoir System during Droughts." *Journal of Water Resources Planning and Management*, 139(2), 139–148.

Gupta, H. V., Sorooshian, S., and Yapo, P. O. (1999). Status of Automatic Calibration for Hydrologic Models: Comparison with Multilevel Expert Calibration. *Journal of Hydrologic Engineering, 4*(2), 135–143. https://doi.org/10.1061/

Hadka, D. and Reed, P. (2013). "Borg: An Auto-Adaptive Many-Objective Evolutionary Computing Framework." *Evolutionary Computation*, 21(2), 231–259.

Halim, R., Clemente, R. S., Routray, J. K., and Shrestha, R. P. (2007). Integration of biophysical and socio-economic factors to assess soil erosion hazard in the upper Kaligarang watershed, Indonesia. *Land Degradation and Development*, *18*(4), 453–469. https://doi.org/10.1002/ldr.774

Hamed, K. H. and Rao, A. R. (1998). A modified Mann-Kendall trend test for autocorrelated data. *Journal of Hydrology,* 204(1-4), 182-196. https://doi:10.1016/S0022-1694(97)00125-X

Hamill, T.M., Bates, G.T., Whitaker, J.S., Murray, D.R., Fiorino, M., Galarneau, T.J., Zhu, Y., Lapenta, W., Hamill, T.M., Bates, G.T., Whitaker, J.S., Murray, D.R., Fiorino, M., Jr., T.J.G., Zhu, Y., Lapenta, W. (2013). NOAA's Second-Generation Global Medium-Range Ensemble Reforecast Dataset. *Bull. Am. Meteorol. Soc.* 94, 1553–1565. https://doi.org/10.1175/BAMS-D-12-00014.1

Hao, Z. and AghaKouchak, A. (2013). Multivariate standardized drought index: a parametric multi-index model. *Advances in Water Resources*, 57, pp.12-18. https://doi.org/10.1016/j.advwatres.2013.03.009

Hargreaves, G. H., and Samani, Z. A. (1985) Reference crop evapotranspiration from temperature. *Applied engineering in agriculture*, 1(2), 96-99. https://doi.org/10.13031/2013.26773

Heffernan, J. E. and Tawn, J. A. (2004). A conditional approach for multivariate extreme values (with discussion). *Journal of the Royal Statistical Society: Series B (Statistical Methodology)*, *66*(3), 497-546.

Herrera-Estrada, J.E. Satoh, Y. and Sheffield, J. (2017). Spatiotemporal dynamics of global drought. *Geophysical Research Letters*, *44*(5), pp.2254-2263. https://doi.org/10.1002/2016GL071768

Hobbins M.T., Ramírez, J.A. and Brown T.C., (2004). Trends in pan evaporation and actual evapotranspiration across the conterminous US: Paradoxical or complementary?. *Geophysical Research Letters*, *31*(13). https://doi.org/10.1029/2004GL019846

Hoey T.B. and Sutherland A.J. (1991). Channel morphology and bedload pulses in braided rivers: a laboratory study. *Earth Surface Processes and Landforms*, *16*(5), pp.447-462.

Holeman, J. N. (1968). The Sediment Yield of Major Rivers of the World. *Water Resources Research*, *4*(4), 737–747. https://doi.org/10.1029/WR004i004p00737

Horton, R. E. (1945). Erosional development of streams and their drainage basins; Hydrophysical approach to quantitative morphology. *Bulletin of the Geological Society of America*. https://doi.org/10.1130/0016-7606

Hosking, J. R. (1994). The four-parameter kappa distribution. *IBM Journal of Research and Development*, 38(3), 251-258.

Hosking, J. R. M., and Wallis, J. R., (1997). Regional Frequency Analysis. Regional Frequency Analysis. Cambridge University Press. https://doi.org/10.1017/cbo9780511529443

Hotelling, H. (1931). The Generalization of Student's Ratio. *The Annals of Mathematical Statistics*, *2*(3), 360-378.

Hsu, N. S., and Cheng, K. W. (2002). Network flow optimization model for basin scale water supply planning. *J. Watr Resour. Plann. Manage.*, https://doi.org/10.1061/(ASCE)0733-9496

Huang J, Chin-Ping, L. and Yu-Min, W. (2012). Soil loss and erodibility factor for improving conservation specification design in Southwestern Taiwan. *International Journal of Physical Sciences*, *7*(17), pp.2616-2628.

Huang, H. Q. (2010). Reformulation of the bed load equation of Meyer-Peter and Müller in light of the linearity theory for alluvial channel flow. *Water Resources Research*, *46*(9), 9533. https://doi.org/10.1029/2009WR008974

Jain A., Maier H.R., Dandy G.C. and Sudheer K.P. (2009). Rainfall runoff modelling using neural networks: State-of-the-art and future research needs. *ISH Journal of Hydraulic Engineering*, *15*(sup1), pp.52-74.

Jain S., Salunke, P., Mishra S. K., Sahany S., Choudhary N. (2019). Advantage of NEX-GDDP over CMIP5 and CORDEX data: Indian summer monsoon. *Atmospheric Research*, *228*, 152-160. https://doi.org/10.1016/j.atmosres.2019.05.026

Jena, P. P. Chatterjee, C. Pradhan, G. and Mishra, A. (2014). Are recent frequent high floods in Mahanadi basin in eastern India due to increase in extreme rainfalls?. *Journal of Hydrology*, 517, 847-862.

Joshi, S. and Xu, Y. J. (2017). Bedload and suspended load transport in the 140-km reach downstream of the Mississippi River avulsion to the Atchafalaya River. *Water (Switzerland)*, *9*(9). https://doi.org/10.3390/w9090716

Julien, P. Y., G. J. Klaassen, W. B. M. Ten Brinke, and A. W. E. Wilbers. (2002). "Bed resistance of the Bovenrijn River during the 1998 flood." *J. Hydraul. Eng.* 128 (12): 1042–1050.

https://doi.org/10.1061/(ASCE)0733-9429(2002)128:12(1042).
Kankara, R.S., Ramana Murthy M.V., and Rajeevan, M., (2018). National Assessment of shoreline changes along Indian coast- A status report of 26 years 1990-2016. NCCR Publication
Kannan, S., and S. Ghosh (2013). A nonparametric Kernel regression model for downscaling multisite daily precipitation in the Mahanadi basin, *Water Resour. Res.*, 49, http://dx.doi.org/10.1002/wrcr.20118.
Kao, S.C. and Govindaraju, R.S. (2010). A copula-based joint deficit index for droughts. *Journal of Hydrology*, 380(1-2), pp.121-134. https://doi.org/10.1016/j.jhydrol.2009.10.029
Keef, C., Papastathopoulos, I., and Tawn, J. A. (2013). Estimation of the conditional distribution of a multivariate variable given that one of its components is large: Additional constraints for the Heffernan and Tawn model. *Journal of Multivariate Analysis*, 115, 396-404.
Keef, C., Svensson, C. and Tawn, J. A. (2009). Spatial dependence in extreme river flows and precipitation for Great Britain. *Journal of Hydrology*, 378(3-4), 240-252.
Kendall, M. G. (1955) Further contributions to the theory of paired comparisons. *Biometrics*, 11(1), 43-62. https://doi.org/10.2307/3001479
Kiran K. G. and Srinivas V. V. (2021a). A Mahalanobis distance based automatic threshold selection method for Peaks Over Threshold (POT) model, *Water Resources Research*, American Geophysical Union & Wiley, Vol. 57, Issue 1, January 2021, e2020WR027534, https://doi:10.1029/2020WR027534
Kiran K. G. and Srinivas V. V. (2021b). "Fuzzy Ensemble Clustering Approach to Address Regionalization Uncertainties in Flood Frequency Analysis" *Water Resources Research*, American Geophysical Union & Wiley, https://doi.org/10.1029/2020WR028412
Kitanidis P.K. and Bras R.L. (1980). Real-time forecasting with a conceptual hydrologic model: 2. Applications and results. *Water Resources Research*, *16*(6), pp.1034-1044.
Kokkonen, T. S., Jakeman, A. J., Young, P. C., & Koivusalo, H. J. (2003). Predicting daily flows in ungauged catchments: Model regionalization from catchment descriptors at the Coweeta Hydrologic Laboratory, North Carolina. *Hydrological Processes*, *17*(11), 2219–2238. https://doi.org/10.1002/hyp.1329
Krause P., Boyle D.P. and Bäse F. (2005). Comparison of different efficiency criteria for hydrological model assessment. *Advances in geosciences*, *5*, pp.89-97.
Kumar, K. (1989). Management of water in Hirakud dam project. *Report submitted to Centre of Science and Environment*.
Kumar, T. S., Mahendra, R. S., Nayak, S., Radhakrishnan, K. and Sahu, K. C. (2010). Coastal vulnerability assessment for Orissa State, East Coast of India. *J. Coast. Res.* **26**(3), 523–534. http://doi:10.2112/09-1186.1
Lanfear, K.J. and Hirsch, R.M. (1999). USGS Study reveals a decline in long-record streamgages. *Eos, Transactions American Geophysical Union*, 80(50), pp.605-607.
Lang, M., Ouarda, T.B.M.J. & Bobée, B. (1999). Towards operational guidelines for over-threshold modelling. *Journal of Hydrology*, 225(3-4), 103-117.
Le Nguyen H.T. and Luong, H.P.V. (2019). Erosion and deposition processes from field experiments

of hydrodynamics in the coastal mangrove area of Can Gio, Vietnam. *Oceanologia*, *61*(2), pp.252-264.

Lemma, H., Nyssen, J., Frankl, A., Poesen, J., Adgo, E., and Billi, P. (2019). Bedload transport measurements in the Gilgel Abay River, Lake Tana Basin, Ethiopia. *Journal of Hydrology*. https://doi.org/10.1016

Li, J.Z., Wang, Y.X., Li, S.F. and Hu, R. (2015). A nonstationary standardized precipitation index incorporating climate indices as covariates. *Journal of Geophysical Research: Atmospheres*, *120*(23), pp.12-082. https://doi.org/10.1002/2015JD023920

Lin, K., Lin, Y., Xu, Y., Chen, X., Chen, L. and Singh, V. P. (2017). Inter- and intra- annual environmental flow alteration and its implication in the Pearl River Delta, South China. *Journal of Hydro-Environment Research*, *15*, 27–40. http://doi:10.1016/j.jher.2017.01.002

Liu X., Zhang X.J., Tang Q. and Zhang X.Z., (2014). Effects of surface wind speed decline on modeled hydrological conditions in China. *Hydrology and Earth System Sciences*, *18*(8), pp.2803-2813. https://doi.org/10.5194/hess-18-2803-2014, 2014

Lomba, J. S, & Alves, M. I. F. (2020). L-moments for automatic threshold selection in extreme value analysis. *Stochastic Environmental Research and Risk Assessment*, 34(3), 465-491.

Maddock, T., and Borland, W. M. (1950). Sedimentation studies for the planning of reservoirs by the bureau of reclamation. Bureau of Reclamation Denver Library. United States Bureau of Reclamation. https://books.google.co.in/books?id=sIeMNAAACAAJ

Madsen H., Rosbjerg D., (1997). The partial duration series method in regional index-flood modelling. *Water Resources Research*, *33*(4), 737-746. https://doi.org/10.1029/96WR03847

Madsen, H., Rasmussen, P.F. & Rosbjerg, D. (1997). Comparison of annual maximum series and partial duration series methods for modeling extreme hydrologic events: 1. At-site modeling. *Water Resources Research*, 33(4), 747-757.

Mahalik, N. (2000). Stratigraphy, palaeography and evolution history of Mahanadi delta. In *Mahanadi Delta: Geology, Resources & Biodiversity* (pp. 53-70). New Delhi: AIT Alumni Association (Indian Chapter).

Mahesh, Y., Sastri, A. S. R. A. S., Chandrawanshi, S. K., Bobade, P., Bhuarya, H. K., Singh, P. & Kaushik, D. K. (2018). Studies on Drought Climatology of Different Districts of Chhattisgarh in the Backdrop of Climate Change. *Int. J. Curr. Microbiol. App. Sci*, 7(11), 252-260.

Mallya, G., Tripathi, S., Kirshner, S. and Govindaraju, R.S. (2013). Probabilistic assessment of drought characteristics using hidden Markov model. *Journal of Hydrologic Engineering*, *18*(7), pp.834-845. https://doi.org/10.1061/(ASCE)HE.1943-5584.0000699

Mann, H. B. (1945). Nonparametric tests against trend. *Econometrica: Journal of the Econometric Society*, 245-259. https://doi.org/10.2307/1907187

Mao L. and Carrillo, R. (2017). Temporal dynamics of suspended sediment transport in a glacierized Andean basin. *Geomorphology*, *287*, pp.116-125.

Maraun D., Wetterhall F., Ireson A.M., Chandler R.E., Kendon, E.J., Widmann, M., Brienen, S., Rust, H.W., Sauter, T., Theme, M. and Venema, V.K.C. (2010). Precipitation downscaling under climate change: Recent developments to bridge the gap between dynamical models and the end user.

Reviews of geophysics, *48*(3). https://doi.org/10.1029/2009RG000314

Mardia, K.V. (1970). Measures of multivariate skewness and kurtosis with applications. *Biometrika*, 57(3), 519-530.

Masanta, S.K. and Srinivas, V.V. (2020a). Development of Nonstationary Standardized Precipitation-Evapotranspiration Drought Index (nSPEI) using Climate Indices as Covariates. In *AGU Fall Meeting Abstracts* (Vol. 2020, pp. H136-0003).

Masanta, S.K. and Srinivas, V.V. (2020b). Regionalization of evapotranspiration using fuzzy dynamic clustering approach. Part 1: Formation of regions in India. *International Journal of Climatology*, 40(7), pp.3514-3530. https://doi.org/10.1002/JOC.6411

Masanta, S.K. and Srinivas, V.V. (2021). Regionalization of evapotranspiration in India using fuzzy dynamic clustering approach. Part 2: Applications of regions. *International Journal of Climatology*, *41*, pp.E1371-E1395.

Masanta, S.K. and Srinivas, V.V. (2022). Proposal and Evaluation of Nonstationary versions of SPEI and SDDI based on Climate Covariates for Regional Drought Analysis. *Journal of Hydrology*. 610. https://doi.org/10.1016/j.jhydrol.2022.127808.

Masselot, P., Chebana, F., & Ouarda, T. B. (2017). Fast and direct nonparametric procedures in the L-moment homogeneity test. *Stochastic Environmental Research and Risk Assessment*, 31(2), 509-522.

Matteson, D. S., and James, N. A. (2014). A Nonparametric Approach for Multiple Change Point Analysis of Multivariate Data. *Journal of the American Statistical Association* **109**(505): 334–345. https://doi.org/10.1080/01621459.2013.849605.

McGuinness, J. L. and Bordne, E. F. (1972). A comparison of lysimeter-derived potential evapotranspiration with computed values (No. 1452). US Dept. of Agriculture.

McKee, T.B., Doesken, N.J. and Kleist, J. (1993). January. The relationship of drought frequency and duration to time scales. In *Proceedings of the 8th Conference on Applied Climatology* (Vol. 17, No. 22, pp. 179-183).

Mehrotra, R., Sharma, A. and Cordery, I. (2004). Comparison of two approaches for downscaling synoptic atmospheric patterns to multisite precipitation occurrence. *Journal of Geophysical Research D: Atmospheres*, *109*(14), 14107. https://doi.org/10.1029/2004JD004823

Milliman, J. D., & Meade, R. H. (1983). World-wide delivery of sediment to the oceans. *Journal of Geology*, *91*(1), 1–21. https://doi.org/10.1086/628741

Milly P.C., Kam J. and Dunne K.A., (2018). On the sensitivity of annual streamflow to air temperature. *Water Resources Research*, *54*(4), pp.2624-2641. https://doi.org/10.1002/2017WR021970

Mishra A.K. and Coulibaly P. (2009). Developments in hydrometric network design: A review. *Reviews of Geophysics*, *47*(2).

Mishra A.K. and Singh V.P. (2010). A review of drought concepts. *Journal of hydrology*, 391(1-2), pp.202-216. https://doi.org/10.1016/j.jhydrol.2010.07.012

Mishra M. and Panda G.K. (2016). Studies on shoreline changes using space born data along the part of Mahanadi delta, East Coast of India. *Journal of Coastal Sciences*, *3*(2), pp.18-25.

Misri R.L., Garde R.J. and Ranga Raju K.G. (1984). Bed load transport of coarse nonuniform

sediment. *Journal of Hydraulic Engineering*, *110*(3), pp.312-328.

Mohammed, I. N., Bomblies, A. and Wemple, B. C. (2015). The use of CMIP5 data to simulate climate change impacts on flow regime within the Lake Champlain Basin. *Journal of Hydrology: Regional Studies*, *3*, 160–186. https://doi.org/10.1016/j.ejrh.2015.01.002

Monalisha, M., and Panda, G., 2018. Coastal Erosion and Shoreline Change in Ganjam Coast along East Coast of India. *Journal of Earth Science & Climatic Change,* 9(4). http://doi:10.4172/2157-7617

Montanher, O. C., Novo, E. M. L. de M. & Souza Filho, E. E. de. (2018). Temporal trend of the suspended sediment transport of the Amazon River (1984–2016). *Hydrol. Sci. J.* **63**(13–14), 1901–1912. http://doi:10.1080/02626667.2018.1546387

Moriasi, D. N., Gitau, M. W., Pai, N., and Daggupati, P. (2015). Hydrologic and water quality models: Performance measures and evaluation criteria. *Transactions of the ASABE, 58*(6), 1763–1785. https://doi.org/10.13031/trans.58.10715

Moriasi, D. N., J. G. Arnold, M. W. Van Liew, R. L. Bingner, R. D. Harmel, and T. L. Veith. (2007). Model Evaluation Guidelines for Systematic Quantification of Accuracy in Watershed Simulations. *Transactions of the ASABE, 50*(3), 885–900. https://doi.org/10.13031/2013.23153

Mukhopadhyay, A., Ghosh, P., Chanda, A., Ghosh, A., Ghosh, S., Das, S., . . . Hazra, S. (2018). Threats to coastal communities of Mahanadi delta due to imminent consequences of erosion – Present and near future. *Science of The Total Environment,* 637-638, 717-729.

Nash J.E. and Sutcliffe, J.V. (1970). River flow forecasting through conceptual models part I—A discussion of principles. *Journal of hydrology*, *10*(3), pp.282-290.

Neitsch, S.L., Arnold, J.G., Kiniry, J.R. and Williams, J.R. (2011). Soil and Water Assessment Tool Theoretical Documentation Version 2009. Texas Water Resources Institute.

Nordin C.F.Jr. (1985). The sediment loads of rivers. In: J.C. Rodda (Editor), Factors of Hydrology II. John Wiley, New York, pp. 184 203.

NRLD, (2018). National Register of Large Dams. Government of India

Obi Reddy, G. P., Maji, A. K., and Gajbhiye, K. S. (2004). Drainage morphometry and its influence on landform characteristics in a basaltic terrain, Central India - A remote sensing and GIS approach. *International Journal of Applied Earth Observation and Geoinformation*, *6*(1), 1–16. https://doi.org/10.1016/j.jag.2004.06.003

Oudin, L., Hervieu, F., Michel, C., Perrin, C., Andréassian, V., Anctil, F., and Loumagne, C. (2005) Which potential evapotranspiration input for a lumped rainfall-runoff model? Part 2 - Towards a simple and efficient potential evapotranspiration model for rainfall-runoff modelling. *Journal of Hydrology*. Elsevier **303**(1–4): 290–306. https://doi.org/10.1016/j.jhydrol.2004.08.026.

Palmer, W.C. (1965). Meteorological Drought. *U.S. Weather Bur. Res*. Pap, No, pp. 45.

Panda D.K., Kumar A., Ghosh S. and Mohanty R.K. (2013). Streamflow trends in the Mahanadi River basin (India): Linkages to tropical climate variability. *Journal of Hydrology*, *495*, pp.135-149.

Pandey, D. Tiwari, A. D. and Mishra, V. (2022). On the occurrence of the observed worst flood in Mahanadi River basin under the warming climate. *Weather and Climate Extremes*, 38, 100520.

Panigrahy B.K. and Raymahashay B.C. (2005). River water quality in weathered limestone: a case

study in upper Mahanadi basin, India. *Journal of earth system science*, *114*(5), pp.533-543.
Parhi, P.K., Mishra, S.K., Singh, R., Tripathi, V.K. (2012). Water Week 2012-Water, Energy and Food Security: Call for Solutions.
Pektaş, A. O., and Doğan, E. (2015). Prediction of bed load via suspended sediment load using soft computing methods. *Geofizika*, *32*(1), 27–46. https://doi.org/10.15233/gfz.2015.32.2
Perrin, C. Michel, C. Andre, V. (2003). Improvement of a parsimonious model for streamflow simulation 279, 275–289. https://doi.org/10.1016/S0022-1694(03)00225-7
Pettitt, A. N. (1979). A Nonparametric Approach to the Change-Point Problem. *Journal of the Royal Statistical Society,* 28(2), 126-135.
Pilon, P.J., Yuzyk, T.R., Hale, R.A. and Day, T.J. (1996). Challenges facing surface water monitoring in Canada. *Canadian Water Resources Journal*, *21*(2), pp.157-164.
Priestley, C. H. B., and Taylor, R. J. (1972) On the assessment of surface heat flux and evaporation using large-scale parameters. *Monthly weather review*, *100*(2), 81-92. https://doi.org/10.1175/1520-0493(1972)100<0081:OTAOSH>2.3.CO;2
Pruski, F. F., and Nearing, M. A. (2002). Runoff and soil-loss responses to changes in precipitation: A computer simulation study. *Journal of Soil and Water Conservation*, *57*(1), 7–16
Rainato, R., Mao, L., García-Rama, A., Picco, L., Cesca, M., Vianello, A., et al. (2016). Three decades of monitoring in the Rio Cordon instrumented basin: Sediment budget and temporal trend of sediment yield. *Geomorphology*, *291*, 45–56. https://doi.org/10.1016/J.GEOMORPH.2016.03.012
Recking, A. (2013). Simple Method for Calculating Reach-Averaged Bed-Load Transport. *Journal of Hydraulic Engineering*, *139*(1), 70–75. https://doi.org/10.1061/(asce)hy.1943-7900.0000653
Renard, K., Foster, G., Weesies, G., McCool, D., and Yoder, D. (1997). Predicting soil erosion by water: a guide to conservation planning with the Revised Universal Soil Loss Equation (RUSLE). *Agricultural Handbook No. 703*
Reshmidevi, T. V., Nagesh Kumar, D., Mehrotra, R., and Sharma, A. (2018). Estimation of the climate change impact on a catchment water balance using an ensemble of GCMs. *Journal of Hydrology*, *556*, 1192–1204. https://doi.org/10.1016/j.jhydrol.2017.02.016
Roderick, M. L., Rotstayn, L. D., Farquhar, G. D., and Hobbins, M. T. (2007) On the attribution of changing pan evaporation. *Geophysical Research Letters* **34**(17): 1–6. https://doi.org/10.1029/2007GL031166.
Ruhi, A., Messager, M.L. and Olden, J.D. (2018). Tracking the pulse of the Earth's fresh waters. *Nature Sustainability*, *1*(4), pp.198-203.
Sadeghi, S. H. R., Saeidi, P., Singh, V. P., and Telvari, A. R. (2019). How persistent are hysteresis patterns between suspended sediment concentration and discharge at different timescales? *Hydrological Sciences*, 64(15), 1909–1917. https://doi.org/10.1080/02626667.2019.1676895
Saliha, A. H., Awulachew, S. B., Cullmann, J., and Horlacher, H. B. (2011). Estimation of flow in ungauged catchments by coupling a hydrological model and neural networks: Case study. *Hydrology Research*, *42*(5), 386–400. https://doi.org/10.2166/nh.2011.157
Salvi, K., S. Kannan, and S. Ghosh (2013). High-resolution multisite daily rainfall projections in India with statistical downscaling for climate change impact assessment, *J. Geophys. Res. Atmos*., 118,

3557-3558, http://dx.doi.org/10.1002/jgrd.50280.
Sankarasubramanian, A., Vogel, R. M., and Limbrunner, J. F. (2001). Climate elasticity of streamflow in the United States. *Water Resources Research* **37**(6): 1771–1781. https://doi.org/10.1029/2000WR900330.
Santhi C., Arnold J.G., Williams J.R., Dugas W.A., Srinivasan R. and Hauck L.M. (2001). Validation of the swat model on a large river basin with point and nonpoint sources. *JAWRA Journal of the American Water Resources Association*, *37*(5), pp.1169-1188.
Sarath, M. and Srinivas, V. V. (2019). Short to medium range probabilistic streamflow forecasting for Tel river using the Hydrologic Ensemble Forecast Service. In proceedings of national conference on flood early warning for disaster risk reduction, Organised by NRSC, & CWC under National Hydrology Project, 30-31 May 2019, Hyderabad, pages 80-87.
Schoklitsch, A. (1962). Vol. 1 of Handbuch des wasserbaues, 173–177. [In German.] Vienna, Austria: Springer
Schumm, S. A. (1956). Evolution of drainage systems and slopes in bad lands at Perth Amboy, New Jersey. *Bulletin of the Geological Society of America*, *67*(5), 597–646. https://doi.org/10.1130/0016-7606(1956)67[597:EODSAS]2.0.CO;2
Sen, P. K. (1968). Estimates of the regression coefficient based on Kendall's tau. *Journal of the American statistical association*, 63(324), 1379-1389. https://doi.org/10.1080/01621459.1968.10480934
Serfling, R., & Xiao, P. (2007). A contribution to multivariate L-moments: L-comoment matrices. *Journal of Multivariate Analysis*, 98(9), 1765-1781.
Sharma, T.C. and Panu, U.S. (2010). Analytical procedures for weekly hydrological droughts: a case of Canadian rivers. *Hydrological Sciences Journal–Journal des Sciences Hydrologiques*, 55(1), pp.79-92. https://doi.org/10.1080/02626660903526318.
Shiau, J.-T., Hung, Y.-N., and Sie, H.-E. (2018). "Effects of Hedging Factors and Fuzziness on Shortage Characteristics During Droughts." Water Resources Management, *Water Resources Management*, 32(5), 1913–1929.
Shields, A. (1936). Anwendug der Aehnlichkeitsmechanik und der Turbulenzforschung auf die Geschiebebewegung. [In German]. Berlin: Mitteilungen der Preussiischen Versuchsanstalt fur Wasserbau and Schiffhau
Shukla, S. and Wood, A.W. (2008). Use of a standardized runoff index for characterizing hydrologic drought. *Geophysical research letters*, 35(2). https://doi.org/10.1029/2007GL032487.
Singh V.P., Frevert D.K., Rieker J.D., Leverson V., Meyer S. and Meyer S. (2006). Hydrologic modeling inventory: Cooperative research effort. *Journal of Irrigation and Drainage Engineering*, *132*(2), pp.98-103.
Singh, R., Kumar, R. (2015). Vulnerability of water availability in India due to climate change: A bottom-up probabilistic Budyko analysis. *Geophysical Research Letters*, *42*(22), 9799-9807. https://doi.org/10.1002/2015GL066363
Singh, R., Kundu, D.K., and Kumar, A. (2009). Characterisation of dominant soil subgroups of Eastern India for formulating water management strategies. *Research bulletin no.44*. Bhubaneswar, India:

Water Technology Center of Eastern Region (Indian Council of Agricultural Research)
Singh, V.P. and Woolhiser, D.A. (2002) Mathematical Modelling of Watershed Hydrology. *Journal of Hydrological Engineering*, ASCE, 7, 270-292. https://doi.org/10.1061/(ASCE)1084-0699(2002)7:4(270)
Soľáková, T., De Michele, C. and Vezzoli, R., (2014). Comparison between parametric and nonparametric approaches for the calculation of two drought indices: SPI and SSI. *Journal of Hydrologic Engineering*, 19(9), p.04014010. https://doi.org/10.1061/(ASCE)HE.1943-5584.0000942
Solari, S., Egüen, M., Polo, M.J. and Losada, M.A. (2017). Peaks Over Threshold (POT): A methodology for automatic threshold estimation using goodness of fit p-value. *Water Resources Research*, 53(4), 2833-2849.
Sonali, P. and Nagesh Kumar, D. (2013). Review of trend detection methods and their application to detect temperature changes in India.*Journal of Hydrology,* 476, 212-227. https://doi:10.1016/j.jhydrol.2012.10.034
Song, X., Zhuang, Y., Wang, X., Li, E., Zhang, Y., Lu, X., Yang, J., and Liu, X. (2020). Analysis of hydrologic regime changes caused by dams in china. *Journal of Hydrologic Engineering,* 25 (4).
Spence, C., Saso, P. and Rausch, J. (2007). Quantifying the impact of hydrometric network reductions on regional streamflow prediction in northern Canada. *Canadian Water Resources Journal*, *32*(1), pp.1-20.
Sreeparvathy, V. and Srinivas, V.V. (2020). A fuzzy entropy approach for design of hydrometric monitoring networks. *Journal of Hydrology*, *586*, p.124797.
Sreeparvathy, V. and Srinivas, V.V. (2022). A Bayesian Fuzzy Clustering Approach for Design of Precipitation Gauge Network Using Merged Remote Sensing and Ground-Based Precipitation Products. *Water Resources Research*, *58*(2), p.e2021WR030612.
Stedinger, J. R. (1983). Estimating a regional flood frequency distribution. *Water Resources Research*, 19(2), 503-510.
Subramanya, K. (2013). *Engineering Hydrology*. 4th Edition. New Delhi (India): McGraw Hill Education Pvt.Ltd.
Sveinsson, O. G. B., Salas, J. D., and Boes, D. C. (2003). Uncertainty of quantile estimators using the population index flood method. Water Resources Research, 39(8).
Sveinsson, O. G., Boes, D. C., and Salas, J. D. (2001). Population index flood method for regional frequency analysis. *Water Resources Research*, 37(11), 2733-2748.
Syvitski, J. P., 2003. Supply and flux of sediment along hydrological pathways: research for the 21st century.*Global and Planetary Change,* 39(1-2), 1-11. https://doi:10.1016/S0921-8181(03)00008-0
Syvitski, J. P., Morehead, M. D., Bahr, D. B., and Mulder, T. (2000). Estimating fluvial sediment transport: The rating parameters. *Water Resources Research*, *36*(9), 2747–2760. https://doi.org/10.1029/2000WR900133
Syvitski, J. P., Peckham, S. D., Hilberman, R. and Mulder, T. (2003). Predicting the terrestrial flux of sediment to the global ocean: a planetary perspective. *Sedimentary Geology,* 162(1-2), 5-24. https://doi:10.1016/S0037-0738(03)00232-X

Syvitski, J., Vörösmarty, C., Kettner, A., and Green, P. (2005). Impacts of humans on the flux of terrestrial sediment to the global coastal ocean. *Science,* 308(5720), 376-380. https://doi:10.1126/science.1109454

Taghian, M., Rosbjerg, D., Haghighi, A., and Madsen, H. (2014). Optimization of Conventional Rule Curves Coupled with Hedging Rules for Reservoir Operation. *Journal of Water Resources Planning and Management*, 140(5), 693–698.

Thiessen, A. H. (1911). Precipitation Averages for Large Areas. *Monthly Weather Review*, *39*(7), 1082–1089. https://doi.org/10.1175/1520-0493(1911)39<1082b:pafla>2.0.co;2

Tigkas, D., Vangelis, H. and Tsakiris, G. (2019). Drought characterisation based on an agriculture-oriented standardised precipitation index. *Theoretical and applied climatology*, 135(3), pp.1435-1447. https://doi.org/10.1007/s00704-018-2451-3

Trenberth K.E., Dai, A., Rasmussen, R.M. and Parsons, D.B. (2003). The changing character of precipitation. *Bulletin of the American Meteorological Society*, *84*(9), pp.1205-1218. https://doi.org/10.1175/BAMS-84-9-1205

Tsakiris, G. and Vangelis, H.J.E.W. (2005). Establishing a drought index incorporating evapotranspiration. European water, 9(10), pp.3-11.

Tu, M.-Y., Hsu, N.-S., and Yeh, W. W.-G. (2003). Optimization of Reservoir Management and Operation with Hedging Rules. *Journal of Water Resources Planning and Management*, 129(2), 86–97.

Tu, M.-Y., Hsu, N.-S., Tsai, F. T.-C., and Yeh, W. W.-G. (2008). Optimization of Hedging Rules for Reservoir Operations. *Journal of Water Resources Planning and Management*, 134(1), 3–13.

Vanoni, V. A. (2006). *Sedimentation engineering*. *Sedimentation Engineering*. https://doi.org/10.1061/9780784408230

Vercruysse, K., Grabowski, R. C., and Rickson, R. J. (2017). Suspended sediment transport dynamics in rivers: Multi-scale drivers of temporal variation. *Earth-Science Reviews*, 166, 38–52. https://doi.org/10.1016/j.earscirev.2016.12.016

Vergni, L., Vinci, A. and Todisco, F. (2021). Effectiveness of the New Standardized Deficit Distance Index and other Meteorological Indices in the Assessment of Agricultural Drought Impacts in Central Italy. *Journal of Hydrology*, pp.126986. https://doi.org/10.1016/j.jhydrol.2021.126986

Vicente-Serrano, S.M., Beguería, S. and López-Moreno, J.I. (2010). A multiscalar drought index sensitive to global warming: the standardized precipitation evapotranspiration index. *Journal of climate*, 23(7), pp.1696-1718. https://doi.org/10.1175/2009JCLI2909.1.

Wagener T., Sivapalan M. and McGLYNN B.R.I.A.N. (2008). Catchment classification and services. Toward a new paradigm for catchment hydrology driven by societal needs. *Encyclopedia of Hydrological Sciences, John Wiley, Chichester, UK*.

Waikhom, S. I., and Yadav, S. M. (2017a). Prediction of total load transport of an Indian alluvial river to estimate unmeasured bed load through an alternative approach. *Current Science*, *113*(6).

Waikhom, S. I., and Yadav, S. M. (2017b). A total load approach to predict bed load transport of Indian alluvial river. *ISH Journal of Hydraulic Engineering*, *24*(1), 92–99. https://doi.org/10.1080/09715010.2017.1354338

Walling, D. E., and Fang, D. (2003). Recent trends in the suspended sediment loads of the world's rivers. *Global and Planetary Change*, *39*(1–2), 111–126.

Walling, D., (1995). Suspended sediment yields in a changing environment. In A. Gurnell, and G. Petts (Eds.), *Changing River Channels* (149-176). Chichester: Wiley.

Wang, H. J., Yang, Z. S., Saito, Y., Liu, J. P., Sun, X. X., and Wang, Y. (2007). Stepwise decreases of the Huanghe (Yellow River) sediment load (1950–2005): Impacts of climate change and human activities, *Global Planet. Change*, 57, 331–354.

Wang, Q.J. (1991). The POT model described by the generalized Pareto distribution with Poisson arrival rate. *Journal of Hydrology*, 129(1-4), 263-280.

Wang, W., and Fu, J. (2018) Global assessment of predictability of water availability: A bivariate probabilistic Budyko analysis. *Journal of Hydrology*. Elsevier B.V. **557**: 643–650. https://doi.org/10.1016/j.jhydrol.2017.12.068.

Webster, R., and Mcbratney, A. B. (1989). On the Akaike Information Criterion for choosing models for variograms of soil properties. *Journal of Soil Science*, *40*(3), 493–496. https://doi.org/10.1111/j.1365-2389.1989.tb01291.x

Wheaton, J., Brasington, J., Darby, S., and Sear, D. (2010). Accounting for uncertainty in DEMs from repeat topographic surveys: improved sediment budgets. *Earth Surface Processes and Landforms,* 35(2), 136-156. https://doi:10.1002/esp.1886

Willmott, C.J. (1982). Some comments on the evaluation of model performance. *Bulletin of the American Meteorological Society*, *63*(11), pp.1309-1313.

Wischmeier, W.H., Smith, D.D., and Uhland, R.E. (1958). Evaluation of Factors in the Soil Loss Equation. *Agricultural Engineering, 39*, 458-462

Wood, J. (1996). The geomorphological characterisation of digital elevation models. University of Leicester (United Kingdom).

World Meteorological Organization (WMO), (2012). Standardized Precipitation Index user guide. WMO-No. 1090. Geneva, Switzerland. Retrieved from. http://library.wmo.int/pmb_ged/wmo_1090_en.pdf

Xu, N. (2018). Detecting Coastline Change with All Available Landsat Data over 1986–2015: A Case Study for the State of Texas, USA. *Atmosphere,* 9(3), 107. https://doi:10.3390/atmos9030107

Yadav, A., Chatterjee, S. and Equeenuddin, S.M. (2021). Suspended sediment yield modeling in Mahanadi River, India by multi-objective optimization hybridizing artificial intelligence algorithms. *International Journal of Sediment Research*, *36*(1), pp.76-91.

Yadav, S. M. and Samtani, B. K. (2008). Bed Load Transport in Tapi River, India. *Global Journal of Environmental Research*, *2*(2), 96–101.

Yang, H., and Yang, D. (2011) Derivation of climate elasticity of runoff to assess the effects of climate change on annual runoff. *Water Resources Research*. John Wiley & Sons, Ltd **47**(7). https://doi.org/10.1029/2010WR009287.

Yang, H., Yang, D., and Hu, Q. (2014) An error analysis of the Budyko hypothesis for assessing the contribution of climate change to runoff. *Water Resources Research* **50**(12): 9620–9629. https://doi.org/10.1002/2014WR015451.

Yu, J., Fu, Y., Li, Y., Han, G., Wang, Y., Zhou, D. and Meixner, F. X. (2011). Effects of water discharge and sediment load on evolution of modern Yellow River Delta, China, over the period from 1976 to 2009. *Biogeosciences*, 8(9), 2427-2435.

Yue, S. (1999). Applying bivariate normal distribution to flood frequency analysis. *Water international*, 24(3), 248-254.

Yue, S., and Rasmussen, P. (2002). Bivariate frequency analysis: discussion of some useful concepts in hydrological application. *Hydrological Processes*, 16(14), 2881-2898.

Yue, S., Pilon, P., and Phinney, B., (2003). Canadian streamflow trend detection: impacts of serial and cross-correlation. *Hydrological Sciences,* 48(1), 51-63. https://doi:10.1623/hysj.48.1.51.43478

Zeng, Z., Ziegler, A. D., Searchinger, T., Yang, L., Chen, A., Ju, K., Piao, S., Li, L.Z.X., Ciais, P., Chen, D., Liu, J., Azorin-Molina, C., Chappell, A., Medvigy, D. and Wood, E.F. (2019) A reversal in global terrestrial stilling and its implications for wind energy production. *Nature Climate Change*. Nature Publishing Group 1–7. https://doi.org/10.1038/s41558-019-0622-6.

Zhang, L. S. V. P., and Singh, V. P. (2006). Bivariate flood frequency analysis using the copula method. *Journal of hydrologic engineering*, 11(2), 150-164.

Zhang, L., Dawes, W. R., and Walker, G. R. (2001) Response of mean annual evapotranspiration to vegetation changes at catchment scale. *Water resources research*, *37*(3), 701-708. https://doi.org/10.1029/2000WR900325.

Zhang, L., Hickel, K., Dawes, W. R., Chiew, F. H., Western, A. W., and Briggs, P. R. (2004) A rational function approach for estimating mean annual evapotranspiration. *Water Resources Research* **40**(2). https://doi.org/10.1029/2003WR002710.

Zhongbao, X., Bofu, Y., and Yuguo, H. (2015). Spatiotemporal Variations in Annual Sediment Yield from the Middle Yellow River, China, 1950–2010. *Journal of Hydrologic Engineering,* 20(8).

Zounemat-Kermani, M., Kişi, Ö., Adamowski, J., and Ramezani-Charmahineh, A. (2016). Evaluation of data driven models for river suspended sediment concentration modeling. *Journal of Hydrology*, *535*, 457–472.